STUDYING YOUNG STELLAR OBJECTS WITH NEAR-IR

NON-REDUNDANT APERTURE MASKING AND MILLIMETER

INTERFEROMETRY

By

Dary Alexandra Ruíz Rodríguez

A thesis

Submitted for the degree of Doctor of Philosophy of

The Australian National University.

October, 2017

DECLARATION

I hereby declare that the work in this thesis is that of the candidate alone, except where indicated below or in the text of the thesis, and it has not been submitted in whole or in part for any other degree at this or any other university.

Chapter 3: "*The ALMA Early Science View of FUor/EXor objects. II. The Very Wide Outflow Driven by HBC 494*", is published in Monthly Notices of the Royal Astronomical Society as D. Ruiz-Rodriguez, L. A. Cieza, J. P. Williams, J. J. Tobin, A. Hales, Z. Zhu, K. Muzic, D. Principe, H. Canovas, A. Zurlo, S. Casassus, S. Perez, and J. L. Prieto, 2017, MNRAS 466, 3519-3532

Chapter 4: " *The ALMA Early Science View of FUor/EXor objects. III. The Slow and Wide Out ow of V883 Ori*". is published in Monthly Notices of the Royal Astronomical Society as D. Ruiz-Rodriguez, L. A. Cieza, J. P. Williams, J. J. , D. Principe, Tobin, Z. Zhu, and A. Zurlo, 2017, MNRAS 468, 3266-3532.

Chapter 5: "*The Frequency Of Binary Star Interlopers Amongst Transitional Disks*" is published in Monthly Notices of the Royal Astronomical Society as D. Ruiz-Rodriguez, M. Ireland, L. Cieza, and A. Kraus 2016, MNRAS 463, 3829-3847.

Chapter 6: is a preliminary version of the paper in preparation titled "*ALMA Survey Of Class II Disks In The IC 348 Cluster*".

Sean Andrews (CfA/Harvard-Smithsonian Center for Astrophysics) performed a Monte Carlo Analysis which appears in the fourth paper and Chapter 6.

The four published or in preparation papers presented in this thesis use data from the following instruments: NIRSPEC, a cross-dispersed echelle spectrograph designed for the Keck II Telescope at Maunakea, U.S.A; The Atacama Large Millimeter/submillimeter Array (ALMA) at the Atacama desert of northern Chile; and the Magellan Inamori Kyocera Echelle (MIKE), a double echelle spectrograph at the Magellan (Clay) 6.5 m telescope, located in Las Campanas, Chile. The data reduction, analysis, writing of the papers and the thesis was performed by the candidate in its entirety, incorporating feedback from co-authors and referees.

Dary A. Ruíz-Rodríguez

October, 2017

ACKNOWLEDGMENTS

Foremost, I would like to express my sincere gratitude to my advisor Dr. Lucas A. Cieza. Probably the best thing that could have happened to me was a challenging beginning in my Ph.D. Because in my most exhausting period as a Ph.D. student and with a pinch of hope, I contacted Lucas and asked him basically to be insane, and accept a student based in Australia, while he was working in Chile. Fortunately, he was as crazy as me and accepted me as his Ph.D. student. Since that time, I found support, motivation, enthusiasm, and immense knowledge on the other side of the world and 12 hours of difference. He was always available to answer my questions, advise me, and show me that science can take place anywhere. Lucas made my dissertation possible with his immense patience and dedication every day at any minute. At some point, I realized that I was growing up as a researcher and Lucas was preparing a colleague with an eternal student soul. Each time, during our meetings, very early for him and very late for me, we had always some stunning description or discussion about something that I did not before understand or could not visualize, and I am still learning from him. In short, I owe you so much that simple words could never be enough to express my gratitude. I only can say that WE DID it! I could not have imagined having a better advisor and mentor for my Ph.D. study.

I would also like to thank Dr. David Yong for taking the trouble to help me, support me and for his excellent cooperation. In Australia, I could not find a better adviser.

And my mom, Patricia, Diego, Henry, and my friends, Rondon and Yamile,

thanks for your support and listening. You are always there for me.

Thank you very much, everyone! All of you made this possible.

ABSTRACT

Thesis Advisor: Lucas A. Cieza

Thesis by: Dary A. Ruíz-Rodríguez

Circumstellar disks and outflows play a central role in the growth of low-mass ($M < 2$ $M_\odot$) stars and the formation of planetary systems. These disks are ubiquitous at young ages (< 1 Myr), as they are naturally formed during the gravitational collapse of protostellar cores due to the conservation of angular momentum. Circumstellar disks feed the forming stars and provide an environment for small grains to eventually grow into rocky planets and the cores of giant planets at a wide range of stellocentric distances ($\sim$ 0.1-100 au). In parallel to the growth solids in the disk, bipolar outflows and winds are generated on similar physical scales. Outflows carry angular momentum away and help the accretion of circumstellar material onto the central object. They also play an important role in the dissipation of the envelope that marks the transition from the Class I (a deeply embedded protostar) to Class II stage (an optically visible T Tauri star). Eventually, the primordial disk disperse, leaving a star surrounded by a remnant debris (Class III) object and likely a system of planetesimals and planets.

This thesis incorporates high-sensitivity millimeter-wavelength interferometry and near-infrared Non-Redundant Mask (NRM) Interferometry to assess molecular outflow and disks properties in Class I-II objects. It explores the physical mechanisms dispersing the disk and envelope system (e.g., outflows and dynamical interactions in binary systems) and the properties of protoplanetary disks as a function of stellar mass at an age of 2-3 Myr.

We investigate the properties of the Class I molecular outflows present in HBC 494 and V883 Ori, two young stellar objects experiencing episodic events of extreme accretion known as FU Ori outbursts. These outflows help to disperse the surrounding envelope at very early stages while removing angular momentum from the disk. We estimate the kinematic properties and describe physical structures of the outflows using the ^{12}CO and ^{13}CO emissions lines. Similarly, the C^{18}O emission line is used to describe envelope material of both sources. An outstanding result is the wide-opening angle of the outflow cavities of $\sim$ 150° for both sources. Outflows masses in both FUors are on the same order of magnitude, while V883 Ori shows an outflow component that is much slower (characteristic velocity of only 0.65 km s^{-1}) than seen in other FUors such as HBC 494. To date, interferometric studies of FUors are scarce and more observations needed in order to compare with other objects at a similar sensitivity and resolution.

In addition, using NRM, we searched for binary companions to objects previously classified as Transitional Disks (TD, disks with inner opacity holes) in nearby (d < 300 pc) star-forming regions (Ophiuchus, Taurus-Auriga, and IC348) and investigate the interaction with (sub)stellar companions as a possible mechanism for the depletion of their inner disks. We implement a new method of completeness correction using a combination of randomly sampled binary orbits and Bayesian inference. We find that $\sim$ 0.38$\pm$0.09 of the TDs are actually circumbinary disks, while the remaining objects are transitional disks where the inner holes are the result of other internal processes such as photoevaporation, and/or planet-disk interactions.

Finally, we present an ALMA 1.3 mm survey of Class II sources in the bench-

mark 2-3 Myr stellar cluster IC 348 to investigate the properties of disks at the time 50% of the disks have already been completely dispersed. We find that the detection rate in 1.3 mm continuum is a strong function of stellar mass. Most targets with masses 0.3< $M_\odot$ remain undetected down to a 3-σ sensitivity of 0.45 mJy, corresponding to a disk dust mass of $\sim$0.9 $M_\oplus$. A stacking analysis of the non-detections suggests that the typical dust mass around most 2-3 Myr old M-type stars is 0.2 $M_\oplus$ (or 0.07 $M_{\rm JUP}$ of gas + dust, assuming a standard gas to dust mass ratio of 100). A Bayesian analysis is used to statistically compare IC 348 to other star-forming regions. As a general result, this analysis shows that IC 348 disks are a factor of 5 fainter on average than in Taurus, Cha I, and Lupus. While, IC 348 and σ Ori have similar distributions. On the other hand, Upper Sco disks are definitely fainter on average than IC 348. The resulting cumulative distribution functions confirm a clear evolution (depletion of mm-sized grains) of the circumstellar disks in these regions over a period of 1-10 Myr.

Life is not about excuses, life is about actions.

<div style="text-align: right">DAR, *Life...*</div>

x

Contents

4 The ALMA Early Science View of FUor/EXor objects. III. The Slow and Wide Outflow of V883 Ori. **103**

Figure Index

Table Index

1

Introduction

The star-formation process begins when a slowing-rotating molecular core collapses as a result of gravity. The collapsing material eventually forms a young stellar object at the center. During this process, and as a result of the conservation of the angular momentum, the material does not fall directly towards a point, instead, a disk-like structure is formed around the protostellar core. As angular momentum is moved outward, some of the material in the disk moves inwards and fall onto the protostar, building up the stellar mass. Another mechanism to release angular momentum from the is the spurting out of mass in a bipolar-shape flow. These outflows clear out the feeding material surrounding the forming star, and thus are important to determine the final stellar mass (e.g. Williams & Cieza, 2011; Armitage, Livio & Pringle, 2001; Hartmann, Herczeg & Calvet, 2016).

The combination of intensive ground- and space-based observations and state-of-the-art theoretical simulations have established that circumstellar disks and molecular outflows are an integral part of the formation and evolution of stars

(Williams & Cieza, 2011). Also, it is well established that planets form in such disks composed of gas, dust, and ices. To date, more than 3500 exoplanets have been detected with a wide variety of masses and orbital parameters (Batalha, 2014). Despite all the efforts to observationally constrain the location and age of planet formation, a comprehensive picture of where, when, and how these planets are formed is still largely incomplete. **Wide-separation exoplanet discoveries at 50 − 300 au (Marois et al., 2008; Kuzuhara et al., 2013; Rameau et al., 2013; Lafrenière, Jayawardhana & van Kerkwijk, 2008) are particularly difficult to explain by current planet-formation theories: *core-accretion* vs. *disk instability*. Based on these theoretical models, the core-accretion scenario is more suitable for explaining the formation process of planets ($<$ 0.3 M$_{Jup}$), whose orbits lie at $<$ 5 au from the host star (Pollack et al., 1996). While the disk instability scenario predicts the rapid formation of giant planets ($>$2 M$_{Jup}$) in the outer regions of the disk ($>$ 30 au). A caveat with the latter scenario is that it requires a disk-star mass ratio of $>$10^{-2}, and if the disk is sufficiently massive, it is more likely a fragmentation into a stellar companion instead of a planetary companion (Boss, 2001). More relevant for this thesis, these two models predict different planet formation timescales (core accretion: 3-5 Myr vs. disk instability: 0.5 Myr), which extends to the disk dispersal timescales.**

A major challenge today is to discern which processes disperse the dust and gas in the disk-envelope system and to constrain the initial conditions, timescales, and planet-formations mechanisms, as well as the role of environment. In

addition, it is imperative to investigate the relationship between accretion and energetic outflows in young stellar systems, to understand 1) the low-mass star-formation efficiency of in turbulent clouds and 2) the efficient transport of angular momentum that allows the accretion of circumstellar material onto the central star. These circumstellar disks and molecular outflows are the focus of this thesis, which consists of 3 related but independent projects, distributed in four first-author papers.

In the first project, we use interferometric millimeter-wavelength observations to investigate the circumstellar environments (disks, outflows, and envelopes) of two embedded (Class-I) young stellar objects undergoing events of intense disk accretion known as FU Ori outburst (Hartmann & Kenyon, 1996). In the episodic accretion paradigm (e.g., Audard et al. 2014), these FU Ori outbursts are believed to be short-lived but relative common events during early stages (age <0.5 Myr) of the star-formation process and to play a crucial role in building up stellar masses. In particular, we present the kinematic study of the HBC 494 and V883 Ori systems using ALMA 1.3mm/230 GHz images at $0.2''$ resolution of the ^{12}CO, ^{13}CO and $C^{18}O$ molecular lines. Both objects show spectacular wide-angle outflows that are likely to impact disk evolution and the surrounding cloud environment. The intense outflow activity of these outbursting sources also highlights the inmate connection between accretion and outflows.

In the second project, we study primordial (gas-rich) disks with inner opacity holes. Since these systems are believed to be in a "transition phase" between an optically thick and an optically thin disk (i.e. between Class II and Class III objects), they are commonly known as Transitional Disks (TDs). TDs are a

relatively rare (20% of the general disk population depending on exact adopted definition) and heterogeneous group of objects (e.g., Cieza et al. 2012). They have attracted significant attention as they present signatures of different disk evolution process, including planet formation. TDs are identified and classified using their Spectral Energy Distributions (SEDs), and their main characteristic is a decreased level of IR excess emission with respect to typical T Tauri stars (Espaillat et al., 2012) indicating an inner opacity hole. However, the origin of these holes (planet formation, photo-evaporation or binary interactions) can not be established from the SED alone. In Ruíz-Rodríguez et al. (2016a) we use near-IR Non-Redundant Aperture Masking (NRM) to search for (sub)stellar companions in TD objects in order to identify Circumbinary Disks (CDs), i.e. a binary star surrounded by a disk. With these observations, we investigate the fraction of TDs that have companions that could explain the opacity holes in their inner disks.

The last project is a 1.3 mm continuum survey of 136 Class II disks in the 2-3 Myr benchmark cluster, at an age where 50% of the disk population has already been dispersed. We detect 46 of them and construct the disk luminosity function for the cluster. An staking analysis of the 90 non-detections suggest that the typical (average) disk in the cluster should have a dust mass of just 0.2 $M_\oplus$, although disk masses are a strong function of stellar mass. We compare the luminosity function of IC 348 to those of younger and older regions taking into consideration the differences in Initial Mass Functions of the samples and find a clear evolution of disk masses from 1 to 10 Myr.

1.1   Overview

Observations in the infrared and (sub-) millimeter region of the electromagnetic spectrum have allowed the discovery of embedded sources in dusty envelopes, known as protostars. These objects presumably have undergone the freefall collapse of dusty material and contain high extinct central sources that remain undetected at optical wavelength range but become visible in the infrared spectral region (Figure 1.1). These deeply embedded objects are believed to be early stages of the young stellar objects that are eventually classified as T Tauri stars. Young Stellar Objects (YSOs) can be described by the slope of their SED, α, measured between $\sim$2 and 20 microns (Figure 1.1).

From these SEDs, spectral classes 0, I, II and III have been defined with approximate characteristics shown in Figure 1.1, from top to bottom, respectively. Class 0 and Class I sources are deeply embedded YSOs with $\alpha > 3$. Class 0 sources are characterized by bolometric temperatures < 70 K (Chen et al., 1995). Their high ratio of sub-millimeter to bolometric luminosity, suggesting that the envelope mass exceeds the central stellar mass. Class I sources also have strong sub-millimeter emission, but their bolometric temperatures are > 70 K. Both Class 0 and Class I sources typically have bipolar molecular outflows that carry away mass and angular momentum. The infalling envelope material settles into a rotating flattened disk around the source, due to the conservation of angular momentum. As the envelope the dissipates, Class I sources transition to a Class II source with $-1.6 < \alpha < -0.3$ (Greene et al., 1994). At this stage, the central star becomes optically visible and the SED is characterized by the IR excess an optically thick disk. Eventually, the dissi-

pation of this circumstellar material will lead to the Class III with $\alpha < -1.6$, where most of the detectable emission is from the central star (Greene et al., 1994).
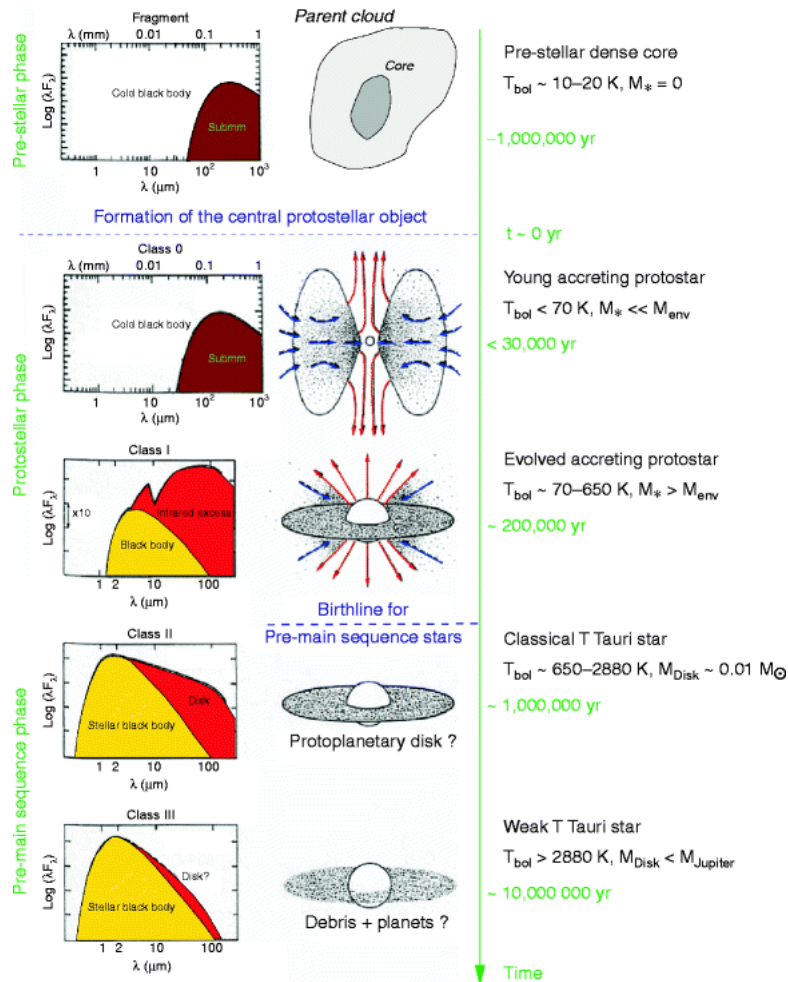
Figure 1.1: Artistic image of a protostellar evolution process together with its corresponding observed Spectral Energy Distribution (SED). Right: Star Formation Process. Left: SED at the different stages. This image is Figure 1 from André (2002).

1.2   Protoplanetary disks and their evolution

During the core collapse process in a collapsing molecular core and while the central protostellar his building up, one of the most significant consequences is the formation of a circumstellar disk due to the conservation of the angular momentum. With a persisting small amount of material still accreting (Dullemond et al., 2007), the accretion rate decreases from $\dot{\mathrm{M}} \sim 10^{-5} - 10^{-6}\mathrm{M_\odot}$/year to $\dot{\mathrm{M}} \sim 10^{-7} - 10^{-9}\mathrm{M_\odot}$/year. This disk evolves rapidly, reaching an extension of approximately $R(t) \propto \Omega^2 t^3$, where Ω is the angular momentum of the system and has to be conserved with an infall time of magnitude t^3 (Terebey, Shu & Cassen, 1984). However, since the inclusion of magnetic fields in simulations, it has been shown that the extension of the disk might grow only linearly (Basu, 1998), thus giving way for new uncertainties in the initial disk sizes and masses.

The disk can achieve extensions of up to 100 au or more in a period of approximately few x 10^5 years. More specifically, this disk is named a *protoplanetary disk*, a term that is typically only applied to the **the primordial, gas-rich** phase of the disk. The emission of these disks can be locally approximated as blackbodies emitting at different wavelengths and globally described as the sum of the fluxes from annuli emitting at different radii. Equation 1.1 states the flux of a spatially thin disk,

$$F_\nu = \frac{cos\theta}{D^2} \int_{r_{inner}}^{r_{outer}} B_\nu(T_d)(1 - e^{-\tau_\nu})2\pi r dr. \qquad (1.1)$$

where, θ represents the inclination of the disk to the line of sight, D is the

distance to the system, r_{inner} and r_{outer} are the disk's inner and outer radii, $B_\nu(T_d)$ is the Plank's function at a specific temperature and τ_ν is the optical depth of the dust. While optically thick IR emission provides no useful information on disk masses (e.g. Calvet et al., 2002), an appropriate use of Equation 1.1 in the optically thin (sub)millimeter regime is the determination of dust masses, of fundamental importance for the formation of different types of planets. However, because dust grains emit more efficient at wavelengths comparable to their size, (sub)millimeter dust continuum observations only traces a limited range of grain sizes. Multi-wavelength (sub)millimeter and centimeter-wavelength observations have provided evidence for centimeter sized grains. Radiative transfer models can be used to calculate the properties of these systems from the observed SEDs (e.g. Dullemond et al., 2007). Figure 1.2 shows the predicted excess emission from different types of circumstellar disks, using the CGPlus code Dullemond, Dominik & Natta (2001).

Numerical models for protoplanetary disks typically use an approximation of radial density profiles and apply the equation of the state to these profiles to derive the vertical structure of the disk at different radii and surfaces. By considering the disk as a thin viscous disk with physical characteristics such as a vertical scale height $H << r$ and a mass $M_{Disk} << M_*$, it is possible to express the variation of the surface density over time. Then, assuming an azimuthal velocity much larger than the radial velocity of the particles in the disk, we have a negligible gas gradient pressure along the radial direction and the orbital motion is mainly dictated by the centripetal acceleration in a gravitational potential.

The surface density in a Keplerian potential ($\Omega = (GM/r^3)^{1/2}$) is described
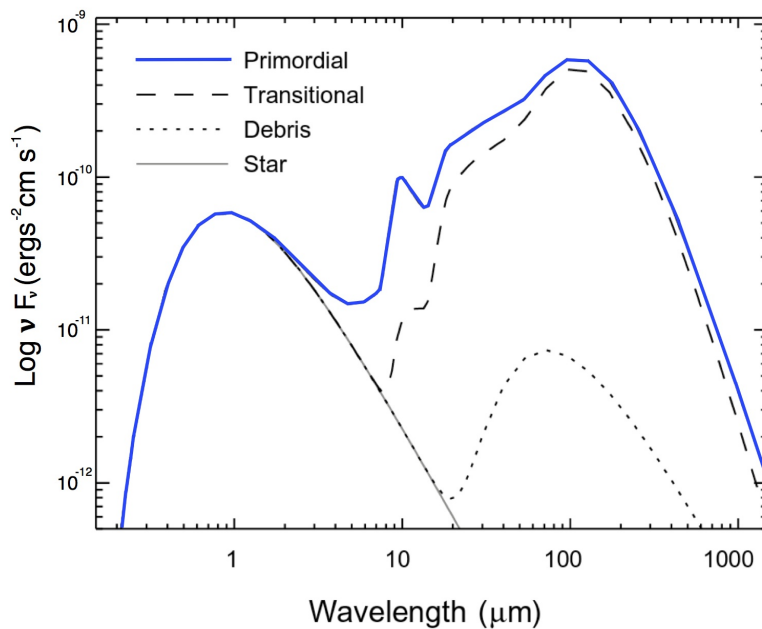
Figure 1.2: Theoretical Spectral Energy Distribution for a primordial disk, a transitional disk, and a debris disk. The star SED is a 3200 K blackbody. The primordial and transitional SEDs were produced by using the CGPlus code (Dullemond, Dominik & Natta, 2001)

by equation 1.2, the time-dependent solutions of which show that a fraction of the gas accretes onto the star while spreading diffusively to large radii (Frank, King & Raine, 2002).

$$\frac{\partial \Sigma}{\partial t} = \frac{3}{r} \frac{\partial}{\partial r} \left[r^{\frac{1}{2}} \frac{\partial}{\partial r} (\nu \Sigma r^{\frac{1}{2}}) \right] . \tag{1.2}$$

Where Σ is the surface density, ν is the viscosity as a function of local conditions in the disk, and r is the disk radius. This transport process allows the transfer of matter from the surrounding material to the growing protostar and defines the basic structure and viscous evolution of the disk. However, measurements of mass accretion rates are not fully consistent with a "weak" molecular viscosity,

particularly after the active infall phase has stopped; suggesting an incomplete understanding of the transport of mass and angular across the disk (Hartmann, 2008). For simplicity and in the absence of a well-defined physical transporting mechanism, the viscous stress can be parameterized in a dimensionless value. In order to find a "temporal" solution for the unknown source of viscosity in a geometrically thin non-self gravitating disk, Shakura & Sunyaev (1973) introduced an α-viscosity parameter. Assuming a scale height H larger than the length scale of the turbulence, the kinematic viscosity is defined as:

$$\nu = \alpha c_s H_{gas}.$$ (1.3)

Where c_s is the gas sound speed and H_{gas} is the vertical scale height of the gas.

Possible mechanisms to produce "strong" viscosity are convection, gravitational instabilities, and magnetorotational instability (MRI) (Dullemond et al., 2007), nevertheless, for the main purpose of this document, these processes will be omitted. Finally, if the disk is assumed to be vertically isothermic, the vertical density structure can be found by,

$$\rho(r, z) = \rho_c(r)e^{-z^2/2H_{gas}^2}$$ (1.4)

where $\rho_c(r)$ is the density at the midplane and H_{gas} is the gas scale height.

$$H_{gas} = \sqrt{\frac{kT_c r^3}{\mu m_p GM_\star}} = \frac{C_s}{\Omega}$$ (1.5)

where T_c is the temperature at the disk midplane, μ is the mean molecular weight in units of the proton mass m_p and $M_\star$ is the stellar mass.

On the other hand, the gas and dust temperature can be calculated by using the conservation of energy in terms of heating and cooling processes. Although in reality the dust and gas have different temperatures, most models assume that both have the same temperature (the well-coupling between the dust and gas, thermally and dynamically). By assuming a disk optically thin at the surface and optically thick at the midplane with a vertical profile in hydrostatic equilibrium (two-layer model), the dust grains in the disk surface scatter a fraction of the stellar photons and absorb the other fraction of photons to re-emit them with the magnitude of the local surface dust temperature (Chiang & Goldreich, 1997). If we take the ratio between the height above the midplane where the disk becomes optically thick and the gas (pressure) scale height as a constant, it can be found that the gas scale height increases with radius at a rate of $H_{gas} \propto r^{1.286}$, indicating a disk with a "bowl" shape or flaring disk. In general, the disk midplane temperature scales as $T_c \propto r^{-0.428}$ (Chiang et al., 2001). Figure 1.3 shows a schematic gas temperature profile of a disk based on the two-layer model of Chiang & Goldreich (1997). At the optically thick layer, the dust and gas are well-coupled due to collisions.

1.3 FU Ori Objects

Overall, young stellar objects show optical variability mainly by accretion, extinction events, and stellar spots (Joy, 1945). An outstanding eruptive phenomenon is the large episodic accretion in some of these YSOs, where much
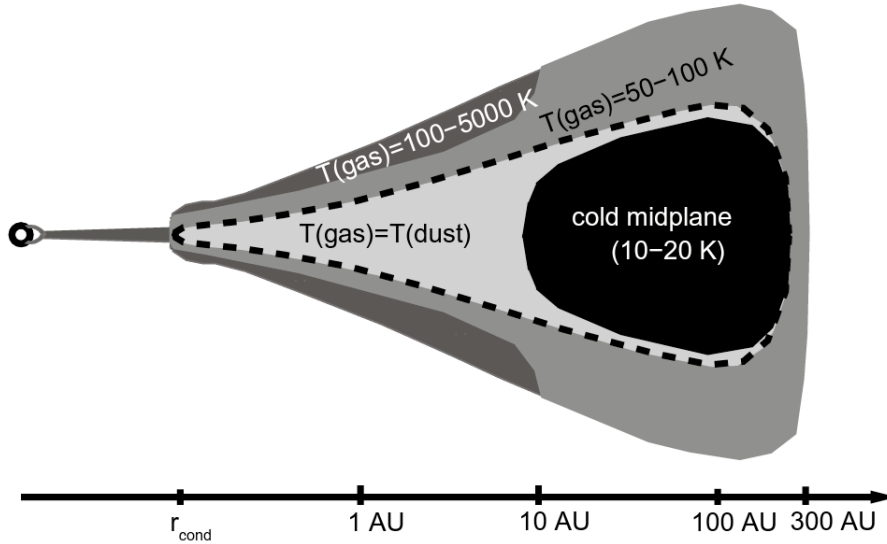
Figure 1.3: Gas temperature structure of a protoplanetary disk, based on the two-layer model of Chiang & Goldreich (1997).

disk material is added to the central object in a short period of time. The frequency and intensity of these episodes affect the circumstellar environment at young stellar ages and the final mass of the forming star. The most intense bursts are believed to take place during early stages (Class I objects) of star formation. However, some outbursting sources display flat SEDs near the Class I/II boundary (Evans et al., 2009a; Green et al., 2013) or even Class II SEDs with no signs of molecular envelopes. These bursts, which can last years to centuries, punctuate long periods (10^4-10^5 yr) of relative quiescence. Observationally, the most extreme events of episodic accretion are known as FU Orionis outburst (hereafter FUors), whose main characteristic is an increase in optical light that can reach 5 mag or even more (Herbig, 1977). During these periodic outbursts, FUors have a bolometric luminosity of $\sim$ 100-400 L$_\odot$ with accretion rates between 10^{-6}, and 10^{-4} M$_\odot$ yr^{-1} and are fueled by material

still falling from the circumstellar envelope to the disk and eventually onto the central star. FUors show spectra similar to F/G supergiant spectral types in the optical regime, while in the near-infrared these objects show spectra like K/M supergiant spectral types and first-overtone CO absorption at 2.2 μm. The Fe I, Li I, and Ca I optical lines observed in FUors are double-peaked and broader than a YSO, consistent with a rotating disk origin (Hartmann & Kenyon, 1996). FUors present blue SED typical of a mildly flared disk with pristine silicate emission features around 10 μm (Green et al., 2006). These features can be observed either in absorption or in emission, where objects with absorption features are likely FUors embedded in an envelope and objects with silicates in emission are less-embedded FUors (Quanz et al., 2007). Submillimeter observations show that FUors disks are more similar to those of Class I protostars, with larger and more massive accretion disks than a classical T Tauri star (Sandell & Weintraub, 2001).

1.3.1   Molecular outflows

The large mass accretion rate can increase as much as a factor of 100 and as a result, produces strong winds and eventually, they can produce massive bipolar outflows (Figure 1.4). These outflows are composed of H_2, carbon monoxide (CO), and other molecules present in the disk. As H_2 lines are weak, CO emission is used to trace the cooler swept-up material (i.e. interaction of the outflows and their surrounding envelope), with temperatures < 100 K. From sub-millimeter observations, CO lines typically have a line width of $1-3$ km s^{-1} in a quiescent molecular cloud, while towards a YSO, CO lines showed widths of $6-8$ km s^{-1} that can be attributed to the gravitational collapse of

the cloud around forming-stars (Lada, Dickinson & Penfield, 1974). Higher sensitive observations in active star-forming regions have shown velocities that are higher than the ambient cloud velocity by up to $60-70$ km s^{-1} (Kwan & Scoville, 1976). These high velocities are due to energetic outflows. FUors have been detected with molecular outflows of a bipolar shape with mass-loss rates ranging from 10^{-8} up to 10^{-6} M$_\odot$, without correcting for optical effects. These molecular outflows are believed to carry angular momentum away, permitting the accretion of mass onto the central object at higher rates. The strong outflows inject large quantities of energy to their surroundings and hence, perturb and modify the surrounding molecular cloud.

It is believed that these outflows might originate mainly through two outflow-launching mechanisms: (1) the X-wind, which is launched at a few stellar radii from the star (Shu et al. 2000), and (2) the disk wind, which is launched from a wide region throughout the disk (Konigl & Pudritz, 2000). The exact launching position of the disk wind is difficult to establish. Recently, ALMA has observed outflows launched within the inner $\sim$25 au radius of a disk (Bjerkeli et al., 2016), while there are other exceptional cases where outflows can be launched at a distance of $\sim$90$-$130 au from the rotational axis (Alves et al., 2017). Therefore, more observations with a higher sensitivity are required to constrain the launching point of disk winds.

In general, ^{12}CO emissions are optically thick in dense cores, however, ^{12}CO is often used to estimate outflow properties because it might become optically thin over the higher velocity outflow gas. Given its strength, ^{12}CO is used to obtain shapes, physical extensions, kinematic properties and, outflow masses. However, ^{12}CO observations could underestimate the outflow masses if the

emission becomes optically thick (Bradshaw, Offner & Arce, 2015). Therefore, ^{13}CO and C^{18}O data are used to correct for ^{12}CO optical depth effects (e.g. Goldsmith et al., 1984) and measure masses, momentum, and energy flux with higher accuracy. These estimates typically assume that the gas is in local thermodynamic equilibrium (LTE) and CO emits at a single excitation temperature (e.g. Curtis et al., 2010; Bradshaw, Offner & Arce, 2015), see Chapters 3 and 4.
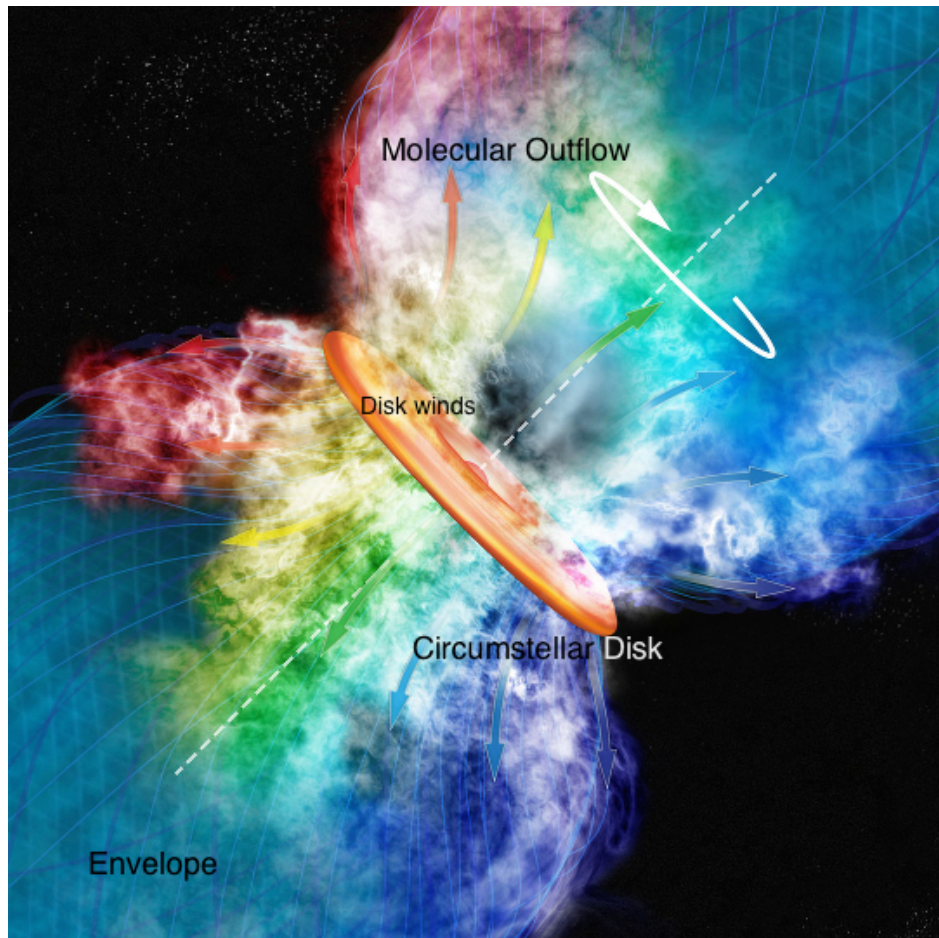
Figure 1.4: Sketch of a FUor object. Image Credit http://insciences.org

The first part of my Ph.D. thesis includes ALMA observations of two FU Ori

objects, HBC 494 and V883 Ori. We use of ^{12}CO, ^{13}CO and C^{18}O emission lines as tracers of the different components of the systems, their disks, outflows, and envelopes. This part of my Ph.D. thesis aims to answer the following outstanding questions:

1. **What are the basic properties of FU Ori outflows (mass, size, morphology, and kinematics) and how do these properties compare to those of quiescent systems?**

2. **How do FU Ori outflows affect the evolution of the disk/envelope system?**

3. **What are the physical mechanisms responsible for the observed outflows?**

1.4   Transitional Disk

By the time young stellar objects become optically visible T Tauri stars, the star-building process is mostly over, and the mass remaining in the circumstellar disks represents $< 1\%$ of the mass of the stars (Andrews & Williams, 2007; Andrews, 2015). Primordial disks typically last 2-3 Myrs before dissipating through different processes and becoming disk-less (Class III) stars. The transitional stage between Class II and III objects is characterized by decreased levels of NIR and/or MIR excess (NIR: 1-5μm, MIR: 5-20μm), and an excess emission at wavelengths $\geq 20\mu$m similar to that of a primordial disk. This can be explained by an inner disk region devoid of hot dust grains. The first

objects showing such observational signatures were identified by Strom et al. (1989) and are currently known as **transitional disks**. In general, the term "transitional disk" (TD) is used to describe protoplanetary disk which is optically thick and gas-rich with central clearings due to a non-continuos dust distribution. Observations of transitional disks have shown dust-poor cavities that contain significant gas material (Pérez et al., 2014). Although the composition of the inner disk is only $\sim 1\%$ dust, it dominates the opacity of the disk. The lack of near-IR excesses implies that the small particles in the inner disk region should be depleted by around 10^{-4} from standard full disk values. Therefore, the transitional disk classification is based on the evolution of dust particles instead of gas, which represents 99% of the mass and drives the dynamics in the disk. Understanding the evolution of the dust particles is key because they are the "raw" material for the formation of *terrestrial planets* and the cores of the *giants planets*.

TDs are a diverse group of objects. Their central cavities have a wide range of radii ($\sim$1-100 au); however, more massive stars tend to have TDs with larger cavities (Merín et al., 2010). Owen & Clarke (2012a) showed observational evidence for two "different" types of transitional disks based on their millimeter flux. The first type is characterized by low millimeter flux, inner holes of less than 10 au and low accretion rates of around $< 10^{-9}\mathrm{M_\odot/yr}$. This type of disk is consistent with the last stages of disk dissipation. The second type presents high millimeter fluxes, inner holes larger than 10 au and accretion rates of around 10^{-9}-10^{-8} $\mathrm{M_\odot/yr}$. Different physical mechanisms are proposed in the literature to explain inner holes of transition disks: 1) planetary formation, 2) photoevaporation, 3) grain growth/coagulation/settling, 4) magnetorotational

instability, and 5) dynamical effects of the presence of a stellar companion, as discussed below.

Planet Formation

In general, there are two main models proposed for the formation of gas giant planets: *core accretion* and *gravitational instability*. In the *core accretion model*, micron-sized dust grains stick together to build up mm-to-cm-sized aggregates. Although important barriers exist, these aggregates eventually form 10-100 km planetesimals (e.g., as a product of a gravitationally unstable dust layer; Furuya & Nakagawa, 2001). Gravitational interactions allow the oligarchic growth of some of these objects to create planetary embryos. Eventually, these embryos collide and grow into a core with a critical mass of ~ 10 $M_{\oplus}$, starting a phase of rapid gas accretion. This gas accretion phase continues until the planet opens a gap in the protoplanetary disk (Chambers, 2011). The pressure gradient at the edge of the gaps filters the dust being transported inward from the outer disk (Pinilla et al. 2015) and the forming planets divert most of the material onto itself. The combination of both effects results in the dust poor inner disks characteristic of transition objects.

Photoevaporation

Another probable mechanism responsible for opening gaps in the inner regions of disks is photoevaporation by its central star. It has been shown that at the surface layers of the inner disk, the temperature of the gas can be higher than the dust temperature as a result of the radiation from the central star. This

gas flows off the disk and escapes from the gravitational field of the host star. The main sources of heating are the strong EUV and FUV acting at different radii in the disk and penetration depth. The evaporative mass depends on the penetration depth of the FUV and EUV photons and the temperature of the heated gas (Dullemond et al., 2007). FUV dominates at r > 50 au and EUV affects mostly the planet-forming region, r << 50 au. While the mass transport across the disk is high, material moving in from the outer disks compensates any loses due to photoevaporation. As both the disk mass and the accretion rate decrease, the mass-loss rate becomes important and a gap is formed in the disk at a critical radius. Eventually, the inner disk dissipates in dynamical timescales, leaving an empty, photo evaporating cavity that expands from the inside-out.

Binary Stars

Dynamical interactions in binary systems can also produce inner holes in protoplanetary disks and transition disk SEDs (Ireland & Kraus, 2008). Most stars are formed in binary or multiple systems; therefore, understanding the effects of this multiplicity on disk evolution is important for planet formation theory. Observationally, planets in binary systems are less common than planetary systems in single stars, which is reflected with only ∼60 planets detected that reside around binary systems. To date, most of these circumbinary planets reside in binary systems with a relatively large separation, often with separations of > 500 au (Roell et al., 2012), while only ∼10 of these binaries have a separation of less than 100 au, and 5 exoplanets reside in close binaries with separations of ∼20 au. Those planets orbiting only one of the stars,

with the second star acting as a perturber, are known as S-type configuration planets(Dvorak, Froeschle & Froeschle, 1986). Planets orbiting both stars in a binary system are known as P-Type or circumbinary planets (e.g. Beuermann et al., 2011).

From theoretical and observational studies, it is established that a single star is more suitable for the formation of a planet. In binary stars, especially those orbiting closer than ~ 100 au, the protoplanetary disk is hotter and dynamically more excited impacting the initial steps for planet formation, such as the coagulation and growth of planetesimals or the gravitational instability process. However, planets in S-Type configuration can still form at small distances from the star (Nelson et al., 2000). Close-binary stars with separations < 1 au are more suitable for the formation of a P-type of circumbinary planets.

The second part of my thesis assesses these transitional disks in the context of their impact on disk evolution, and addresses questions such as:

1. **How many disks classified as transitional disks are actually circumbinary disks?**

2. **How long does the true pre-transitional and transitional disk phase last for single stars?**

1.5   Characterizing Disks at An Intermediate Age (2-3 Myr)

The combination of intensive ground- and space-based observations over the last decades has established the basis of our current understanding of disk evolution (e.g., Williams & Cieza, 2011). Much of our knowledge about the evolution and dispersal of protoplanetary disks comes from IR and millimeter surveys of clusters at different ages. From these surveys, we know that at 1 Myr, 80% of stars have accretion disks, while at 10 Myr, a disk frequency of 1% is seen, see Figure 1.5, (Mamajek, 2009). Even though more than 3500 extra-solar planets have been detected to date and current exoplanet statistics indicate that planet formation is the typical end product of disk evolution, the picture of when, how, and where these planets are formed is still largely incomplete. Characterizing disks (i.e. their masses, sizes, structures, and accretion rates) in young star-forming clusters of a given age, and then comparing these properties to those of clusters at different ages, allows us to investigate how disk properties change with time, and thus constrain disk evolution mechanisms and timescales.

The IC 348 cluster is an attractive target for disk surveys (2-3 Myr). It contains one of the richest populations of Class II stars, an ideal evolutionary stage to estimate dust and gas of the protoplanetary disks already undergoing a dispersal phase.

The third part of my thesis investigates and characterize mass (dust+gas) and size of the disks in the IC 348 star-forming cluster, using ALMA Cycle 3 observations, to improve our understanding of the initial conditions for planet

formation and contribute in the comprehension of:

1. **Why giant planets are rare and Earth-like planets are more frequent around M stars (Howard et al., 2012; Burke et al., 2015)?**

2. **How disk properties at 2-3 Myr define the planet-formation potential of different systems.**
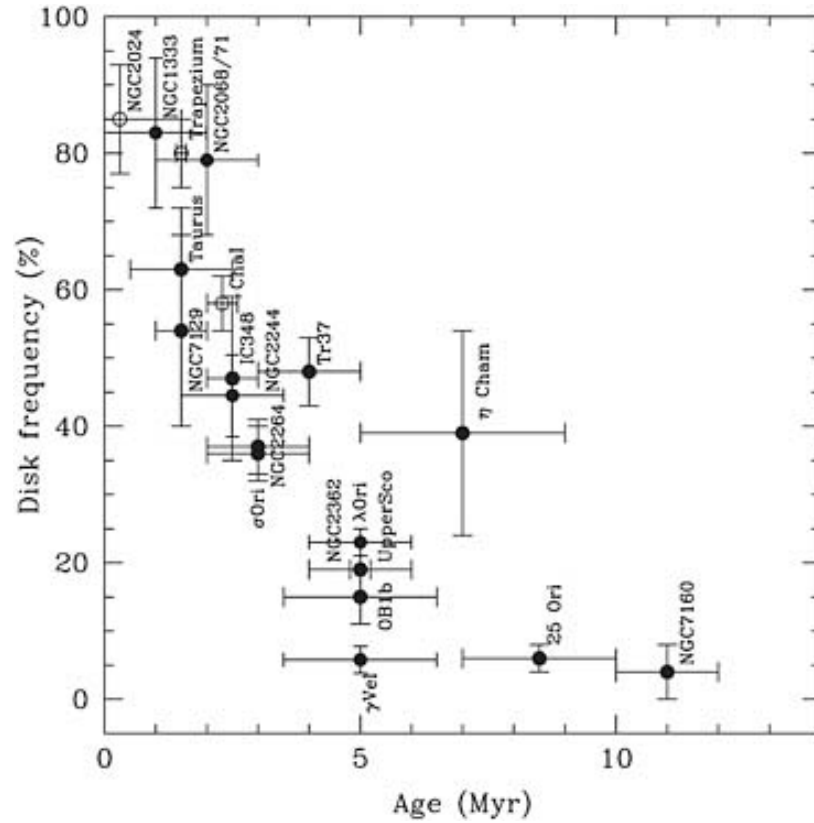
Figure 1.5: The disk frequency as a function of cluster age from Spitzer observations. The Spitzer data is optically thick and only measure the presence of a disk. Millimeter wavelength observations of the same clusters provide the distribution of disk masses. Most recent results show a decrease of disk mass with age in Taurus, Lupus, IC 348, and Upper Sco. Figure 1 from Mamajek (2009)

<div style="text-align: center">

2

METHODOLOGY AND OBSERVATIONAL TECHNIQUES

</div>

This chapter discusses the various observations and analyses techniques included in this thesis. Observations used in this thesis and the results are presented in separate chapters and publications such as Ruíz-Rodríguez et al. (2016a, 2017b,a). Chapers 3, 4, and 6 presents observations of carbon monoxide (CO), including ^{12}CO, ^{13}CO and C^{18}O with energy level transition J = 2 - 1, as well as dust continuum observations, which were taken with the Atacama Large Millimeter/submillimeter Array (ALMA). Chapter 5 presents observations using the Non-Redundant Mask interferometry technique from Keck Observatory.

2.1   Observing Techniques

The formation of stars and planets occurs deep inside molecular clouds and circumstellar disks. Because at these early stages these objects are mostly com-

posed of dust and gas, the study can be best performed by using infrared and (sub-)millimeter wavelengths. For instance, in the past decade, the sensitivity and improved spatial resolution of *Spitzer* made possible the identification of populations of T Tauri stars in several star-forming regions, enriching the knowledge of dust distributions in the disks. More recently, ALMA allowed probing continuum and molecular lines in deeply embedded young stellar objects, revealing new structures in disks and the kinematics of the molecular gas. Therefore, infrared and (sub-)millimeter are essential for our understanding young stellar objects and their disk-envelope system.

In Section 2.2, we present a brief discussion of ALMA, the world's most advanced millimeter-wavelength interferometer, which was used to observe two FUors: HBC 494 and V883 Ori. Interferometers sample the visibility function[1]; therefore, we also present a description of this complex quantities.

2.2   Millimeter-wavelength Interferometry

Basically, interferometry can be described as receiving light from two apertures separated at a distance **b** and the recombination of these two light "sources", see Figure 2.1. The propagation of these two electromagnetic waves have different relative path lengths and the difference in phase produces a constructive and destructive diffraction pattern. Mathematically, these interferences take place as:

---

[1]Visibilities are the Fourier transform of the sky brightness distribution.
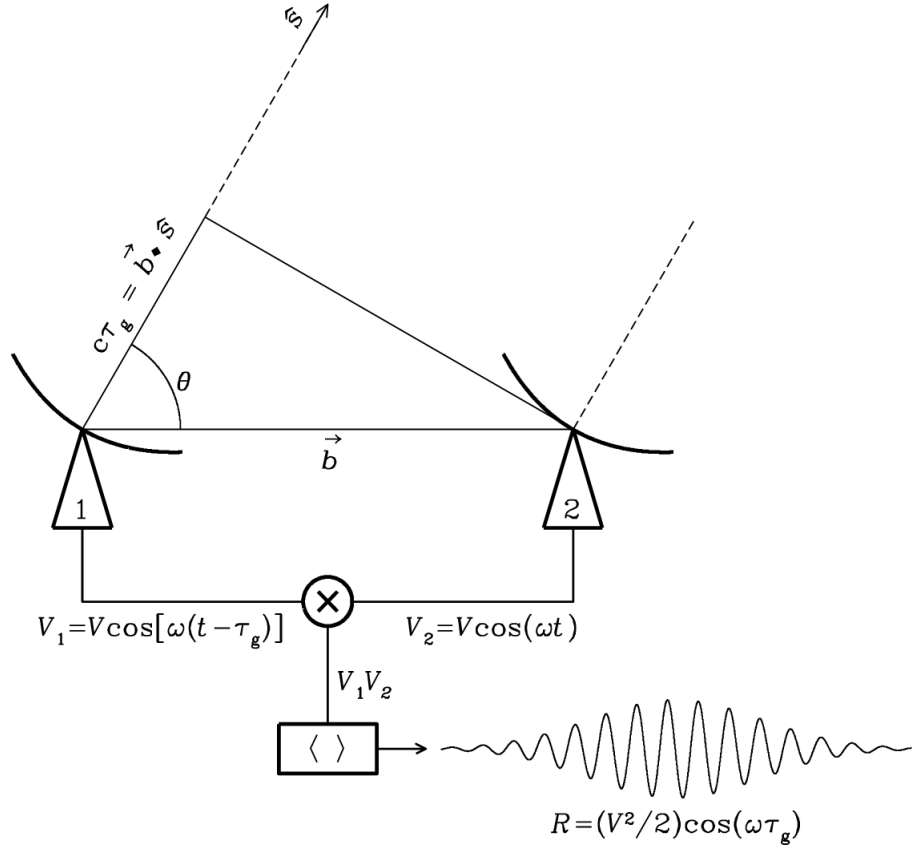
Figure 2.1: Diagram showing two identical antennas that receive signal from a point source in the direction specified by $\hat{s}$. Each antenna generates a voltage output, V_1 and V_2, where the correlator generates an output response of amplitude $R = \left(\frac{V^2}{2}\right)\cos(\omega\tau_g)$ by time averaging them. V_1 and V_2 have the same magnitude with a geometric delay of $\tau_g = \frac{\vec{b}.\hat{s}}{c}$ in V_1, where $\vec{b}$ is the distance between antennas and $\hat{s}$ is the unit vector in the direction of a distant point source.

$$I = I_1 + I_2 + 2\sqrt{I_1 I_2}\cos(\delta). \tag{2.1}$$

with maximum interference at phase difference $|\delta| = 0, 2\pi, 4\pi, ...,$ and minimum interference at $|\delta| = \pi, 3\pi, 5\pi$. The features of the aperture and wavelength of the light will determine the interference fringes at a determined frequency.

The degree to which a source is resolved on a given baseline can be measured with the fringe contrast named as **visibility** and written as:

$$V = \frac{I_{max} - I_{min}}{I_{max} + I_{min}} = \frac{2\sqrt{I_1 I_2}}{I_1 + I_2} = \frac{\text{Fringe} \quad \text{Amplitude}}{\text{Average} \quad \text{Intensity}}. \tag{2.2}$$

where I_{max} and I_{min} are the maximum and minimum intensity of the fringes. The visibility is a dimensionless number between zero and one ($I_1 = I_2$) and contains spatial and spectral information of the source. **Then, the spatial interferometry is about measuring the contrast of the fringe pattern, i.e. its maxima and minima. As a result, the intensity distribution at different frequencies is obtained by adding up interference patterns like those described by equation 2.1. This fringe pattern determines the spatial coherence of the intensity distribution and due to the light source being incoherent, we can denote the visibility function as μ(b), where b is the distance between two apertures, see Section 2.2. This complex function has a *phase* denoted as ϕ(b) and defines the position of the central fringe. The definition of the visibility function is:**

$$\mu(\mathrm{b}) = \frac{\int \mathrm{I}(\delta)\mathrm{e}^{-\mathrm{i}k\delta\cdot\mathrm{b}}\mathrm{d}\delta}{\mathrm{I}_0}. \tag{2.3}$$

This function is known as *The Van Cittert-Zernike theorem*. The visibility is proportional to the amplitude of the image Fourier component, which corresponds to the fringe spatial frequency and studying the variation of this quantity with respect to the fringe contrast, it is possible to estimate the spatial intensity distribution.

Angular Resolution and Sensitivity:

In interferometers, as well as conventional imaging telescopes, the resolution is defined by the "Rayleigh Criterion", where a pair of close objects are resolved if the fringe contrast goes to zero at the longest baseline. This can be achieved when the angular separation is:

$$R = \frac{\lambda}{2\mathrm{b}}, \tag{2.4}$$

where b is the largest baseline of an interferometer or the diameter of the telescope mirror, and λ is the wavelength detected.

In our case, in order to detect faint objects, the sensitivity of the telescope must reach a minimum signal above the background or noise. The sensitivity is defined as:

$$S = \frac{\pi b^2}{4}, \tag{2.5}$$

where b denotes same as above. The sensitivity is proportional to the collecting area of a telescope or the collecting area of all of the antennas of an interferometer. Thus, for an interferometer, we have:

$$S = N\frac{\pi b^2}{4}, \tag{2.6}$$

where N is the number of elements of the interferometer. Thus, it implies that for a better sensitivity, it is required large baselines for point sources or more compact sources such as outflows. Also, it can be defined for a pair of antennas as follows:

$$S = \frac{N(N-1)}{2}. \tag{2.7}$$

Atacama Large Millimeter/submillimeter Array (ALMA):

The Atacama Large Millimeter/submillimeter Array (ALMA) is located at an altitude of 5000 meters at Llano Chajnantor in northern Chile, see Figure 2.2. ALMA is a 12-m antennas array (50 antennas) with baselines up to 16 km, which can form different array configurations with different distributions of baseline lengths. The longest baselines are designed to provide higher spatial resolution, while a more compact array configuration provides better sensitivity for extended sources such as large molecular clouds because the compact array

Figure 2.2: ALMA Observatory.

can detect emission on larger angular scales. For these cases, there is also the Atacama Compact Array (ACA) that consists of twelve 7-m antennas and four 12-m antennas.

Interferometry uses multiple antenna dishes to achieve a specific resolution and sensitivity [2]. In this thesis, we present ALMA[3] band-6 (230 GHz/1.3 mm) continuum and ^{12}CO, ^{13}CO and C^{18}O J=2-1 line observations of HBC 494 and V883 Ori, which were taken under program 2013.1.00710.S during Cycle-2 phase. Our correlator setup was centered at 230.5380, 220.3987, and 219.5603 GHz, respectively. This correlator was configured to provide a spectral resolution of 0.04 km s^{-1} for ^{12}CO and of 0.08 km s^{-1} for ^{12}CO and C^{18}O. More details of the observations and data reduction process can be found in Chapters 3, 4 and 6.

---

[2]The maximum resolution is determined by the longest baseline or distance between two antennas.

[3]This thesis makes use of the following ALMA data: ADS/JAO.ALMA No. 2013.1.00710.S . ALMA is a partnership of ESO (representing its member states), NSF (USA) and NINS (Japan), together with NRC (Canada), NSC and ASIAA (Taiwan), and KASI (Republic of Korea), in cooperation with the Republic of Chile. The Joint ALMA Observatory is operated by ESO, AUI/NRAO and NAOJ. The National Radio Astronomy Observatory is a facility of the National Science Foundation operated under cooperative agreement by Associated Universities, Inc.

2.3   Methodology and Data Analysis In Molecular Outflows: HBC 494 and V883 Ori (FUors)

Observing molecular lines:

Regions of cold gas and dust with temperatures around 10-80 K and densities of $\sim 10^3$-10^4 cm^{-3} emit in the (sub-)millimeter (30 - 300 GHz) and radio regime of the electromagnetic spectrum. These bands are optimal to detect kinematic details in disks, outflows, and envelopes that are forming dust grains. Observations of the detailed spatial distribution of the dust and gas in disks and molecular outflows, either spatial visibility functions or intensity distribution, provide information to constrain the initial steps for planetary formation, our ultimate goal.

Therefore, images of molecular lines at very high spatial and spectral resolution are necessary to describe motions due to infall, rotation, and outflow in FUors. The molecular isotopologues of CO J=2-1 line presented here, ^{12}CO, ^{13}CO, and C^{18}, trace the material ranging from optically thick to optically thin, respectively. Although H$_2$ is the most abundant molecule in the interstellar medium, this molecule does not have a permanent dipole moment and ^{12}CO, ^{13}CO, and C^{18} molecules are used to trace indirectly H$_2$, because CO has the advantage of having a strong dipole moment. For that matter, the standard process for deriving gas properties uses a conversion factor from CO intensity-to-column density of H$_2$. In chapter 3 and 4, we use a method based on Local Thermodynamic Equilibrium (LTE), which assumes the H$_2$/CO abundance and a specific excitation temperature.

Molecular outflows emit at a different optical depth depending on the medium velocity. For instance, ^{12}CO is optically thick in outflowing gas at low velocities near that of the surrounding envelope, and ^{13}CO, as a medium-density gas tracer, can be used to estimate the opacity of the ^{12}CO line (Dunham et al., 2014). After correcting for optical depth effects, we use ^{12}CO and ^{13}CO to estimate outflow gas properties such as mass, momentum, energy, and morphology. C^{18} emission traces denser regions than the ^{12}CO, ^{13}CO lines, and it was used to infer the morphology and structure of the envelope. For HBC 494 and V883 Ori, we were limited to infer the entire structure of the outflows and surrounding envelope allowing us to obtain a higher resolution with the interferometer, see Chapters 3 and 4.

2.4 Near-IR interferometry

2.4.1 Image Formation

Understanding the formation of an infrared astronomical image is fundamental in the analysis needed to carry out this thesis. In chapter 5, we only use the *Fraunhofer approximation* or far-field approximation, which takes place at large distances from the light source and is large enough that at the diffraction aperture the wavefront may arrive as "plane wave".

Assume small field of view with shift invariance of the optical system or iso-planatism[4]. By considering a point object at θ, see Figure 2.3, we have the

---

[4]Iso-planatism in an optical system requires that if the translation of a object point source

expression:

$$K\left(\alpha - \theta\right) \propto \int P\left(\lambda\vec{u}\right) e^{-2\pi(\alpha-\theta)\cdot\vec{u}} d\vec{u} \qquad (2.8)$$

where $K\left(\alpha - \theta\right)$ is the **amplitude spread function** and can be thought to represent an infinite set of waves planes describing the far-field diffraction (Saha, 2007). $P\left(\lambda\vec{u}\right)$ is the complex **pupil function** and expresses the transmission of light through the telescope pupil, where a zero value means light blocked and one means light fully transmitted. It also contains the information from the phase disturbances introduced by aberrations. For convenience, $\vec{u} = \vec{x}/\lambda$ is dimensionless and represents the pupil plane scaled to one wavelength equal to unity. In 2-D $(u, v) = (x, y)/\lambda$ is the spatial frequency vector in the pupil plane.
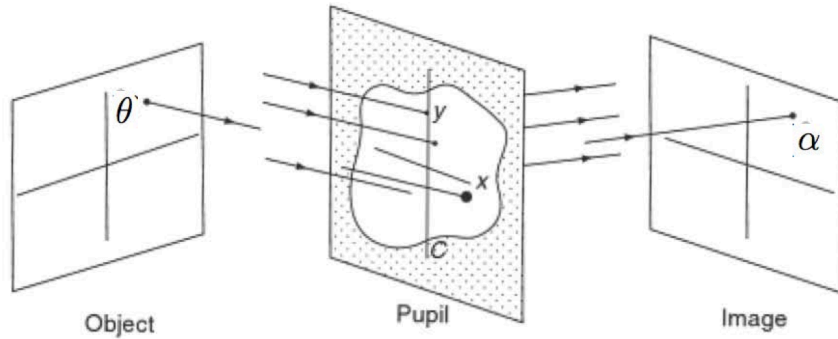
Figure 2.3: The relation between object and image. Figure taken from Léna et al. (2012), (Chapter 6, Figure 6.5).

---

at x produces a PSF $f(x)$ in the image plane, then the translation of the object point to $(x + \Delta x)$ produces the PSF $f(x + m\Delta x)$, where m is the magnification of the system.

In this thesis, we will approximate the electric field as a scalar, $U(\vec{\theta})$. However, the electric field is not accessible to be measured at the optical detector and then the intensity must be averaged over many cycles of oscillation, leading to the specific case of a stellar source with spatial incoherence between two different points, $U(\vec{\theta_j})$ with $j = 1, 2$, in its electric field distribution, we have then:

$$< U(\vec{\theta_1}), U^*(\vec{\theta_2}) >= O(\vec{\theta})\delta(\theta_2 - \theta_1) \tag{2.9}$$

where the intensities from different elements U_j of the above equation are additive due to nature of its incoherent source. The system is meant to be linear in its intensity and thus,

$$I(\alpha) =< |U(\theta)|^2 > \tag{2.10}$$

where the bracket notation denotes a time average over many cycles on U_j. Then, for a "small" source the total intensity is[5]:

$$I(\vec{\alpha}) = \int_{-\infty}^{\infty} O(\vec{\theta})|K(\alpha - \theta)|^2 d\vec{\theta}. \tag{2.11}$$

The equation 2.11 is the convolution of the spatial intensity distribution in the

---

[5]According to the Van Cittert-Zernike theorem, the degree of coherence is correlated to the diffraction pattern resulting from a telescope aperture with the size and shape of the stellar source.

object with the amplitude spread function, written as:

$$I(\vec{\alpha}) = O(\vec{\alpha}) * |K(\vec{\alpha})|^2 \qquad (2.12)$$

In other words, the "incoherent" PSF is the power spectrum of the pupil function and by replacing $\tau(\vec{\alpha}) = |K(\vec{\alpha})|^2$ in Equation 2.12 , the aperture's PSF is:

$$I(\vec{\alpha}) = O(\vec{\alpha}) * \tau(\vec{\alpha}) \qquad (2.13)$$

In summary, the *Fraunhofer pattern* or image intensity pattern is a *Fourier Transform* of the aperture and hence in an *iso-planatic* approximation, an astronomical object appears as the convolution of the aperture's point spread function (PSF) [6], $\tau(\alpha)$, with the object intensity distribution, $O(\alpha)$.

Atmospheric and Optical Aberrations

The intensity pattern is equal to the convolution of the aperture's PSF with the function that describes the astronomical object, see equation 2.13. However, the phase in the pupil plane is affected by corrugations of many radians introduced to the phase front of the incoming starlight. Thus, the PSF includes an additional component, which represents a "distortion" in the image. Those aberrations can be written as:

---

[6]The point spread function is invariant under spatial shifts of the entire electric field.

$$A(x) = e^{i\phi(\vec{x})} \tag{2.14}$$

Then, the distortion in the PSF can be expressed in terms of the pupil function information, see equation 2.8, as follows:

$$P\left(\lambda\vec{u}\right) = P_o\left(\lambda\vec{u}\right) e^{i\phi(\lambda\vec{u})} \tag{2.15}$$

Then, the modification to the pupil function by $A(x)$ affects the form of the PSF in short and long exposures. In a long exposure, the function of the aperture and atmospheric seeing can be well-defined by its exposure average value. On the other hand, in a short exposure, the phase in $A(x)$ can be approximated as static and can be seen in the resulting image as a granular structure of **speckles**.

2.4.2   Adaptive Optics

There are three atmospheric parameters that provide essential information to design an Adaptive Optics (AO) system; Fried parameter, isoplanatic angle, and coherence time. Figure 2.4 shows an AO system that measures the variations of the wavefront of the incoming light with the *wavefront sensor*. The measured wavefront is used to obtain an estimate for the best correction and applies it to a deformable mirror. This process is performed hundreds of times per second or more. The wavefront sensor uses the measurements of a single guide star to correct the wavefront in its direction. Because the AO wavefront

sensing requires a bright single guide star ($\sim$ 15 mag) and close to the astronomical target ($\sim$ 10", the isoplanatic angle), a Laser Guide Star (LGS) can be used to achieve the sky coverage (Davies & Kasper, 2012).

Keck II Telescope:

Our facility to perform part of this thesis, Keck II (see Figure 2.5), uses a sodium (Na) laser emitting light at 589 mm with a magnitude range of 9.5< V <11.0. Keck II can operate in the natural guide star (NGS) and LGS mode. Figure 2.6 shows the Keck II AO control loops with the corresponding modes, LGS and NGS.
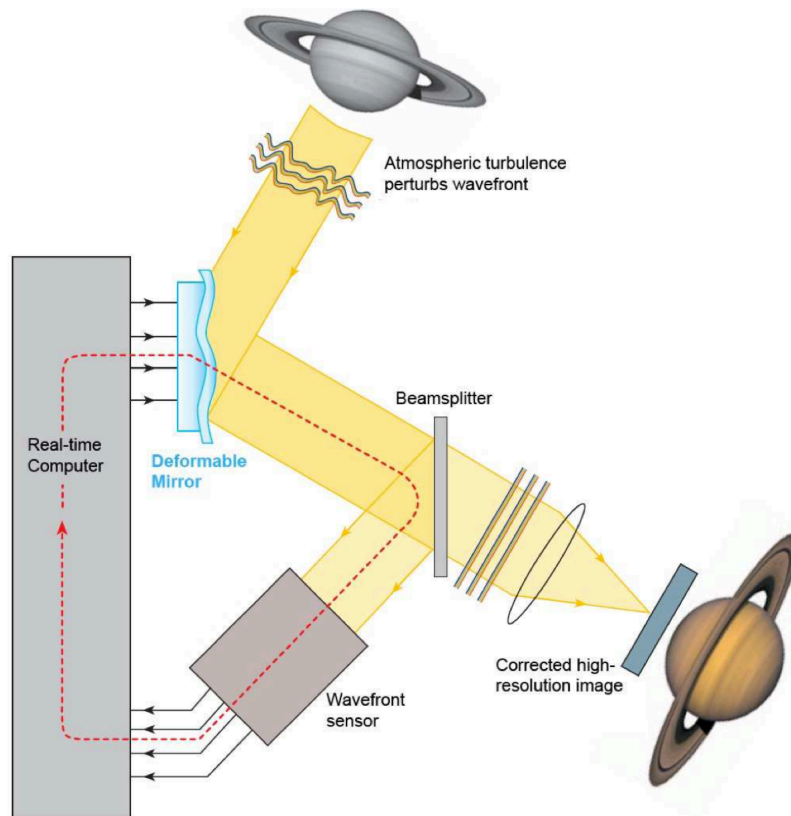
Figure 2.4: Adaptive Optics System, figure 3 from Davies & Kasper (2012).
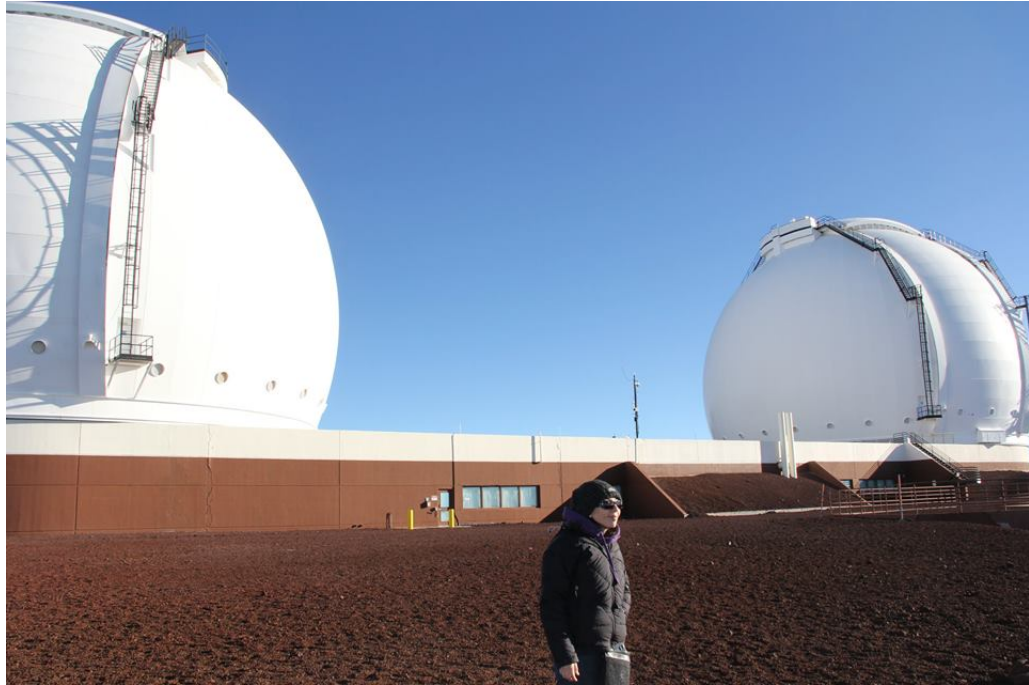
Figure 2.5: Keck Observatory.

One of the most challenging issues in resolving a faint companion at small angular separations is the residual wavefront phase errors uncorrected by the AO system. Variations by the atmosphere in the wavefront produces *the speckles* in the image. Addition of these wavefronts will produce a wave whose amplitude and intensity varies randomly. It can litter the astronomical image with bright speckles that are located in the diffraction pattern. These wavefront errors are produced by temperature and pressure gradients, guiding errors, a non-uniform reflectivity of the primary mirror, etc. Purely static speckles can be subtracted by using a reference star as a calibrator.

On the other hand, *non-common path wavefront errors* in the optical system cause *quasi-static speckles*, which originate in the optical components located between the wavefront sensor and uncorrected aberrations from the primary
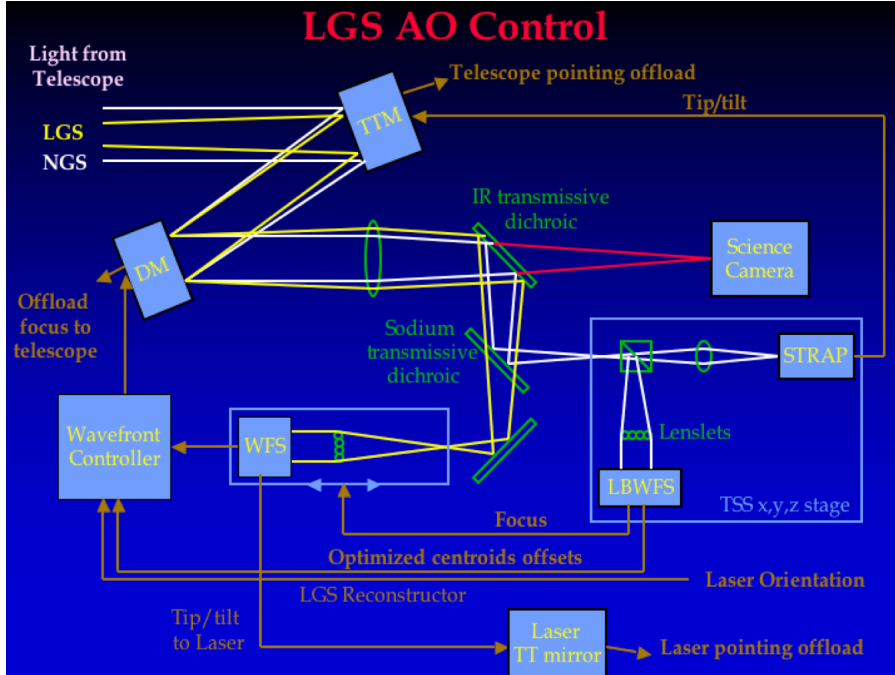
Figure 2.6: Keck LGS AO control loops.

mirror. The evolution of the quasi-static speckles is slow, leading to a difficulty in the calibration process. Because of their slow evolution, they cannot be effectively averaged out over long exposures times (even more than one hour!). The mean brightness of the quasi-static speckles sets the companion detection limit. Several techniques have been designed to overcome the contrast limits set by the residual of quasi-static speckles such as Spectral Deconvolution (SD), Spectral Differential Imaging (SDI), Angular Differential Imaging (ADI), Polarimetric Differential Imaging (PDI), Coherence Differential Imaging (CDI) and non-redundant aperture masking.

2.5   Methodology and Data Analysis Used In The Frequency of Transitional Disks: Binary vs. Single Stars

In this section, I present a more detailed discussion of the observational technique used in Ruíz-Rodríguez et al. (2016a), together with the Bayesian analysis to rule out or confirm a stellar companion as sources for those objects classified as TDs by using their SEDs.

Non-Redundant Aperture Mask Interferometry

If two-pairs of coherent sub-apertures, or more, contribute with the same spatial frequency are redundant, then the final baseline power will be a result of a repetitive and random number of contributions from the "same" baseline within the pupil. However, the noise inherent to this *random walk* process dominates the Signal-to-Noise Ratio (SNR) and produces wavefront errors or speckles. The final intensity distribution will be a diffraction pattern with Airy rings increasingly degraded outwards with a halo of random speckles.

An alternative approach is the use of **Non-Redundant Aperture Mask Interferometry (NRM)**, which can be produced by blocking most of the light with an opaque mask placed at the telescope pupil, see Figure 2.7. This mask will transform the pupil plane into an interferometric array and will lose most of the light. One significant requirement in the NRM is that in the design of the mask, each "baseline" creates a unique vector. Thus, the aperture mask
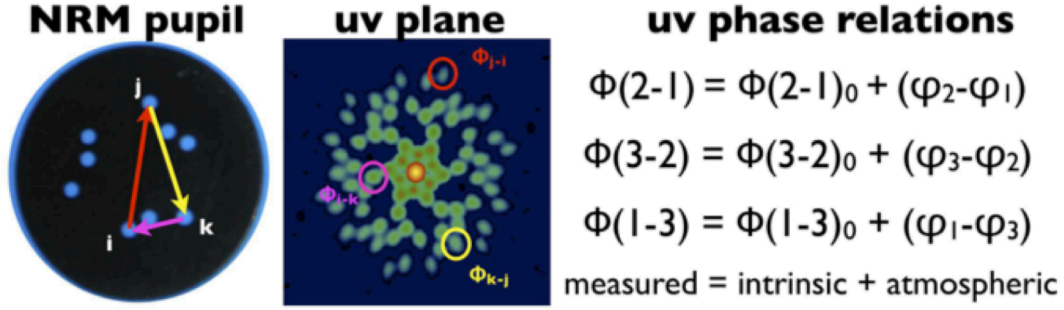
Figure 2.7: Example of the closure phase relation taken from Martinache (2011). Left panel shows a non-redundant pupil of 9 hole-pattern mask with a possible closure phase relation of i, j and k sub-apertures represented by the arrows. The central panel portraits the power spectrum resulted from the 9-hole mask, it illustrates the sampling of the complex visibility function. The right panel shows the relation for the corresponding visibility phases around the closure "triangle" 1-2-3.

has a selected pattern of holes, which are not at the same distance from each other, e.g., Figure 2.7.

By adding a triangle of these baselines, one can remove all the atmospheric random phasors and cancel out the non-common path errors responsible for the presence of the quasi-static speckles in the recorded image (Martinache, 2011). The sum of these phases (triangle) is a self-calibrating quantity called *Closure Phases* and can be shown as:

$$\phi_{123} \equiv (\phi_{12}+\Delta\phi_1-\Delta\phi_2)+(\phi_{23}+\Delta\phi_2-\Delta\phi_3)+(\phi_{31}+\Delta\phi_3-\Delta\phi_1) = \phi_{12}+\phi_{23}+\phi_{31}.$$

$$(2.16)$$

where $\Delta\phi$ are the phase errors and ϕ are the phase relations. From equation

2.16, for the closure phase ϕ_{123}, only the true phases contribute to the observed source acquired with a sparse aperture mask.

The open gap in the inner region of the disk might have different physical origins, but here we seek to answer whether the dispersion of the primordial material in the inner region of the disk is a result of the interaction with a binary system or the presence of a single star. Therefore, the observed transitional disks harbor a binary or single star, leading to the question: How many disks classified as transitional disks are actually circumbinary disks?

In order to answer this question, we make use of the Bayesian approach by using prior information of binary and single systems and observations of transitional disks. The orbit of a binary system is fully determined by seven parameters, providing information of the position in the sky for each stellar component. For a single system, we assume the position of the star at the center of the field of view. Then, prior information of position and contrast ratio of the stars can be built into a Bayesian analysis.

2.5.1 Bayesian Analysis

There is not a direct method to measure the presence of a dimmer companion in the observed image. However, Bayesian statistics can be used, providing the advantage of using prior information for updating our state of belief or knowledge. For our purposes, this prior information is provided by the orbital parameter distribution and randomly sampled using a simple uniform Monte Carlo algorithm, which generates a set of outputs for each set of parameters.

Each set of "predictions" can be quantitatively compared with actual observations. This is known as *Bayes's Theorem* and can be described as the product rule:

$$p(H_i|D, I) = \frac{p(H_i|I)p(D|H_i, I)}{p(D|I)} \qquad (2.17)$$

where:

$H_i \equiv$ The truth of a hypothesis of interest,

$I \equiv$ proposition representing prior information,

$D \equiv$ proposition representing data,

$p(D|H_i, I) \equiv$ probability of obtaining data D, if H_i and I are true, (likelihood function),

$p(H_i|I) \equiv$ prior probability of hypothesis,

$p(H_i|D, I) \equiv$ posterior probability of H_i.

Bayes's theorem shows us how to manipulate known probabilities in order to find other probabilities. However, the probabilities are not independent in this sense and we need to know the probabilities on the right side of equation 2.17

A normalization factor is needed to ensure that the sum of all posterior probabilities is equal to 1.

$$\sum_i p(H_i|D, I) = 1 \quad then, \quad p(D|I) = \sum_i p(H_i|I)p(D|H_i, I). \qquad (2.18)$$

Measuring Odds Ratio, Bayes's Factor and Occam's Razor

Until now, we have been working on solving the question of whether there is a binary star or a single star in the observed target, whose presence or absence could be responsible for the gap opening of the "transitional" disk or formation of a circumbinary disk. To quantitatively identify the type of object present in the data, the highest constrast as a function of position obtained from the calibrated data can help with this answer. In the hypothesis space of interest, the simulated binary and single systems [7] lead us to write Bayes's theorem for each hypothesis as follows:

$$p(B_i|D, I) = \frac{p(B_i|I)p(D|B_i, I)}{p(D|I)} \quad \text{and} \quad p(S_i|D, I) = \frac{p(S_i|I)p(D|S_i, I)}{p(D|I)}.$$
(2.19)

Here, we want to know how the probability of a hypothesis should be modified upon obtaining new information, in this case, new D. In the absence of new D, the probabilities for the hypothesis are called their prior probabilities $p(H_i|I)$. In the presence of new D, the probabilities are called their posterior probabilities, $p(H_i|D, I)$. The global *likelihood*, $\mathcal{L}(M_i) = p(D|H_i, I)$, shows the probability of measuring the observed data, if the hypothesis B_i or S_i is true.

Comparing both hypotheses or models, we compute the ratio of the posterior probabilities, known as *Odds Ratio* and written as odds ratio in favor of the

---

[7]Theoretical models to measure contrast limits as a function of position. For a single star the contrast ratio is equal to zero.

binary system model over the single system model:

$$O_{B,S} = \frac{p(B|D,I)}{p(S|D,I)} = \underbrace{\frac{p(B_i|I)}{p(S_i|I)}}_{Prior\,Ratio} \underbrace{\frac{p(D|B_i,I)}{p(D|S_i,I)}}_{Bayes's\,Factor} \qquad (2.20)$$

where the first factor is the prior *odds ratio* and the second is known as *Bayes's Factor* ($B_{B,S}$). Therefore, $B_{B,S} > 1$ means that a binary model rises from the data, $B_{B,S} < 1$ the data comes from a single star and $B_{B,S} \approx 1$ means that the odds are not modified and a binary and/or single star are equal probable.

Comparing the two models makes it easier to deal with the normalization constant because it vanishes.

Also, the prior information for binary or single system models are 1:1 or with equal probability of 50%, then they cancel out. So our proposition representing prior information $I = \gamma = 0.5$ and our prior ratio is:

$$\frac{P(B|I)}{P(S|I)} = \frac{\gamma}{1-\gamma} = 1. \qquad (2.21)$$

Predicted Model Probabilities

In order to know if the observed data shows the presence of a secondary component, we compare a binary system model with a single system model as the odds ratio states. Therefore, we need to be able to compute the global

likelihood [8]. This will be subject to conditional statements about the model parameters and can be calculated from the conditional likelihood and its joint prior probability (see equation 5.4).

In the data reduction process, after computing closure phases and squared-visibilities for each model and comparing with the observed data, the final quantity is subject to the correct acquisition of a 3-D χ^2 for each observed epoch that depends on the position in the field of view and the contrast of the secondary relative to the primary. Then, the global likelihood for a binary system model, lies in the precise prediction of angular separation and position angle values for a stellar companion. These position values depend on seven orbital parameters, which are unknown. From equation 2.19a, we have that the global likelihood for a binary system model is:

$$p(D|B_i, I) =$$

$$\int dq \int dT \int de \int a \int \Omega \int \omega \int i \int C p(q, T, e, a, \omega, \omega_2, i, C | B_i, I)$$
$$\times p(D|B_i, q, T, e, a, \omega, \omega_2, i, C)$$

$$(2.22)$$

where $p(q, T, e, a, \Omega, \omega, i, C | B_i, I)$ is the joint prior probability for the model parameters and $p(D|B_i, q, T, e, a, \Omega, \omega, i, C)$ is the conditional likelihood.

---

[8]The global likelihood of a model is equal to the weighted average likelihood for all the parameters in consideration.

Joint Prior Probability

The prior beliefs for each one of the parameter values can be expressed as a probability density function before obtaining new data. Because the global likelihood in the Bayes's factor depends on the conditional likelihood weighted by the prior probabilities distributions of each one of the parameters, it is necessary to compute the eight-dimensional integral shown in equation 5.4. To deal with this tedious integral, we made use of *Monte Carlo Integration* to estimate the value of the global likelihood by generating a number of random samples according to a determined function in a spatial domain. This process is based on computing the average value of this function for multiple random samples, which means an estimate of the value of the multi-dimensional integral.

We start by defining the joint prior probability of each prior parameter, which are mutually independent and distributed in a specific range. The probabilities for a binary system for T, ω, ω_2 and C are assumed to have a uniform distribution, so $p(T, \Omega, \omega_2, C|B_i, I) = 1$ and for q, a, e and i are explained in section 2 with more detail, thus:

$$p(q, T, e, a, \Omega, \omega, i, C|B_i, I) \propto q^{\beta} \left(\frac{e^2}{a} \right) \sin(i). \tag{2.23}$$

The joint prior probability for a single system model without parameters to find and a contrast equal to zero, will be:

$$p(C|S_i, I) = 1. \tag{2.24}$$

Conditional Likelihood

The conditional likelihood of the binary system can be computed as follows:

$$p(D|B_i, q, T, e, a, \omega, \omega_2, i, C) = A \times \exp\left[-\sum_{i=1}^{N} \underbrace{\left(\chi_o^2(x, y) + \frac{(\mu(x, y) - C)^2}{\sigma^2(x, y)}\right)}_{\chi^2(x, y, C)}\right]$$

(2.25)

where $\chi^2(x, y, C)$ is the best fit as a function of contrast and position (x, y) in the field of view, $\mu(x, y)$ is the best contrast ratio, $\sigma(x, y)$ the corresponding error for that position and A is a normalization constant. The IDL program binarygrid2.pro outputs functions $\mu(x, y)$ and $\sigma(x, y)$ such that the value of χ^2 for 3-dimensional (x,y,C) fits to the data is given by the formula:

$$\chi^2(x, y, C) = \frac{(\mu(x, y) - C)^2 - \mu^2(x, y)}{\sigma^2(x, y)}.$$

(2.26)

Using equation 2.25 and 2.26, we have:

$$p(D|B_i, P, T, e, a, \omega, \omega_2, i, C) \propto A \times \exp\left[-\sum_{i=1}^{N} \left(\frac{(\mu(x, y) - C)^2 - \mu^2(x, y)}{\sigma^2(x, y)}\right)\right] \propto \mathcal{L}_{B_i}(C, x, y).$$

(2.27)

where $\mathcal{L}_{B_i}(C, x, y)$ is the likelihood for the model that represents the binary star as a function of position and contrast ratio. In the case of a single system

model, there is only one parameter, meaning integration over only the contrast ratio to find the conditional likelihood.

$$p(D|S_i, I) = \int C p(C|S_i) p(D|S_i, C) \tag{2.28}$$

where,

$$p(D|S_i, C) = A \times \exp\left[\sum_{i=1}^{N} \frac{\chi^2(x, y, C)}{2}\right] \tag{2.29}$$

Since the hypothesis has an unknown parameter C equal to zero at the center of the search region, then its global likelihood will be:

$$p(D|C, S_i) = \mathcal{L}_{S_i}(C, x, y) \propto 1. \tag{2.30}$$

Then the global likelihood will be:

$$\mathcal{L}(S_i) \propto 1. \tag{2.31}$$

Occam Razor Factor

Now, we can compute the odds ratio, see equation 5.7. Just to be clear, the Bayes's factor does not rely on the ratio of the maximum likelihood, this factor depends on the global likelihood. However, the global likelihood of a model with α_i number of parameters can be expressed as its maximum likelihood by computing the product of the global likelihood times a factor called the *Occam Razor factor* Ω_{α_i}. For our binary and single systems hypothesis, we have:

$$p(D|B_i, q, T, e, a, \Omega, \omega, i, C) = \mathcal{L}_{max.}(B_i)\Omega_q, \Omega_T, \Omega_e, \Omega_a, \Omega_\Omega, \Omega_\omega, \Omega_i, \Omega_C \quad (2.32)$$

and

$$p(D|S_i, C) = \mathcal{L}_{max.}(S_i)\Omega_C. \quad (2.33)$$

The above equations can be interpreted as a penalization for miscalculating the appropriate prior range for each parameter. Penalization that, in our case, will be present in the calculation of position parameters for the stellar components, angular separation, and position angle, in other words, Occam factor arises automatically in the marginalization process. However, we are not interested in this factor, instead, we focus on the Bayes factor or marginal (global) likelihood ratios of the competing models.

2.5.2 Angular separation and Position angle

Position angle (PA) and angular separation are not well characterized in young close low-mass binary stars, therefore, in order to obtain a prior information of these measurable orbital parameters, I simulated N number values of *unknown* orbital parameters such us, time of periastron passage (T, years), period (P,year), semi-major axis (a,arc second), eccentricity (e), nodes (Ω), longitude of periastron (ω), inclination (i,degrees), epoch of observation (t2,year) and stellar masses (M_1, M_2) by sampling a corresponding distribution. To generate these orbital parameters, first, we assume an appropriate probability distri-

bution $f(x)$ for each one in the range between a and b. However, the key for generating these orbital parameters is based on the use of random values from a uniform distribution (U) on the interval between 0 and 1. Then, for a given parameter X in the range between a and b can be represented by a random value of U, such that the cumulative density function $F(x)$ of $f(x)$ in the interval [a,b] is equal to U.

$$F(x) = \int_a^x f(x)dx = U, \tag{2.34}$$

where X is any continuos random variable between a and b, and $F(a) = 0$ and $F(b) = 1$. Then, any random variable X with a propability density function $f(x)$ can be produced by the inverse function of $f(x)$, $F(x)$:

$$X = F^{-1}(U) \tag{2.35}$$

This procedure is known as Monte Carlo.

2.5.3   Orbital Parameters

- **Semi-major axis::** In the case for the semi-major axis, I used the approach followed by Metchev and Hillenbrand (2009) as:

$$f(a) = \int_{a_1}^{a_2} \frac{1}{a}da. \tag{2.36}$$

where a_1 and a_2 are semi-major axis values corresponding to inner and outer radii in the gap of the disk, respectively, and by following equation 2.34, we have:

$$F(a) = \int_{a_1}^{N_a} \frac{1}{a * K} \, da = U,$$ (2.37)

with $F(a_1) = 0$ and $F(a_2) = 1$, and $K = (\ln(a_2) - \ln(a_1))$. U represents a vector with N random values between 0 and 1. N_a random values on the interval of a_1 and a_2 are generated by the inverse of $F(a)$:

$$N_a = a_1 \exp^{(U*(\ln a_2 - \ln a_1))}$$ (2.38)

- **Eccentricity:** The eccentricity of the orbit was sampled by using the distribution (Brandeker et al. 2006):

$$f(e) = \int_{e_{min}}^{e_{max}} 2e \, de$$ (2.39)

where e_{min} and e_{max} are the minimum and maximum of eccentricity values for the probability density function. Then, the CDF:

$$F(e) = \int_{e_{min}}^{N_e} \frac{2e}{K} \, de = U,$$ (2.40)

where $K = e_{max}^2 - e_{min}^2$. To generate a random value of N_e for a given uniform variate U in the interval 0 and 1, we have:

$$N_e = \sqrt{U(e_{max}^2 - e_{min}^2) + e_{min}^2} \tag{2.41}$$

- **Inclination**: The inclination was sampled considering that the orbital plane of the generated binary stars might have any orientation in space. Then, the normal vector perpendicular to the orbital plane can point out in any portion of the solid-angle (η), meaning that it has an equal probability everywhere to be sampled as $p(\eta)d\eta = Constant$. The solid-angle can be expressed by spherical coordinates as follows:

$$d\eta = \sin(\theta)d\theta d\varphi \tag{2.42}$$

where for our observational purposes the co-latitude θ is equal to the inclination i. Now, if the probability of distribution of the normal vector with coordinates of i and θ is equal to $p(\eta)$, it can be expressed as:

$$p(i, \varphi) = \sin(i) \tag{2.43}$$

$$f(i) = \int_0^\pi \sin(i)di \tag{2.44}$$

Then, for the inclination we have a probability density function evaluated between 0 and π and equivalent to $p(i) \propto sin(i)$. So, if we take the Cumulative Density Function (CDF) to find the probability of a continuous random variable, we get:

$$F(i) = \frac{1}{K} \int_0^{N_i} \sin(i)di \tag{2.45}$$

where the constant $K = cos(0) - cos(\pi) = 2$. For a given CDF $F(0) = 0$ and $F(\pi) = 1$. To obtain N random values with a PDF $f(i)$, we obtain the inverse of $F(i)$, then:

$$N_i = \arccos(1 - KU) \tag{2.46}$$

with U a vector of random values distributed uniformly between 0 and 1.

- **Mass-Ratio**: For the stellar masses in the range of $M_2, M_2 + dM$ are generated N number values of companion masses by randomly sampling a mass-ratio q and linearly interpolating into isochrones of Baraffe (1998), see next section. The number of random mass ratios from Monte-Carlo approach has the following distribution:

$$f(q) = \int_{q_o}^{1} q^{\beta} dq \tag{2.47}$$

where q_o cannot be equal to zero because $f(q)$ will tend to infinity. The CDF of $f(q)$ has the form:

$$F(q) = \int_{q_o}^{N_q} = \frac{q^{\beta}}{K} dq = U \tag{2.48}$$

from the limits of the CDF, we have that $F(q_o) = 0$ and $F(1) = 1$ and where the constant K equal to:

$$K = \frac{\left(1 - q_o^{\beta+1}\right)}{\beta + 1} \tag{2.49}$$

The N_q random values generated from the uniform distribution U are

found by sampling:

$$N_q = \left(UK(\beta + 1) + q_o^{\beta+1}\right)^{\left(\frac{1}{\beta+1}\right)}. \tag{2.50}$$

where β is a power index of 0, see Metchev and Hillenbrand (2009) for more information.

- **Orbital Period:** For the orbital period, I used the values of total mass, semi-major axis and by using Kepler's law, the square of the period of any orbiting object is proportional to the cube of the semimajor axis of its orbit:

$$P = \sqrt{\frac{4\pi^2}{G * M_T} a^3} \tag{2.51}$$

where $M_T = M_1 + M_2$ obtained from interpolating Baraffe's models and a is the semimajor axis in AU obtained from Monte Carlo approach.

- **Longitude of Periastron and Ascending Node**: The element ω can take any values in the range $0 \leq \omega \leq 2\pi$ and its PDF is a constant s of the form:

$$f(\omega) = \int_0^{2\pi} s d\omega \tag{2.52}$$

Then, its CDF is equal to:

$$F(\omega) = \int_0^{N_\omega} \frac{s}{K} d\omega, \tag{2.53}$$

with $F(q_o) = 0$ and $F(2\pi) = 1$. N_ω random values are generated by

finding the inverse of $F(\omega)$ and s=1, then,

$$N_\omega = UK, \tag{2.54}$$

where $K = 2\pi$ and U a vector of random numbers from 0 to 1. Similarly, the PDF of the position angle of the ascending node, Ω, is a constant within the domain $0 \leq \omega \leq \pi$. Then, $K = \pi$ with a sampling of the form:

$$N_\Omega = UK, \tag{2.55}$$

- **Time of periastron passage**: random values were obtained by sampling a uniform distribution with a domain that best represents the companion orbit.

2.5.4 Computing Odd Ratio

After computing the Bayes factor $B_{B,S} = \frac{P(D|B)}{P(D|S)}$ for every target and assigned with a prior distribution γ that represents the best prior state of knowledge, we proceed to modify the γ values as follow:

$$P(\gamma|D) = P(\gamma)[P(D|B)P(B|\gamma) + P(D|S)P(S|\gamma)]$$
$$= P(\gamma)[P(D|B)\gamma + P(D|S)(1-\gamma)]$$
$$= P(\gamma)[\gamma B_{B,S} + (1-\gamma)]\}$$
$$\tag{2.56}$$

The odds ratio is computed by considering all TDs in our sample and additionally, TDs from previous studies, therefore:

$$P(\gamma|D_n) \propto P(\gamma) \prod_{n=1}^{n} [\gamma(B_{B,S})_n + (1 - \gamma)] \tag{2.57}$$

Choice of Prior Information

The Bayesian approach requires prior probabilities to all unknown hypothesis or models and their resultant parameters. In our case, whether there are two interacting stars or a single star in the observed data. This information rises from data of single stars surrounded by a transitional disk and then, modified by predictions of the frequency of binary stars among transitional disks. Because subjective information is unavailable from inside the inner region, we assumed that the observed data have arisen from one of two models. Therefore, we look for assigning prior probabilities to each model. A non-informative probability distribution for the frequency of binary or single systems is a parameter representing two unique scenarios, binary or not binary. Thus, $P(B|I) = \gamma$ represents the event of binarity and $P(S|I) = (1 - \gamma)$ not binarity, where the parameter $\gamma \in [0,1]$, and in the case of (B,S) $\in [(1,0),(0,1)]$ the PDF given γ is $P(B|\gamma) \propto \gamma^B (1 - \gamma)^{1-B}$. We made use of the well-known Bayesian method that represents uniform probability: *Jeffreys prior*. Also, an unimodal sampling distribution in the interval between 0 and 1 representing the γ values, is the family of *beta distributions*.

$$f(\gamma) = f(\gamma|\alpha, \beta) = \begin{cases} \frac{1}{\text{ß}(\alpha|\beta)}\gamma^{\alpha-1}(1-\gamma)^{\beta-1} & ; 0 < \gamma < 1, \quad \text{with} \quad \alpha, \beta > 0 \\ \\ 0; & \text{elsewhere} \end{cases}$$

$$(2.58)$$

where the beta function, $\text{ß}(\alpha|\beta)$, ensures a probability equal to unity, and to provide uniform probability to both events $\alpha, \beta = 1/2$. Therefore the Jeffreys prior for the sampling distribution γ is:

$$P(\gamma) \propto \frac{1}{\sqrt{\gamma(1-\gamma)}} \propto \frac{1}{\sqrt{B * S}} \qquad (2.59)$$

Statement of Contribution

This thesis is submitted as a Thesis by Compilation in accordance with
https://policies.anu.edu.au/ppl/document/ANUP_003405

I declare that the research presented in this Thesis represents original work that I carried out during my candidature at the Australian National University, except for contributions to multi-author papers incorporated in the Thesis where my contributions are specified in this Statement of Contribution.

Title and authors: The ALMA Early Science View of FUor/EXor objects. II. The Very Wide Outow Driven by HBC 494. This paper is published in Monthly Notices of the Royal Astronomical Society as D. Ruiz-Rodriguez, L. A. Cieza, J. P. Williams, J. J. Tobin, A. Hales, Z. Zhu, K. Muzic, D. Principe, H. Canovas, A. Zurlo, S. Casassus, S. Perez, and J. L. Prieto, 2017, MNRAS 466, 3519-3532

Current status of paper: Not Yet Submitted/Submitted/Under Revision/Accepted/Published

Contribution to paper: 95, 5% advise/comments/suggestions from collaborating authors_____

Senior author or collaborating authors endorsement: _____Lucas A. Cieza_____

Dary Alexandra Ruiz-Rodriguez		10/Oct/2017
Candidate − Print Name	Signature	Date

Endorsed

David Yong		10/Oct/2017
Chair of Supervisory Panel – Print Name	Signature	Date
Gary Da Costa		10/Oct/2017
Delegated Authority – Print Name	Signature	Date
Lucas A. Cieza		10/Oct/2017
Primary Supervisor and endorsement − Print Name	Signature	Date

3

The ALMA Early Science View of FUor/EXor objects. II. The Very Wide Outflow Driven by HBC 494.

We present Atacama Large Millimeter/sub-millimeter Array (ALMA) Cycle-2 observations of the HBC 494 molecular outflow and envelope. HBC 494 is an FU Ori-like object embedded in the Orion A cloud and is associated with the reflection nebulae Re50 and Re50N. We use ^{12}CO, ^{13}CO and $C^{18}O$ spectral line data to independently describe the outflow and envelope structures associated with HBC 494. The moment-1 map of the ^{12}CO emission shows the *widest* outflow cavities in a Class I object known to date (opening angle $\sim 150°$). The morphology of the wide outflow is likely to be due to the interaction between

winds originating in the inner disc and the surrounding envelope. The low-velocity blue- and red-shifted ^{13}CO and C^{18}O emission trace the rotation and infall motion of the circumstellar envelope. Using molecular line data and adopting standard methods for correcting optical depth effects, we estimate its kinematic properties, including an outflow mass on the order of 10^{-1} M$_\odot$. Considering the large estimated outflow mass for HBC 494, our results support recent theoretical work suggesting that wind-driven processes might dominate the evolution of protoplanetary discs via energetic outflows.

3.1   Introduction

FU Orionis objects (FUors) belong to an embedded pre-main-sequence phase of young stellar evolution, usually associated with reflection nebulae (Herbig, 1966, 1977). Observational features of these objects include similarities to the F-G supergiant optical spectra and overtone CO absorption, in addition to water vapour bands in the near-infrared wavelengths characteristic of K-M supergiants (Mould et al., 1978). At far-infrared/submillimeter wavelengths, the Spectral Energy Distributions (SED) of FUors are largely dominated by the envelope emission. Where such envelopes are massive enough to replenish the circumstellar disc in the stellar formation process (Sandell & Weintraub, 2001). Usually, these types of young stellar objects (YSO) are explained with a disc in Keplerian rotation that produces the observed double-peaked line profiles as seen in FUors (Hartmann & Kenyon, 1985); however, those objects that do not present line broadening consistent with pure Keplerian rotation might require an additional contribution from another component such as a

high-velocity inner disc wind (Eisner & Hillenbrand, 2011).

The main observational feature of FUors is their eruptive variability in optical light that can reach 5 mag or even more. This variability is due to outbursts that rise in short periods of time of around $\sim 1-10$ yrs and decay timescales that take place from decades to centuries (Herbig, 1966, 1977). It is believed that material falling from a massive circumstellar disc to the central protostar at high disc accretion rates ($\sim 10^{-4}$ $M_{\odot}yr^{-1}$) is responsible for these events (Hartmann & Kenyon, 1996), although their outburst frequency is unknown. During the outburst phase, large amounts of disc material (~ 0.01 $M_{\odot}$) are accreted onto the parent star, thus increasing the luminosity during these short events. If the episodic accretion scenario (Audard et al., 2014) is correct, most systems undergo multiple FU Ori events during their evolution and the study of these outbursts represents a key element of the star and planet formation process.

Additionally, the outbursts might be connected to the evolution and extension of the observed outflows in FUors. It has been suggested that the formation, evolution and widening of molecular outflows are the result of the wide-angle wind that arises from the interaction of the highly accreting disc inner edges with a strongly magnetised central star (Snell, Loren & Plambeck, 1980; Shu et al., 2000); or highly collimated jets that propagate into the surrounding envelope material (Raga & Cabrit, 1993; Ostriker et al., 2001). However, the triggering mechanism for an FUor outburst has yet to be established. The proposed mechanisms for the FU Ori outburst include: 1) Tidal interaction of a massive disc and an eccentric binary system or a giant planet (Bonnell & Bastien, 1992; Lodato & Clarke, 2004), 2) Magnetorotational instability (MRI)

activated by gravitational instabilities (GI) (Armitage, Livio & Pringle, 2001; Zhu et al., 2009; Martin & Lubow, 2011) and 3) Disc Fragmentation developing spiral structures, more specifically, clump accretion events (Vorobyov & Basu, 2005). Testing the proposed theoretical scenarios requires measuring disc masses of FUor objects and spatially resolving structures such as asymmetries in the disc and close binaries. For instance, clumps would indicate large-scale disc fragmentation, while knowledge of disc mass can constrain if GI operates in these discs. Interferometric observations in the millimetre and sub-millimetre of FU Orionis objects can spatially and spectrally resolve the envelope, bipolar outflows, and disc emissions and thus, provide a more accurate description of these embedded systems than possible with single-dish observations.

HBC 494 is an FUor object, Class I protostar, located in the Orion molecular cloud, which has an estimated distance of 414 $\pm$7 pc (Menten et al., 2007). Initially, this luminous object was identified from its associated reflection nebulae, Re50 and Reipurth 50 N (Re50N). Reipurth (1985) detected a very bright nebulous object by performing an optical survey in the Orion molecular cloud. A more detailed study by Reipurth & Bally (1986) reported the sudden appearance of an intense and variable conical nebula: Reipurth 50 N (Re50N). This brightening episode is believed to be a consequence of an outburst event in HBC 494. This infrared source has a luminosity of ~ 250 L$_\odot$ and is located about 1.5 arc min north of Re50 (Reipurth & Bally, 1986). Supporting this hypothesis, Chiang et al. (2015) reported a new brightening event in Re50N at some point between 2006 and 2014, while Re50 has faded considerably. From recent ALMA observations, Cieza et al. (In Prep.) reported an asymmetry in the 230 GHz continuum at the South-West of HBC 494 and they speculated that this
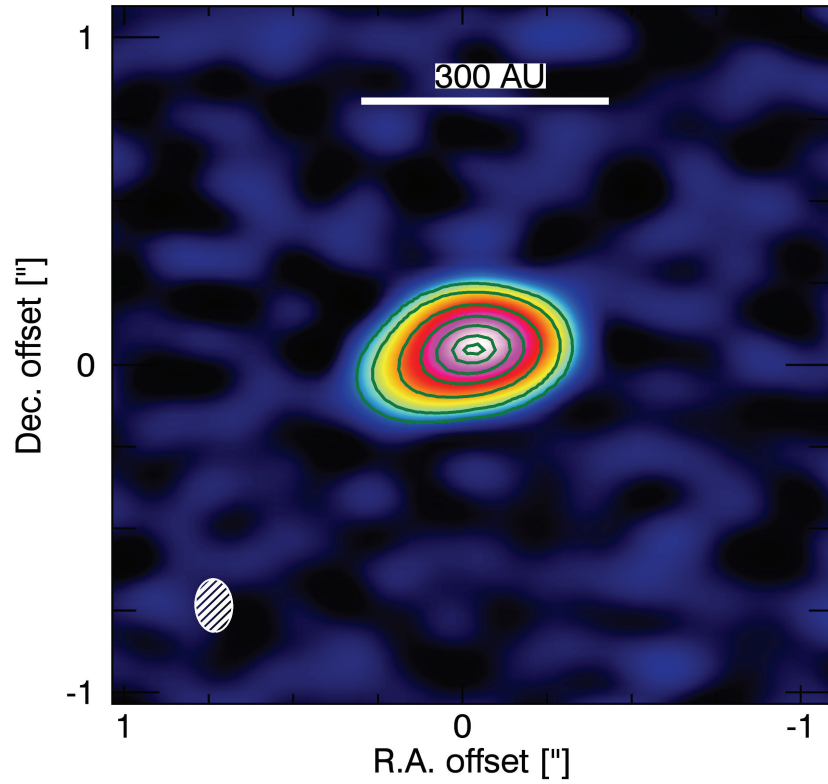
Figure 3.1: 230 GHz Continuum emission of HBC 494 together with contour levels with steps of 10, 30, 80, 150 and 250 $\times$ rms (0.25 mJy beam^{-1}). The $0.35'' \times 0.27''$ with P.A. $= -90^{\circ}$ synthesised beam is shown on the lower left corner of the image.

feature might be a result of a binary object undergoing a formation process and triggering an outburst in HBC 494. Binary objects are becoming strong candidates to trigger these outburst events as they are being resolved more efficiently in the ALMA era, such as the case of the FU Ori system (Hales et al., 2015). Only for guidance to the reader, an illustration of the 230 GHz continuum of HBC 494 is presented in Figure 3.1 to highlight the non-symmetric emission. From the major and minor axes of the continuum emission, Cieza et al. (In Prep.) found a very high inclination (i) of $\sim 70.2^{\circ} \pm 2.5$ (i.e. close edge-on). However, at this resolution, the continuum observation reveals an asymmetry towards the south-east side of the disk, leading to an uncertain estimation of this parameter, a more detailed description and analysis can be found in Cieza et al. (In Prep.). With a total flux density of 113 ± 2.5 mJy and adopting a distance to the Orion nebula of 414 ± 7 pc, they estimated a dust disc mass of 2.0 M$_J$ at 20 K, and assuming a gas-to-dust mass ratio of 100, a total disc mass of 0.2 M$_{\odot}$.

Here, we present ALMA band-6 (230 GHz/1.3 mm) continuum and ^{12}CO, ^{13}CO and C^{18}O J=2-1 line observations of HBC 494. We use the more optically thin tracers ^{13}CO and C^{18}O to study the envelope material and the optically thick ^{12}CO emission to investigate the strong bipolar outflow. The ALMA observations and the data reduction process are described in section 4.2. The results are presented in Section 6.4, and their implications discussed in section 6.5. The summary and conclusion are presented in Section 6.6.
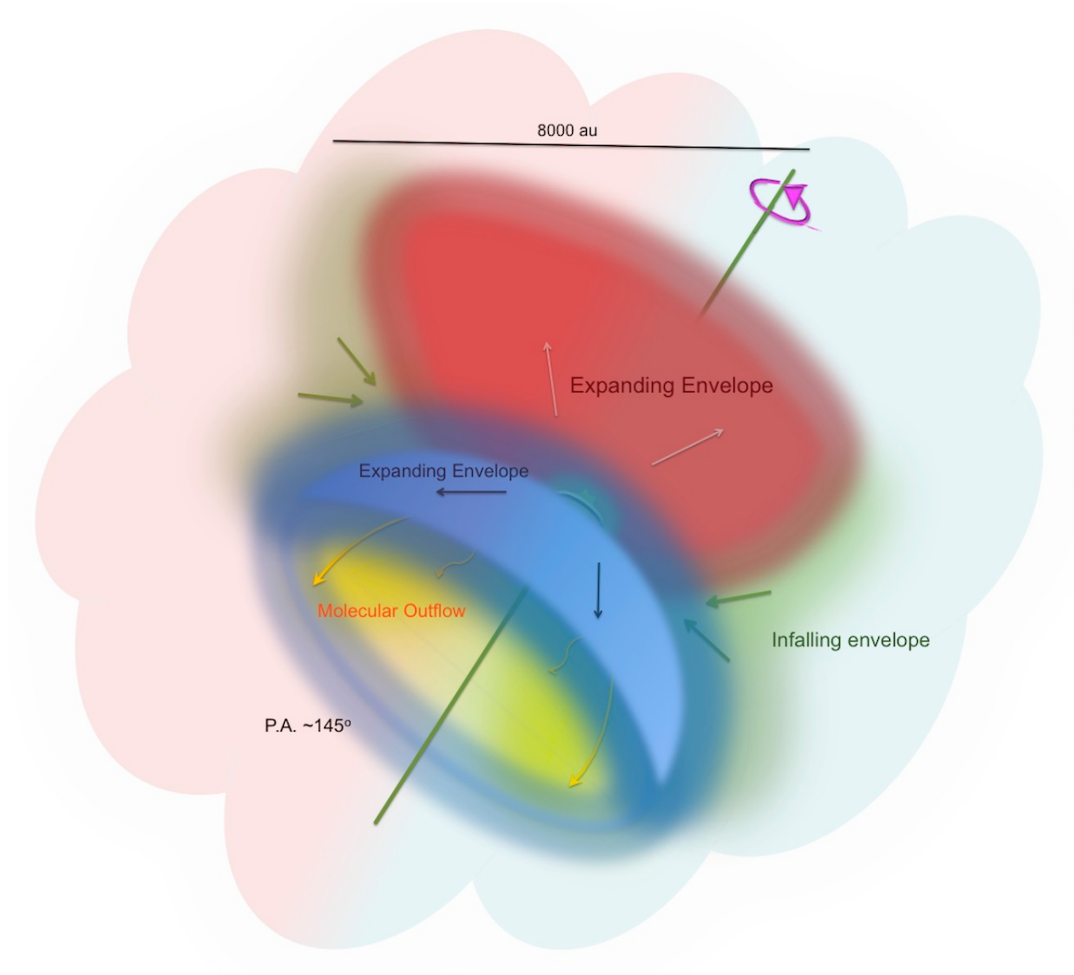
Figure 3.2: Cartoon showing the different dynamical and flux components traced by ^{12}CO, ^{13}CO and $C^{18}O$ of HBC 494. The envelope and the cavities are coloured with red to illustrated the red-shifted emission, while blue illustrates the blue shifted emission. Envelope material close to and accreting onto the disc is coloured with green and its infalling motion is indicated by the small green arrows. The green line with a position angle of $\sim 145^{\circ}$ depicts the rotation axis of the entire system.

3.2   Observations

ALMA observations for HBC 494, located at 05^h 40^s 27.45^s -07° $27'$ $29.65''$, were taken under program 2013.1.00710.S during Cycle-2 phase and over three different nights. This program involves the observation of eight FUor/EXor objects with results to be published in Cieza et al. (2016), Zurlo et al. (2016), Ruíz-Rodríguez et al. (2016b), Principe et al. (In Prep.) and Cieza et al. (In Prep.). The first two nights are December 12th, 2014 and April 15th, 2015 using 37 and 39 antennas on the C34-2/1 and C34/2 configurations, respectively. These configurations are quite similar with the shortest baseline of $\sim$ 14 m and longest of $\sim$ 350 m. The precipitable water vapor ranged from 0.7 to 1.7 mm with an integration time of $\sim$ 2 min per each epoch. Additionally, a third night, on August 30th, 2015 HBC 494 was observed with 35 antennas in the C34-7/6 configuration with baselines ranging from 42 m to 1.5 km, an integration time of $\sim$3 min, and a precipitation water vapor of 1.2 mm. The quasars J0541-0541, J0532-0307 and/or J0529-0519 (nearby in the sky) were observed as phase calibrators. J0423-013 and Ganymede were used as Flux calibrators, while the quasars J0607-0834 and J0538-4405 where observed for bandpass calibration.

Our correlator setup included the J=2-1 transitions of ^{12}CO, ^{13}CO and $C^{18}O$ centered at 230.5380, 220.3987, and 219.5603 GHz, respectively. The correlator was configured to provide a spectral resolution of 0.04 km s^{-1} for ^{12}CO and of 0.08 km s^{-1} for ^{13}CO and $C^{18}O$. The total bandwidth available for continuum observations was 3.9 GHz. The observations from all three nights were concatenated and processed together to increase the signal to noise and *uv*-coverage.

The visibility data were edited, calibrated and imaged in CASA v4.4 (McMullin et al., 2007). The uncertainty for calibrated flux is estimated to be 10 %. We used the CLEAN algorithm to image the data and using a robust parameter equal to zero, a briggs weighting was performed to adjust balance between resolution and sensitivity. From the CLEAN process, we obtained the following synthesized beams: $0.35'' \times 0.27''$ with P.A. = -90° for ^{12}CO, $0.37'' \times 0.28''$ with P.A. = 86.5° for ^{13}CO and $0.37'' \times 0.29''$ with P.A. = 87° for C^{18}O. The rms is 12.5 mJy beam^{-1} for ^{12}CO, 16.0 mJy beam^{-1} for ^{13}CO and 13.9 mJy beam^{-1} for C^{18}O. For the integrated continuum, we obtained a synthesized beam and rms of $0.25'' \times 0.17''$ with P.A. = -85.5° and 0.25 mJy beam^{-1}, respectively. The maximum resolvable angle is 11 arc sec.

3.3 Results

Our data reveal the impressive extension of the outflow and envelope surrounding HBC 494 allowing us to piece together the main physical components of this object. The close edge-on configuration of the system means that the red- and blue-shifted outflow lobes are spatially separated. The complex gas kinematics and density gradients are traced by the blue-shifted and red-redshifted components of the CO emission. ^{12}CO traces the bipolar and extension cavities of the outflow with a rotation axis oriented at $\sim$ 145° [1] (Section 4.3.1). ^{13}CO probes the infalling and rotating envelope surrounding the protostar and disc. A fraction of the mass of this part of the envelope is eventually transported

---

[1] All position angles are specified north through east.
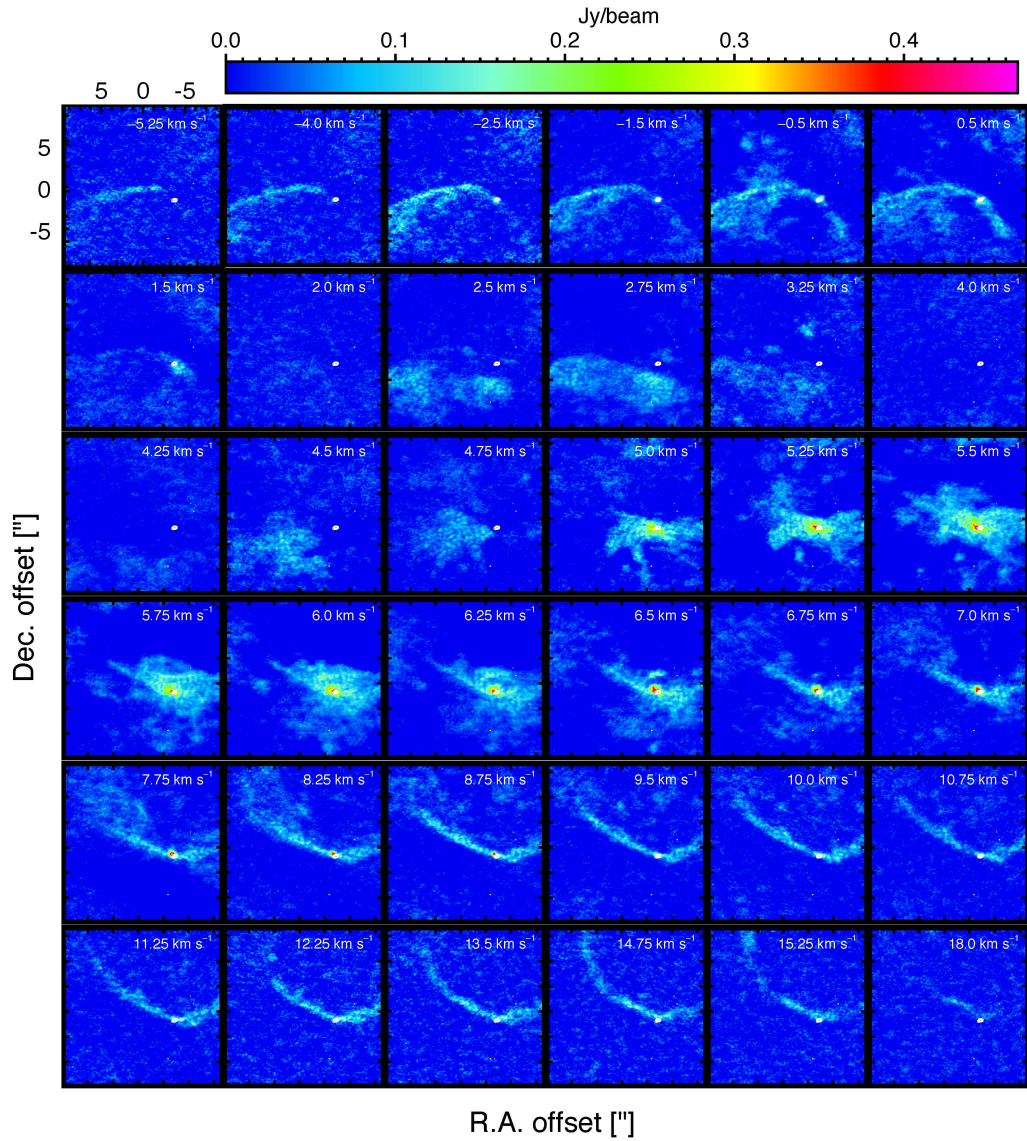
Figure 3.3: Channel maps of the ^{12}CO. LSR velocities are shown at the top-right corner of each panel with a systemic velocity of $\sim$4.6 km s^{-1}. White contours represent the continuum emission around HBC 494 as shown in Figure 4.2a.

onto the disc to be accreted onto the protostar, while at more distant regions from the central object, another fraction is being pushed away to external regions by the opposing outflow (Section 4.3.2). $C^{18}O$ traces similar regions as ^{13}CO at the northern side of the central object, while at larger distances, the envelope is driven out by the wider-angle portions of the wind (Section 3.3.3). Also, the $C^{18}O$ is weak at the southern region of the system, suggesting lower densities. Using the $C^{18}O$ line, we estimated a systemic velocity of $\sim$4.6 km s^{-1}, see section 3.3.5. We further estimate the kinematics and masses of the outflow and envelope from the emission and its velocity structure (Section 4.3.4). To picture HBC 494 in a more comprehensive way, we provide a cartoon showing the main components drawn from the ^{12}CO, ^{13}CO and $C^{18}O$ emissions, see Figure 3.2.

3.3.1 ^{12}CO Moment Maps

The ^{12}CO emission traces the highly energetic outflow blowing through the gas and creating a bipolar cavity in the molecular cloud. In our data cubes, significant ^{12}CO emission is detected at the velocities ranging from -5.25 to 18 km s^{-1}, see Figure 3.3. We integrated separately, the channels corresponding to the "Northern" and the "Southern" outflows to show structural shapes in a more clear manner. The moments 0 and 1 of the high-velocity blue- and red-shifted outflow cavities are shown in Figures 3.4a, 3.4b and 3.4c and their corresponding zoomed version in the small windows next to each figure. Figure 3.4a and 3.4b have a velocity range, with respect to the Local Standard of Rest (LSR), between -5.25 and 4.75 km s^{-1} for the blue-shifted region and between 6.75 and 18 km s^{-1} for the red-shifted emission. Although the complete

(a) Moment 0: Southern Outflow

(b) Moment 0: Northern Outflow

(c) Moment 1: Entire System.
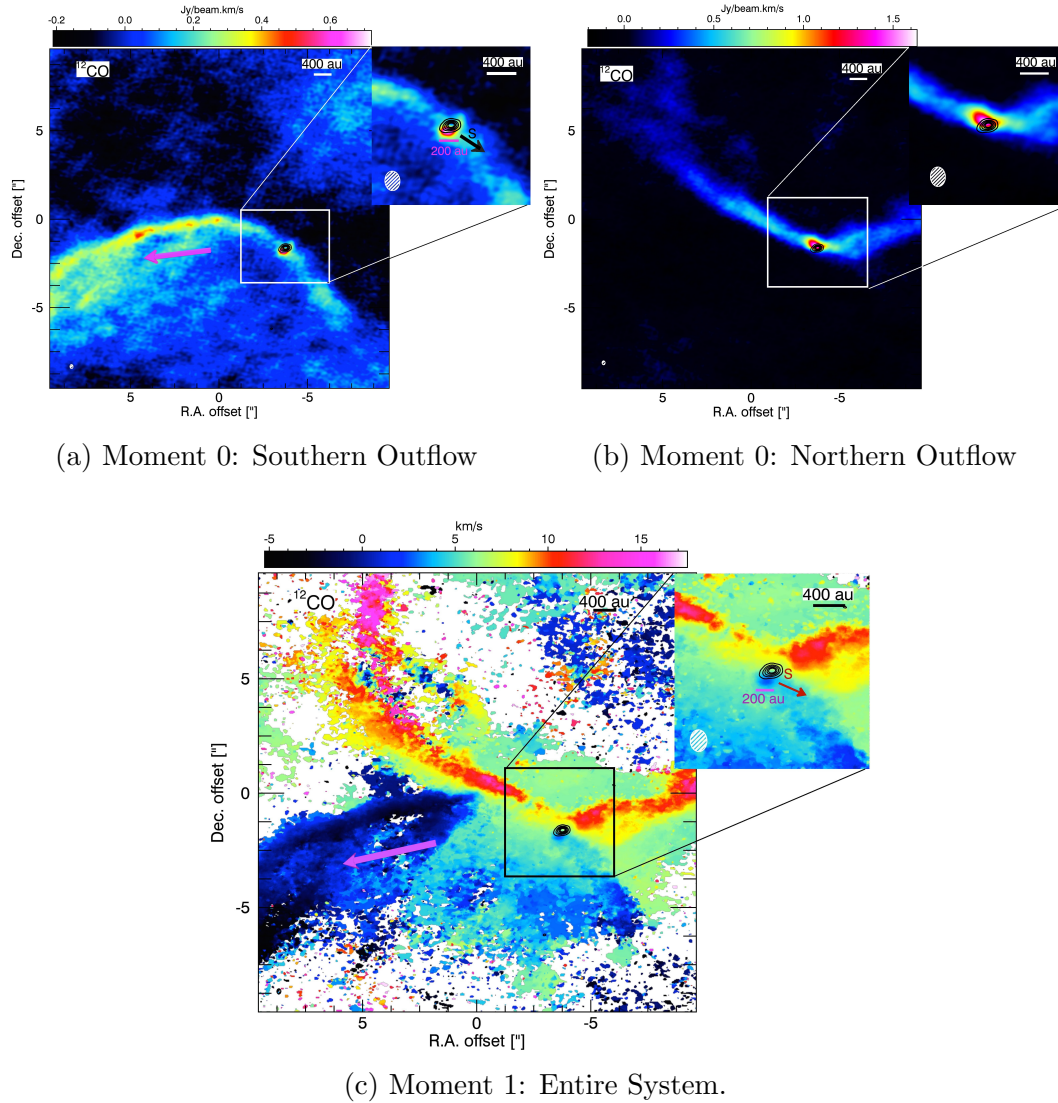
Figure 3.4: Figure a: Integrated intensity maps of the ^{12}CO blue- shifted emission from -5.25 to 4.75 km s^{-1} channels. Figure b: Integrated intensity maps of the ^{12}CO red- shifted emission on the velocity range between 7.0 and 18 km s^{-1} . Figure c: ^{12}CO velocity field map that was obtained from the integration over the velocity range from -5.5 to 18 km s^{-1}. Black contours show the continuum emission around HBC 494 at 10, 30, 80, 150 and 250 $\times$ rms (0.25 mJy beam^{-1}). The $0.35'' \times 0.27''$ with P.A. = -90° synthesised beam is shown on the lower left corner of each panel. The upper right insets are a closeup ($\pm$ 2.7") of the central object. The black and red arrows shown in the insets of Figures 3.4a and 3.4c point out the "stream" described in section 4.3.1. While the purple arrow shows the material interacting with the surrounding envelope, also detected at ^{13}CO and C^{18}O emissions, see Figures 4.2b and 4.2c.

extension of these bipolar cavities is not observed because it falls outside of our field of view, the very *wide* outflow cavities reach an apparent opening angle of $\sim 150°$ with an extension of at least 8000 au at a distance of 415 pc. Such a sculpted and defined outflow cavity is among the widest known to date and is remarkable for a Class I object, which typically have narrower cavities at these early stages. The overall range of these Class I outflows varies between 30 and 125° (Arce & Sargent, 2006; Klaassen et al., 2016; Zurlo et al., 2016; Principe et al., In Prep.). In addition, the ^{12}CO emission comes predominantly from the material directly influenced by the outflow, indicating the deep sweeping of surrounding material inside out acquiring a higher temperature. This might be a product of the interaction between the surrounding material and the high luminosity central protostar ($\sim 250\ L_\odot$; Reipurth & Bally, 1986). The lack of uniform emission in the extension of the cavities as seen in Figures 3.4a and 3.4b, is likely related to the ALMA maximum recoverable scale of $11''$ that would correspond to ~ 4500 au and prevents resolving larger scale structures. Thus, the "missing" emission does not imply a lack of ^{12}CO gas emission in between cavity arms (e.g. Bradshaw, Offner & Arce, 2015).

The red-shifted velocity field of ^{12}CO, considering emission merely from the outflow, can be described in terms of the degree of interaction with the surrounding envelope. The Northern outflow presents a velocity pattern with a gradient field perpendicular to the outflow axis that ranges between 7.0 and 18 km s^{-1}. This suggests that its opening angle increases as the abundant envelope material is being removed inside out from the outflow axis. Additionally, at the base of the bipolar cavities, a large amount of material with velocities from 5.0 to 6.75 km s^{-1} seems to follow an infalling motion surrounding the central
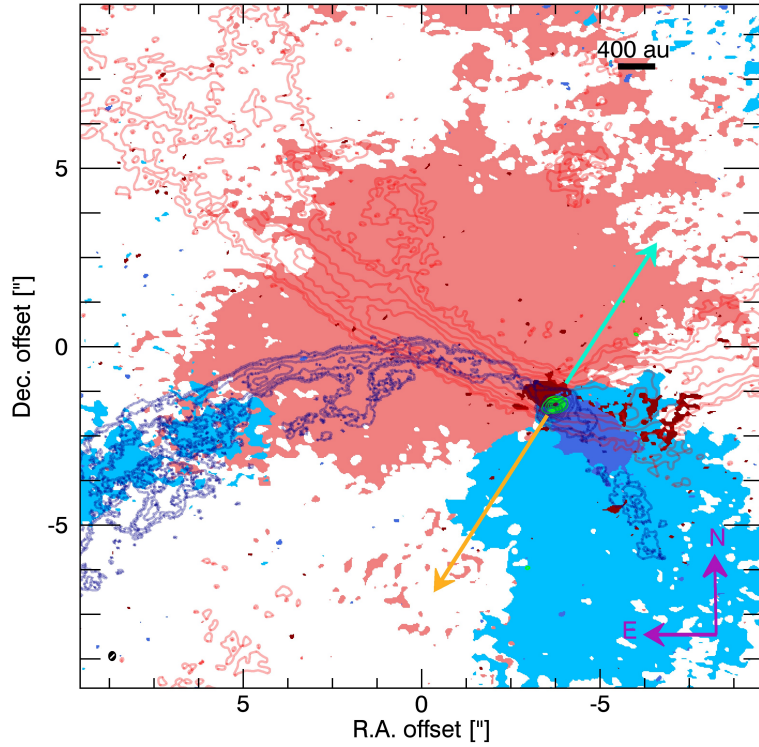
Figure 3.5: Comparison of the ^{12}CO and ^{13}CO velocity range-integrated intensity maps (moment 0). Blue and red contours show the integrated intensity of the ^{12}CO blue- and red shifted lobes, respectively, at 80, 150, 300, 450 and $600 \times 3\sigma$ levels. Light and dark red regions correspond to the red-shifted low (extended emission) and high (compact emission) velocities, respectively. Light and dark blue regions correspond to the blue-shifted low (extended emission) and high (compact emission) velocities, respectively. The extended and compact emission covers in blue-shifted emission velocities between 1.0 and 1.75 km/s and 2.5 and 3.5 and in red-shifted emission between 6.5 and 8.0 km/s and 4.5 and 5.5, which are explained in Section 4.3.2. Green contours show the continuum emission around HBC 494 at 10, 30, 80, 150 and 250 $\times$ rms (0.25 mJy beam^{-1}). The synthesized beam is shown on the lower left corner. Cyan and yellow arrows show the projected axis alignment along the Southern outflow - disc - Northern outflow system.

object, see Figure 3.3 and Figure 3.4c. This red-shifted outflow emission at velocities close to the ambient molecular cloud is dense gas being impacted by the outflow that belongs to the infalling envelope, which might be composed of ionized and hot material as a result of the direct interaction with the launched outflows. This slab of material closer to the rotation plane partially overlaps with the ^{13}CO emission tracing medium densities corresponding to the envelope material, a more detailed explanation can be found in Section 4.3.2.

The ^{12}CO blue-shifted emission probes at the Southern side of HBC 494 a complex geometry of the outflowing molecular material. The emission arises from the accelerated molecular gas depending on the medium properties (e.g. geometry, density). Indeed, it is detected at a velocity range between -5.25 and 1.5 km s^{-1} that the Southern cavity shows a brighter region, more concentrated at the southwest of the object, possibly due to the interaction with a significant amount of gas in the surrounding envelope, see purple arrow in Figure 4.2a. While, the ^{12}CO blue-shifted emission between 2.5 and 3.5 km s^{-1} might be outflow-envelope interactions with expanding motions.

In contrast to the wide angle outflow, it can be noted in the moments 0 and 1 maps and shown in the insets of Figures 3.4a and 3.4c, an "intensity maximum" with a diameter of around ~ 200 au that lies at the southwest from the continuum emission. This intensity maximum has a blue-shifted component that reaches 2.9 km s^{-1} and coincides with the location of the asymmetry found in the continuum by Cieza et al. (In Prep.), see Figure 3.1. However, it is not straightforward to attribute a physical origin to this feature and future observations with higher resolution are required.

The integrated flux on both sides of the bipolar outflow differ by a factor of ~ 2.5. At the Northern cavity the integrated flux is 39.65 ± 0.09 Jy km s^{-1} and at the Southern cavity a value of 93.32 ± 0.12 Jy km s^{-1}, see Figures 3.4a and Figure 3.4b. This might be evidence of the non-uniformity of the molecular cloud, where the evolution of this Class I object is taking place. Considering that CO transitions are thermalised at or close to their critical densities (~ 1.1 x 10^4 cm $^{-3}$; Carilli & Walter, 2013), the absence of a stronger emission at the Northern region indicates a slightly denser cloud material; while the stronger emission at the Southern region might point out a more widespread region that interacts with the ejected material from the central object. Additionally, the alignment among the South outflow $-$ disc $-$ North outflow at the base of both lobes, is evident in their ^{12}CO contours delineating the limb-brightened walls of the parabolic outflow cavities and the continuum, see Figure 3.5. This alignment allows us to draw a line through it and then, compute the outflow position angle (PA) of $\sim 145^{\circ}$ north through east.

3.3.2 ^{13}CO Moment Maps

We find that the ^{13}CO emission traces the rotating, infalling and expanding envelope surrounding the central system. The blue-shifted emission is detected at velocities from 1.0 to 4.25 km s^{-1} and the red-shifted material has a range of velocities from 4.5 to 9.0 km s^{-1} (Figure 4.4b). Figure 3.7a and 3.7b shows the moment-0 and moment-1 maps of the ^{13}CO line, while the small windows are a zoomed image to the central object. Since the ^{13}CO shows a complex structure with compact and extended emission that comes from different regions of the envelope, we integrated channel maps of blue- and red-shifted low (extended
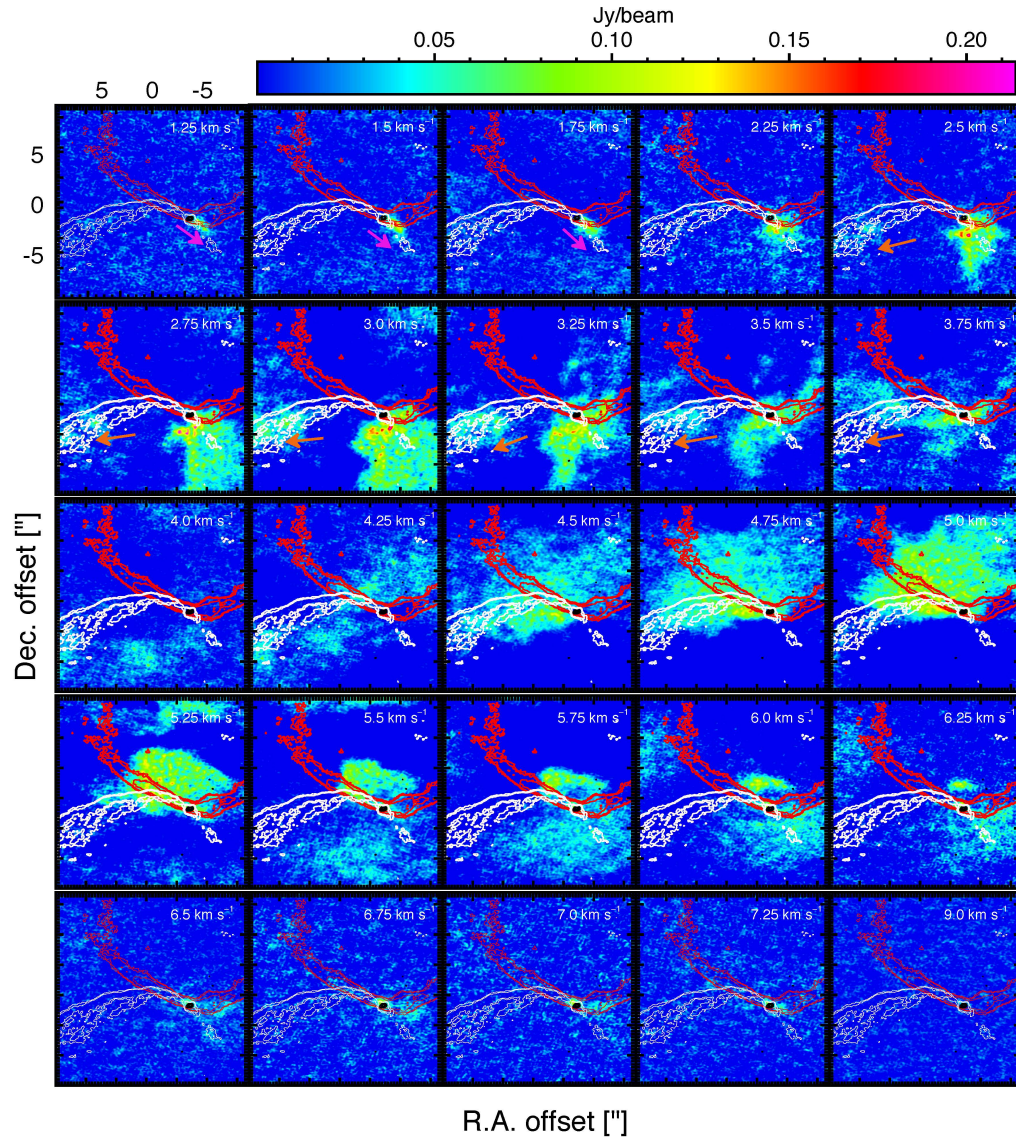
Figure 3.6: Channel maps of the ^{13}CO. LSR velocities are shown at the top-right corner of each panel with a systemic velocity of $\sim$4.6 km s $^{-1}$. White and red contours show the integrated intensity of the ^{12}CO blue- and red shifted lobes, respectively, at 150 and 300 $\times$ 3σ levels. Magenta arrows in the channels with velocities from 1.25 to 1.75 km s $^{-1}$ point out the emission of the streamline on this side of the system. Brown arrows in the channels with velocities from 2.5 to 3.75 km s $^{-1}$ point out the interaction between the Southern outflow and the surrounding envelope and showing how as a result there is expelling material on this side of the envelope directed toward us. Black contours show the continuum emission around HBC 494 at 10, 30, 80, 150 and 250 $\times$ rms.
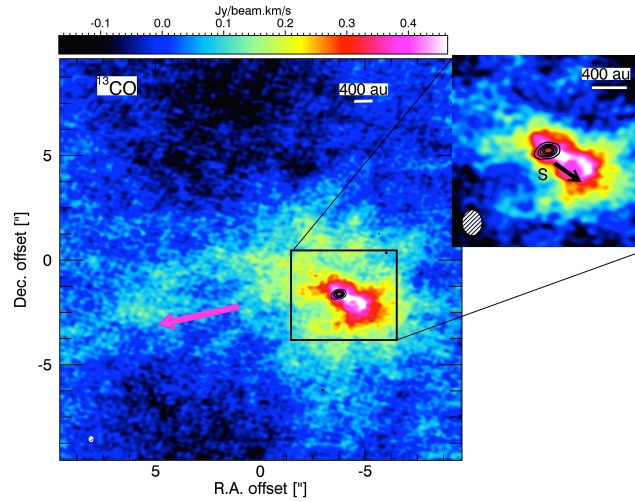
(a) Moment 0
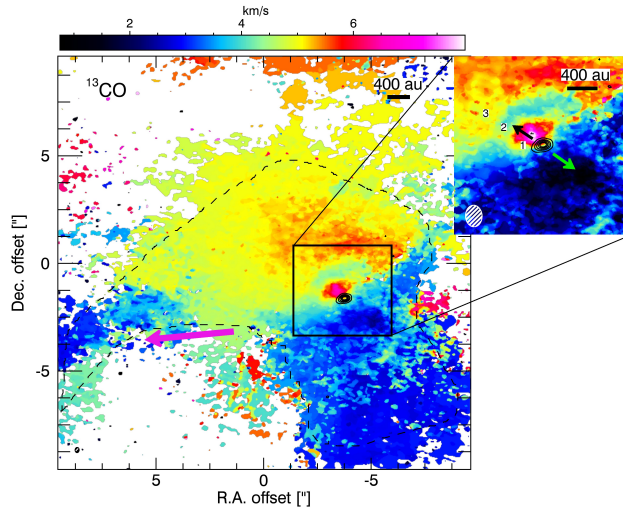
(b) Moment 1

Figure 3.7: Figure a: ^{13}CO intensity maps (moment-0) integrated over the velocity range of $1.0 - 9.0\ \mathrm{km\,s^{-1}}$. Figure b: Intensity - weighted mean velocity (moment-1) map of ^{13}CO in the velocity range $1.0 - 9.0\ \mathrm{km\,s^{-1}}$ over values higher than a 3σ ($\sigma \sim 15\ \mathrm{mJy\,beam^{-1}\,km\,s^{-1}}$). The $0.37'' \times 0.28''$ with P.A. $= 86.5°$ synthesised beam is shown on the lower left corner of each panel. Black contours show the continuum emission around HBC 494 at 10, 30, 80, 150 and $250 \times \mathrm{rms}$ ($0.25\ \mathrm{mJy\,beam^{-1}}$). The upper right insets are a closeup ($\pm\ 2.7$") of the central object. The black and green arrows shown in the insets of Figures 3.7a and 3.7b point out the streamline described in section 4.3.2. While the purple arrow shows the material interacting with the outflow detected at ^{12}CO emission, see Figures 4.2a. The region enclosed with dashed lines correspond to the region in which we integrated the line profile shown in Figure 3.11.

emission) and high (compact emission) velocities in order to see a more detailed velocity structure and a direction of the velocity gradient (e.g. Aso et al., 2015). Figure 3.5 shows the moment 0 with integration of the blue-shifted emission at velocities between 1.0 and 1.75 km s^{-1} and 2.5 and 3.5 km s^{-1} and red-shifted emission between 6.5 and 8.0 km s^{-1} and 4.5 and 5.5 km s^{-1}. The light red and blue and dark blue and red areas correspond to the extended and compact regions, respectively. Using the compact emission, we draw a line along the gradient velocity and then, estimate a PA of $\sim 50°$ north through east, which is almost perpendicular to the outflow PA of $\sim 145°$. Similarly, the low velocity components (extended structure) show a velocity gradient with a PA of $\sim 50°$.

The compact blue-shifted emission protrudes with a high flux density that we named as "stream" (S) located at the southeast of the disc and indicated by the black arrow along the feature in Figure 3.7a. In Figure 3.7b a green arrow is shown representing the location of the stream detected in the moment 0. The direction of this compact structure is difficult to indicate, but it might have originated in wide-angle winds from the central object blowing into the envelope (Snell, Loren & Plambeck, 1980; Shu et al., 2000; Gardiner, Frank & Hartmann, 2003) and expelling material to larger radii, following the Southern outflow. Figure 4.4b presents the channel maps of the ^{13}CO line, where this stream or compact blue-shifted emission is indicated with a magenta arrow and ^{12}CO contours are over plotted to spatially compare these emissions. On the other hand, the extended blue-shifted emission is more likely to be part of the surrounding envelope, being pushed toward us by the outflow. In addition, on the bottom-left side of Figure 3.7b an elongated structure appears, indicated with a purple arrow, and with blue-shifted velocities of 2.5 and 3.75 km s^{-1},

coincides with the ^{12}CO emission detected in the Southern region of a velocity range of $2.5 - 3.25$ km s^{-1}. Thus, the "extended" emission is likely tracing the internal structure of the envelope and showing how the southern outflow is expelling material on this side of the envelope directed toward us.

The ^{13}CO red-shifted emission also originates from two different regions in the envelope: one close and other farther away from the central system. The red-shifted compact emission source is the envelope material located very close to the protostar that reaches velocities of 6.5 and up to 9 km s^{-1} (Figure 4.4b). The origin of this emission is likely related to the dragged gas by the ejection of matter at the Northern cavity and indicated in Figure 3.7b as region 1. The second region, shown as regions 2 and 3 in the inset of Figure 3.7b, suggests that the emission at velocities between ∼4.5 and 6.25 km s^{-1} corresponds to material being accreted onto the system and thus, indicates the kinematics of the infalling and rotating envelope at the base of the bipolar outflows. As mentioned in Section 4.3.1, the slab of material closer to the rotation plane partially overlaps with the ^{12}CO emission at the base of the cavities, thus strongly suggesting their accreting nature onto the central object. In addition, the emission in the velocity range between ∼5.5 and 6.25 km s^{-1} extends around the central system forming a feature with the shape of a half symmetric "ring" with a distance between the inner and outer ring of around ∼ 200 au, shown as region 2 in Figure 3.7b. Although, the origin of this feature is not clear, we speculate that it is a signature of material being accreted with a rotation motion.
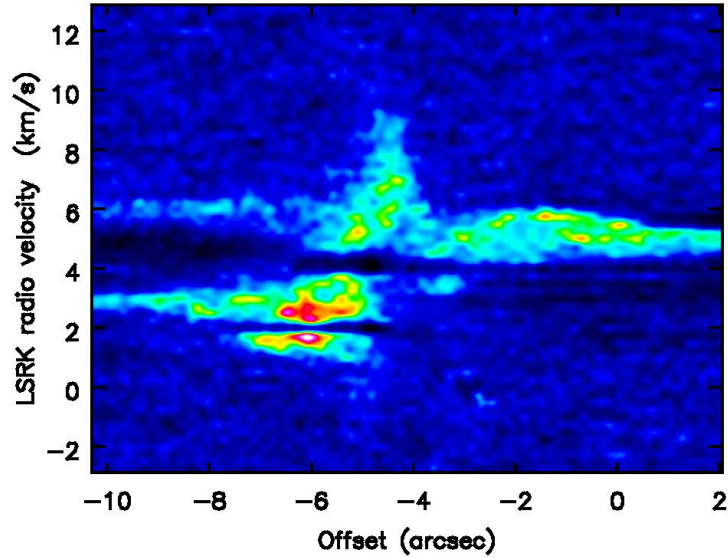
Figure 3.8: Position - velocity map of ^{13}CO along the axis perpendicular to the rotating outflow, see Figure 3.5.

Position-Velocity Diagram

The velocity gradient in the emission of ^{13}CO is perpendicular to the direction of the outflow. Thus, we have created a position−velocity (PV) diagram by cutting along the axis perpendicular to the rotating outflow and throughout the continuum emission of the disc, see Figure 3.8. In Figure 3.5 the cyan+yellow line indicates the outflow rotation axis and perpendicular to it, the image-space PV diagram cut at a position angle of $\sim 50^{\circ}$ and the averaging width is $\sim 0.45''$. This diagram shows higher velocities toward the center of the system as expected for envelope material feeding a central proto-stellar source.
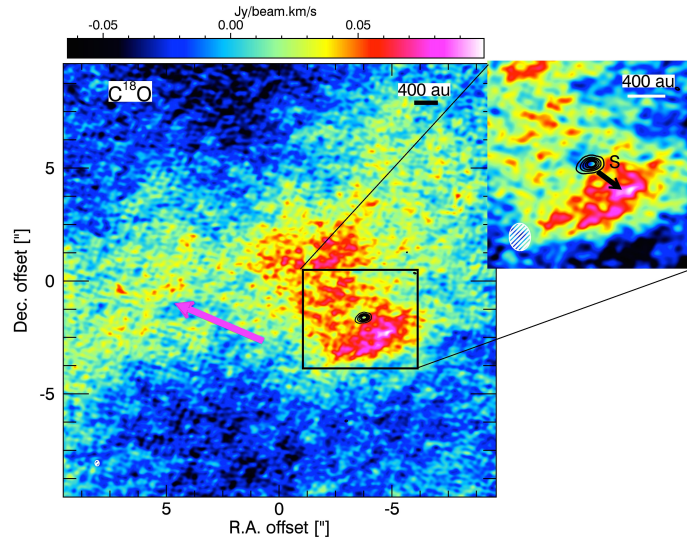
(a) Moment 0
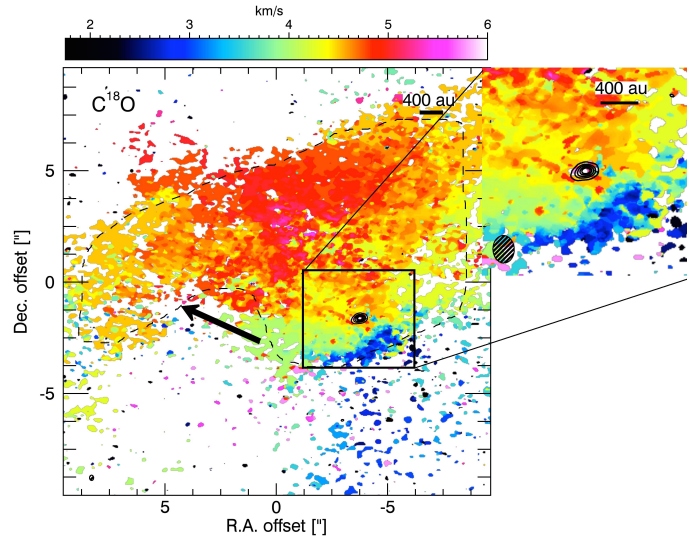
(b) Moment 1

Figure 3.9: Figure a: Integrated C^{18}O intensity over the velocity range between 1.75 and 6 km s^{-1}. Figure b: Intensity weighted mean velocity. The 0.37$''$ × 0.29$''$ with P.A. = 87° synthesized beam is shown on the lower left corner of each panel. Black contours show the CO continuum emission around HBC 494 at 10, 30, 80, 150 and 250 × rms (0.25 mJy beam^{-1}). The upper right insets are a closeup (±2.7$''$) of the central object. The black arrow shown in the inset of Figure 3.9a point out the streamline described in section 3.3.3. While the purple and black arrows show the material interacting with the outflow detected at ^{12}CO emission, see Figures 4.2a. The region enclosed with dashed lines correspond to the region in which we integrated the line profile shown in Figure 3.11.

3.3.3 C^{18}O Moment Maps

Of the 3 isotopologues, C^{18}O has the lowest abundances and thus traces higher gas density regions inside the molecular cloud, where it sublimates off dust grains. Therefore, we used this line to map the morphology of the envelope surrounding HBC 494. With a channel width of 0.25 km s^{-1}, the emission is detected within a range of 1.75 and 6 km s^{-1}. Figure 3.9a shows the integrated flux over the spectral line and Figure 3.9b is the intensity-weighted velocity of the spectral line. The blue-shifted outflow is seen at velocities from 1.75 to 4.25 km s^{-1}. The stream feature detected in ^{13}CO at $1-1.75$ km s^{-1} is also seen in C^{18}O emission at 1.75-2.0 km s^{-1}, see Figure 3.9a for stream location, while the C^{18}O emission in the range of 2.25 and 4.25 km s^{-1} traces the shape of the envelope. Additionally, the C^{18}O blue-shifted emission is very weak compared to the red-shifted emission and is located mostly at regions close to the central source. The faint or lack of blue-shifted emission at larger distances from the central object in the southern direction might be an indication of a significant extended and diffuse gas, where the emission origin corresponds to a break out of the surrounding molecular cloud.

The C^{18}O red-shifted emission detected at velocities from 4.5 and 6 km s^{-1} is bright and overlaps the ^{13}CO red-shifted emission, see Figure 3.9b, meaning that this probes infalling and expanding envelope material at different locations from the central source. Following our assumption that the northern side of the cavity is more denser than the southern side, given the lower ^{12}CO emission at the northern outflow, then this traces out the colder and denser structures composing the infalling envelope. In addition, gas swept up by the southern

outflow is seen to the west with low velocities of around ~ 4.25 and 4.75 km s^{-1} and connected to rotating material in between the limbs of the outflows. The swept up gas is located slightly above the ^{13}CO arm emission and indicated with purple and black arrows in Figures 3.9a and 3.9b.

3.3.4   Outflow Masses and Kinematics

We use our molecular line data to derive the mass and kinematics of the outflow. However, as demonstrated in Cabrit & Bertout (1990), the estimated outflow masses and dynamical properties computed from an optically thick line such as ^{12}CO can be considerably underestimated if they are not corrected for optical depth effects (τ_{12}). Therefore, before computing the outflow properties, we corrected our molecular line data following standard methods such as those found in Arce & Goodman (2001), Curtis et al. (2010) and Dunham et al. (2014) to evaluate τ_{12} numerically. Essentially, these methods are based on computing abundance ratios of optically thin CO emissions. Then, assuming identical beam-filling factors and the same excitation temperature for both isotopes, also considering that ^{13}CO traces the optically thin emission of the outflow in detections at low velocities, we compute the ratio of the brightness temperatures between ^{12}CO and ^{13}CO, $\frac{T_{12}}{T_{13}} = X_{12,13} \frac{1-\exp(-\tau_{12})}{\tau_{12}}$, where the abundance ratio $X_{12,13} = [^{12}\mathrm{CO}]/[^{13}\mathrm{CO}]$ is taken as 62 (Langer & Penzias, 1993). $\frac{T_{12}}{T_{13}}$ in each channel is estimated by computing the weighted mean values, where the weight was performed using the sigma values of every channel. To compute the ^{12}CO mass, we apply the correction factor to all the channels with ^{13}CO detection above 5σ. For those channels where ^{13}CO is too weak to be detected, we extrapolate values from a parabola fitted to the weighted mean values of

the form:

$$\frac{T_{12}}{T_{13}} = 0.2 + 0.23(\text{v-v}_{\text{LSR}})^2.$$

As a part of the fitting process, we only use the channels with ^{12}CO and ^{13}CO emission above 3σ and the minimum ratio value was fixed at zero velocity. Figure 3.10 shows the fit with a χ^2 of 0.4 as a solid green line and the blue dots correspond to the weighted mean values and the error bars are the weighted standard deviations in each channel. For this fit, we did not use the last three points, presented as the red dots, because at these velocities ^{12}CO starts becoming optically thin.

After applying the correction factors to every channel and using the emission that traces the outflow in the blue- and red shifted components, we start from the assumption that the emission is optically thin and in Local Thermodynamic Equilibrium (LTE). Next, we integrated the intensity from pixels with detections above 5σ over all of these velocity channels to measure the N_{CO} column density. Then, with an $X_{\text{co}} = 10^{-4}$, which is the abundance of CO relative to H_2 taken from Frerking, Langer & Wilson (1982), we inferred the column density of N_{H_2}. The interested reader can find a detailed description available in Appendix C of Dunham et al. (2014). This quantity is multiplied by pixel area and then, summing over all the pixels, we obtain estimates of mass (M_{ch}) and using velocity channels, estimates of momentum (M_{ch} v_{ch})^2 and energy (0.5 M_{ch} v_{ch}^2) of the outflow. To obtain total values of these parameters, it is

---

[2]Properties not corrected from inclination effects

integrated over the whole range of velocities with detections.

In order to avoid contamination by ambient cloud emission or material not related to the outflows of HBC 494, we integrate only over those channels with emissions that shape the outflow; for example, in Figure 3.3, the ^{12}CO emission in the channels with a velocity range between 1.75 and 7.25 km s^{-1} were not considered, because they are related to the emission that arises from around the protostar and parcels of matter that belong to the surrounding envelope. Additionally, in order to assure emission only from the outflow, we built a mask around HBC 494 of radius size $\sim$ 1.5", where pixels inside this area were removed from the final analysis. Thus, separating the red- and blue shifted components, the blue shifted outflow kinematics were estimated by integrating channels in the range between -5.25 and 1.5 km s^{-1} for ^{12}CO and, 1.0 and 4.0 km s^{-1} for ^{13}CO. The range of channels in the red shifted emission are between 7.25 and 16.5 km s^{-1} for ^{12}CO and, 4.5 and 6.25 km s^{-1} for ^{13}CO.

For simplicity and considering how the excitation temperature varies the estimated parameters (e.g. Curtis et al., 2010; Dunham et al., 2014), we adopted for this quantity, values of 20 and 50 K in our analysis. The estimated parameters are shown in Table 6.6. Additionally, taking the extent of the ^{12}CO emission (20") and the maximum speed of the ^{12}CO gas extension, obtained using $\frac{v_s - v_b}{2}$ where v_s and v_b are the red- and blue-shifted maximum velocities, we estimated a kinematic age for HBC 494 of $\sim$5400 years to obtain the mechanical luminosity and mass loss rate of the outflow, see Table 6.6. However, these property estimations are lower limits of the outflow because HBC 494 is not detected completely in the extension of 20" of the image, see e.g. Figures 4.2a and 4.2c, and implicit assumptions in the method.

Envelope Mass and Kinematics

Following the process described above, we use the $C^{18}O$ emission to estimate the lower limits of mass and dynamical properties of the envelope surrounding HBC 494. Taking into account that as an optically thin tracer only provides information of distant regions from the central object, we did not build a mask for the $C^{18}O$ cube. Also, it is not necessary to apply a correction factor to compute the parameters of the cloud. As previously performed, we also separated the blue- and red-shifted components to integrate over ranges between and 1.75 and 4.25 km s^{-1} for blue-shift velocities and 4.5 and 6.25 km s^{-1} for red shift velocities. Estimated parameters of the molecular cloud are shown in Table 6.6.

Table 3.1: Mass, Momentum, Luminosity and Kinetic Energy of the Outflow and Envelope

Isotope	Property	Blue shifted[1]		Red shifted[2]	
		20 (K)	50 (K)	20 (K)	50 (K)
^{12}CO	Mass (10^{-2} M$_\odot$)	3.40 (52.00)	5.03 (77.00)	5.54 (50.00)	8.20 (74.00)
	Mass loss (10^{-5} M$_\odot$ yr^{-1})	0.64 (9.70)	1.00 (14.32)	1.03 (9.32)	1.53 (13.80)
	Momentum (M$_\odot$ km s^{-1})	0.20 (2.60)	0.30 (3.90)	0.28 (1.90)	0.40 (3.02)
	Energy (10^{43} ergs.)	1.10 (13.24)	1.60 (19.60)	1.71 (9.44)	2.53 (14.00)
	Luminosity (10^{-2}L$_\odot$)	2.00 (20.00)	3.00 (30.00)	3.00 (15.00)	4.00 (22.00)
^{13}CO	Mass (10^{-2} M$_\odot$)	3.46	5.20	3.10	4.70
	Mass loss (10^{-6} M$_\odot$ yr^{-1})	6.50	9.80	5.81	8.80
	Momentum (10^{-2} M$_\odot$ km s^{-1})	6.10	9.20	1.70	2.60
	Energy (10^{42} ergs.)	1.14	1.73	0.14	0.21
	Luminosity (10^{-3} L$_\odot$)	1.76	2.70	0.21	0.32
C^{18}O	Mass (10^{-4} M$_\odot$)	3.78	5.74	11.91	18.09
	Mass loss (10^{-7}M$_\odot$ yr^{-1})	0.71	1.10	2.22	3.39
	Momentum (10^{-4} M$_\odot$ km s^{-1})	2.00	3.00	2.35	3.60
	Energy (10^{39} ergs.)	1.90	2.90	0.68	1.04
	Luminosity (10^{-6} L$_\odot$)	2.92	4.44	1.05	1.60

[1] Blue shifted outflow kinematics were estimated after a cut above 5σ and integration of channels between -5.25 and 1.5 km s^{-1} for ^{12}CO, 1.0 and 4.0 km s^{-1} for ^{13}CO, and 1.75 and 4.25 km s^{-1} for C^{18}O

[2] Red shifted outflow kinematics were estimated with a threshold value above 5σ and integration of channels between 7.25 and 16.5 km s^{-1} for ^{12}CO, 4.5 and 6.25 km s^{-1} for ^{13}CO, and 4.5 and 6.25 km s^{-1} for C^{18}O.

[3] Parameters inside the parentheses correspond to the computed values after applying the correction factors for optical depth effects to all the channels with ^{13}CO detection above 5σ.

3.3.5 Spectral Lines

To further explore the kinematic properties of the envelope interacting with the outflow cavities, we obtained spatially integrated ^{13}CO and C^{18}O spectral lines from the regions where most of the radiation arises from the envelope while trying to avoid background emission. The regions enclosed with dashed lines in Figures 3.7b and 3.9b correspond to the regions in which we integrated the line profiles and figure 3.11 shows the line profiles of both isotopes. As expected, the observed C^{18}O spectral line shows a typical width previously seen in quiescent envelopes of around 0.7-2 km s^{-1} (e.g. Jørgensen, Schöier & van Dishoeck, 2002; Kristensen et al., 2012).

The observed C^{18}O line has a FWHM of 0.84 ± 0.04 and is centred at 4.60 ± 0.02 km s^{-1}, which is taken as the systemic velocity. The ^{13}CO profile shows a dip around 4.0 km s^{-1} and is slightly blue-shifted from the systemic velocity. This particular profile is not a real absorption and might be due to missing short-spacing information in the u-v coverage. The C^{18}O line is not affected by this spatial filtering because it is less abundant and traces a more compact region. In contrast to that, the ^{13}CO traces a more extended and energetic envelope region, which is evident in its full width of around 4.5 km s^{-1}. Hence, the ^{13}CO profile is broader than the C^{18}O indicating the complex outflow motion in ^{13}CO, previously seen in very young objects embedded in molecular clouds (e.g Kristensen et al., 2012). This profile might be evidence of an expanding envelope mostly in the Southern region, likely due to the stream emission observed with the ^{13}CO and C^{18}O isotopes at the southeast of the disc. Additionally, it might also indicate how the outflow cavities are
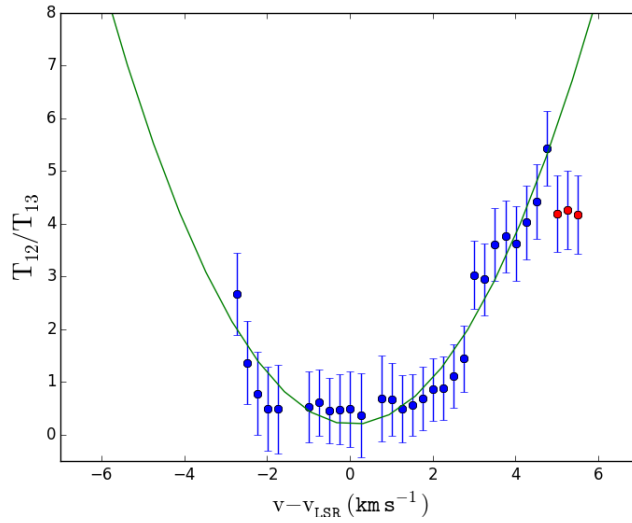
Figure 3.10: Ratio of the brightness temperatures $\frac{T_{12}}{T_{13}}$ as a function of the velocity from the systemic velocity. The blue solid dots are the weighted mean values and the error bars are the weighted standard deviations in each channel. The red solid dots are weighted mean values not used in the fitting process. The green solid line is the best-fit second-order polynomial with a χ^2 of 0.4.

efficiently pushing aside envelope material, see Figures 3.4a and 3.7a. For a Class I object with a low mass envelope, it becomes relatively easy to expel material to outer regions of the molecular cloud and thus, modify the geometry of the molecular cloud and surroundings (e.g Kristensen et al., 2012; Mottram et al., 2013). We provide a more detailed discussion about this scenario in Section 3.4.4.
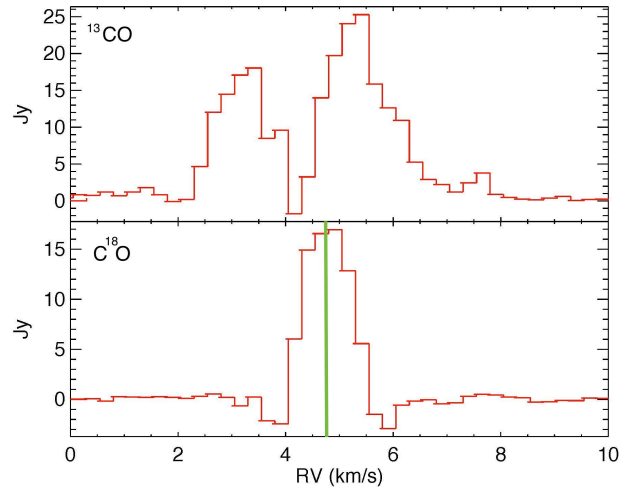
Figure 3.11: ^{13}CO and C^{18}O line profiles of the envelope shown as red solid lines. The spectrum for C^{18}O is centered at 4.60 ± 0.02 km s^{-1} and is shown as a green vertical line.

3.4 Discussion

3.4.1 The Wide Angle Outflow

Figures 4.2a and 3.5 illustrate a double-lobed ^{12}CO structure of HBC 494. The main characteristics of these shell-like structures are the *wide*-angle outflows extending (~ 8000 au) in opposite directions with a projected opening angle of $\sim 150°$ and a velocity pattern with high and low velocity components along and at the wake of the lobes, see Figure 3.3. This defined wide-angle morphology of the cavities has previously been observed in only a few Class I objects such as RNO 129 ($\sim 125°$; Arce & Sargent, 2006) and more recently in the FU Ori V883 Ori ($\sim 150°$; Ruíz-Rodríguez et al., 2016b) that, with an outflow mass on the order of 10^{-2} M$_\odot$, are observational evidence of the evolutionary trend found

in the morphology of the molecular outflows by Arce & Sargent (2006). This trend basically indicates how the opening angles increase with source age, leading to a stronger outflow-envelope interaction during the evolutionary process. Additionally, in Figure 4.2b, a "stream" is observed to the southeast of HBC 494 with velocities between $1-1.75$ km s^{-1} and partially linked to this stream, a $C^{18}O$ emission is detected with a velocity range of $1.75-2.0$ km s^{-1}, see Figure 3.9a. The direction of this stream likely follows the blue-shifted outflow component on this side of the bipolar cone and might be related to flows that arise from the interaction of the highly accreting disc inner edges with an existing threading strong magnetic field (e.g. Donati et al., 2005). It has been suggested that outflows can be centrifugally accelerated along net vertical magnetic field lines threading the disc; when non-ideal magnetohydrodynamical effects are taken into account, the MRI turbulent activity disappears, allowing that the disc launches a strong magnetocentrifugal wind (Bai & Stone, 2013). If so, the wind sweeps up the ambient molecular gas in the vicinity of the surrounding envelope when it interacts with a collapsing environment (Snell, Loren & Plambeck, 1980; Shu et al., 2000; Gardiner, Frank & Hartmann, 2003; Bjerkeli et al., 2016). Figure 3.2 depicts a computer illustration of HBC 494 to better show the dynamic properties of the system components. The effectiveness of the removal of envelope material depends on the age of the protostar and the degree of collimation of the wind. Thus, a highly collimated wind with high density profile would flow along the rotation axis (e.g. Class 0), while for a more evolved protostar with a reduction of envelope material, the collimated wind would decrease with its density at increasing angles from the axis (Shang, Shu & Glassgold, 1998). For a Class I object, the gas entrained by the wide-angle component of the wind will be the dominant structure in the molecular

outflow, producing the observed widening angle outflows seen in HBC 494.

Also, it is expected that the energetic outflows impact an homogeneous surrounding envelope, because the bipolar extension are largely symmetric in their opening-angles. Nevertheless, as mentioned previously the envelope material interacting with the outflow in the Northern region of HBC 494 might be slightly denser than in the Southern region, see Figures 3.4a and 3.4b. Figure 3.12 shows an image of the Re50N nebula taken as part of The Two Micron All Sky Survey (Skrutskie et al., 2006) in H band (1.6 μm), where the continuum and ^{12}CO contours are over-plotted indicating the position of HBC 494 and its wide outflows. From this image, the inhomogeneous molecular cloud hosts the outflow evolution with an embedded outflow emerging at the Southern side, while the Northern cavity is still deeply embedded. However, it is difficult to confirm this from our estimates of the outflow parameters, see Table 6.6, because are subject to the maximum recoverable scale and the spatial filtering, e.g. Figure 3.11. Therefore, these values are underestimated and biased by the visibility sampling, which require observations for a larger scale structure. Although, the parent molecular cloud might not be homogeneously distributed around HBC 494, this does not mean that both lobes would evolve in a distinguishable way and might vary only in the extension of their outflows. Unfortunately, information with respect to the extension projected onto the rotation axis is more ambiguous due to the observing limitations, which did not detect the complete structure of the outflow cavities. In addition, we might be facing a very young binary object as the triggering mechanism of the outburst (Cieza et al., In Prep.), and considering that FUor outbursts are usually accompanied by strong winds (e.g Bastian & Mundt, 1985) and if most

of the stellar mass is accreted during these events, we speculate that the origin of the wide-angle cavities of HBC 494 is a combination of binarity and magnetocentrifugally-driven winds.

3.4.2   Role of Outflows in Star Formation

Inspecting Table 6.6, the parameters estimated from the corrected ^{12}CO emissions are increased by a factor ranging from ~ 10 to 20. This supports the claim by Dunham et al. (2014) that molecular outflows are much more massive and energetic than commonly reported. Our mass estimations from the blue- and red-shifted emissions, after correcting for optical depth, are on the order of outflows previously presented using a similar approach (e.g Arce & Sargent, 2006; Curtis et al., 2010; Dunham et al., 2014). If we are indeed facing the fact that outflows are more massive than expected, and from a theoretical point of view, these outflows are responsible for extracting angular momentum from the proto-stellar core-disc system to allow the accretion onto the central object, then we might expect a huge impact on the final stellar mass and indirectly, the shape of the Initial Mass Function (IMF). It has been suggested by theoretical models that including outflow feedback the average stellar mass would decrease by a factor of ~ 3, while the number of stars increases by a factor of ~ 1.5 (Federrath et al., 2014). Energetic outflows may be responsible for triggering star formation by perturbing other regions of the same cloud, which leads to the formation of multiple stars instead of a single one (Federrath et al., 2014).

Additionally, we note that the outflow mass, momentum, and energy for HBC 494 are higher than those found recently for the Class I objects, HL Tau and

V2775 Ori (Klaassen et al., 2016; Zurlo et al., 2016). However, these quantities highly depend on the outflow mass and in the case of HL Tau and V2775 Ori, these values were not corrected for optical depth effects. On the other hand, HL Tau and V2775 Ori present a kinematic age of 2600 yr with opening angles of 90° and 30°, respectively, while HBC 494 has a kinematic age of $\sim$5400 yr and an opening angle of 150°. For both HL Tau and V2775 Ori the opening angle differs considerably and these objects, differ in their kinematic age from HBC 494. In spite of the fact that the outflows present a significant discrepancy in their spatial extension, it highlights the importance of understanding and constraining the initial conditions of the stellar formation process, which might be controlled by the parent molecular cloud and perturbations from external agents to develop this variety of FU Ori objects.

3.4.3   Role of Outflows in Disc Evolution

The physical source generating the wide angle outflow in HBC 494 could be connected to the evolution of the disc and as a requirement, it must play an important role in the removal of angular momentum from the accreted material. Indeed, it has been indicated that outflowing gas from an accretion disc might provide an efficient transport of angular momentum to permit the accretion of matter onto the central star (Blandford & Payne, 1982). In addition, to determine the disc lifetime it is necessary to constrain properties such as mass accretion and mass loss rates, which might be intrinsically coupled to angular momentum transport (Gressel et al., 2015; Bai, 2016). In recent years, the ratio of the wind mass loss rate to the wind driven accretion has been suggested to be on the order of 0.1 with large uncertainties (e.g Klaassen et al., 2013; Watson

et al., 2015). As shown in Dunham et al. (2014), and from HBC 494 as well, the mass loss rates are underestimated, leading to suggest that the mass loss rate is not a small fraction of the accretion rate. Then, if increasing the mass outflow by factors of ~ 20 or even higher (50-90 in the most extreme cases; Dunham et al., 2014) , it might limit the accretion directly by factors of similar magnitude. Recently, Bai et al. (2016) suggested a scenario where discs might lose mass at a considerable fraction of the accretion rate. Enhancing the FUV penetration depth would lead to considerable increases of the outflow rates, while the accretion rate would also present an increase in a more moderate way (Bai, 2016). Using the relation $\dot{M} = 1.25\frac{L_{acc}R_\star}{GM_\star}$ (Hartmann et al., 1998) and if we consider HBC 494 as a Class I star of 1 $M_\odot$ with a 250 $L_\odot$ (Reipurth & Bally, 1986), 3 $R_\odot$ (Baraffe et al., 2015) and assuming an age of 0.5 Myrs, typical of Class I objects, then its accretion rate is $\sim 3\mathrm{x}10^{-5}$ $M_\odot$ y^{-1}, which is of the order of typical FU Ori objects. From Table 6.6, the estimates for mass loss rates are of the order of the accretion rate, however, these values might be taken with caution because our approach to estimate the accretion rate might failed in the limits of very large accretion luminosities (Hartmann et al., 1998), or a lower stellar mass would imply a higher accretion rate. More importantly, the rate of mass outflow and angular momentum transport increase with increasing net vertical magnetic field, however, we are still limited to accurately predict the timescale of disc evolution due to the lack of knowledge of magnetic flux distribution threading the disc (Bai & Stone, 2013; Bai, 2016).

As mentioned above, our outflow mass and kinematic estimates of HBC 494 are massive and energetic, meaning that in order to raise these massive outflows via winds might require a fully ionised inner disc. For a normal classical T

Tauri star, it has been shown that the low ionisation levels in the disc prevent the rise of winds from the inner region. The wind outflow rate sensitively depends on the FUV and X-ray penetration depth which on the other hand are determined by the abundance of small grains (Bai, 2016) and the photon energy (Ercolano & Glassgold, 2013). For FUors, in the region interior to the dust sublimation radius, the disk is sufficiently ionised so that the magneto-centrifugal wind can be launched efficiently. A very important consequence of this strong penetration depth and hence, the wind mass loss, is that mass is primarily removed from the disc surface as a function of the distance (Bai, 2016). This creates favorable conditions for planetesimal formation in outer regions of the disc, where most dust grains settle at the disc midplane. Recently, from high resolution ALMA observations, Cieza et al. (2016) reported the detection of the water snow line at a distance of $\sim$ 42 au from the central star, V883 Ori. They suggested that the location of the water snow-line at these early stages is largely affected by outburst events. In addition, observational evidence has been found for preferential loss of gas relative to dust in CO isotopologue surveys by Williams & Best (2014) and Ansdell et al. (2016). Thus, the disc evolution and initial conditions for planetary formation at these early stages might be strongly influenced by the intimately connected processes of outflows and accretion (Bai et al., 2016).

3.4.4   Role of Outflows in Star-Forming Molecular Clouds

Class I objects are able to disperse their surrounding envelope effectively, through their short outburst events. Thus, the outflows could energetically expel a large amount of material from the molecular cloud modifying neigh-

bouring structures (Federrath et al., 2014). A possible change of structure in the neighbouring regions of HBC 494 could have origin in a previous outburst event. As previously mentioned, HBC 494 seems to start digging out from the molecular cloud, exposing its Southern side and thus, expelling material more efficiently to large distances. It was noticed by Chiang et al. (2015) that Re50 located at the south of Re50N (1.5 arc min, associated nebula to HBC 494), started fading to the west and moved eastwards by a curtain of obscuring material, while the Re50N suffered a dramatic increase in brightness sometime between 2006 and 2014 (Chiang et al., 2015). Considering the direction of the observed ^{12}CO emission in HBC494 and making a projection of the emerging outflows, it coincides with the direction of the expulsion of material directed towards the northeast side of Re50 (see Figure 2 in Chiang et al., 2015). Therefore, material that was possibly pushed by a HBC 494 outflow could be responsible for the significant decrease in brightness of this neighbouring object.

3.5   Summary

We studied the HBC 494 system using ^{12}CO, ^{13}CO and C^{18}O images at 0.2″ resolution. With a large expansion of the molecular outflows (~ 8000 au), the likely non-uniformity of the envelope material of HBC 494 lead us to suggest that the evolution of the outflows is largely influenced by a differential density and degree of interaction between outflow and surrounding envelope on both sides of the bipolar cone. This scenario might be a result of the binarity and magnetocentrifugally-driven wind present in the system (e.g Bastian & Mundt,
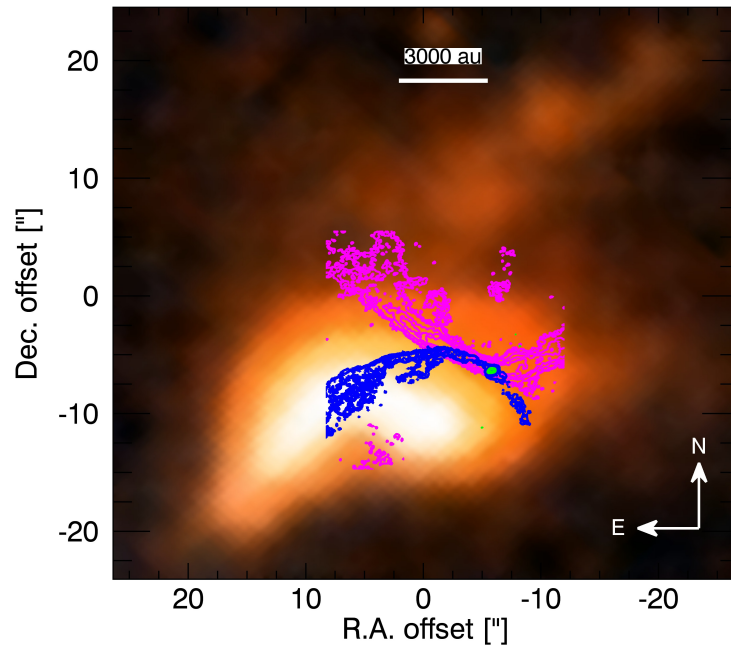
Figure 3.12: Projection of the blue and red ^{12}CO emission delineating the outflows over the H-band (1.6 μm; Skrutskie et al., 2006) image of HBC 494. Blue and magenta contours show the integrated intensity of the ^{12}CO blue- and red shifted lobes, respectively, at 80, 150, 300, 450 and 600 $\times$ 3σ levels. The green contours are the continuum emission and represent the position of HBC 494.

1985; Terquem et al., 1999). Although, higher-resolution images are needed to confirm whether HBC 494 is a close binary like FU Ori itself (Hales et al., 2015). Using the ^{12}CO, ^{13}CO and C^{18}O emissions, we derived the mass and kinematics of the outflow on the order of 10^{-2} M$_\odot$ for the mass and 10^{-3} M$_\odot$ km s^{-1} for the momentum. After correcting for optical effects, these properties increased by a factor ranging from 10-20. This increase in the kinematic properties might be observational evidence of the important role played by the outflows in FU Ori objets to drive the evolution of the disc via winds and hence, the conservation of angular momentum (Bai, 2016).

Wide-Angle Outflows: Energetic vs. Slow Components

Outflows play an important role in the formation and evolution of the stars and protoplanetary disks. Outflows are the physical mechanism to connect small and large scales (i.e. disks vs. envelopes) because these flows are able to carry away the excess of the angular momentum from rotating disk, allowing the material to accrete onto the protostar. Meanwhile, the disk mass can be replenished by the surrounding envelope. At large scales, they **disperse** circumstellar envelope material. Outflows are detected at different velocities from the central stars (Dunham et al., 2011). In this chapter, we present an FUor object, V883 Ori, with a wide-angle and slow-velocity outflow observed with ALMA.

Statement of Contribution

This thesis is submitted as a Thesis by Compilation in accordance with
https://policies.anu.edu.au/ppl/document/ANUP_003405

I declare that the research presented in this Thesis represents original work that I carried out during my candidature at the Australian National University, except for contributions to multi-author papers incorporated in the Thesis where my contributions are specified in this Statement of Contribution.

Title and authors: The ALMA Early Science View of FUor/EXor objects. III. The Slow and Wide Outow of V883 Ori.. This paper is published in Monthly Notices of the Royal Astronomical Society as D. Ruiz-Rodriguez, L. A. Cieza, J. P. Williams, J. J. , D. Principe, Tobin, Z. Zhu, and A. Zurlo, 2017, MNRAS 468, 3266-3532

Current status of paper: Not Yet Submitted/Submitted/Under Revision/Accepted/Published

Contribution to paper: 95, 5% advise/comments/suggestions from collaborating authors_____

Senior author or collaborating authors endorsement: _____Lucas A. Cieza_____

Dary Alexandra Ruiz-Rodriguez		10/Oct/2017
Candidate – Print Name	Signature	Date

Endorsed

David Yong		10/Oct/2017
Chair of Supervisory Panel – Print Name	Signature	Date
Gary Da Costa		10/Oct/2017
Delegated Authority – Print Name	Signature	Date
Lucas A. Cieza		10/Oct/2017
Primary Supervisor and endorsement – Print Name	Signature	Date

4

The ALMA Early Science View of FUor/EXor objects. III. The Slow and Wide Outflow of V883 Ori.

We present Atacama Large Millimeter/ sub-millimeter Array (ALMA) observations of V883 Ori, an FU Ori object. We describe the molecular outflow and envelope of the system based on the ^{12}CO and ^{13}CO emissions, which together trace a bipolar molecular outflow. The C^{18}O emission traces the rotational motion of the circumstellar disk. From the ^{12}CO blue-shifted emission, we estimate a *wide* opening angle of $\sim 150°$ for the outflow cavities. Also, we find that the outflow is very *slow* (characteristic velocity of only 0.65 km s^{-1}), which is unique for an FU Ori object. We calculate the kinematic properties of the outflow in the standard manner using the ^{12}CO and ^{13}CO emissions. In

addition, we present a P Cygni profile observed in the high-resolution optical spectrum, evidence of a wind driven by the accretion and being the cause for the particular morphology of the outflows. We discuss the implications of our findings and the rise of these slow outflows during and/or after the formation of a rotationally supported disk.

4.1   Introduction

During the early stellar evolution process the key to understanding outflow motions is hidden. In stellar formation, these outflow motions might regulate the final stellar mass with a core-to-star efficiency of only 30% (Offner et al., 2014). In addition, it is believed that these outflows carry matter back to the molecular cloud, transporting energy and momentum to it, which may affect the dynamics of the surrounding envelope. However, the formation, evolution and effects of these flows is highy debated. Thus, a full understanding of the origin and evolution of these winds/outflows, might disentangle the unknown physical mechanisms that dictate the 1) low mass star formation efficiency in turbulent clouds (Krumholz, Klein & McKee, 2012) and 2) an efficient transport of angular momentum to permit the accretion of matter onto the central star (Blandford & Payne, 1982). However, the physical origin(s) and features of these outflows are not well understood and our current knowledge of the entrainment process is limited due to the inability to trace the molecular gas a scale of a few au. In the ALMA era, observations of higher sensitivity and spatial resolution of young stellar objects surrounded by structures carved out by these outflows are required (see Frank et al., 2014, for a review). FU Orionis

objects (FUors) are ideal candidates to observe and analyse due to their main characteristics: strong outflows and massive envelopes.

FUors are generally identified by their large and sudden increase of luminosity in optical light. This increase takes place in around $\sim 1-10$ yrs and can amount to ≥ 5 mag in optical light. Although this optical variability has not been completely incorporated in the big picture of stellar formation and the evolution process, a large amount of matter (~ 0.01 $M_\odot$) accreting from the circumstellar disc onto the central object ($\sim 10^{-4}$ $M_\odot yr^{-1}$), is the most likely cause of this variability (Hartmann & Kenyon, 1996). These short events might be outbursts that are connected to the broad range of outflows observed in FUors. The surrounding envelope directly interacts with these outflows, which are likely the main dispersing mechanism of the natal circumstellar gas and dust, driving the evolution from a Class 0/I object to a Class II. From an observational perspective, an evolutionary trend in the opening angle of general protostellar outflows has been detected (Velusamy & Langer, 1998; Arce & Sargent, 2006; Seale & Looney, 2008), where the outflow erodes the envelope and the widening of the cavity increases as the outflow ram pressure highly dominates over the infall ram pressure (Arce & Sargent, 2004). The concept that cavities widen with time, postulates that Class 0 objects present opening angles ranging from $20°$- $50°$, Class I between $80°$ and $125°$ and Class II objects present outflows with cavities ≥ 125 $°$ (Arce & Sargent, 2006). Highly collimated and wide-angle molecular outflows differ in their gas velocities and mass. The former usually presents velocities on the order of v$\sim 100-1000$ km s^{-1}, while the latter, less collimated outflows, are more massive with velocities on the order of v $\sim 10-30$ km s^{-1} (see Audard et al., 2014, for a review). Theoretically, the observed

widening in outflows might be connected to the interaction of highly accreting disc inner edges with a strongly magnetised central star, raising energetic winds. Among these models are the X winds (Shu et al., 2000), disk winds (Pelletier & Pudritz, 1992; Pudritz et al., 2007), and accretion-powered stellar winds (Romanova et al., 2005). More collimated outflows might be explained by a jet-driven bow shock, which essentially is an expanding bow shock produced by a dense and collimated jet that propagates through the ambient material, forming a thin shell of gas entrained in the wake of the outflow and extending from the jet head back to the star (Raga & Cabrit, 1993; Ostriker et al., 2001).

In addition, the detection of P Cygni profiles[1] mainly in Hα and Na D lines are suggestive of energetic mass outflows/winds. These profiles, which are usually prominent in the spectra of FUor type stars (e.g. Calvet, Hartmann & Kenyon, 1993; Reipurth et al., 2002; Aspin, 2011), are predicted by the presence of strong winds rising from the inner region of the disc (Herbig, 1977; Bastian & Mundt, 1985; Welty et al., 1992). Therefore, the association of outflows and disc through energetic winds has begun one of the most promising scenarios to explain kinematic and dynamic motions at early stages of stellar formation.

As FUors are promising "laboratories" to contribute in the understanding of the envelope dissipation and core-to-star formation efficiency, we have conducted a new millimeter study of FUors and FUor-like stars presented in a series of papers by Zurlo et al. (2016), Ruíz-Rodríguez et al. (2017b), Principe et al. (In Prep.) and Cieza et al. (In Prep.). Here, we present ALMA band-6 (230

---

[1]Line profile composed of a red-shifted emission peak together with a blue-shifted absorption feature.

Table 4.1: V883 Ori Properties

Property	Value	Reference
R.A. (J2000)	$05^h\ 38^s\ 18.10^s$	1
Dec. (J2000)	$-07^o\ 02^{'}\ 26.00^{''}$	1
M_* ($M_\odot$)	1.3 ± 0.1	2
$\dot{M}_{acc}$ ($M_\odot yr^{-1}$)	7.5e-5	2
L_* ($L_\odot$)	6	2
L_{bol} ($L_\odot$)	400	3
A_V(mag)	19	4

Reference: (1) 2MASS All-Sky Point Source Catalog, (2) Cieza et al. (2016), (3) Strom & Strom (1993), (4) Spectral parameters from Caratti o Garatti et al. (2012).

GHz/1.3 mm) continuum and ^{12}CO(J=2-1), ^{13}CO(J=2-1) and C^{18}O(J=2-1) line observations of an FUor type object identified initially as a faint star in the Hα emission line survey of Haro (1953) and designated as **V883 Ori**. We also report the optical spectrum of the Hα line at 6563 Å taken with the MIKE spectrograph (Bernstein et al., 2003).

Since its detection, V883 Ori, located at a distance of 414 $\pm$7 pc (Menten et al., 2007), has been a source of major findings, thus providing hints about the formation and evolution of pre-main sequence stars. At first, its associated reflection nebulosity, IC 340, presented a morphological structure that suggested a star formation event involving the faint star, V883 Ori (Haro, 1953). Some years later, Nakajima et al. (1986) noticed a decrease in luminosity since V883 Ori was observed by Allen et al. (1975). However, the first team to describe this event and suggest this source as an FUor type object with a bolometric luminosity of $\sim$400 $L_\odot$ was Strom & Strom (1993). Although it was classified as an FUor type, no jet or molecular outflow was previously detected from

V883 Ori (e.g. Sandell & Weintraub, 2001), until these observations. More recently, Furlan et al. (2016) fitted the spectral energy distribution of V883 Ori (a.k.a HOPS-376) and they classified it as a flat spectrum protostar, where the mass of the envelope within 2500 au was found to be 2.87×10^{-2} M$_\odot$ and a cavity opening angle of $\sim 41°$. As a part of the Protostellar Optical-Infrared Spectral Survey On NTT (POISSON) performed by Caratti o Garatti et al. (2012), V883 Ori was included and using Brγ as an accretion tracer, an equivalent width (EW) of -3.6 Å was found, corresponding to an accretion luminosity L$_{\mathrm{acc}}$(Brγ) of 61.3 L$_\odot$. More recently, Cieza et al. (2016) described V883 Ori as a pre-main sequence object with a dynamical stellar mass of 1.3 ± 0.1 $M_\odot$ and photospheric luminosity of just $\sim$6 $L_\odot$ (based on the stellar mass, an assumed age of 0.5 Myr and the evolutionary tracks by Siess, Dufour & Forestini (2000)). Based on the stellar mass and the bolometric luminosity of 400 $L_\odot$, they derived an accretion rate of 7×10^{-5}M$_\odot$ year^{-1}, which is typical of FUor objects. More significantly, they reported the detection of the water snow line[2] at a distance of $\sim$ 42 au from the central star, a distance $\sim$10 times larger than expected for a disk passively heated by the stellar photosphere.

This relevant finding in an FUor ratified the importance of studying the evolution of circumstellar discs parallel to the outflows characteristic of these objects, in order to understand the main mechanisms involving the accretion flow and the high mass-loss rates. Table 4.1 summarises the estimated stellar parameters of V883 Ori.

We use ^{12}CO and ^{13}CO to describe the bipolar outflows of V883 Ori and the

---

[2]Region of the disk where the temperature falls below the sublimation point of water.
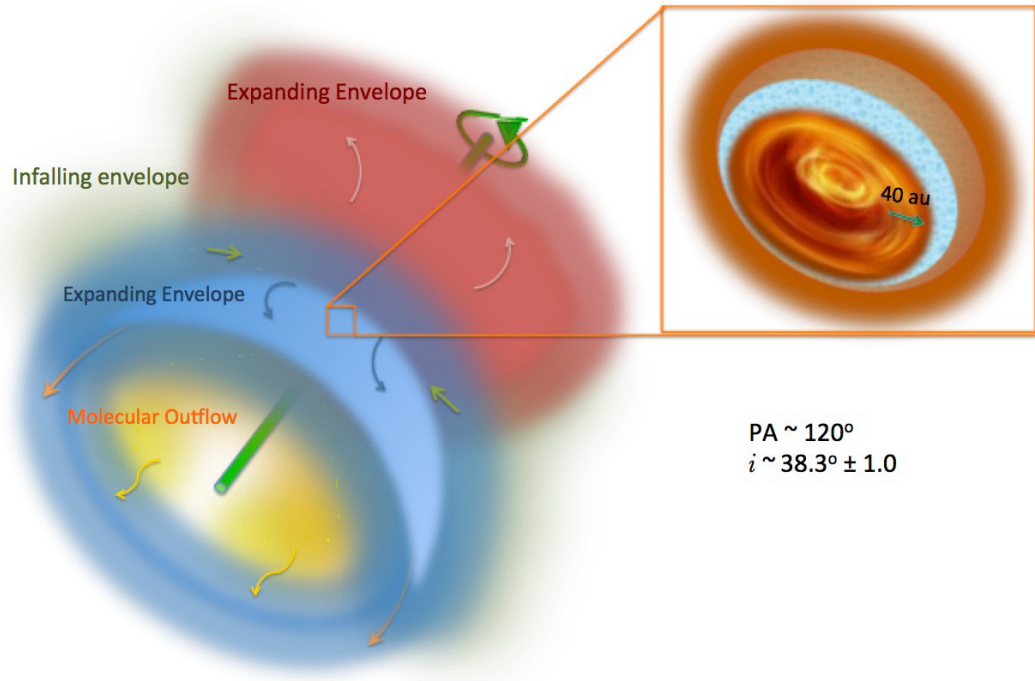
Figure 4.1: Illustration showing the different dynamical and flux components traced by ^{12}CO, ^{13}CO and C^{18}O of V883 Ori. The outflows are coloured with red to illustrate the red-shifted emission, while blue illustrates the blue shifted emission. Envelope material close to and accreting onto the disc is coloured with green and its infalling motion is indicated by the small green arrows. The green line with a position angle of $\sim 120^{\circ}$ depicts the rotation axis of the entire system. The inset shows a Keplerian disk probed by the C^{18}O emission, where a water snow-line at $\sim$40 au reported by Cieza et al. (2016) is represented by the brown-blue gradient colour. Outward of the snow line, grain growth is accelerated by the high coagulation efficiency of ice-covered grains.

envelope material surrounding this source. We present the results of these observations in this article organised as follows. Section 4.2 describes the ALMA and MIKE observations, together with the reduction process. In Section 6.4, we report the results obtained from interferometry and spectroscopy, additionally, we described the detected spectral features of this FUor. The implications and impact of our findings are discussed in Section 6.5. The summary and conclusion are presented in Section 6.6.

4.2   Observations

4.2.1 ^{12}CO(J = 2-1), ^{13}CO(J = 2-1) and C^{18}O(J = 2-1) Lines

ALMA observations of V883 Ori, located at 05^h 38^s 18.10^s -07° $02^{'}$ $26.00^{''}$, were taken under program 2013.1.00710.S during Cycle-2 over the course of three different nights. This program involves the observations of eight FUor/EXor objects: V883 Ori (Cieza et al., 2016), V2775 Ori (Zurlo et al., 2016), HBC 494 (Ruíz-Rodríguez et al., 2017b), V1647 Ori (Principe et al., In Prep.), V1118 Ori, NY Ori, V1143 Ori and ASASSN-13db (Cieza et al., In Prep.). Two of three observations were performed on December 12th, 2014 and April 15th, 2015 using 37 and 39 antennas on the C34-2/1 and C34/2 configurations, respectively. These configurations are similar with the shortest baseline of $\sim$ 14 m and longest of $\sim$ 350 m. The precipitable water vapor ranged from 0.7 to 1.7 mm with an integration time of $\sim$ 2 min per each epoch.

Additionally, a third observation of V883 Ori was performed on August 30th, 2015 with 35 antennas in the C34-7/6 configuration with baselines ranging from 42 m to 1.5 km, an integration time of $\sim$3 min, and a precipitation water vapor of 1.2 mm. The quasars J0541-0541, J0532-0307 and/or J0529-0519 (nearby in the sky) were observed as phase calibrators. J0423-013 and Ganymede were used as Flux calibrators, while the quasars J0607-0834 and J0538-4405 where observed for bandpass calibration.

Our correlator setup included the J=2-1 transitions of ^{12}CO, ^{13}CO and C^{18}O

(a) ^{12}CO

(b) ^{13}CO
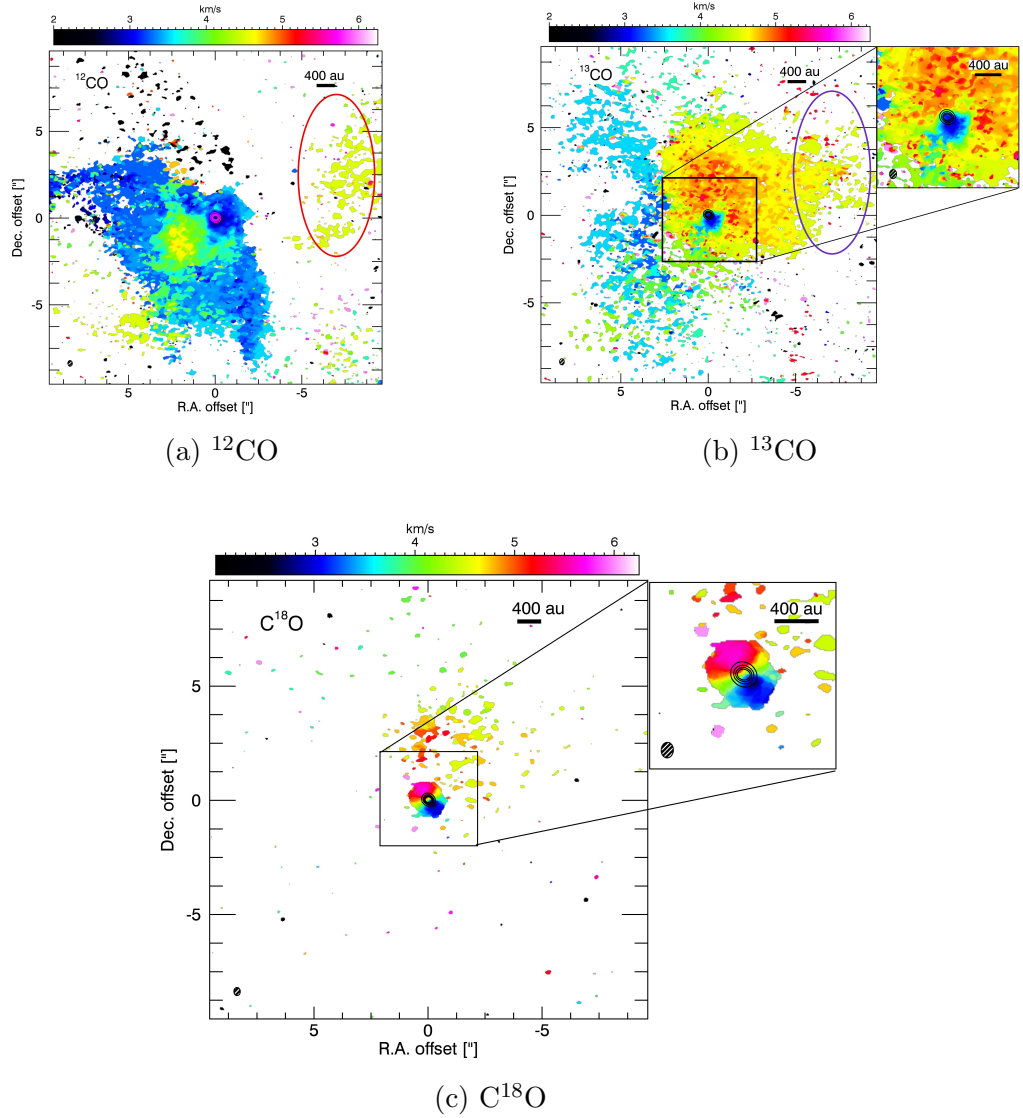
(c) C^{18}O

Figure 4.2: Figure a: ^{12}CO velocity field map (moment-1) that was obtained from the integration over the velocity range from 2.0 to 6.25 km s^{-1}. Figure b: Moment 1 of the ^{13}CO emission integrated on the velocity range between 2.0 and 6.25 km s^{-1}. Figure c: C^{18}O velocity field map integrated over the velocity range from 2.0 to 6.25 km s^{-1}. The ^{12}CO traces mostly the southern outflow with well defined edges, while the ^{13}CO traces both the norther and southern outflows, but with a less defined shape. The C^{18}O emission reveals the Keplerian disk embedded within the envelope. Black contours show the continuum emission around V883 Ori at 10, 30, 80, 150 and 250 $\times$ rms (0.25 mJy beam^{-1}). The $0.35'' \times 0.27''$ with P.A. = -90° synthesised beam is shown on the lower left corner of each panel. The upper right insets are a closeup of $\pm$ 2.7" for ^{13}CO and $\pm$ 2.1" for C^{18}O of the central object. The purple and red ovals indicate the emissions traced by ^{12}CO and ^{13}CO as described in Sections 4.3.1 and 4.3.2.

centered at 230.5380, 220.3987, and 219.5603 GHz, respectively. The correlator was configured to provide a spectral resolution of 0.04 km s^{-1} for ^{12}CO and of 0.08 km s^{-1} for ^{13}CO and C^{18}O. The total bandwidth available for continuum observations was 3.9 GHz. The observations from all three nights were concatenated and processed together to increase the signal to noise and *uv*-coverage. The visibility data were edited, calibrated and imaged in CASA v4.4 (McMullin et al., 2007). The flux density calibration uncertainty is 10 %. We used the CLEAN algorithm to image the data and, using a robust parameter equal to zero, a briggs weighting was performed to adjust balance between resolution and sensitivity. From the CLEAN process, we obtained the following synthesized beams: $0.35'' \times 0.27''$with P.A. = -90° for ^{12}CO, $0.37'' \times 0.28''$ with P.A. = 86.5° for ^{13}CO and $0.37'' \times 0.29''$ with P.A. = 87° for C^{18}O. The rms is 12.5 mJy beam^{-1} for ^{12}CO, 16.0 mJy beam^{-1} for ^{13}CO and 13.9 mJy beam^{-1} for C^{18}O. For the integrated continuum, we obtained a synthesized beam and rms of $0.25'' \times 0.17''$with P.A. = -85.5° and 0.25 mJy beam^{-1}, respectively.

4.2.2   Optical Spectrum

Additionally, we observed V883 Ori on the night of 29 February, 2016 with the Magellan Inamori Kyocera Echelle (MIKE, Bernstein et al., 2003), a double echelle spectrograph at the Magellan (Clay) 6.5 m telescope, located in Las Campanas, Chile. This high resolution spectrograph covers a full optical wavelength range in the blue (320-480 nm) and the red (440-1000 nm) regime with spectral resolutions of 25000 and 19000, respectively. Our observations were taken with a slit size of 0.7×5 $''$ and the data have been binned 2×2 in a slow readout mode with an exposure time of 1860 s. During the observation run
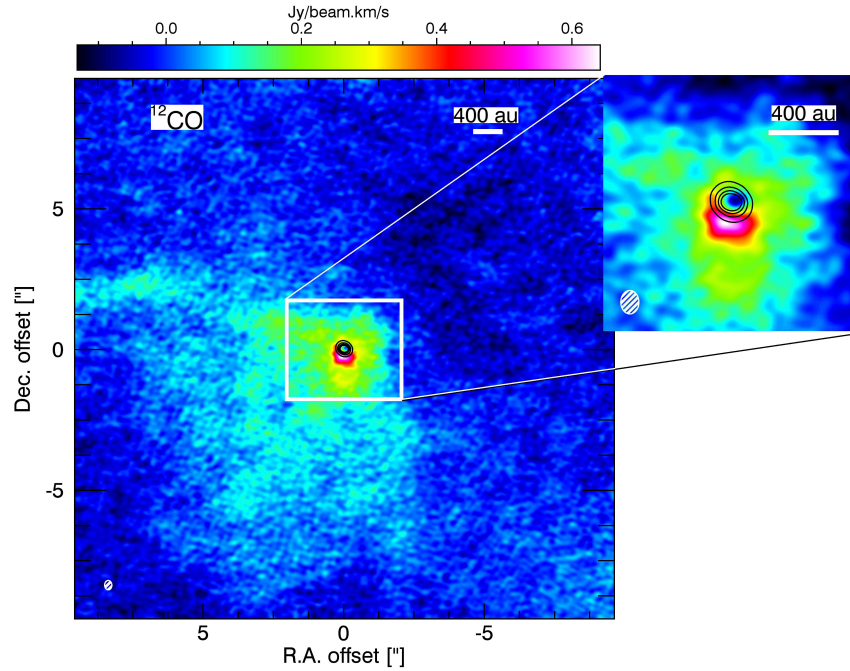
Figure 4.3: ^{12}CO intensity maps (moment-0) integrated over the velocity range of $0.75 - 8.0$ km s^{-1}. Black contours show the continuum emission around V883 Ori at 10, 30, 80, 150 and 250 × rms (0.25 mJy beam^{-1}). The upper right inset is a closeup ($\pm$ 1.8") of the central object. The $0.35'' \times 0.27''$ with P.A. = -90° synthesised beam is shown on the lower left corner.

were taken: Milky flats, Quartz flats, Twilight flats, ThAr comparison lamps and bias frames to use in the data reduction process. Thus, the data were bias-subtracted and flat-fielded to correct pixel to pixel variations by using the Carnegie Python tools[3] (CarPy; Kelson, 2003).

---

[3]http://code.obs.carnegiescience.edu/mike

4.3   Results

We obtained emission line profile data from V883 Ori of isotopologues ^{12}CO, ^{13}CO and C^{18}O with transitions J $= 2 \rightarrow 1$ to trace the different components of this FUor object. Figure 4.1 is a cartoon of the components detected with these optically thick and thin emissions, with a systemic velocity of 4.3 km s^{-1} (Cieza et al., 2016). The CO emissions with bipolar shaped lobes, symmetrically placed around the central object (V883 Ori) are the product of the direct interaction between young outflows and the surrounding envelope, where the molecular outflows entrain part of the gas along the outflow axis independent of the physical origin. Then, from ^{12}CO and ^{13}CO emissions a bipolar shape is probed, where the cavity traced by the ^{12}CO and pointing towards us, is less embedded in the surrounding envelope, while the cavity traced by the ^{13}CO is more embedded than its counterpart. Unfortunately, we could not rule out faster gas towards the outflow axis from this data set or previous observations in databases. The colder and denser material close to the central object is traced by the ^{13}CO and C^{18}O isotopes, where a disk with a Keplerian rotational profile is probed by the C^{18}O emission. For simplicity throughout the text, the blue- and red-shifted ^{12}CO and ^{13}CO emissions probing the bipolar cone are referred to as the southern and northern cavities, respectively. In order to estimate the outflow position angle (PA), we drew a line along the velocity gradient observed in C^{18}O and through the 1.3 mm continuum and thus, we obtained a PA of $\sim 120^{\circ}$ north through east [4]. From the 1.3 mm continuum emission, Cieza et al. (2016) found a position angle of $\sim 32.4^{\circ}$ and from the major and minor

---

[4]All position angles are specified north through east.

axes of this emission an inclination (i) of $\sim 38.3^{\circ} \pm 1.0$. Here, we adopted this inclination value to describe the orientation of the outflows.

4.3.1 ^{12}CO Emission

Figure 4.2a presents the integrated intensity of the weighted velocity (moment-1) maps of V883 Ori. This moment is integrated over the narrow velocity range with respect to the Local Standard of Rest (LSR) of $2.0 - 6.25$ km s^{-1}, where the emission is detected at levels higher than 3σ ($\sigma = 1.5 \times 10^{-2}$ Jy beam^{-1}). This integration range for ^{12}CO is chosen to match the moment-1 of ^{13}CO and to display the kinematic structure of the ^{12}CO and ^{13}CO line emission, see Section 4.3.2. The ^{12}CO emission tracing the southern molecular outflow has a range between ~ 0.75 km s^{-1} and ~ 4.25 km s^{-1}, while the red-shifted emission is observed in the range between 4.5 and 8.0 km s^{-1}. The former emission is bright and extends up to the systemic velocity, which clearly traces the shape of the southern cavity. The latter is detected mostly close to the central object, and at what seems to be the end of the right arm of the outflow. However, emissions at velocities of ~ 4.5 km s^{-1} are more likely to correspond to the parent molecular cloud. Thus, the emission indicated with a red oval in Figure 4.2a, at a velocity of ~ 4.5 km s^{-1}, seems to be better explained as being dominated by ambient emission rather than from an outflow emission, see also Figure 4.4. A slab of colder and denser envelope material located in the northern region of the outflow might be blocking the ^{12}CO emission, making its interpretation ambiguous because the optically thin ^{13}CO emission is brighter on this side of the object (see Section 4.3.2 for more details). Another possibility is that the surrounding envelope might be built

with different velocity components, and in the case of V883 Ori, the narrow velocity range of this emission causes the red-shifted ^{12}CO emission on this side of the cavity to be spatially filtered out.

Figure 4.4a shows the ^{12}CO channel maps, with a channel width of 0.25 km s^{-1}, where the outflow cavity of a parabolic shape is more predominant at velocities of $\sim 3.25-3.50$ km s^{-1}. Interestingly, there is a slightly noticeable elongated feature towards the southeast, while in the ^{13}CO channel maps a more pronounced feature is displayed in the same velocity range and location, which geometrically overlaps the ^{12}CO feature, see Figure 4.4b . This feature seems to move further away from the central source, and could potentially be explained as outflowing layers entrained by a wide-angle wind. For this matter, we further explore kinematic features in the position-velocity (PV) diagrams to identify a possible parabolic PV structure, which can be produced by a wide-angle wind model at any inclination (Shu et al., 2000; Lee et al., 2000). Unfortunately, we did not find any signature of this characteristic, however, this does not rule out a radial wind producing a molecular outflow with a wide-opening angle.

From the southern cavity emission, we estimate an apparent opening angle of the outflow following the relation:

$$\theta_{\rm o} = 2 \tan^{-1} \left[\left(1 - {\rm e}^{-1}\right) \frac{{\rm R_o}}{{\rm z_o}} \right]$$

where R_o is the transverse radius or radius to the rotation axis and z_o is the distance along the outflow where the angle is measured (e.g. Lee & Ho, 2005).

Thus, an opening angle of $\sim 150^{\circ}$ is revealed beyond ~ 600 au from the central source and an extension of 7300 au assuming a distance of 414 ± 7 pc (Menten et al., 2007).

The narrow velocity range shown in the channel maps of ^{12}CO data at velocity resolution of 0.25 km s^{-1}, Figure 4.4a, leads to the conclusion that the outflow is not as highly energetic as other FU Ori objects in a similar evolutionary stage (Class I).

A hole in the ^{12}CO emission?

In Figure 4.3, we present integrated intensity maps of the ^{12}CO emission over the velocity range between 0.75 and 8.0 km s^{-1}. Overall, this emission traces the southern outflow as described above,however, it also also presents a particular flux drop coincident with the central dust continuum peak. The inset of Figure 4.3 a zoomed in image of the hole, which is significantly weaker by a factor of $\sim$15 compared with the immediately surrounding emission. This feature is more likely due to dust absorption of the line emission and with a contrast of this magnitude, this implies that the dust continuum is considerably more optically thick than the CO emission around the central star.

4.3.2 ^{13}CO and C^{18}O Emissions

Usually, millimeter observations of ^{12}CO in star-forming environments tend to probe optically thick gas due to the high fractional abundance ($\chi_{CO} \approx 10^{-4}$) of the isotope, while a less abundant CO isotope such as ^{13}CO probes optically
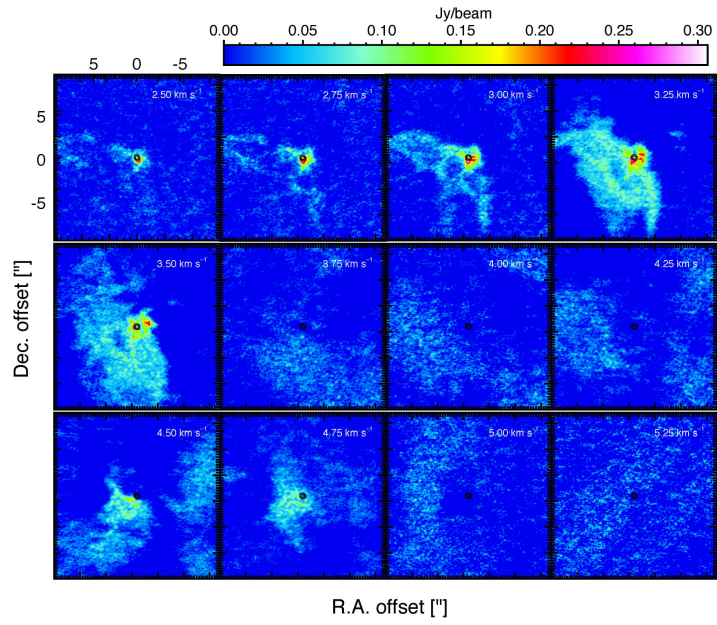
(a) ^{12}CO
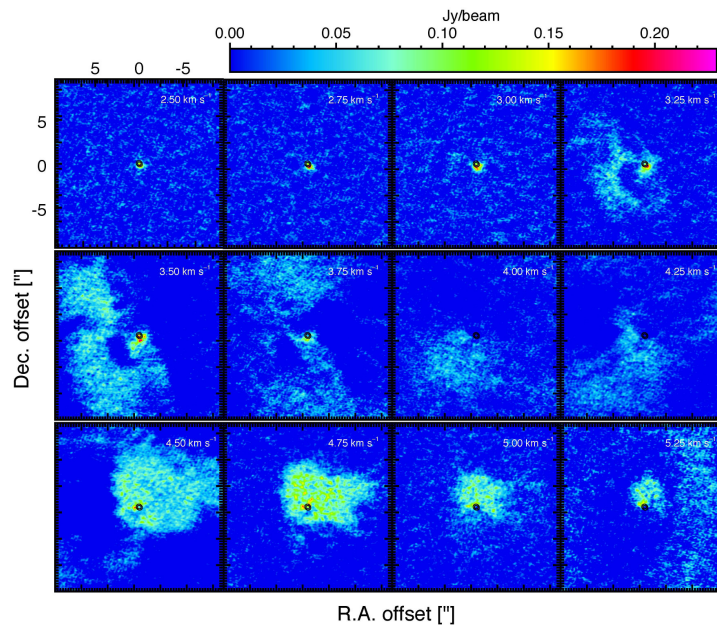
(b) ^{13}CO

Figure 4.4: Channel maps of the ^{12}CO and ^{13}CO. LSR velocities are shown at the top-right corner of each panel with a systemic velocity of $\sim$4.3 km s^{-1}. Black contours represent the continuum emission around V883 Ori as shown in Figure 4.2a.

thin material. Thus, ^{13}CO as a medium density tracer allows us to probe a higher density region than the low density tracer, ^{12}CO. Figure 4.2b shows the ^{13}CO moment-1 map integrated in the velocity range between 2.0 and 6.25 km s^{-1}. The ^{13}CO gas has a bipolar distribution with respect to the outflow source on the northern side of V883 Ori, which covers the red-shifted velocities between 4.5 and 6.5 km s^{-1}. This emission likely rises from the outer envelope that surrounds the protostellar core and the material interacting with the immediate surroundings of the outflow. The southern cavity (blue-shifted ^{13}CO emission) is more diffuse and weaker than on the northern side. The southern cavity emits at velocities between 1.75 and 4.25 km s^{-1} and probes envelope material that might indicate that the outflow has been able to accelerate medium-density gas at large distances away from the central object, where the highest velocity components are observed close to the central object and ambient velocity components widen from the central source.

In figures 4.2a and 4.2b the moment-1 maps of ^{12}CO and ^{13}CO are shown, integrated over the same velocity range for comparison (2.0 − 6.25 km s^{-1}). The physical connection between the base of the cavity-envelope system traced by the ^{13}CO isotope and what seems to be envelope material traced by ^{12}CO, that reaches velocities of only 4.5 km s^{-1} , is indicated by a red oval in the ^{12}CO moment-1 map and the physical location of the ^{12}CO emission in the moment-1 of ^{13}CO is indicated by a purple oval. The velocity field shows a gradual decrease in speed from the inside out. At small radii, the outflow may be entraining inner envelope material, while at large distances from the central source it widens and acquires the systemic velocity.

Indeed, Figure 4.4 presents the ^{12}CO and ^{13}CO channel maps, where the emis-

sion of both isotopes overlap and trace envelope-outflow material. Both, ^{12}CO and ^{13}CO emissions peak on the central star, where the central disc is located. The blue shifted ^{12}CO and ^{13}CO line emission maps of V883 Ori reveal the low and medium density material expanding, part of which have already been noticed in optical images, since the northern outflow is not observed, such as in the I-band image shown in Figure 4.5 where only the southern outflow appears illuminated. An important implication of these emissions is that the cavity traced by the ^{12}CO gas and pointing towards us, is less embedded in the surrounding envelope, while the cavity traced by the ^{13}CO is more embedded than its counterpart. This is supported by the lack of detection of the ^{12}CO gas and the bright detection of ^{13}CO on the northern side of the object.

Besides the progressive dispersion of dense molecular gas at the northern region, an infalling and rotating motion is also observed close to the central star-disk system. It can be noted in the inset of Figure 4.2b that at the base of the cavities, the ^{13}CO gas probes a velocity gradient along the major axis of the 1.3 mm continuum, consistent with a Keplerian rotation and indicating the rotating and infalling material onto the central source. The infalling envelope near systemic velocity agrees with the rotating equatorial disc (Cieza et al., 2016), also observed with C^{18}O, the lowest abundant isotope.

The densest material in V883 Ori is traced by the observations of the C^{18}O molecule, and presented in Figure 4.2c as the moment-1 map integrated over the velocity range $2.0-6.25$ km s^{-1}. It is evident that this velocity map shows a structure delineating the material rotating around central object. In addition, the shape of the C^{18}O emission of these maps is very similar to the shape of the ^{13}CO gas towards the base of the cavities.
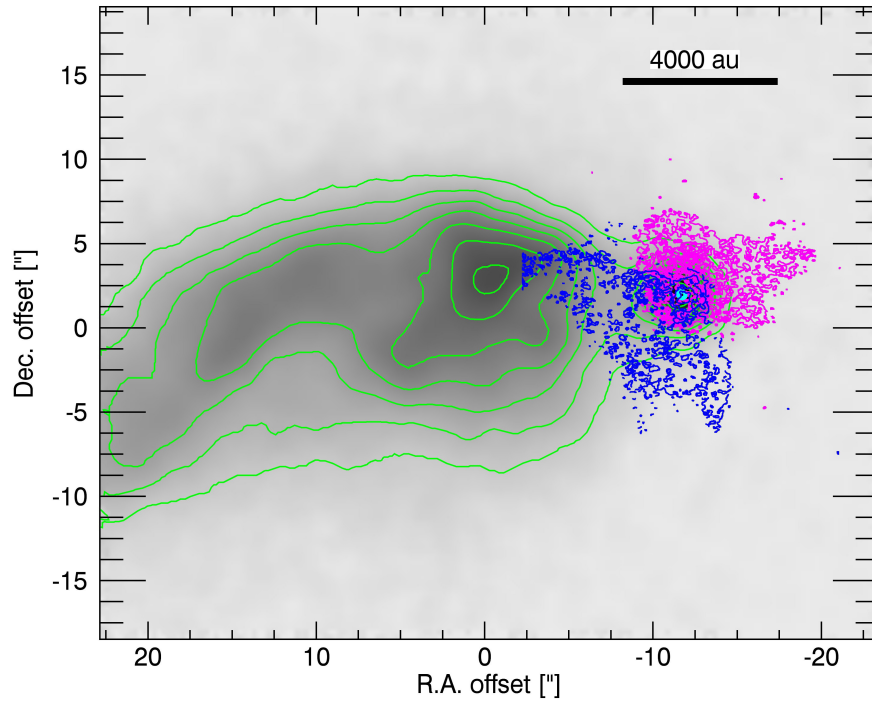
Figure 4.5: Comparison of the 1.3 mm continuum, ^{12}CO and ^{13}CO emissions (contours) and the optical I-band (0.75 μm; Ahn et al., 2012) image of V883 Ori. Blue and magenta contours show the integrated intensity of the ^{12}CO and ^{13}CO lines, respectively, at 20, 40, 80, 160, 240 $\times$ 3σ levels. The cyan contours are the continuum emission and represent the position of V883 Ori. The green contours are the I-band data at 80, 150, 300, 450 and 600 $\times$ 3σ levels.
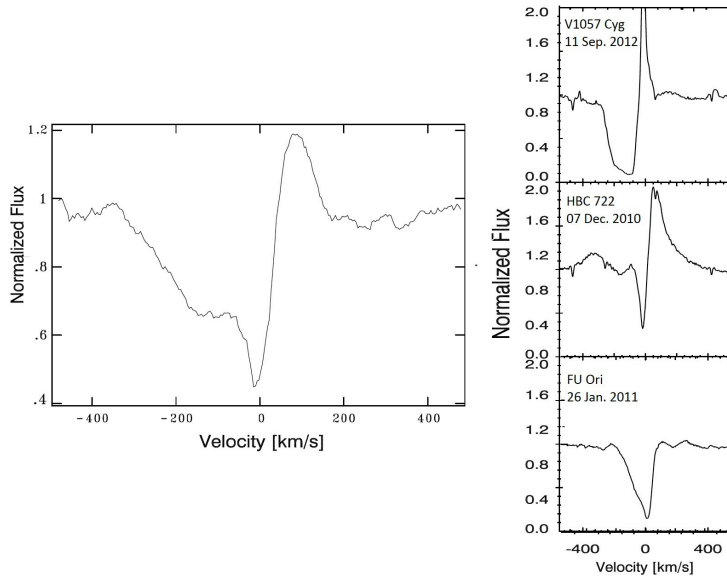
Figure 4.6: V883 Ori spectrum of the Hα line at 6563 Å taken with the MIKE spectrograph. On the right column, we present the Hα velocity profiles of the FUor objects V1057 Cyg, HBC 722, and FU Ori itself. Spectra taken from Lee et al. (2015).

4.3.3   Optical Spectra

In order to study the winds detected in the optical regime, we obtained from MIKE the spectrum of one the most commonly observed outflow tracers, the Hα line at 6563 Å. Clearly visible in Figure 4.6 is the line characterised by a P-Cygni profile representing a wind/outflow, which is built of a strong and asymmetric blue-shifted absorption component together with a red-shifted component. The slightly blue-shifted absorption feature shows a wing profile that extends to ~-360 km s^{-1}, while the emission line extends up to ~ 180 km s^{-1}. The blue-shifted feature shows a very asymmetric line with the deepest absorption at ~-14 km s^{-1} with the edge extending up to ~-65 km s^{-1}, which remains relatively invariant until it reaches ~-150 km s^{-1}, then it weakens as

the blue-shifted profile increases. Thus, the blue-shifted absorption seems to be composed of different features: a low-velocity and strong feature and a weaker structure fading as the velocity increases. The sharp change in the equivalent width (EW) of this feature indicates a recent increase in mass loss rate of the system (e.g. Laakkonen, 2000). On the other hand, the red-shifted emission peaks at ~ 90 km s^{-1} and its intensity is not as strong as the blue-shifted absorption.

4.3.4 Outflow Masses and Kinematics

Table 4.2: Mass, Momentum, Luminosity and Kinetic Energy of the Outflow

Isotope	Property	Blue shifted[1]		Red shifted[2]		Combined	
		20 (K)	50 (K)	20 (K)	50 (K)	20 (K)	50 (K)
^{12}CO	Mass (10^{-2} M$_\odot$)	3.00 (172.20)[3]	4.50 (254.70)	1.00 (99.70)	1.50 (147.50)	2.00 (136.00)	3.00 (201.10)
	Mass loss (10^{-6} M$_\odot$ yr^{-1})	1.15 (65.30)	1.71 (96.70)	0.38 (37.80)	0.56 (55.91)	0.77 (51.60)	1.14 (76.30)
	Momentum (10^{-2} M$_\odot$ km s^{-1})	3.10 (170.02)	4.55 (251.50)	0.38 (32.00)	0.57 (47.40)	1.74 (101.00)	2.56 (149.50)
	Energy (10^{41} ergs.)	3.18 (172.30)	4.71 (255.00)	0.32 (17.80)	0.48 (26.20)	1.80 (95.10)	2.60 (140.60)
	Characteristic Velocity (km s^{-1})	1.03 (1.00)	1.01 (1.00)	0.38 (0.32)	0.38 (0.32)	0.71 (0.66)	0.70 (0.66)
	Luminosity (10^{-5} L$_\odot$)	9.95 (538.50)	14.50 (797.00)	1.00 (55.50)	1.49 (82.10)	5.50 (297.00)	8.00 (439.50)
^{13}CO	Mass (10^{-2} M$_\odot$)	0.56	0.85	3.65	5.53	2.22	3.20
	Mass loss (10^{-6} M$_\odot$ yr^{-1})	0.21	0.32	1.39	2.10	0.80	1.21
	Momentum (10^{-2} M$_\odot$ km s^{-1})	0.39	0.59	1.50	2.23	0.94	1.41
	Energy (10^{40} ergs.)	3.33	5.10	7.50	11.40	5.42	8.30
	Characteristic Velocity (km s^{-1})	0.70	0.69	0.41	0.40	0.56	0.55
	Luminosity (10^{-5} L$_\odot$)	1.04	1.60	2.35	3.56	1.70	2.58
Total	Mass (10^{-2} M$_\odot$)	3.56	5.35	4.65	7.03	4.22	6.20
	Mass loss (10^{-6} M$_\odot$ yr^{-1})	1.36	2.03	1.77	2.66	1.57	2.35
	Momentum (10^{-2} M$_\odot$ km s^{-1})	3.48	5.13	1.90	2.80	2.68	3.97
	Energy (10^{41} ergs.)	6.51	9.81	7.82	11.88	7.22	10.90
	Characteristic Velocity (km s^{-1})	0.98	0.96	0.41	0.40	0.64	0.64
	Luminosity (10^{-5} L$_\odot$)	10.10	16.10	3.35	5.05	7.20	10.58

[1] Blue-shifted outflow kinematics were estimated after a cut above 5σ and integration of channels between 1.5 and 4.25 km s^{-1} for ^{12}CO and ^{13}CO.

[2] Red-shifted outflow kinematics were estimated with a threshold value above 5σ and integration of channels between 4.5 and 7.0 km s^{-1} for ^{12}CO and ^{13}CO.

[3] Parameters inside the parentheses correspond to the computed values after applying the correction factors for optical depth effects to all the channels with emission above 5σ

The fact that most of the ^{12}CO emission in the southern cavity has a much higher intensity than the ^{13}CO line, indicates that the ^{12}CO line can be used as a tracer of the gas column density of the southern cavity. Likewise, the ^{13}CO emission can trace the northern side of V883 Ori. Considering that both the ^{12}CO and ^{13}CO lines trace the bipolar cavity, we use these emissions to derive estimates of the mass of the outflow, M_{flow}, and its kinematic properties (kinetic energy, E_{flow}, momentum, P_{flow}, and luminosity, L_{flow}) in the standard manner (e.g. Cabrit & Bertout, 1990; Dunham et al., 2014). Thus, following the process described in Section 3.4 in Ruíz-Rodríguez et al. (2017b), we estimate these quantities from the blue- and red-shifted emissions, separately. However, as is often stated, the ^{12}CO emission is optically thick and to derive accurate gas column densities, it is necessary to correct for the optical depth of this line. For that matter, ^{13}CO, as an optically thin tracer, is used to correct for optical depth effects in the ^{12}CO data. Hence, after computing the ratio of the brightness temperatures:

$$\frac{T_{12}}{T_{13}} = X_{12,13}\frac{1 - \exp(-\tau_{12})}{\tau_{12}}$$

where the abundance ratio $X_{12,13} = [^{12}CO]/[^{13}CO]$ is taken as 62 (Langer & Penzias, 1993), from all the channels with detection above 3.5σ. We also consider that ^{12}CO and ^{13}CO probe opposite regions in the bipolar shape of V883 Ori, meaning that the number of channels with a computed ratio is small because ^{12}CO and ^{13}CO trace different regions at a narrow velocity range. Therefore, in order to apply the correction factor to all the channels with ^{12}CO detection, it is necessary to extrapolate values from a parabola fitted to the weighted mean

values of the form

$$\frac{T_{12}}{T_{13}} = 0.57 + 0.34(v\text{-}v_{LSR})^2.$$

In the fitting process, the minimum ratio value was fixed at zero velocity and we did not include those data points presented as the red dots in Figure 4.7, because at these velocities ^{12}CO starts becoming optically thin. The best fit with a χ^2 of 0.6 is shown in Figure 4.7 as a solid green line, where the blue dots correspond to the weighted mean values and the error bars are the weighted standard deviations in each channel. In this particular case, the fitted parabola and the derived outflow parameters must be taken with caution because of the poor fitting, which highly depends on the weighting of the last data point to the right, see Figure 4.7. This is because the ^{13}CO emission is usually not detectable or is very weak in most mapping positions and velocities where the ^{12}CO emission is detected, and vice versa.

To assure we are using the emission mostly from the outflow, we performed a first cut to values above 5σ and the integration of channels between velocities ranging from 1.5 to 4.25 km s^{-1} and between 4.5 and 7.0 km s^{-1}. In order to obtain a total estimate of these values, the range and number of channels in the integration are the same for ^{12}CO and ^{13}CO. The characteristic velocity of the outflow of $\sim$0.65 km s^{-1} is estimated using $v_{flow} = \frac{P_{flow}}{M_{flow}}$, where P_{flow} and M_{flow} are the momentum and mass of the outflow, respectively (e.g. Dunham et al., 2010). Taking the extent of the ^{12}CO blue-shifted emission of $\sim$7300 au (17.5$''$) and the maximum speed of the gas extension, obtained using $\frac{v_{13}-v_{12}}{2}$ where v_{13} and v_{12} are the ^{13}CO red- and ^{12}CO blue-shifted maximum velocities,

we estimated a kinematic age for V883 Ori of $\sim$10000 years to obtain the mechanical luminosity and mass loss rate of the outflow. Here, it is important to note that the estimate of the dynamical timescale is a lower limit since we have only used our ALMA data and ignored the apparent extension observed in optical wavelengths of $\sim 64''$, see e.g. Figure 4.5. Thus, the outflow with an apparent extension of ~ 27000 au, could be 4 times older than our estimate. We note that this estimated age ($> 10^4$ yr) is larger than the typical duration of an FU Ori outburst ($\sim 10^2$ yr). This implies that the ongoing accretion outburst cannot be directly responsible for the properties of the observed outflow. Table 6.6 shows the estimates[5] at temperatures of 20 and 50 K. The actual values could be higher than those listed in Table 6.6 because the estimated properties highly depend on the true values of the outflowing gas temperatures for both the ^{12}CO and ^{13}CO lines, and our observations have a maximum resolvable angular scale (MRS) of $\sim 11''$, meaning that a fraction of the total outflow emission might be missing. In other words, the outflow cavities are $\sim 15''$ across, and thus larger than the MRS. Hence, an extended component ($>11''$) between the outflow cavities might not be resolved out. Future observations with the ALMA Compact Array would be useful to image the outflow at larger angular scales. In addition, taking into account that the difference between the outflow and envelope emission is marginal based on the small number of channels of ^{12}CO and ^{13}CO with emissions above 3σ, these estimates could be contaminated by envelope emission.

---

[5]Properties not corrected for inclination and optical effects.
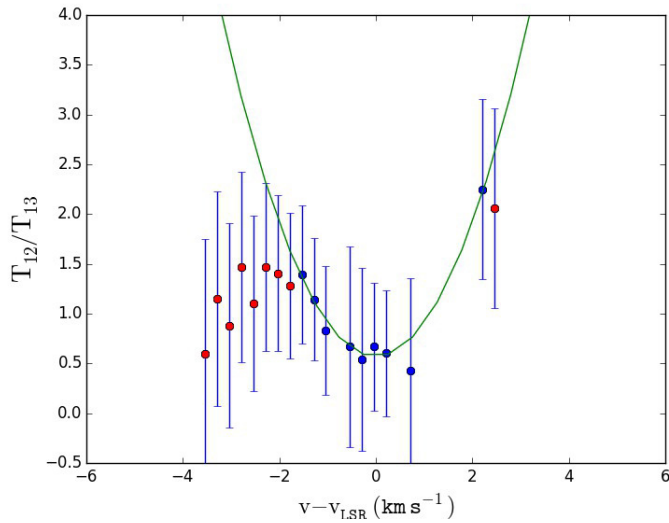
Figure 4.7: Ratio of the brightness temperatures $\frac{T_{12}}{T_{13}}$ as a function of the velocity from the systemic velocity. The blue solid dots are the weighted mean values and the error bars are the weighted standard deviations in each channel. The red solid dots are weighted mean values not used in the fitting process. The green solid line is the best-fit second-order polynomial with a χ^2 of 0.6.

4.4   Discussion

4.4.1   The extension and velocity of the outflow in the V883 Ori system

From Figure 4.2, it is evident that the southern cavity is traced by the ^{12}CO emission, while the ^{13}CO emission traces the shape of the northern cavity. Together, these emissions delineate the bipolar outflow of V883 Ori. In optical images (Ahn et al., 2012), the southern cavity seems to have a much larger extension than in our ALMA data. However, this could be an effect of the illumination caused by the interaction of the dusty material and the high luminosity of the central object. Figure 4.5 shows a comparison of the optical

image and the bipolar outflow (^{12}CO and ^{13}CO emissions), and although the outflows roughly coincide in the projection over the I-band image, comparing these observations is not straightforward and thus, it does not ensure that the I-band image shows the real and physical extension of the cavity. Also, it is worth noting that the relatively limited field of view (FOV) of our ALMA data of only 0.1 arcminutes^2 cannot be compared well with other facilities with considerably larger FOV, such as the I band image shown in Figure 4.5 with FOV of ~ 0.5 arcminutes^2. Future mosaicking observations with ALMA or imaging by interferometers with a larger field-of-view, such as the Submillimeter Array, are needed to better determine the real extension of the outflow.

From the ^{12}CO blue-shifted emission, an opening angle of $\sim 150^{\circ}$ is estimated, where one of the most striking characteristics of the outflows is the relatively slow velocity with a characteristic velocity of only ~ 0.65 km s^{-1}, see Figure 4.4. The typical FUor outflow velocity ranges between 10 and 40 km s^{-1} with a wide range of collimation (Evans et al., 1994; Zurlo et al., 2016; Ruíz-Rodríguez et al., 2017b), although, some FUors do not show CO emission associated with outflows (e.g. FU Orionis itself does not show an outflow (Evans et al., 1994)). While our observational findings can be used as inputs to test slow-velocity outflows in FU Ori objects, yet, we are unable to compare to other FUors with similar outflow features because to date, these wide and slow-outflows have only been detected in V883 Ori. Thus far, these low-velocity outflows have been observed only in other Class 0/I objects, such as Per-Bolo 58 (2.9 km s^{-1}), CB 17 MMS (2.4 km s^{-1}), L1451-mm (1.3 km s^{-1}), L1148-IRS (1.0 km s^{-1}), L1014-IRS (1.7 km s^{-1}) (Dunham et al., 2011, and references therein). However, these are younger, still embedded cores, with low luminosity and are

not experiencing high accretion rates (i.e. outburst). V883 Ori is a stellar object of 1.3 $M_\odot$ and extremely luminous, accreting a large amount of matter onto the central source through a disk with Keplerian rotation (Cieza et al., 2016). This Keplerian disk, from the 1.3 mm continuum map, is observed without asymmetries, discarding a stellar companion influencing the geometry and kinematics of the outflows. Thus, the physical mechanism responsible for these particular slow and wide-angle outflows must be triggered during and/or after the formation of a rotationally supported disk.

Recently, a similar opening angle was observed in the FU Ori Class I, HBC 494 (Ruíz-Rodríguez et al., 2017b). The authors attributed the wide opening angle due to the presence of energetic winds as a result of the interaction of highly accreting disc inner edges with a strongly magnetised central star (Snell, Loren & Plambeck, 1980; Blandford & Payne, 1982; Shu et al., 2000). However, HBC 494 presents a very energetic outflow with a velocity gradient perpendicular to the outflow axis of rotation, while V883 Ori does not harbour an energetic driving source. This can be noted in the moment-1 of the ^{12}CO and ^{13}CO emissions shown in Figure 4.2 and obtained from an integration of a very narrow velocity range (2.0 - 6.5 km s^{-1}). This narrow emission suggests that the triggering mechanism of these wide opening outflows in V883 Ori might have occurred 1) a long time ago, where another FUor outburst event could take place with an average time span of thousands of years between outbursts (Scholz, Froebrich & Wood, 2013) or 2) in a quiescent disk without the creation of a high velocity outflow component, which might be related to rotation of the central protostar (Romanova et al., 2005; Königl, Romanova & Lovelace, 2011). Unfortunately, there is not a record of the outflow onset or

evidence of a high velocity component emission to rule out and/or confirm any of these possibilities.

While the narrow velocity of the ^{12}CO and ^{13}CO emission implies a slow outflow (see Figure 4.4), it also impacts the estimates of the mass and kinematic parameters shown in Table 6.6 (i.e. mass-loss rate, the mechanical luminosity, momentum, and kinetic energy). Nevertheless, these values are on the order of other FU Ori objects such as, V2775 Ori, L1165, HBC 494 (Zurlo et al., 2016; Dunham et al., 2014; Ruíz-Rodríguez et al., 2017b). Similarly, compared to previous studies a total outflow mass in the range of 10^{-4} and $10^{-1} M_\odot$ is typical of outflows in other young stars (e.g. Wu et al., 2004; Curtis et al., 2010; Arce & Sargent, 2006; Dunham et al., 2014; Klaassen et al., 2016). Inspecting Table 6.6, the outflow parameters increased by a factor of ∼60-70, after correcting for optical depth effects, in agreement with previous results that established that these outflow parameters can increase by factors of up to 90 after correcting for inclination and optical effects (e.g. Curtis et al., 2010; Dunham et al., 2014; Ruíz-Rodríguez et al., 2017b). However, it is not easy to directly compare these parameters because 1) uncertainties in the method used and 2) the estimates in the literature differ by observing method, i.e. single dish vs. interferometer observations. For instance, parameters from single-dish data may take contributions from the extended cloud emission, increasing these estimates by a few factors when compared with the smaller scales sampled by the interferometer. Therefore, a more complete characterisation of the kinematics and dynamics of the outflows in FUors is required in the near future.

4.4.2 Comparison with other P-Cygni profiles.

In addition to the viscous accretion and the photo-evaporation, the role of magnetically driven disc winds might be a viable mechanism that disperses the inner region of the disc, leading to the loss of mass and angular momentum. In general, the presence of a P-Cygni optical profile indicates powerful winds likely rising from the disc (Hartmann & Kenyon, 1996), allowing the accretion of matter onto the central stellar core (e.g. Bai & Stone, 2013). As P-Cygni profiles have been observed in Hα lines of FUors such as FU Ori, V1057 Cyg and HBC 722 (Herbig, Petrov & Duemmler, 2003; Powell et al., 2012; Miller et al., 2011; Lee et al., 2015), here we compare our spectrum to those objects as is shown in Figure 4.6. These spectra were previously presented in Lee et al. (2015) and observed with the High Resolution Spectrograph (Tull, 1998) of the Hobby$-$Eberly Telescope (HET) (Ramsey et al., 1998) at McDonald Observatory and the Bohyunsan Optical Echelle Spectrograph (BOES) at Bohyunsan Optical Astronomy Observatory.

Although comparing the Hα profile of these objects is difficult because they differ in: 1) time from last outburst and 2) amount of envelope material; these objects have shown observational evidence of the main features and variability of their profiles. For instance, HBC 722 is an FU Ori object observed pre- and post-outburst (Cohen & Kuhi, 1979; Semkov et al., 2010) and thus, it offers the opportunity to compare the spectrum of an FUor in a quiescent state and during the outburst ($\sim$ 6 years from outburst). The spectra of this object have changed significantly pre- and during outburst. In short, pre- and during outburst the Hα profile remained mostly in emission, while decreasing

its EW (between Aug and Sept. 2010; Semkov et al., 2010), until finally a few months later they acquired the shape of a P-Cygni profile (on Dec. 2011; Semkov et al., 2012). Subsequently, the detected P-Cygni profile presented a constant strength variability in the following years, (more details in Lee et al., 2015). In Figure 4.6, it can be noted that the blue-shifted absorption feature is considerably less broader than the Hα profile of V883 Ori. Then, if the EW strongly depends on the physical events taking place around the central star, an increase in the mass loss rate might broaden the EW (Laakkonen, 2000). That is the case of the Hα profile of V1057 Cyg, which also has varied in time since its outburst ($\sim$ 40 years from outburst) (Laakkonen, 2000). The width of this profile is more similar to the Hα of V883 Ori, however, the latter shows a particular shape, see Figure 4.6. This peaked feature seems to be built by different components and located at different distances from the central star, one is a weaker and high velocity component and the other(s) is a strong and low velocity component(s). In fact, it has been argued that a narrow central absorption comes from the central object and the "wings" correspond to the disc (Lee et al., 2015). However, V883 Ori with a bolometric luminosity of 400 $L_{\odot}$ (Strom & Strom, 1993) complicates the identification of these components, independently.

On the other hand, the Hα profile of FU Ori highly differs from the Hα profile of V883 Ori. To begin, a P-Cygni profile has vanished almost completely, where the red-shifted emission line has decreased considerably ($\sim$ 79 years from outburst). A similar feature was observed in HBC 722, soon after the outburst when the wind diminished, leaving mostly an Hα absorption profile (Lee et al., 2015). Although, we cannot directly compare or make a conclusion

about the evolutionary state of the system, the Hα profile of V883 Ori indicates the presence of strong and persistent winds, which might be related to the wide-opening angle of the outflows. In fact, if the Hα absorption profile of V883 Ori arises solely via the accreting shock on the stellar photosphere, this would lead to the launching angle of the wind to be $\gtrsim 52^{\circ}$.

P Cygni and Slow Winds.

In general, the blue-shifted absorption features in FUors highly depend on the velocity shift, where larger blue-shifts are related to the strength of the profile line (Petrov & Herbig, 1992; Calvet, Hartmann & Kenyon, 1993; Hartmann & Calvet, 1995). If one assumes the strong winds originate in the accretion disk, the strongest lines show the largest expansion velocities, while the weak lines originate close to the disk photosphere. Potentially, magnetic fields anchored in the rotating disc itself could accelerate disk winds outwards (Blandford & Payne, 1982; Shu et al., 2000). However, the slow winds in V883 Ori might originate in the outer part of the disk, where the location of the footpoints of wind-launching magnetic field lines on the disk, might determine the velocity components of the system.

4.5   Summary

In this paper, we have presented the results of the ALMA observations, together with the optical spectrum of V883 Ori. This object is an FU Ori source with a *wide* opening angle of $\sim 150^{\circ}$ (measured east through north) with an extension

of $\sim$7300 au that was detected from the ^{12}CO blue-shifted emission. From the ^{12}CO and ^{13}CO emissions a bipolar shape of the outflow cavities is traced, while C^{18}O emission probes a Keplerian circumstellar disk. V883 Ori is a unique FU Ori object because it presents such a slow outflow with a characteristic velocity of only 0.64 km s^{-1}. This is surprising as current models predict outflow velocities of around $10-50$ km s^{-1} (e.g. Pudritz & Norman, 1986; Federrath et al., 2014). Therefore, further theoretical and observational studies are needed to investigate the origin of the slow and wide angle outflow in V883 Ori. A P Cygni profile observed in the Hα line centred at 6563 Å provides evidence of the presence of winds likely rising from the disc and being the physical mechanism responsible for the morphology of the outflows. We estimate the kinematic properties of the outflow in the standard manner, these values are on the order of other FUors and young stars with outflows; after these parameters were corrected for optical effects, they increased by a factor of $\sim$ 60-70. However, as discussed in Section 4.3.4, this optical depth correction must be taken with caution.

Outflows and companions as Dispersing Mechanisms

Outflows and dynamical interactions are some of the mechanisms through which primordial disks dissipate (other mechanisms include accretion onto the star and photoevaporation). At early stellar stages, accretion and outflows are correlated. In this thesis, we study Class I objects with energetic outburst (FU Ori sources) and outflows to investigate the **outflows as a dispersing mechanism** of the disk/envelope system. These outflows must be considered when developing models of disk evolution and establishing the initial conditions for planet formation.

Transition Disks (TDs), are primordial (gas rich) circumstellar disks with inner opacity holes. Despite of lack of dust in the inner regions, most TDs were found to present accretion features inferred from ultraviolet/optical excess emission (Najita et al., 2007; Espaillat et al., 2012, 2014), implying gap-crossing streams of gas. The cavity of TDs could have been created by dynamical clearing due to internal processes such as photoevaporation, grain growth, or planet formation or the tidal interactions with low-mass companions. In the latter case, they should be classified as Circumbinary Disks (CDs).

Statement of Contribution

This thesis is submitted as a Thesis by Compilation in accordance with
https://policies.anu.edu.au/ppl/document/ANUP_003405

I declare that the research presented in this Thesis represents original work that I carried out during my candidature at the Australian National University, except for contributions to multi-author papers incorporated in the Thesis where my contributions are specified in this Statement of Contribution.

Title and authors: THE FREQUENCY OF BINARY STAR INTERLOPERS AMONGST TRANSITIONAL DISKS. This paper is published in Monthly Notices of the Royal Astronomical Society as D. Ruiz-Rodriguez, M. Ireland, L. Cieza, and A. Kraus 2016, MNRAS 463, 3829-3847

Current status of paper: Not Yet Submitted/Submitted/Under Revision/Accepted/Published

Contribution to paper: 95, 5% advise/comments/suggestions from collaborating authors_____

Senior author or collaborating authors endorsement: _____Lucas A. Cieza_____

Dary Alexandra Ruiz-Rodriguez		10/Oct/2017
Candidate – Print Name	Signature	Date

Endorsed

David Yong		10/Oct/2017
Chair of Supervisory Panel – Print Name	Signature	Date
Gary Da Costa		10/Oct/2017
Delegated Authority – Print Name	Signature	Date
Lucas A. Cieza		10/Oct/2017
Primary Supervisor and endorsement – Print Name	Signature	Date

5

THE FREQUENCY OF BINARY STAR INTERLOPERS AMONGST TRANSITIONAL DISKS.

Using Non-Redundant Mask interferometry (NRM), we searched for binary companions to objects previously classified as Transitional Disks (TD). These objects are thought to be an evolutionary stage between an optically thick disk and optically thin disk. We investigate the presence of a stellar companion as a possible mechanism of material depletion in the inner region of these disks, which would rule out an ongoing planetary formation process in distances comparable to the binary separation. For our detection limits, we implement a new method of completeness correction using a combination of randomly sampled binary orbits and Bayesian inference. The selected sample of 24 TDs belong

to the nearby and young star forming regions: Ophiuchus ($\sim$ 130 pc), Taurus-Auriga ($\sim$ 140 pc) and IC348 ($\sim$ 220 pc). These regions are suitable to resolve faint stellar companions with moderate to high confidence levels at distances as low as 2 au from the central star. With a total of 31 objects, including 11 known TDs and circumbinary disks from the literature, we have found that a fraction of 0.38 $\pm$ 0.09 of the SEDs of these objects are likely due to the tidal interaction between a close binary and its disk, while the remaining SEDs are likely the result of other internal processes such as photoevaporation, grain growth, planet disk interactions. In addition, we detected four companions orbiting outside the area of the truncation radii and we propose that the IR excesses of these systems are due to a disk orbiting a secondary companion

5.1   Introduction

After the formation of a star, the lifetime of a disk is estimated to be $\lesssim$ 10 Myrs. At an age of $\sim$5 Myrs, around 90% of these objects already went through an evolution process of dispersion of their optically thick primordial disks (Sicilia-Aguilar et al., 2006). The dispersion of the inner disk material creates unique morphologies in the disk that can be detected by their unusual spectral energy distributions (SED) (Strom et al., 1989). Assuming that all disks go through this dispersing phase, then approximately 10$-$20% of the disks are in a "transition" phase with time-scales within $<$ 0.5 Myr; (Furlan et al., 2011; Koepferl et al., 2013). In comparison with the characteristic continuum level of the SED of a Classical T Tauri Star (CTTS), these objects are defined as: stellar objects with small near-infrared (NIR) and/or mid-infrared (MIR) excesses and large

MIR and/or far-infrared (FIR) excesses (e.g. Espaillat et al., 2014). Given the ambiguity in the literature as to whether a disk in a "transition phase" makes reference exclusively to a disk with an inner hole surrounding a single star or also includes binary systems in a transition phase, we will describe disks around single stars exclusively as *Transitional Disk* (TD) and to describe disks around binary stars as *Circumbinary Disks* (CD).

Detailed modelling of TD disk SEDs has interpreted the reduction of excess in the NIR-MIR as the dearth of small dust grains and thin gas in the inner region of the disk (Espaillat et al., 2012). In addition, mm-interferometric observations have mapped this particular disk morphology of the TDs, showing a dust-depleted region in the inner disk and/or gaps (Andrews et al., 2011; Canovas et al., 2016). Although the physical origins causing these particular shapes in the disks are still unclear, several theories have been proposed to explain the clearing mechanisms in the disk from inside out, such as grain growth (Dullemond, Dominik & Natta, 2001), magnetorotational instability (Chiang & Murray-Clay, 2007), photoevaporation (Clarke, Gendrin & Sotomayor, 2001; Alexander & Armitage, 2007), dust filtration (Rice et al., 2006a), and disk-planet(s) interactions (Kraus & Ireland, 2012; Dodson-Robinson & Salyk, 2011). However, it has been difficult to reconcile the main process of dispersion of the disk, especially since these mechanisms might dominate at different time-scales and radii. For instance, planet formation and photoevaporation may play a sequential dominating role in the disk dispersion phase, since photoevaporation disperses more rapidly once a planet is formed and has carved a gap in the disk (Rosotti, Ercolano & Owen, 2015).

Unfortunately, these models are still not able to simultaneously explain the

evolution process of all TDs, especially those with high accretion rates and large inner cavities full of large amounts of gas near the central star. However, fully understanding the disk dispersal process is of a vital importance, because it provides insights about the formation of planetary systems like our own (Dodson-Robinson & Salyk, 2011). In particular, knowledge of the timescales of gas survival sets constraints on the time available for the formation of a gas rich planet via core accretion (Pollack et al., 1996). Alternatively, another clearing mechanism has been proposed for the truncation of the inner disk: the presence of a *stellar companion.* Artymowicz & Lubow (1994) showed that in the binary−disk interaction, the stellar companion will truncate the CD at a distance, which depends highly on the eccentricity and mass ratio of the binary system. These theoretical models predict that the ratio of the inner radii (r_d) about the center of mass and the semi-major axis (a) of the binary system ranges from 1.7 to 3.3 for nearly circular orbits (e $= 0-0.25$) and highly eccentric binaries ($e \sim 0.75$), respectively. Although, previous surveys of stellar companions in a range of $\sim 3 - 50$ au have indicated that binary truncation might not be a primary mechanism for the clearing inner region of the disk (Pott et al., 2010; Kraus & Ireland, 2012), there are different factors that prevented the detection of faint stellar companions in general, such as inner working angle and a small separation of the binary at the observing epoch.

In addition, a misleading interpretation of the SEDs can occur in the classification process of TDs through the SEDs of the CDs. Since an unresolved faint infrared companion can aggregate NIR flux to the net SED and if this object is surrounded by a disk, it could emit MIR levels similar to the MIR excess seen in the SED of TDs (e.g Duchêne et al., 2003; Kraus et al., 2015). Although, the

SED of these CDs present several overlapping features with a "normal" SED of TDs, it would be misleading to treat them in a similar way. For instance, the implications for the presence of another star in the star-disk system entails an incorrect measurement of the luminosity and temperature, which translates into inaccurate age and mass estimates. This is the case of Coku Tau/4 and CS Cha that were originally described as TDs (Forrest et al., 2004; Espaillat et al., 2007), but eventually were presented as CDs (Ireland & Kraus, 2008; Guenther et al., 2007). This misclassification would be reflected in the estimation of birthplaces and timescales for formation of sub-stellar companions (brown dwarfs) and/or planetary systems, and the demographic properties of these populations (e.g. Najita, Andrews & Muzerolle, 2015).

Therefore, determining a more accurate relative picture of the lifetime of TDs and CDs requires a comprehensive survey capable of resolving close binaries ($\lesssim$ 30 au) and measuring their frequency in objects previously classified as TDs through their SEDs. Although, the open gap in the inner region of the disk might have different physical origins, in this paper we seek to identify if the dispersion of the primordial material in the inner region of the disk is a result of the tidal interaction between a close binary system and the disk. At small separations, detecting faint companions orbiting bright stars, that in addition, are surrounded by dusty material, can be challenging due to the high contrast between the companion and the primary star. However, observations of objects at early ages provide favorable IR contrast ratios for the detection of so far, unresolved faint companions because of their intrinsically higher luminosity (ΔK < 5 mag).

We use the *Non-Redundant Mask interferometry* (NRM) technique and NIRC2

instrument located at the Keck II telescope, which offers a solution to reach angular resolutions with the necessary contrast and is resistant to speckle noise in the image by measuring a self-calibrating quantity known as *closure-phase* (e.g. Martinache, 2011). In order to achieve a higher accuracy in the detection limits of our data, the NRM completeness as a function of position and contrast utilizes a combination of a *MonteCarlo Integration* approach, giving a randomly sample of artificial binary stars, and *Bayesian Inference*, which uses prior probability density functions of the binary orbital parameters. We have restricted the selection of objects to regions with an age of $\sim 1 - 3$ Myrs and within a distance of about 220 pc. Taurus-Aurigae , IC348 region (Perseus) and Ophiucus star forming regions satisfy these criteria (Loinard et al., 2008; Wilking, Gagné & Allen, 2008).

This article is arranged as follows. In Section 2. we present the motivation for the sample selection, description of observations together with the data analysis and a review of the target properties such as distance to the star-forming regions and estimations of the inner radii. A simple *Bayesian* modelling analysis of these data is conducted in Section 3, with an emphasis on prior probabilities and description of binary and single models. The results of fitting to closure$-$phases in the χ^2 minimization are synthesized with other information in the literature in Section 4. To perform a statistical Bayesian analysis of the fraction of the binarity as the main responsible mechanism opening the gaps in the TDs, we present a *Jefreys Prior* and its posterior probability in Section 5. Based on that analysis and observational results, we attempt to reconcile the observations with theoretical predictions from tidal interaction models and possible scenarios of planetary formation in Section 6. Finally, we provide an overall review of

the work done and results in Section 7.

5.2   TARGET SELECTION, OBSERVATIONS AND PROPERTIES

In the past decade, the identified populations of T Tauri stars in the Taurus−Auriga, IC348 and Ophiuchus star forming regions have been well studied since the *Spitzer* data enriched the knowledge of dust distributions in the disks, providing large samples of Young Stellar Object members. Thus, we selected a sample in terms of their decreased flux (with respect to the CTTS median) in the wavelength range between ~ 3 and 24 μm, which tracks dust out to separations of at least ~ 30 au. Our targets were selected based on clear inner regions in the disk seen in their SEDs. Sources with excess at wavelength in the range of ~ 8 to 24 μm and a lack of excess between ~ 3 to 5 μm are taken as disks with small or no dust excess in the inner region. Also, we included sources with strong emission between ~ 3 to 5 μm, but with a small excess emission at $\sim$ 8 to 24 μm and excess beyond ~ 40 μm. The sample of objects were selected mostly from the work of Muzerolle et al. (2010); Cieza et al. (2010, 2012b); Espaillat et al. (2012) and Rebollido et al. (2015). These programs aimed to characterize SEDs for those objects in a "transition" phase and provided disk masses and accretion rates of the targets. The Two Micron All Sky Survey (2MASS) catalog Ks magnitudes are used to assign apparent magnitudes to these objects classified as TDs. To maximise sensitivity in our observations and achieve an image resolution of ~ 20 mas, we make use of the Kp filter to probe binary separations in this limit (e.g. Kraus & Ireland, 2012). Consid-

ering that the maximum Kp-Ks colour of our objects is only 0.10 mag [1], we did not apply a magnitude conversion because it is less than the combination of our uncertainties in contrast ratio and the effects of stellar variability. Our final target list shown in Table 5.1 is composed of 24 transitional disks with R magnitudes brighter than 18 and spectral types in the range of G3−M5. For this final target list of TDs, only 2MASS J04210934+2750368 and EM* SR 24S have known stellar companions at 770 mas ($\sim$ 108 au) (Cieza et al., 2010) and at 6000 mas ($\sim$ 650 au) (Simon et al., 1995), respectively. These are not a close companion located in the range of our area of detection and do not affect the main purpose of the observations.

We observed our target list in August and December 2014 with the Adaptive Optics (AO) system of the near-infrared instrument (NIRC2) located at the Keck II 10 m telescope. The AO rotator tracking mode was set in vertical angle mode. A nine-hole mask located at the telescope pupil re-samples the light into a non-redundant interferogram of 36 pairwise fringes in the a Kp filter (Figure 5.1, top left panel). This pattern is specially designed to reach a near complete Fourier coverage. The Aladdin detector was configured to a 512 x 512 subarray and a multiple correlated double sampling readout mode was used in a narrow camera with a pixel scale of 9.952 $\pm$ 0.002 mas/pixel (Yelda et al., 2010). An overall exposure time of 20 seconds is used, except for the calibrators LRL 410, CIDA 2 and UX Tau A with 60, 5 and 5 seconds, respectively. Because some TDs have been previously observed using identical settings as our observational method, we access the Keck Observatory Archive

---

[1]We use the relation $(K' - K) \cong 0.11(H - K)$ from Vacca, Sheehy & Graham (2007).
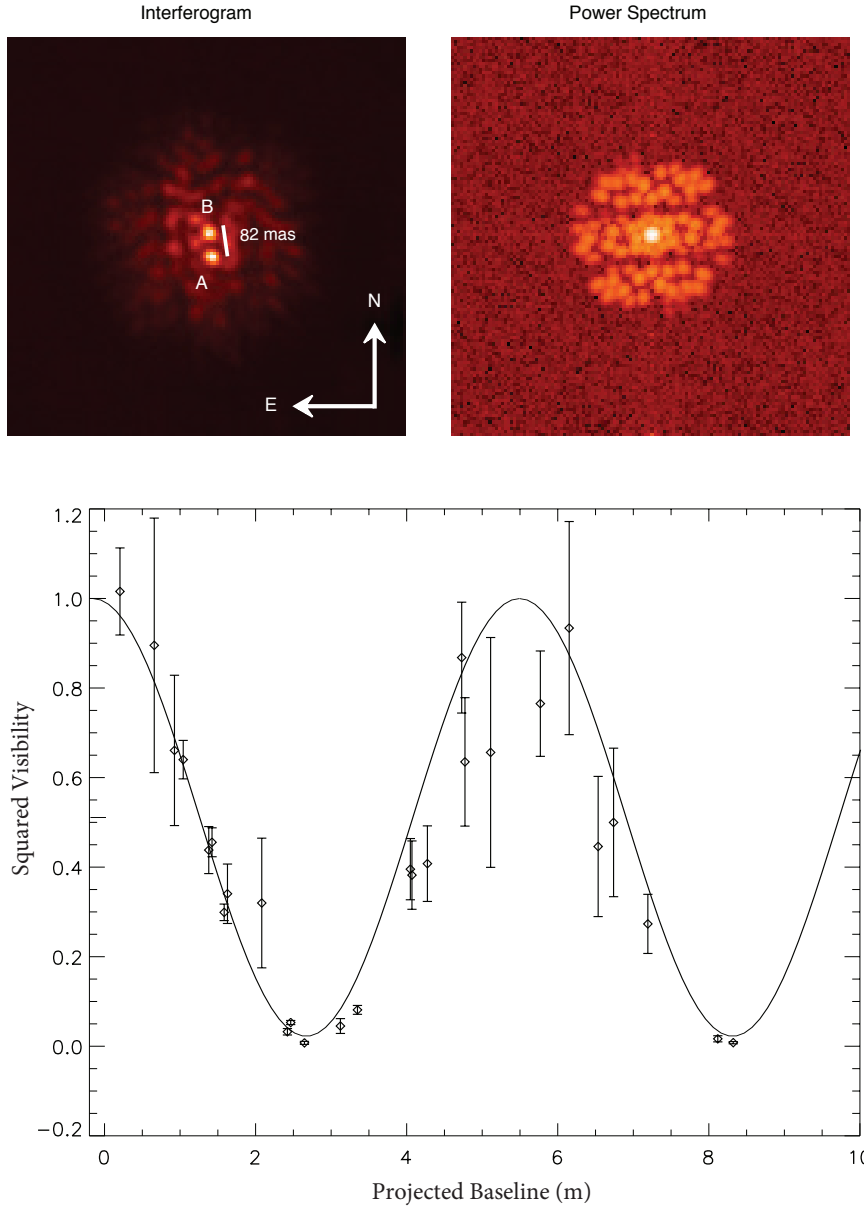
Figure 5.1: Top: Interferogram and Power spectrum of the new reported binary LRL 135. Bottom: Squared visibilities as a function of the projected baseline. The solid line shows the best-fit of the binary parameters, angular separation and position angle.

(KOA) and complete our sample of TDs that were unfit to observe in our 2014 runs. Table 6.3 shows a summary of the observational settings of the targets, calibrators and their observing epochs.

The observed data have been corrected by flat-fielding, removal of bad pixels and dark subtracted to be spatially filtered with a super-Gaussian function to maximise sensitivity (Ireland et al., 2008). The aperture masking analysis is based on the extraction and calibration of closure-phase and squared-visibility, then carrying out least squares binary fitting. The interested reader can find a detailed description available in e.g. Kraus et al. (2016). In the case of fitting to binaries with an angular separation (ρ) of $\gtrsim$ 25 mas at high contrast, we fit only to closure-phase because of its immunity to changes in the AO point-spread function (PSF). We determined that any solutions with a significance of more than 6-σ are detections of secondary components (Kraus et al., 2016). Then, we conducted a Bayesian analysis for marginal detections and contrast limits as described in section 5.3.1. As an input to this Bayesian analysis, for each set of calibrated closure phases, we computed a least squares fit to contrast (secondary/primary flux) in a grid of 80 x 80 models with 5 milli-arcsec spacing.

For reasons of both speed and in order to only consider the regime with symmetrical error bars, we approximated the contrast as being in the linear regime where closure phase is proportional to contrast. The output of this process was a grid of best fit contrasts and uncertainties. The uncertainties were scaled in order to acquire a χ^2 equal to unity in the fit to the closure phases. For detections with $\rho < 40$ mas and ΔK < 1 mag, we included visibility amplitudes for breaking contrast/separation degeneracies. When fitting to squared visibilities, we conservatively added a 20% miscalibration uncertainty in quadrature

to the uncertainties estimated from scatter in our data, and also left, as a free parameter, the scaling of the interferometric visibilities. This was necessary because in AO data, Strehl ratios typically vary from target to PSF calibrator, and visibility amplitudes calibrate much more poorly than closure-phases. This miscalibration uncertainty needed to be added because Strehl variations, caused by e.g. changing atmospheric conditions, cause a variation in the visibility amplitudes between target and calibrator observations. Part of this uncertainty was taken into account by adding the scatter amongst calibrators in quadrature to the visibility amplitude uncertainty from the target.

Additionally, the detection limits are highly dependent on the contemporaneous observations of *calibrators* that must be single stars with high S/N and ideally close to the observed target. The calibrators are used to remove effects of optical aberrations. Raw object visibilities are divided by calibrator visibilities, and calibrator closure phases are subtracted from raw object closure phases. However, we were not able to observe truly isolated stars in these dusty star-forming regions and for those observing epochs taken from KOA, we used likely single stars with non-redundant interferograms taken in the same observing run (Table 6.3). Therefore, in order to assure high S/N and non−binarity in the set of objects to be used as calibrators in each epoch, we perform the following steps:

1. We first identified the set of targets of obvious binarity, e.g LRL 135 shown in Figure 5.1, and targets with significance levels of $> 8\text{-}\sigma$ by fitting only to closure-phase and then, removed them from the source sample of calibrators.

2. The remaining objects, calibrators and science targets, play the role of *inter-calibrating sources*. After fitting closure phases for every observed object, we started eliminating from the set of calibrator sources those objects with a significance of more than 5-σ, assuring an isolated object with high S/N.

3. The closure phases of those remaining objects are used as the final set of calibrators.

In our survey, the aperture masking data identified a well resolved a nearly equal luminosity companion for LRL 135 at 82 mas with a ΔK of 0.17 ± 0.01 and a position angle of 208°, which is shown in Figure 5.1 as the observed interferogram and its power spectrum. We provide a more detailed description about these results in Section 5.4.1, including reference to maser distances. Also, the extracted squared visibilities are plotted, where clearly fringe contrast goes to near zero at the longest baseline of the mask (~ 9 m).

Table 5.1: General Properties of Transitional Disks

Target	Alter. Name	R.A. (J2000) [h m s]	Dec (J2000) [° ′ ″]	R [mag]	J [mag]	H [mag]	Ks [mag]	Sp. Type	Log(Acc. Rate) [$M_\odot yr^{-1}$]	Inner Radii[†] [au]	Reference[*]
				IC 348							
LRL 21[§]	...	03 44 56.15	+32 09 15.50	14.81	11.02	9.99	9.47	K0	-9.4	9	1,2,3,4,16
LRL 67	...	03 43 44.62	+32 08 17.90	14.65	12.05	11.13	10.79	M0.75	-10.2	10	1,2,3,4,16
LRL 72	...	03 44 22.57	+32 01 53.70	15.93	12.12	11.15	10.79	M2.5	<-11	5	1,2,3,4,16
LRL 237	...	03 44 23.57	+32 09 34.00	17.72	13.50	12.74	12.40	M5	n	0.005	1,2,3,5,15
LRL 97	...	03 44 25.56	+32 06 17.00	18.32	12.98	11.70	11.14	M2.25	n	0.005	1,2,3,5,15
LRL 31	...	03 44 18.17	+32 04 57.00	17.22	12.09	10.54	9.69	G6	-7.9	14	1,2,3,4,6,16
LRL 182	...	03 44 18.20	+32 09 59.30	18.10	13.22	12.27	11.87	M4.25	n	--	1,2,3,5
LRL 213	...	03 44 21.27	+32 12 37.30	16.78	13.70	12.92	12.51	M4.75	n	--	1,2,3,5
LRL 58	...	03 44 38.55	+32 08 00.70	16.43	11.94	10.90	10.47	M1.25	n	--	1,2,3,5
LRL 135	...	03 44 39.19	+32 20 09.00	16.90	12.65	11.80	11.44	M4.5	y	--	1,2,3,5
				Taurus-Aurigae							
IRAS04125+2902	...	04 15 42.79	+29 09 59.77	14.34	10.71	9.76	9.38	M1.25	-9.5	18 − 24	1,2,7,8,12
V410 X-ray 6	[GBA2007] 527	04 19 01.11	+28 19 42.05	16.50	10.53	9.60	9.13	M4.5	-10.85	--	1,2,9, 12
J04210934+2750368[¶]	...	04 21 09.34	+27 50 36.84	15.70	11.23	10.66	10.36	M5.25	-10.3	--	1,2,9
				Ophiuchus							
EM* SR 24S[‡]	...	16 26 58.51	-24 45 36.87	14.15	9.75	8.17	7.06	K2	-8.0	29	1,17
EM* SR 21A	...	16 27 10.28	-24 19 12.74	13.50	8.74	7.51	6.72	G3	< -9.0	25	1,2, 13
WSB 12	...	16 22 18.52	-23 21 48.10	13.03	9.52	8.59	8.11	K5	-8.0	--	1,2,10
J16262367-2443138	DoAr 25	16 26 23.68	-24 43 13.86	12.99	9.40	8.40	7.85	K5	-7.2	--	1,2,10
J16273901-2358187	DoAr 33	16 27 39.01	-23 58 18.70	13.88	9.90	8.72	8.21	K5.5	-9.6	--	1,2,10
WSB 63	...	16 28 54.07	-24 47 44.20	15.41	10.68	9.43	8.91	M1.5	-8.1	1.9 ± 0.3	1,2,10, 14
J16335560-2442049	RX J1633.9-2442	16 33 55.61	-24 42 05.00	15.04	10.46	9.36	8.80	K7	-9.9	7.9 ± 2.3	1,2,10,14
J16250692-2350502	...	16 25 06.91	-23 50 50.30	15.55	11.05	9.97	9.51	M3	-8.8	4.8 ± 2.5	1,10,14
J16315473-2503238	WSB 74	16 31 54.73	-25 03 23.80	15.08	10.14	8.66	7.75	K7	-7.2	--	1,10
WSB 40	...	16 26 48.65	-23 56 34.20	15.42	10.43	9.18	8.45	K5.5	--	--	1,2,11
V* V852 Oph	...	16 25 24.34	-24 29 44.30	14.52	10.75	9.87	9.45	M4.5	--	--	1,2,11

[a]References: (1) 2MASS All-Sky Point Source Catalog, (2) Cutri et al. (2003), (3) Luhman et al. (2003), (4) Espaillat et al. (2012), (5) Muzerolle et al. (2010), (6) Flaherty et al. (2011), (7) Luhman et al. (2009) , (8) Espaillat et al. (2015), (9) Cieza et al. (2012b) , (10) Cieza et al. (2010) , (11) Rebollido et al. (2015), (12) Furlan et al. (2011), (13) van der Marel et al. (2016), (14) Orellana et al. (2012), (15) Le Blanc, Covey & Stassun (2011), (16) Espaillat et al. (2010), (17) Andrews et al. (2011)

[b]Inner radii from literature.

[c]Stellar parameters taken from Andrews et al. (2011).

[d]Target IDs of IC348 members are taken from the acronym Cl* IC 348 from Luhman et al. (1998).

[e]Targets with 2MASS identifiers are presented by their designation e.g. J04210934+2750368.

Table 5.2: Summary of Observations.

ID	BJD (2400000 +)	t_{int} [s]	Coadds	N_{frames}	Airmass	Type	Note
June 18, 2008							
Haro 1-6	54635.75	5.00	4	7	1.92	Calibrator	$>5\sigma$
RX J1620.9-2352	54635.75	5.00	4	7	1.82	Calibrator	
EM* SR 24S	54635.75	5.00	4	6	1.86	Target	
EM* SR 24S	54635.75	5.00	4	8	1.81	Target	
Haro 1-6	54635.75	5.00	4	7	1.72	Calibrator	
Haro 1-6	54635.79	1.00	10	11	1.53	Calibrator	
EM* SR 24S	54635.79	1.00	10	7	1.51	Target	
EM* SR 21A	54635.88	1.00	20	7	1.40	Target	
EM* SR 24N	54635.88	2.50	8	2	1.41	Calibrator	$>5\sigma$
J16262367-2443138	54635.88	2.50	8	7	1.42	Target	
WSB 12	54635.88	2.50	8	7	1.40	Target	
EM* SR 21A	54635.88	2.50	8	7	1.43	Target	
J16262367-2443138	54635.88	2.50	8	7	1.45	Target	
WSB 12	54635.88	2.50	8	7	1.43	Target	
EM* SR 21A	54635.92	2.50	8	7	1.47	Target	
J16262367-2443138	54635.92	2.50	8	7	1.50	Target	
WSB 12	54635.92	2.50	8	7	1.49	Target	
V* V2059 Oph	54635.92	20.00	1	7	1.52	Calibrator	$>5\sigma$
RX J1625.2-2455	54635.92	20.00	1	7	1.58	Calibrator	
V* V2059 Oph	54635.92	20.00	1	7	1.61	Calibrator	
November 03, 2009							
J04183030+2743208	55138.92	10.00	1	10	1.05	calibrator	
J04380083+2558572	55138.96	10.00	1	10	1.01	calibrator	
J04350850+2311398	55139.00	20.00	1	10	1.01	calibrator	
V410 X-ray 6	55139.00	10.00	1	9	1.03	Target	
J04244506+2701447	55139.04	10.00	1	9	1.05	calibrator	
April 23, 2011							
J16233462-2308467	55674.92	5.00	4	12	1.67	Calibrator	$>5\sigma$
WSB 63	55674.92	5.00	4	10	1.65	Target	
J16273901-2358187	55674.96	5.00	4	9	1.55	Target	
J16250692-2350502	55674.96	5.00	4	10	1.49	Target	
DoAr 32	55674.96	5.00	4	11	1.47	Calibrator	$>4\sigma$
WSB 63	55674.96	5.00	4	10	1.46	Target	
BKLT J162624-244323	55674.96	5.00	4	11	1.44	Calibrator	$>5\sigma$
WSB12 (RX J1622.3-2321)	55675.00	5.00	4	11	1.38	Target	
J16315473-2503238	55675.00	5.00	4	10	1.42	Target	
BKLT J162624-244323	55675.00	5.00	4	10	1.40	Calibrator	

Table 5.2 – Continued

ID	BJD	t_{int}	Coadds	N_{frames}	Airmass	Type	Note
	(2400000 +)	[s]					
EM* SR 8	55675.00	5.00	4	10	1.40	Calibrator	
J16335560-2442049	55675.00	5.00	4	11	1.40	Target	
DoAr 50	55675.00	5.00	4	10	1.42	Calibrator	
WSB 63	55675.04	5.00	4	10	1.41	Target	
J16335560-2442049	55675.04	5.00	4	10	1.41	Target	
DoAr 50	55675.04	5.00	4	9	1.44	Calibrator	>5σ
DoAr 24	55675.04	5.00	4	10	1.44	Calibrator	
2E 1624.2-2444	55675.04	5.00	4	11	1.49	Calibrator	
RX J1633.9-2442	55675.08	5.00	4	10	1.48	Target	
RX J1624.8-2359	55675.08	5.00	4	11	1.51	Calibrator	no-Binary
ROXs 4	55675.08	5.00	4	11	1.57	Calibrator	
2E 1624.6-2352	55675.08	5.00	4	11	1.60	Calibrator	
IRAS 16114-1858	55675.08	5.00	4	9	1.62	Calibrator	

November 15, 2011

ID	BJD	t_{int}	Coadds	N_{frames}	Airmass	Type	Note
MBO 22	55880.75	5.00	4	25	1.50	Calibrator	>5σ
LRL 21	55880.79	5.00	4	23	1.42	Target	
LRL 72	55880.79	5.00	4	23	1.33	Target	
MBO 22	55880.79	5.00	4	23	1.22	Calibrator	
LRL 21	55880.83	5.00	4	23	1.22	Target	
LRL 67	55880.83	5.00	4	21	1.18	Target	
LRL 21	55880.83	5.00	4	22	1.11	Target	
MBO 22	55880.83	5.00	4	2	1.07	Calibrator	
LRL 67	55880.88	5.00	4	23	1.06	Target	
J03302409+3114043	55880.88	5.00	4	23	1.03	Calibrator	>5σ
V410 X-ray 6	55880.88	5.00	4	23	1.05	Target	
J04300424+3522238	55880.92	5.00	4	18	1.07	Calibrator	>5σ
V410 X-ray 6	55880.92	5.00	4	21	1.02	Target	
J04300424+3522238	55880.92	5.00	4	19	1.04	Calibrator	
HBC 390	55880.96	5.00	4	22	1.04	Calibrator	
J04303235+3536133	55880.96	5.00	4	10	1.04	Calibrator	no-Binary
J04303235+3536133	55880.96	5.00	4	11	1.04	Calibrator	no -Binary
J03302409+3114043	55880.96	5.00	4	14	1.09	Calibrator	>5σ

April 14, 2012

ID	BJD	t_{int}	Coadds	N_{frames}	Airmass	Type	Note
RX J1615.3-3255	56032.04	5.00	4	12	1.66	Calibrator	
RX J1615.9-3241	56032.04	5.00	4	13	1.66	Calibrator	
RX J1625.3-2402	56032.08	5.00	4	3	1.42	Calibrator	no-HighBF
V* V852 Oph	56032.08	5.00	4	3	1.45	Target	
WMR2005 1-38	56032.08	5.00	4	3	1.47	Calibrator	
WSB 40	56032.08	5.00	4	3	1.50	Target	
WMR2005 1-21	56032.12	5.00	4	3	1.61	Calibrator	

August 11, 2014

Table 5.2 – Continued

ID	BJD (2400000 +)	t_{int} [s]	Coadds	N_{frames}	Airmass	Type	Note
V* V711 Per	56881.04	20.00	1	8	1.38	Calibrator	$>5\sigma$
LRL 110	56881.04	20.00	1	6	1.35	Calibrator	
LRL 410	56881.04	60.00	1	5	1.31	Calibrator	
CIDA 2	56881.08	5.00	4	8	1.36	Calibrator	$>5\sigma$
IRAS 04125+2902	56881.12	20.00	1	7	1.16	Target	
V410 X-ray 3	56881.12	20.00	1	5	1.13	Calibrator	$>5\sigma$
UX Tau A	56881.12	5.00	4	8	1.14	Calibrator	

August 12, 2014

LRL 75	56882.04	20.00	1	8	1.54	Calibrator	
LRL 40	56882.04	20.00	1	8	1.46	Calibrator	
LRL 168	56882.04	20.00	1	8	1.42	Calibrator	
LRL 97	56882.04	20.00	1	8	1.35	Target	
LRL 237	56882.04	20.00	1	6	1.31	Target	

August 13, 2014

KOI-137	56883.00	20.00	1	7	1.65	Calibrator	
KOI-0044	56883.00	20.00	1	6	1.66	Calibrator	
KOI-4567	56883.00	20.00	1	7	1.66	Calibrator	
LRL 72	56883.04	20.00	1	7	1.55	Target	
J04311907+2335047	56883.08	20.00	1	7	1.37	Calibrator	$>5\sigma$

December 09, 2014

LRL 53	57000.75	20.00	1	7	1.19	Calibrator	
LRL 182	57000.75	20.00	1	8	1.17	Target	
LRL 58	57000.79	20.00	1	8	1.13	Target	
LRL 355	57000.79	20.00	1	7	1.12	Calibrator	
LRL 135	57000.79	20.00	1	7	1.10	Target	
LRL 233	57000.79	20.00	1	7	1.08	Calibrator	$>5\sigma$
LRL 31	57000.79	20.00	1	4	1.07	Target	
LRL 169	57000.79	20.00	1	7	1.06	Calibrator	
LRL 213	57000.83	20.00	1	7	1.05	Target	
J03302409+3114043	57000.96	20.00	1	13	1.41	Calibrator	$>5\sigma$
MBO 22	57001.00	20.00	1	7	1.46	Calibrator	$>5\sigma$
J04210934+2750368	57001.00	20.00	1	3	1.25	Target	
J04300424+3522238	57001.00	20.00	1	8	1.30	Calibrator	
J04303235+3536133	57001.00	20.00	1	6	1.33	Calibrator	no-binary
Pr 0211	57001.08	20.00	1	7	1.02	Calibrator	
Pr 0225	57001.08	20.00	1	7	1.02	Calibrator	

5.2.1 Target Properties

Our methodology to identify companions that might be responsible for the observed TD SEDs and could be orbiting in the inner region of the disk, requires estimations of the distances to the inner disk wall from the central star (r_d). However, not all TDs have a previous measurements of the inner radii and are not calculated by following a standard approach. Because we seek for uniformity in these estimations, we developed a simple approach highly dependent on the stellar luminosities $(L_\star)$ and the dust temperature in the disk (T_d). The stellar luminosities are calculated with the dereddened J-band photometry method from Kenyon & Hartmann (1995) and adopting the known distances to each different star$-$forming region. We de-reddened the J-band fluxes using the A_J extinction and measured by following the Mathis (1990) extinction law with $A(\lambda)/A(J) \sim (\lambda/1.25)^{-\alpha}$, where $\alpha = 1.7$. We used $A_J = 2.62[(J - H) - (J - H)_0]$, where $(J - H)_0$ is the expected colour of a main-sequence star from Pecaut & Mamajek (2013). We derived the stellar properties based on the spectral types taken from literature and a conversion to the effective temperatures (T_{eff}) taken from Pecaut & Mamajek (2013) with uncertainties of ~ 150 K, corresponding to ± 1 spectral subclass (Table 5.1). Additionally, using T_{eff} and $L_\star$, and assuming a single star system, we estimated the stellar masses $(M_\star)$ for each TD. Those in the range between 0.01 and 1.4 $M_\odot$, were derived from Baraffe et al. (2015) and stellar masses >1.4 $M_\odot$ from the PARSEC evolutionary models (Bressan et al., 2012). For the unknown metallicity values we adopted solar composition, and we also held the surface gravity fixed at the value log g = 4.0, typical for PMS stars. Table 5.1 shows R and Ks magnitudes, spectral types and stellar properties of these

objects.

Distances to the star forming regions were adopted from literature. Thus, a distance of 140 ± 10 pc was adopted to the *Taurus-Aurigae star forming region* (Loinard et al., 2008). However, we found a large range of discrepancies in the distances to Ophiuchus and IC-348 members, leading us to carefully choose the most appropriate values, since these young members placed in the H$-$R diagram are sensitive to any variation of these distances (Figure 6.4). We adopted a distance to the *IC 348 Region* based on the distance to the Perseus molecular cloud, that has been estimated in a wide range between 220 - 380 pc (Harris, Morgan & Roman, 1954; Herbig & Jones, 1983; Cernis, 1993; Scholz et al., 1999; de Zeeuw et al., 1999; Hirota et al., 2008; Hirota, 2010). We examined in detail the distance to the brightest cluster member, LRL 1. As a pair of B5V stars, these objects are zero-age main sequence (ZAMS) so they have a model-derived luminosity that is almost independent of age. Using the same technique as described above, we confirmed the distance of 220 ± 10 pc, excluding ZAMS model uncertainties but including uncertainties in reddening. We provide a more detailed discussion about the IC 348 distance in Appendix A. In the case of the distance to the *Ophiuchus* region and as the position of most of our objects sit around the main cloud, L1688, we based our decision on the distance measured to this association. For our purposes and due to the wide extension in the position of the TDs, we adopted a mean distance of 130 pc to L1688 core (Wilking, Gagné & Allen, 2008, and references therein) and consistent with the distance of 131 ± 3 pc calculated by Mamajek (2008).

Once the distances were found and constrained, we calculated the bolometric luminosities ($L_\star$) of IC 348, Ophiuchus and Taurus-Auriga members. Esti-

mations of stellar masses and ages are obtained from the H-R diagram and Baraffe et al. (2015) evolutionary tracks, except for IC348-21, IC348-31 and EM* SR 21A, where we made use of the PARSEC evolutionary models (Bressan et al., 2012). These values are estimated with the use of $L_\star$ and K absolute magnitudes. Age and stellar mass uncertainties are based mainly on the H-R diagram placement and the determination of $L_\star$, since T_{eff} does not vary with a large magnitude at ages < 5 Myrs in the pre-main sequence evolution tracks of low mass stars. The main sources of error on the $L_\star$ uncertainties are distance and extinction (Hartmann, 2001). In our estimates of A_J, we used the expected colour of a main-sequence star, which underestimates these values up to a factor of 2, and it is reflected in the luminosity and age of the system. In the special case of embedded object EM* SR 24S that belongs to the triple system EM* SR24, we adopted stellar properties from Andrews et al. (2011) to avoid any IR contribution from its nearby binary companion, EM* SR 24N (0".2; Simon et al., 1995). Table 5.3 shows the estimated stellar parameters. Figure 6.4 shows Baraffe evolutionary models with IC348, Taurus-Aurigae and Ophiuchus members. They are dispersed in a range of ages between 0.5 and 10 Myrs, characteristic of T-Tauri stars. Here, we carefully selected the chosen isochrone to derive stellar masses for each target, because these isochrones are also used in our Bayesian analysis, as explained in section 5.3.1.

Dust Temperature and Inner Radii

As demonstrated by Espaillat et al. (2012), the NIR excesses of classical TDs are well reproduced by the emission of a vertical wall directly exposed to stellar radiation. Then, we have computed the TD SEDs from NIR to MIR wave-

Table 5.3: Luminosity and Extinction for Our Sample Members.

Target	Temperature[1]	A_J[2]	Luminosity	Age	Mass[3]
	[K]	[mag]	[$L_\odot$]	[Myrs]	[$M_\odot$]
IC 348 d = 220 pc					
LRL 21	5280	1.70 ± 0.07	2.26 ± 0.25	$5.0^{+3.0}_{-2.0}$	$1.60^{+0.09}_{-0.05}$
LRL 67	3680	0.82 ± 0.06	0.23 ± 0.03	$3.8^{+1.2}_{-1.0}$	$0.50^{+0.05}_{-0.10}$
LRL 72	3550	0.97 ± 0.08	0.27 ± 0.04	$1.9^{+0.4}_{-0.5}$	$0.41^{+0.07}_{-0.04}$
LRL 237	3050	0.47 ± 0.10	0.04 ± 0.01	$3.4^{+0.7}_{-0.6}$	$0.13^{+0.02}_{-0.04}$
LRL 97	3550	1.79 ± 0.08	0.25 ± 0.03	$2.0^{+0.8}_{-0.5}$	$0.37^{+0.07}_{-0.04}$
LRL 31	5590	3.21 ± 0.05	3.44 ± 0.40	$8.0^{+2.0}_{-3.0}$	$1.62^{+0.09}_{-0.06}$
LRL 182	3200	1.03 ± 0.07	0.09 ± 0.01	$2.7^{+0.4}_{-0.6}$	$0.22^{+0.05}_{-0.03}$
LRL 213	3050	0.53 ± 0.16	0.04 ± 0.01	$3.4^{+0.7}_{-0.6}$	$0.13^{+0.02}_{-0.04}$
LRL 58	3680	1.13 ± 0.07	0.39 ± 0.05	$1.7^{+3.0}_{-3.0}$	$0.50^{+0.05}_{-0.07}$
LRL 135	3200	0.74 ± 0.11	0.12 ± 0.02	$1.9^{+0.4}_{-0.3}$	$0.2^{+0.05}_{-0.03}$
Taurus-Aurigae d = 140 pc					
IRAS04125+2902	3680	0.90 ± 0.06	0.39 ± 0.07	$1.7^{+0.4}_{-0.5}$	$0.50^{+0.04}_{-0.02}$
V410 X-ray 6	3200	0.98 ± 0.09	0.41 ± 0.07	$0.1^{+0.4}_{-0.1}$	$0.22^{+0.04}_{-0.05}$
J04210934+2750368	3050	0.00	0.09 ± 0.02	$1.4^{+0.4}_{-0.5}$	$0.17^{+0.02}_{-0.07}$
Ophiuchus d = 130 pc					
EM* SR 24S[4]	4990	7.00	4.00	$-$	2.00
EM* SR 21A	5720	2.46 ± 0.12	14.40 ± 2.40	$2.0^{+2.0}_{-1.0}$	$2.70^{+0.10}_{-0.10}$
WSB 12	4450	0.96 ± 0.13	1.40 ± 0.15	$2.1^{+1.8}_{-0.9}$	$1.11^{+0.16}_{-0.11}$
J16262367-2443138	4450	1.14 ± 0.15	1.90 ± 0.21	$1.3^{+1.2}_{-0.7}$	$0.99^{+0.14}_{-0.10}$
J16273901-2358187	4200	1.49 ± 0.11	1.51 ± 0.17	$0.9^{+0.9}_{-0.4}$	$0.90^{+0.11}_{-0.09}$
WSB 63	3550	1.68 ± 0.08	0.65 ± 0.07	$0.6^{+0.1}_{-0.2}$	$0.35^{+0.09}_{-0.10}$
J16335560-2442049	4050	1.26 ± 0.09	0.70 ± 0.08	$2.0^{+0.8}_{-0.5}$	$0.73^{+0.11}_{-0.09}$
J16250692-2350502	3400	1.32 ± 0.09	0.31 ± 0.03	$1.1^{+0.4}_{-0.2}$	$0.28^{+0.05}_{-0.14}$
J16315473-2503238	4050	2.25 ± 0.18	2.50 ± 0.27	$0.1^{+0.7}_{-0.1}$	$0.86^{+0.20}_{-0.20}$
WSB 40	4200	1.68 ± 0.08	1.11 ± 0.12	$1.5^{+0.6}_{-0.5}$	$0.96^{+0.12}_{-0.08}$
V*V852 Oph	3200	0.84 ± 0.09	0.26 ± 0.03	$0.6^{+0.3}_{-0.1}$	$0.19^{+0.08}_{-0.03}$

[1] References: Effective Temperatures are taken from the scale of Pecaut & Mamajek (2013), with uncertainties of $\sim$ 150 K

[2] Extinctions are calculated following the Mathis (1990) approach.

[3] Masses are estimated assuming single star systems.

[4] Stellar parameters taken from Andrews et al. (2011).
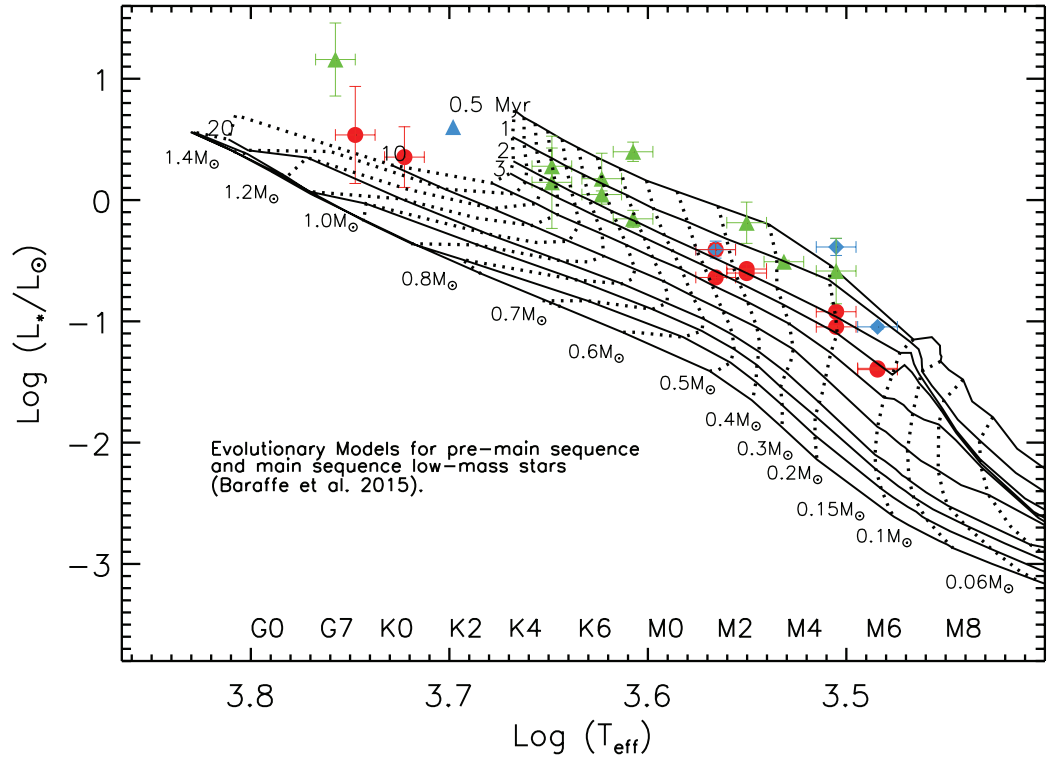
Figure 5.2: Theoretical models from Baraffe et al. (2015) for low mass young stars. Solid lines in descending order are 0.5, 1, 2, 3, 5, 10, 20, 50 and 100 Myrs isochrones and dashed lines represent the evolutionary tracks in the range of 0.06 and 1.4 M. Blue solid diamonds, green solid triangles and red solid dots are TDs from Taurus-Aurigae, Ophiuchus and IC348 star forming regions, respectively. The blue solid triangle corresponds to EM* SR 24S with $L_\odot$ and T (K) taken from Andrews et al. (2011). We used the scale temperatures range from Pecaut & Mamajek (2013) and stellar luminosities are estimate as described in section 6.4.2
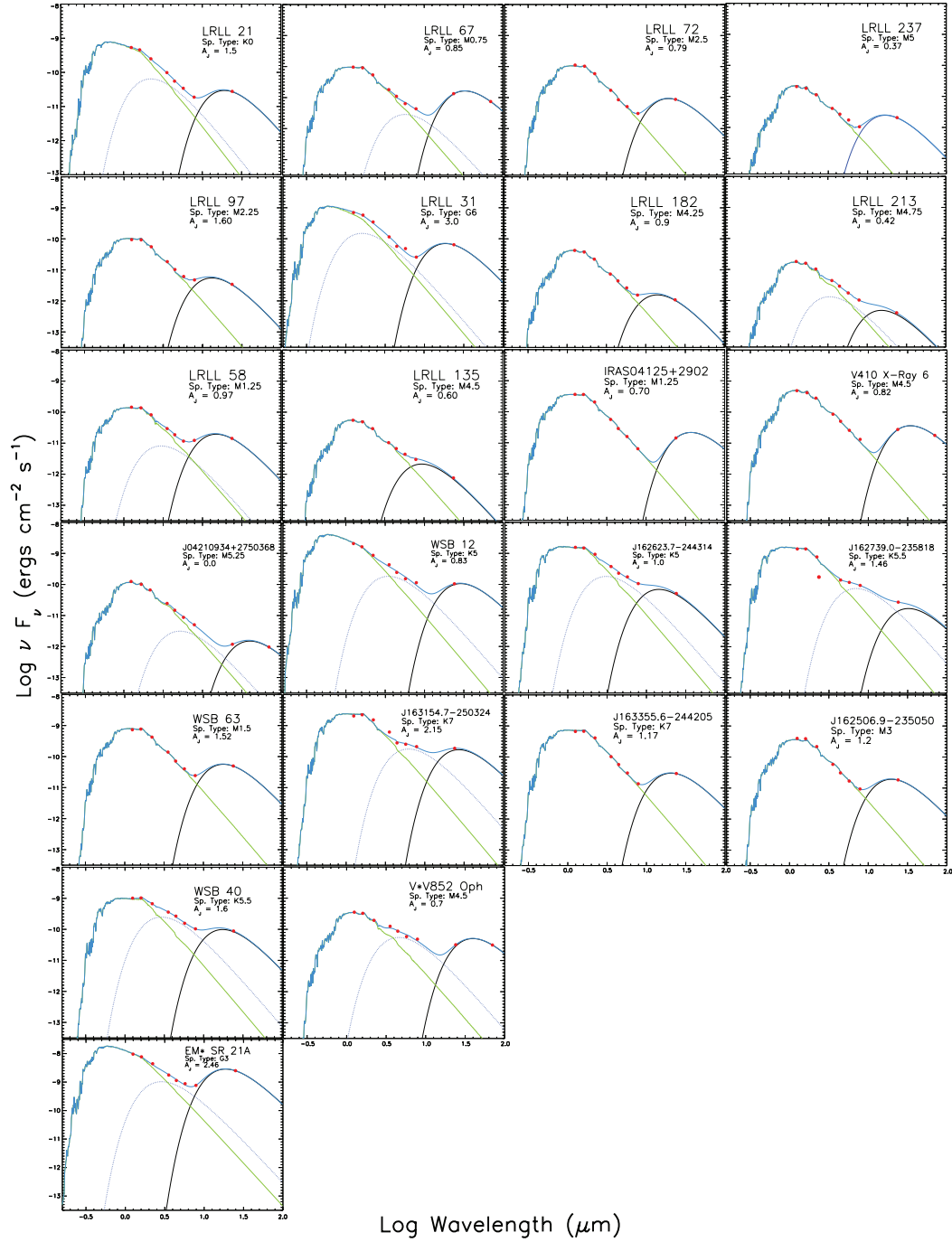
Figure 5.3: Spectral energy distribution of the sources classified as transitional disks. Red dots show photometric data acquired from the literature, green line is the BT-settl spectrum model according to the spectral type, blue line is the best fit, and the solid black and dotted blue lines are the disk black-body function values. A_J values used are in Table 5.3.

lengths in order to estimate inner wall radii for every disk (Figure 5.3). Since the thermal balance between emission and absorption of radiation is dominated by the dust grains as the main opacity source, we computed the dust temperature (T_d) at the truncation radius (r_d) of the disk. Our input photometry for SED fitting were from 2MASS (1.25, 1.65, 2.22 μm) and Spitzer/IRAC (3.6, 4.5, 5.8, 8 and 24 μm) (Skrutskie et al., 2006; Evans et al., 2003, 2009b; Currie & Kenyon, 2009; Rebull et al., 2010).

An estimation of the T_d was computed by fitting the stellar photosphere+disk black body function (F_m) to the observed data (F_ν) and minimizing the sum of squares. Prior to this fitting, the photometric data were dereddened using the Mathis (1990) approach, since the properties of the inner disk material significantly affects flux emission in these bands, and thus, the inner radii approximations (Furlan et al., 2011). To calculate the stellar synthetic photometry with a fixed temperature $T_\star$, which is approximated by the T_{eff}, we 1) interpolated the response curves, for the set of filters used in the fitting, and the BT-Settl spectra models of the corresponding $T_\star$ (Allard, 2014) and 2) convolved the filter response curves with the syntethic spectra, to match the spectral resolution. Because the 2MASS, IRAC, and 24 μm data have a photometric uncertainty of between a few percent and 0.1 mag for the objects investigated here, systematic effects can contribute up to 0.1 mag and also, to account for flux variability of the objects, we added an observational error of 12%. A multiplicative dilution factor relating the central star radius ($R_\star$) and the distance to the object (d) is part of the minimization of the χ^2. Then, the model of received flux is the product of a dilution factor and the blackbody flux. In the case of a star, this dilution factor is given by $M_d = \left(\frac{R_\star}{d}\right)^2$ (e.g.

Bayo et al., 2008)

Finally, the estimations of the truncation radius, r_d, are obtained by assuming Local Thermodynamic Equilibrium, and the ability of the dust to acquire thermal balance between absorption and emission of the radiation. The inner wall, nearly perpendicular to the stellar radiation, is heated only by the central star with a characteristic $R_\star$ and $T_\star$. Additionally, if the scattering of the dust grains is negligible and assuming optically thin gas in the inner region, we have in radiative equilibrium that the inner wall is being truncated at:

$$r_d = \frac{R_\star}{2\sqrt{\varepsilon}} \left(\frac{T_\star}{T_d}\right)^2 \tag{5.1}$$

where $\varepsilon \equiv \frac{\kappa(T_d)}{\kappa(T_\star)}$ is the *thermal cooling efficiency factor* that characterizes the dust properties of a certain size (Dullemond & Monnier, 2010). If the inner wall consist of small dust grains of radius $a << 3$ μm and the backwarming by the grains deeper in the wall is negligible, then $\varepsilon << 3^{-0.5}$. For our purposes, the size of the grains at the location of the inner wall is taken to be $a \sim 0.1$ μm, leading to estimations of r_d with $\varepsilon \sim 0.08$ (Isella & Natta, 2005, and references therein) as shown in Table 5.6. For EM* SR 24S, because of its large inclination and elongated ring with a significant brightness asymmetry along the major axis, and to avoid any flux contamination in the Spitzer/IRAC bands from EM* SR 24N, we adopted the inner radius estimated by Andrews et al. (2011), and recently confirmed by van der Marel et al. (2015). Our r_d estimations are in agreement with those previously measured (Table 5.1).

5.3 Data Analysis

5.3.1 Bayesian Analysis

Although some secondary companions are observed in the interferograms, e.g. Figure 5.1, it is important to carefully account for the assumptions inherent in the imaging completeness. A conservative approach where only secure detections are considered and conservative detection limits are quoted does not make maximum use of the data, especially at the smallest separations where binaries of moderate contrast ratios give relatively small closure-phase signals. Here, we made use of Bayesian statistics to compute confidence levels for detections, providing the advantage of using prior information of the underlying population of faint stellar companions. In essence, our approach to completeness correction, along with extensive Monte Carlo simulations, assigns the probability of detecting the presence of a faint companion or absence of it. We built two hypotheses, binary (B_n) and single (S_n), by using prior information of these models together with the aperture masking data of the TDs. Thus, a Bayes' theorem expresses the strengths of the hypotheses as follows:

$$p(B|D) = \frac{p(B_n)p(D|B_n)}{p(D)} \tag{5.2}$$

$$p(S|D) = \frac{p(S_n)p(D|S_n)}{p(D)} \tag{5.3}$$

where $p(D|B_n)$ and $p(D|S_n)$ are the *global likelihood*[2] functions or probability of obtaining data D, if B_n or S_n are true; $p(B_n)$ and $p(S_n)$ are the prior probabilities; and $p(B_n|D)$ and $p(S_n|D)$ are the posterior probabilities of B_n and S_n, respectively. The index n represents the number of simulations performed to determine the probability for each model.

Global Likelihood: Confirming or Ruling out the Presence of a Binary System.

In the data reduction process, after computing closure phases, the calibrated data set is used to search for faint companions close to the central star and orbiting the inner region of the disk. Our search strategy is based on the computation of the global likelihood that can be maximized from the *conditional likelihood* and its *joint prior probability* (Equation 5.4). Here, the conditional likelihood expresses the probability of observing our data for a specific set of model parameters and is weighted by the joint prior probability that incorporates prior information about the distribution of the model parameters. In our case, we have two hypotheses, B_n and S_n, that can be tested by computing their global likelihood as follows:

Confirming a Binary System: The maximum global likelihood or the odds by which our data favors a binary model, lies in our approach to completeness correction and the extensive binary star simulations to assign all possible con-

---

[2]The global likelihood of a model is equal to the weighted average likelihood for all the parameters in consideration.

trasts of the secondary relative to the primary (C), angular separation (ρ) and position angle (θ) values, as detailed below. Thus, our analysis to compute confidence levels is based on the derivation of the χ^2 goodness-of-fit to the n mock binary system models. From Equation 5.2 and marginalizing over all possible model parameters, we have that the global likelihood for a binary system model is:

$$P(D|B_n) = \int d\Psi p(\Psi|B_n) \times P(D|B_n, \Psi) \qquad (5.4)$$

where, $P(D|B_n, \Psi)$ is the *conditional likelihood*, $P(\Psi|B_n)$ is the *joint prior probability* for the model parameters and $\Psi = (T, a, e, \Omega, \omega, i, t, q)$ is the eight-dimensional parameter space representing all the possible binary orbits with the orbital parameters: Time of periastron passage (T, years), Semi-major axis (a, arc-second), Eccentricity (e), Position angle of the line of nodes (Ω), Longitude of periatron (ω), Inclination (i, degrees), Epoch of observation (t, year) and Mass ratio (q).

To compute the eight-dimensional integral shown in Equation 5.4, we made use of *Monte Carlo Integration* by generating a number of random samples according to a determined probability distribution function (PDF) in a specific spatial domain. The prior PDFs for T, Ω and ω for a binary system are assumed to have a uniform distribution (uninformative prior), so $p(T, \Omega, \omega_2|B_i) = 1$ in the space domain of these parameters. The inclination i is sampled considering that the orbital plane of the generated binaries might have any orientation in space. For q, we considered the mass ratio distribution often modelled in the form $f(q) \propto q^\beta$, where β is a power index of 0 that reasonably describes our TD

sample with spectral types ranging G3-M5 (e.g. Janson et al., 2012; Raghavan et al., 2010). For the prior distribution of e for these very young objets in a process of orbital circularisation, we based our approach on our resolving limitations of up to $\gtrsim 2$ au that corresponds to orbital periods of ~ 1000 days and is sampled well enough by the "thermal" eccentricity distribution $f(e) = 2e$ (Ambartsumian, 1937; Duquennoy & Mayor, 1991). For simplicity, we used the logarithmically flat distribution $dN/d\log a \propto a^0$ approach used by Metchev & Hillenbrand (2009) to sample a. Thus, the joint prior probability is:

$$P(\Psi|B_n) \propto q^\beta \left(\frac{2e}{a}\right) \sin(i) . \tag{5.5}$$

Table 5.4 shows the limits used in the simulations and corresponding prior for the orbital parameters. The sampling ranges for i, e, T, Ω and ω were taken by considering the total orbital plane with any orientation in space. More relevant for our detection limits, we focus our search region, mostly constrained by a, because the dynamics of binary-disk interaction models predict that tidal interaction between the binary star and the disk might truncate the inner region of the disk at radii of 2-3 times the semi-major axis of the binary orbit (Artymowicz & Lubow, 1994). Table 5.6 shows the inner radii estimates that we used as limits to sample the semi-major axis space that ranges between $\frac{r_d}{2}$ and $\frac{r_d}{3}$ at distances of the corresponding star-forming region (Tau-Aur: 140 pc, Ophiuchus: 130 pc and IC348: 220 pc).

Separately, Contrast ratio (C) and Stellar Masses (M_1, M_2) are sampled as a function of the corresponding distribution of the Mass ratio (q), where these stellar masses together with the sample of semi-major values are used as inputs

in Kepler's third law to compute the Orbital Periods (P, year) of each system. Here, we provided a brief summary of our methodology to sample M_1, M_2 and C.

- *Stellar Masses and Contrast Ratios:* Initially, we chose an isochrone (Z_1) from the Baraffe et al. (2015) models, which represents the age of the TD and that in principle, plays the role of the primary component. In order to account for all the possible flux ratios, the following step is to start computing evolutionary tracks that describe the possible secondary stellar component in our data. This is done by randomly sampling a mass-ratio (q_n) distribution and using the relation $Z_{2,n} = Z_1 q_n$, where $Z_{2,n}$ and Z_1 are the tracks for all the possible secondary stars and the track for the primary star, respectively. Then, we computed the theoretical magnitudes of the these new evolutionary tracks by interpolating onto the theoretical stellar masses and K magnitudes of the chosen isochrone (Z_1). Thus, we have generated a series of isochrones that correspond to every value of q_n, $q = 0$ being a single star and $q = 1$ a binary star system with similar masses. Once the evolutionary isochrones describing all the secondary components are computed and taking Z_1, we were able to calculate the total K magnitude of the binary system. Then, we estimated the primary mass (M_1) based on its observed absolute K magnitude interpolated onto the total K magnitude of the binary system and the theoretical mass track; and with the relationship $M_2 = q_{1,n} M_1$, we obtained the secondary mass, M_2. Finally, interpolating the primary and secondary masses onto the total K magnitude of the binary system and the theoretical mass track, we estimated their K magnitudes in order to compute contrast

Table 5.4: Parameter Prior for Binary Model

Orbital Parameter	Prior[1]	Lower Bound	Upper Bound
Semi-major Axis (arc second)	Jeffreys' prior	$\frac{1}{3}R_d$	$\frac{2}{3}R_d$
Period (years)	Keplearian	a_i^3	a_o^3
Time of periastron passage (years)	Uniform	–	–
Eccentricity	$2e$	0.01	0.9
Inclination (degree)	sin (i)	0	180
Node (degree)	Uniform	0	180
Longitude of Periastron (degree)	Uniform	0	360
Mass-ratio	Power-Law	0.01	1

[1] It was used the Cumulative Distribution Function to sample in the orbital parameter space.

ratios.

Finally, the orbital parameters sampled are used to derive the angular separation (ρ) and position angle (θ) (Meeus, 1992) for N simulated binary systems. These values together with the calibrated data are used to compute the maximum likelihood of the contrast ratio and, thus confirm or rule out a stellar companion orbiting in the inner region of the disk.

Confirming a Single System: In the case of a single system as a point-symmetric target, the calibrated closure-phases are nearly equal to zero. Then, the computation of the global likelihood for a single system is basically determined by the conditional likelihood for a single system model with flux ratio equal to zero. From Equation 5.3, the global likelihood is:

$$p(D|S_n) = p(C = 0|S_n). \qquad (5.6)$$

Odds Ratio: After computing the global likelihoods for B_n and S_n, we are interested in comparing the two hypotheses, thus we computed the ratio of

Table 5.5: Companions Identified Outside the Inner Radii with the Aperture Mask

Primary	BJD (2400000+)	ΔK [mag]	Sep [mas]	Sep [au]	PA [deg.]	M_1[1] [$M_\odot$]	M_2[1] [$M_\odot$]	Sig.[2]
LRL 72	55880.79	1.37 ± 0.02	103.72 ± 0.36	22.82 ± 0.04	221.86 ± 0.10	0.41	0.13	49.0
"	56883.04	1.42 ± 0.03	100.45 ± 0.47	22.10 ± 0.08	226.70 ± 0.26	"	"	40.0
LRL 182	57000.75	1.54 ± 0.04	35.30 ±0.74	7.76 ± 0.26	213.42 ± 0.77	0.20	0.05	39.4
LRL 135	57000.79	0.17 ± 0.01	82.01 ± 0.26	18.04 ± 0.01	208.36 ± 0.21	0.18	0.16	90.5
LRL 213	57000.83	0.57 ± 0.18	18.01 ± 0.76	3.96 ± 0.17	50.48 ± 3.23	0.11	0.06	9.30
J04303235+3536133[3]	55880.96	0.40 ± 0.36	20.25 ± 2.88	9.11± 1.30	205.28 ± 2.25	0.72	0.59	10.31
"	57001.00	0.02 ± 0.02	26.24 ± 0.70	11.81 ± 0.32	216.81 ± 2.19	"	"	9.48

[1] The fractional uncertainties on the individual masses are ≤20%.
[2] Significance in σ is calculated as $\sqrt{\Delta\chi^2 \times (N_{\mathrm{df}}/N_{\mathrm{cp}})}$, with N_{df} the number of degrees of freedom and N_{cp} the number of closure-phases, and uncertainties scaled so that the reduced chi-squared of the best fit solution is unity.
[3] Located at Auriga-California molecular cloud (450 ± 23 pc; Lada, Lombardi & Alves, 2009).

$p(B|D)$ and $p(S|D)$ known as *Odds Ratio* and written as $O_{B,S}$ in favor of the binary system model over the single system model:

$$O_{B,S} = \frac{p(B|D)}{p(S|D)} = \frac{p(B_n)}{p(S_n)} \frac{p(D|B_n)}{p(D|S_n)} \qquad (5.7)$$

where the first factor on the right side of Equation 5.7 corresponds to the *prior odds ratio* equal to unity due to its uniformity in the parameter space and the second term is known as *Bayes' Factor* (Υ). Thus, $\Upsilon_{B,S} >> 1$ means that a binary model is preferred by the data, $B_{B,S} << 1$ the data comes from a single star and $B_{B,S} \approx 1$ means that the odds are not modified and a binary and/or single star are equally probable.

5.4   Results

We are considering visual companions to stars in our cluster down to a Ks magnitude of ~15 in IC348 (and significantly brighter limits in other clusters), where the stellar density is approximately 2×10^{-4} stars per square arcsec at

this magnitude limit. Given that we are only considering companions within ∼0.16 arcsec in this paper, the probability of a background star masquerading as a physical companion is no more than 0.002% for each star in the sample, or <0.04% for the entire sample.

As a part of our analysis and election of calibrator objects, we have found that 2MASS J04303235+3536133 is a binary object and although, it is reported as a TD by Cieza et al. (2010), we excluded this object from the sample because it is located at the Auriga-California molecular cloud. Table 5.5 shows contrast and positions for both observing epochs of the object.

5.4.1   Stellar Companions Outside the Inner Radii

In our first identification process, we identified LRL 72, LRL 182, LRL 213 and LRL 135 as cases for a high contrast detection with a confidence level of ≥ 99.5 % (section 6.2). We removed those objects as a part of the sample of TDs because the stellar companion is located outside the area of study and is not responsible for carving out the inner region of the disk. Estimation of the companion mass values were obtained by taking the K mag from the system, ΔK and Baraffe et al. (2015) models. Then, after obtaining an estimate of the K magnitudes for each stellar component, we interpolated linearly onto the evolutionary tracks to obtain the individual masses. Mass uncertainties are dominated by the evolutionary tracks, and depending on the theoretical model used, are of the order of 10-20% (Siess, 2001). In the case of LRL 213, we included visibility amplitudes for breaking contrast/separation degeneracies. Table 5.5 shows the epoch, contrast ratio detection, position parameters and

companion masses of these new binary systems.

The SEDs of these four close binary companions have NIR and MIR fluxes above the level expected for a reddened low mass star of spectral types M2-M5. The qualitative SEDs of these objects can be explained by a system composed of a close low-mass binary star, where the secondary component is surrounded by a "cold and weak" disk, a *"circum-secondary disk"*. For instance, if the LRL 72 components are coeval and using the Baraffe et al. (2015) models, the object would correspond to a spectral type of $\sim$ M5$-$M7 with a temperature between 2900 and 3100 K. As shown in Figure 5.4, the IR excess in the SED might be emitted by a disk orbiting the secondary component, instead of the primary star. Previous studies have shown that disks around *brown dwarfs and very low mass stars* are generally flatter and less massive than their counterpart T Tauri disks (Olofsson et al., 2013; Liu et al., 2015). This would explain the relative weak IR excesses observed in their SEDs of these binary systems.

Additionally, the angular separation of $\sim 100 \pm 0.4$ mas of LRL 72, imposes a limit on the extension of the disk of around 22 au, because the presence of the companion at this close distance would truncate the disk. Similarly, LRL 182 and LRL 213 with a closer companions having mass values of 0.07 $M_\odot$ at $\sim$ 7.7 au and 0.15 $M_\odot$ at $\sim$ 4.0 au, respectively, the disk also undergoes a faster dispersion as shown in its SED with a homogeneously small IR excess, see Figure 5.3. For LRL135, the mass ratio is near unity (q=0.89), and the system has a very weak excess with a disk (Figure 5.3). This system therefore remains a TD candidate, with it being unclear which component of the binary is the TD candidate. This system has a relatively high disk to stellar temperature ratio, with only a very small cleared inner disk region.
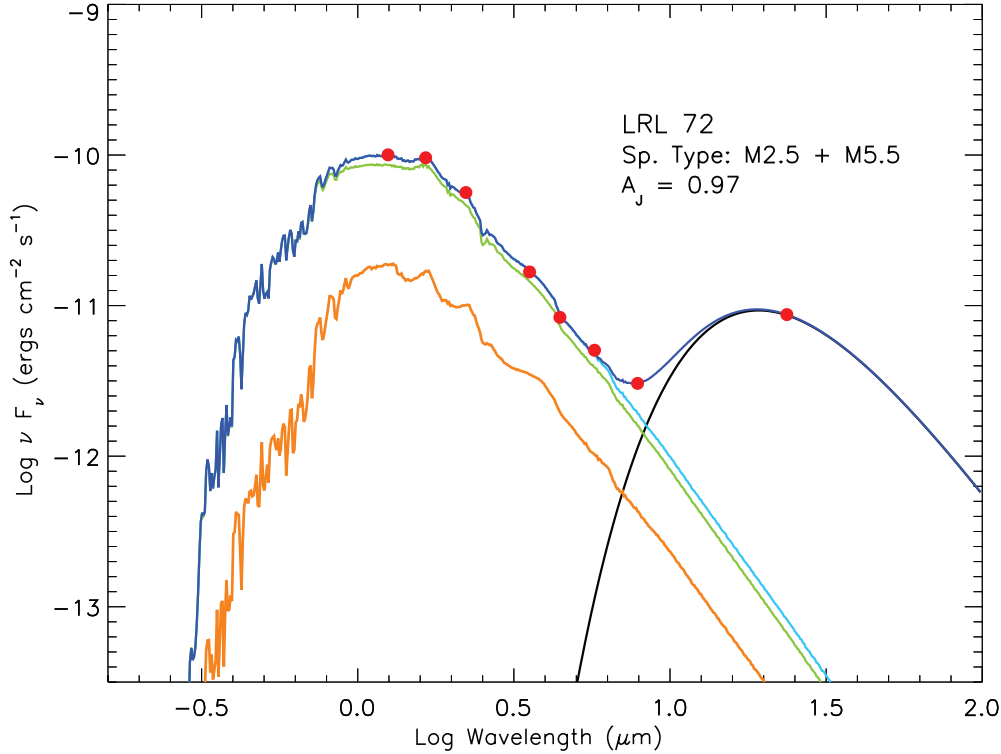
Figure 5.4: Spectral Energy Distribution for LRL 72 and its components with spectral types M2.5 and M5.5. Red dots show photometric data acquired from the literature, green and orange lines are the primary and secondary components BT-settl spectra, respectively. The black line is the disk black-body function values, the cyan line is the best stellar fit and the blue line is the sum of the primary and secondary spectra and the disk black-body function values.

5.4.2   Stellar Companions Inside the Inner Radii

Our fits to closure phases showed detections of 7 new candidate companions. As shown in section 5.3, we computed the Bayes' Factors for every object in the sample. Following the interpretation of Jeffreys (1998), we have found very strong Bayes' factors as an indication of the presence of candidate companions for LRL 31, V∗V X-ray 6, WSB 12 and 2MASS J16335560-2442049 (see Table 5.6). For WSB 40, 2MASS J04210934+2750368 and 2MASS J16315473-

Table 5.6: Bayesian Analysis

Object	Bayes' Factor	r_d [au]	r_d [mas]	$\mathbf{T}_d$ [K]
LRL 21	0.03	10.9 ± 0.8	49.0 ± 4.0	194.2 ± 1.0
LRL 67	0.03	11.6 ± 1.1	53.0 ± 5.0	112.0 ± 2.3
LRL 72[1]	–	3.8 ± 0.4	17.0 ± 2.0	191.3 ± 1.7
LRL 237	1.0	1.2 ± 0.1	5.0 ± 0.4	219.6 ± 5.0
LRL 97	0.98	1.7 ± 0.2	8.0 ± 1.0	279.1 ± 3.4
LRL 31	300	13.1 ± 1.1	60.0 ± 5.0	198.0 ± 4.6
LRL 182[1]	–	1.2 ± 0.1	6.0 ± 0.4	260.1 ± 2.7
LRL 213	–	0.9 ± 0.1	4.0 ± 0.4	242.4 ± 1.0
LRL 58	0.99	2.8 ± 0.3	13.0 ± 1.0	246.5 ± 1.4
LRL 135	0.99	0.6 ± 0.1	2.0 ± 0.4	393.0 ± 2.4
IRAS04125+2902	0.02	19.9 ± 2.0	143.0 ± 14.0	92.3 ± 1.3
V410 X-ray 6	> 300	5.4 ± 0.4	39.0 ± 2.0	183.4 ± 9.6
J04210934+2750368	24	10.5 ± 1.2	75.0 ± 9.0	91.0 ± 1.9
EM* SR 24S[2]	0.01	29.0	223.0	–
EM* SR 21A	0.003	27.2 ± 2.7	209.0 ± 21.0	196.02 ± 9.8
WSB 12	> 300	6.0 ± 0.5	46.0 ± 4.0	230.0 ± 10.7
J16262367-2443138	0.07	8.3 ± 0.7	64.0 ± 5.0	211.0 ± 2.3
J16273901-2358187	0.05	11.1 ± 1.0	85.0 ± 7.0	174.2 ± 1.9
WSB 63	0.05	5.3 ± 0.5	41.0 ± 4.0	204.3 ± 2.0
J16335560-2442049	> 300	7.3 ± 0.7	56.0 ± 5.0	178.2 ± 3.3
J16250692-2350502	1.0	4.4 ± 0.5	35.0 ± 4.0	186.4 ± 3.3
J16315473-2503238[3]	> 300	6.2 ± 0.6	47.0 ± 4.0	266.4 ± 11.5
WSB 40[4]	> 300	6.7 ± 0.6	52.0 ± 4.0	209.8 ± 1.4
V*V852 Oph	0.05	16.2 ± 2.1	125.0 ± 16.0	93.1 ± 3.6

[1] Targets not included in the statistical analysis of TDs.

[2] Estimated inner radius taken from Andrews et al. (2011).

[3] Based on Kohn et al. (2016). The Bayes' factor based on closure-phase alone was 30. See section 5.4.2 for a detailed discussion.

[4] Using visibility amplitude. The Bayes' factor based on closure-phase alone was 3. See section 5.4.2 for a detailed discussion.

Table 5.7: Detection Confidence Limits (99.9%)

Object	BJD (2400000 +)	ΔK^1 10-20	20-40	40-80	80-160	160-240
		Non-Detections				
LRL 21	55880.75	1.13	3.13	3.99	3.72	3.77
LRL 67	55880.83	1.83	3.59	4.44	4.18	4.24
LRL 237	56882.04	-	0.23	1.52	1.00	1.14
LRL 97	56882.04	0.59	2.75	3.80	3.54	3.57
LRL 58	57000.79	2.09	3.77	4.72	4.44	4.48
IRAS04125+2902	56881.12	1.60	3.41	4.29	4.04	4.09
EM* SR 24S	54635.75	-	1.43	2.77	2.40	2.41
EM* SR 21A	54635.88	2.51	4.11	4.98	4.71	4.75
J16262367-2443138	54635.88	2.28	3.91	4.81	4.57	4.58
J16273901-2358187	55674.96	-	0.44	2.01	1.60	1.67
WSB 63	55674.96	0.88	3.00	3.97	3.77	3.82
J16250692-2350502	55674.96	-	0.37	1.81	1.42	1.51
V*V852 Oph	56032.08	1.60	3.41	4.31	4.06	4.12
		Detections Outside Inner Radii				
LRL 72	55880.79	-	-	0.55	0.31	0.38
"	56883.04	-	-	0.54	0.31	0.38
LRL 182	57000.75	-	0.13	1.08	0.70	0.80
LRL 135	57000.79	-	-	0.20	-	0.03
LRL 213	57000.83	0.68	2.85	3.83	3.63	-
		Detections Inside Inner Radii				
LRL 31	57000.79	0.93	3.02	3.91	3.72	-0.00
V410 X-ray 6	55139.00	0.57	2.72	3.63	3.38	3.44
WSB 12	55675.00	0.56	2.69	3.63	3.37	3.41
WSB 40	56032.08	1.45	3.32	4.33	4.06	4.11
J16335560-2442049	55675.04	0.93	3.02	3.91	3.72	-

NOTES: Angular separation ranges are given in mas.
[1] Limits within annuli.

Table 5.8: Companions Identified Inside the Inner Radii with the Aperture Mask

Primary	BJD (2400000+)	ΔK [mag]	Sep [mas]	Sep [au]	PA [deg.]	M_2^1 [$M_\odot$]	Sig.
LRL 31	57000.92	3.92 ± 0.20	38.09 ± 5.30	8.38 ± 1.16	45.56 ± 4.06	0.20	6.70
V410 X-ray 6	55138.92	0.15 ± 0.07	22.96 ± 1.25	3.22 ± 0.18	87.80 ± 2.20	0.21	12.50
WSB 12	55674.92	0.42 ± 0.11	20.29 ± 0.78	2.64 ± 0.10	351.02 ± 2.13	0.75	11.80
WSB 40	56031.51	0.35 ± 0.14	17.42 ± 0.94	2.26 ± 1.12	-11.37 ± 3.80	0.75	8.40
J16335560-2442049	55675.04	0.10 ± 0.05	25.30 ± 0.55	3.29 ± 0.71	344.55 ± 1.77	0.61	14.40

NOTES: Significance in σ is calculated as $\sqrt{\Delta\chi^2 \times (N_{df}/N_{cp})}$, with N_{df} the number of degrees of freedom and N_{cp} the number of closure-phases, and uncertainties scaled so that the reduced chi-squared of the best fit solution is unity.
[1] The fractional uncertainties on the stellar masses are $\leq$20%.

Table 5.9: Degenerate Companion Solutions for 2MASS J04210934+2750368 at ΔK 0.5, 1, 2 and 3.

Primary	BJD (2400000+)	ΔK [mag]	Sep [mas]	Sep [au]	PA [deg.]	M_2 [$M_\odot$]	Sig.
J04210934+2750368	57001.04	0.5	19.28 ± 0.69	2.70 ± 0.09	309.60 ± 3.60	0.09	10.25
"	"	1.0	19.01 ± 0.75	2.66 ± 0.10	307.68 ± 3.92	0.07	9.87
"	"	2.0	21.78 ± 1.32	3.05 ± 0.18	306.30 ± 4.63	0.04	8.54
"	"	3.0	26.40 ± 3.13	3.70 ± 0.94	306.89 ± 6.78	0.02	6.74

2503238, we obtained moderate Bayes' factors ($>$10) from closure-phase alone, and considered these sources in more detail. In all cases, a visibility amplitude signal was found that was consistent with the best closure phase solution. In the case of WSB 40, the use of visibility amplitudes resulted in a clear solution with little degeneracy, as reported in Table 5.8. We assigned a high ($>$300) Bayes' factor to this object in Table 5.6. In the case of 2MASS J04210934+2750368, contrast ratio and separation were highly degenerate, so we list possible statistically significant solutions at plausible contrast ratios as shown in Table 5.9. For reported 2MASS J16315473-2503238, no binary solution was statistically significant (taken as 6σ, e.g. Kraus et al., 2016), and there was only 1 epoch on the target under variable Laser Guide Star conditions. For these reasons, we do not report a binary solution, but note that a binary companion was confirmed as a Double-Line Spectroscopic binary (SB2) star composed of a K7 and a K9, with a semi-major axis of $<$ 0.6 au by (Kohn et al., 2016) and therefore, we assigned a high ($>$300) Bayes' factor to this object in our statistical analysis (Table 5.6).

An interesting case is 2MASS J16335560-2442049, which was initially presented as a giant planet-forming candidate based on the morphology of its SED, large disk mass and modest accretion rate (Cieza et al., 2010; Orellana et al., 2012). Our χ^2 minimization detected a secondary star located at $\sim 3.25 \pm 0.07$ au

and using Baraffe et al. (2015) models and ΔK mag, the stellar mass would correspond to $\sim 0.61~M_\odot$. However, the interpretation of a single-epoch for this object has to be taken with caution because of the high inclination (~ 50 *deg*) of its disk (Cieza et al., 2012a), and the known degeneracy between the contrast ratio and small angular separations in the NRM data (Pravdo et al., 2006). Recently, Cieza et al. (2013) demonstrated that the starlight scattered off the inner edge of the FL Tau disk could mimic the presence of a faint companion, which might be the case of 2MASS J16335560-2442049. Further observing epochs are needed to establish the physical origin of the non-zero closure phases found in our analysis. Other cases of new binary systems are WSB 40 and WSB 12, which were below the detection limits of Cheetham et al. (2015). Our careful reduction process and fits to closure phases resolved companions at $\sim 2.22 \pm 0.12$ au with a mass of $\sim 0.75~M_\odot$ for WSB 40 and at $\sim 2.60 \pm 0.10$ au with a mass of $\sim 0.75~M_\odot$ for WSB 12.

5.4.3   Stars without a companion in the Inner Radii

With a Bayes' factor of < 0.1, the NRM data analysis did not detect binary stars with angular separations ranging from $\sim \frac{1}{3}$ to $\frac{2}{3}$ of the r_d for LRL 21, LRL 67, IRAS04125+2902, EM* SR 21A, DoAr 44, 2MASS J16262367-2443138, 2MASS J16273901-2358187, WSB 63, EM* SR 24S and V*V852 Oph (Table 5.6). Detection limits for these objects are listed in Table 5.7. The absence of a binary companion implies that the inner region mainly is being dispersed by an internal process that determines the lifetime of the disk. To date, the different mechanisms proposed to explain the inner holes of these disks do not accurately predict the observed features of TDs, and produced theoretically

distinct properties of the TDs (e.g. Alexander & Armitage, 2007). Despite all the efforts to develop a unique explanation of the evolution of the disk and its transition phase from a class II to III, *photoevaporation* and *planetary formation*, and its counterpart processes such as dust filtration and grain growth, seem to be the most efficient mechanisms to disperse the disk from the inside out.

5.4.4 Unresolved Transitional Disks

In Table 5.6, LRL 237, LRL 97, LRL 58 and 2MASS J16250692-2350502 are the objects with Bayes' factors of ~ 1, meaning that our NRM observations were not able to rule out or confirm companions for those objects, where the inner radii estimations fall inside our detection limit of 25 mas. These objects have M1 or later spectral types, meaning that they are at the low mass end of our sample. They also have relatively low accretion rates, typical of lower mass objects (Herczeg & Hillenbrand, 2008, $\lesssim 10^{-8}\ M_\odot \mathrm{yr}^{-1}$) . If their lack of a NIR excess is due to clearing by a binary companion, such a companion can only be discovered by multi-epoch radial velocity monitoring. We summarise our detection limits in Table 5.7.

5.5 Statistics

After estimating the stellar properties and computing the Bayes' factor $\Upsilon_{B,S} = \frac{P(D|B)}{P(D|S)}$ for every target, we proceed to estimate the frequency of binary stars producing the "transitional disk SEDs".

Continuing with Bayesian statistics, we assigned prior probabilities to each population, where the prior information for a binary or single system in TDs are equally probable. A non-informative probability distribution for the frequency of binary or single systems is a parameter representing two unique scenarios, binary or non-binary. Thus, $P(B) = \gamma$ represents the probability of binarity and $P(S) = (1-\gamma)$ not binarity, where the paramenter $\gamma \in [0, 1]$ and is sampled by the family of *beta distributions* [3] (Glickman & van, 2007).

The Jeffreys prior for the sampling distribution that provides uniform probability to both events B and S is represented by:

$$P(\gamma) \propto \frac{1}{\sqrt{\gamma(1 - \gamma)}} \propto \frac{1}{\sqrt{P(B)P(S)}}. \tag{5.8}$$

Taking into account that the current work is pioneering in the search for close binary companions (> 40 mas) or confirming a single star in the inner region of TDs, no information was available from inside the inner region of these TDs. Therefore, we have to assume that the data have arisen from one of two systems and being equally probable. Thus, a prior distribution γ with the form that represents the best prior state of knowledge can be modified with the observed data as follows:

$$P(\gamma|D) \propto P(\gamma)P(D|\gamma) \propto P(\gamma)[\gamma(\Upsilon_{B,S}) + (1 - \gamma)] \tag{5.9}$$

---

[3]Beta distribution has parameters $\alpha, \beta = 1/2$ to ensure a probability equal to unity and events equally probable.

where $\Upsilon_{B,S}$ is the computed Bayes' factor of every TD. Considering all TDs in our sample and additionally TDs from previous studies, the posterior density function of the frequency of binary systems responsible of the observed SEDs is:

$$P(\gamma|D) \propto P(\gamma) \prod_{i=1}^{i} [\gamma(\Upsilon_{B,S})_i + (1 - \gamma)] \tag{5.10}$$

with the index i representing the number of objects included in the modification of γ.

5.5.1 Binary Frequency in TDs

Binary and single objects were identified in our sample of TDs with Bayes' factors $\Upsilon < 0.1$, $\Upsilon > 300$ and $\Upsilon \simeq 1.0$, which are likely single stars, binary stars or unresolved systems, respectively, except for 2MASS J04210934+2750368 with a Bayes' factor of 24 (Table 5.6); we proceeded to include objects that were already classified as TDs and eventually, were characterized as binary or single stars[4]. For these binary and single objects a Bayes' factor of 300 and 0.001 were used in the Bayesian statistical analysis, respectively. These objects are summarised in Table 5.10. After computing the posterior probability, see Equation 5.10, our uniform prior has been modified to the posterior probability of 0.38 ± 0.09 and shown in Figure 5.5.

---

[4]For the special cases of 2MASS J16315473-2503238 and previously studied, FL Cha, we opted to include them as binary objects in the statistical analysis.
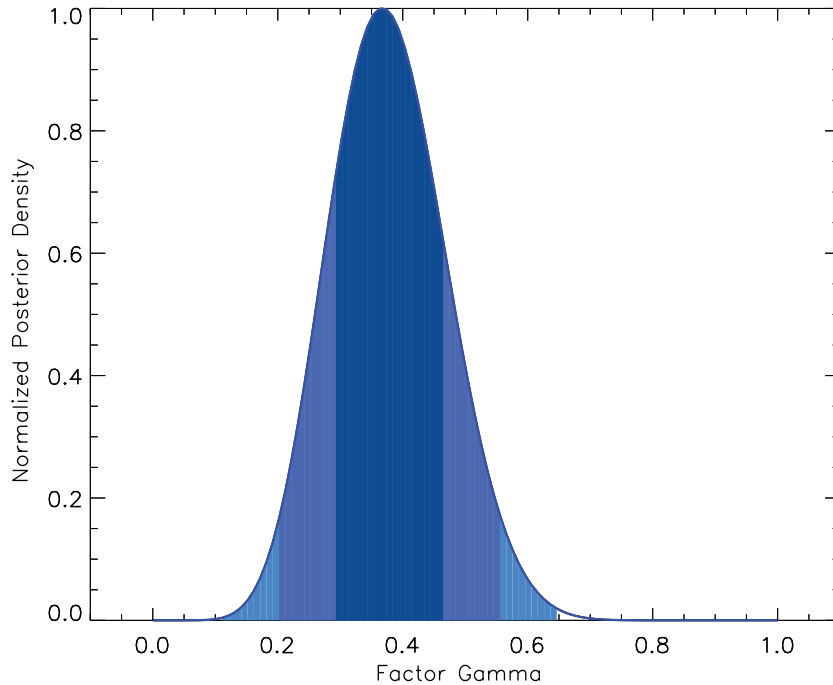
Figure 5.5: The fraction of TD in our sample consistent with a binary system being the main mechanism causing the characteristic SED is 0.38 ± 0.09.

5.6   Discussion

In our combined sample consisting of 31 objects, including 11 TDs and CDs with known multiplicity from the literature, and excluding 3 wide binaries, we find that a fraction of 0.38 ± 0.09 of the SEDs are being produced by the flux emission of a binary star + disk instead of a single star + disk. This means that the remaining SEDs with low NIR and MIR excesses observed to date are the result of the dispersion of the primordial material due to another internal mechanism. Our binary detections inside the fitted disk wall inner radii do not necessarily have projected separations between $\frac{1}{3}$ and $\frac{1}{2}$ of the inner radii, which

Table 5.10: Stellar Properties of Other Known TDs

Object	R.A. (J2000)	Dec. (J2000)	Type	Spec. Type	Accretor	$R_{cav.}$ [au]	Reference
Coku Tauri/4	04 41 16.808	+28 40 00.07	Binary	M1.5	n	10	1, 2,11
LKCa15	04 39 17.796	+22 21 03.48	Single	K5v	y	50	1,3,5,9
DM Tau	04 33 48.73	+18 10 10.0	Single	M1	y	19	1,4,5,9
GM Aur	04 55 10.983	+30 21 59.54	Single	K5	y	28	1,4,5,9
UX Tau A	04 30 03.988	+18 13 49.61	Single	G8	y	25	1,4,5,9
RY Tau	04 21 57.41	+28 26 35.57	Single	K1	y	18	1,5,10
CS Cha	11 02 24.912	-77 33 35.72	Binary	K6	y	38	1,6,10
T Cha	11 57 13.550	-79 21 31.54	Single	K0	y	40	1,6,12
FL Cha	11 08 39.051	-77 16 04.24	Binary	K8	y	8.3	1,7
TW Hydrae	11 01 51.907	-34 42 17.03	Single	K6	y	41	1,8,13
Haro 1-16	16 31 33.46	-24 27 37.3	Single	K3	y	36	1, 14, 15

Reference: (1) 2MASS All-Sky Point Source Catalog, (2) Ireland & Kraus (2008), (3) Kraus & Ireland (2012), (4)Huélamo et al. (2011), (5) Pott et al. (2010), (6) Guenther et al. (2007), (7) Cieza et al. (2013), (8) Rapson et al. (2015), (9) Andrews et al. (2011), (10) Espaillat et al. (2011), (11) D'Alessio et al. (2005), (12) Huélamo et al. (2015), (13) Nomura et al. (2016), (14) Bouvier & Appenzeller (1992), (12) Cheetham et al. (2015)

is the expected semi-major axis range for a binary to cause the truncation of the disk. However, all detections lie within $\frac{1}{2}$ of our calculated inner disk radii, consistent with projection effects.

Given the criteria applied to select our sample and following the standards for disk classification, we emphasize that these objects should be treated as CDs that possibly are in a *transitional phase*, and no longer treat them as TDs with a single star. Originally, the SEDs of these objects were described assuming only one object in the interior of the disk and using detailed disk models to fit the excess continua (e.g. Espaillat et al., 2012). As demonstrated by this work, there is a significant fraction of these SEDs which were misclassified. However, as seen in Figure 5.3, the CD SEDs of LRL 31, V410 X-ray 6, WSB 12, WSB 40 , 2MASS J16335560-2442049, 2MASS J04210934+2750368 and 2MASS J16315473-2503238 are indistinguishable from TDs. Although, to date the resemblance between CD SEDs and TD SEDs is well established (e.g. Ireland & Kraus, 2008), unfortunately we could not set an observational constraint such as accretion rate or flux emission in our sample. For example,

the SEDs of V410 X-ray 6 and 2MASS J16335560-2442049 bear a resemblance to the large MIR emission and zero NIR excess detected in the binary Coku Tau/4 (D'Alessio et al., 2005; Ireland & Kraus, 2008), while the other objects show a more similar SED to a typical TD SED. On the other hand, for those objects shown in Table 5.6 with Bayes' factors $\simeq 1$, that due to resolution limitations we were not able to confirm or rule out their binarity, multi-epoch RV monitoring observations are needed (e.g. Kohn et al., 2016), because there might be more binary objects dispersing the inner region of the disk efficiently.

We have also detected 4 new binary systems with the location of the secondary component outside the inner region of the disk. Interestingly, these systems produced SEDs characteristic of the TDs and are low accretors (Table 5.5). We have proposed that those SEDs composed of a low-mass binary star with one of its components orbiting outside the inner radius of the disk, might have its more "evolved" disk orbiting the sub-stellar companion, instead of the primary component. Although, it is also plausible that the primary component has a circumstellar disk that is being dispersed by the close sub-stellar companion. Previously, Harris et al. (2012) performed a high angular resolution millimeter-wave dust continuum imaging survey of circumstellar material associated with the individual components of multiple star systems in the Taurus−Auriga young cluster. They found that the presence of a close stellar companion (< 30 au) impacts disk properties, producing a disk mass depletion with a factor of ~ 25. In the case of the LRL 72, LRL 182, LRL 213 and LRL 135 systems, a faster dispersion of the disk by the presence of the stellar companion located at ≤ 20 au could influence the initial conditions for the formation of planets and prevent the first steps of this evolutionary process

(e.g. dust settling and grain growth).

5.6.1   Physical Sources of Typical TD SEDs

Planetary formation could potentially explain the estimated inner optically thick disk radii for these objects and therefore, the peculiar shape or decreased flux observed in the NIR/MIR SEDs of these TDs. Depending on the inner hole size, the gap could be cleared up by single or multiple planets orbiting this region (Lubow, Seibert & Artymowicz, 1999; Rice et al., 2006b; Dodson-Robinson & Salyk, 2011). In the context of planet disk interaction, and as a consequence of a massive planet clearing out the inner region of the disk, a local pressure bump is created at the inner edge of the outer disk. In the last decade, this local pressure bump was proposed to act as a filter at the outer edge of a disk gap, filtering particles of size $\gtrsim 10~\mu$m and impeding the drift inward of them (Rice et al., 2006a). As a result of this *dust filtration*, the disk profile is shown with an abrupt discontinuity in its dust radial profile and at the same time permits the presence of small particles closer to the central star ($\lesssim 10~\mu$m) (e.g Garufi et al., 2013). Thus, this optically thin dust might be responsible of the weak NIR/MIR excess present in TD SEDs. In addition, inside this cavity coupling between μm size dust grains and gas is expected (Garufi et al., 2013), while the location to pile-up the dust at a sub- to millimeter scale in a pressure maximum, leads to different locations of gap edges for gas and "bigger" dust particles (Pinilla, Benisty & Birnstiel, 2012). In our approach to estimate inner cavities, we consider the location of particles of $\sim 0.1~\mu$m that might coincide with the gaseous cavity, ingredients necessary to explain the detected accretion rates in our sample of TDs.

Most of our TDs show accretion rates ranging from 10^{-8} to 10^{-10} $M_\odot$/yr and, although these accreting TDs are also ideal targets to test the role of some photoevaporation models (e.g. Alexander, Clarke & Pringle, 2006a,b), there are other missing pieces to the puzzle such as disk mass measurements needed to obtain a complete picture of this transitional phase. Therefore, the observed SEDs of TDs with the presence of a single star might be subject to a dominating internal mechanism and the amount of mass in the disk. Thus, in order to distinguish the dominating dispersal mechanism producing the inner holes in the disks, a follow-up program of millimeter observations of the TDs is required to be able to estimate the disk mass of these objects. Nevertheless, the inner region of these TDs could be depleted by a combination of two or more mechanisms that dominate at different distances from the central star and timescales dictated by the initial physical conditions.

5.6.2   Single vs. Binary Stars: Hosting Planetary Formation

At first glance, it is tempting to suggest that single stars have a higher probability of hosting the formation of planetary systems than close binary systems. However, Pascucci et al. (2008) studied the first steps of planetary formation in single and binary systems with projected separations between ~ 10 and 450 au and they found no statistical significant difference in the degree of dust settling and grain growth of those systems, indicating that expected differences in the exoplanet properties arise in the later stages of their formation and/or migration (e.g. Kley, 2000; Kley & Nelson, 2007). Our close binary companions are

detected at angular separations between $2-10$ au; these small angular separations might affect the initial conditions for the formation of planets in the inner region of the circumbinary disks. This is mainly due to the modification of the binary eccentricity and excitation of density waves generated by the resonant interactions of the binaries with the disk, which remove primordial material (Lubow & Artymowicz, 2000). Based on these assumptions, the "weak" excess from the circumstellar material in the SEDs of the CDs, increased by the secondary flux radiation, could point out a lower probability for the formation of a planet in radii of around $a \leq 10$ au in very close binary stars. On the other hand, single stars are more probable to host forming planets at inner radii around < 10 au than close binary stars, where actually most of the planet formation might take place.

Because the time available to form any planet(s) in a circumstellar disk might vary depending on the initial conditions and the evolution of the disk, it is necessary in future surveys to characterize the distribution of disk masses in CDs with close binary and single stars, that together with the accretion rates will establish the physical parameters constraining where and when planets form in those systems. Additionally, accretion rates have been used to estimate the dissipation of the primordial disks once accretion stops; however, we did not find any trend in $\dot{M}_*$ or difference between close binary and single stars in our sample that helps us to constrain the timescales of these systems.

5.7   Summary

Using infrared NRM interferometry taken with the Keck II telescope, we have observed a sample of 24 TDs located in the Taurus-Auriga, IC-348 and Ophiuchus star-forming regions. We implemented a new method of completeness correction for our detection limits, which combines randomly sampled binary orbits and Bayesian inference. With high confidence levels of 99%, a total of 7 close binary candidates have been detected orbiting the inner radii of the TDs, and likely being the main mechanism responsible for the dispersion inside out the inner disk. Also, we found four binary companions orbiting outside the inner radii of their TDs and we have suggested that the unusual SEDs of these systems are due to a disk orbiting a substellar secondary companion, producing similar SEDs as the single and/or close binary stars surrounded by a more "evolved" disk or weak disk.

Including 11 known TDs from the literature and whose binarity was already confirmed or ruled out, we have a total of 31 TDs that are part of our Bayesian analysis (Section 5.5). Updating a uniform prior distribution, we obtained a significant fraction of 0.38 ± 0.09 objects with TD SEDs that are actually CDs. This fraction represents the unusual SEDs with a lack of excess in the NIR and/or MIR being produced by the flux emission of a close-binary companion and a disk. This fraction must be taken into consideration for future surveys and studies of these transitional objects in order to decode the disk evolution process and the timescales of close binary and single stars, separately. The remaining SEDs are being produced by a single system and a disk in a transition phase, where the main cause of dispersion could be any other in-

ternal mechanism such as photoevaporation, grain growth and/or planet disk interactions.

5.8 Distance to IC348 Region

The distance to the Perseus molecular cloud has been measured in a wide range between 220 - 380 pc (Harris, Morgan & Roman, 1954; Herbig & Jones, 1983; Cernis, 1993; Scholz et al., 1999; de Zeeuw et al., 1999; Hirota et al., 2008; Hirota, 2010), and choosing the most appropriate measurement must be taken with caution because of the influence on other observational estimations, such as age and luminosity of the targets. For our purposes, we base our decision to adopt a distance to IC348 on the astrometric observations of H_2O maser sources by Hirota (2010). They used the VERA long-baseline array to estimate a distance to SVS 13 in the NGC 1333 cluster of 235 ± 18 pc and a distance of 232 ± 18 pc to L1448. In addition, Sun et al. (2006) mapped the Perseus molecular cloud complex simultaneously in ^{13}CO(J=2-1) and ^{12}CO(J=2-1) using the KOSMA 3 m submillimeter telescope. They found a dynamical connection with a velocity gradient between NGC 1333 at $\sim$7 km s^{-1}, L 1448 at $\sim$8 km s^{-1} and IC 348 at $\sim$9 km s^{-1} within a diameter of 20 pc of extension. Considering that the Perseus molecular cloud (containing IC348, NGC1333, L1448, L1445; Hirota, 2010) has a full angular extent of only $\pm 3°$ from its centre, it is expected to have a characteristic distance range of 5%.

Here, we use the most luminous member of the cluster, IC 348 LRL 1, composed of two stars of similar brightness with spectral types B5V to adopt an independent distance to IC348 objects. IC 348 LRL 1 is a binary system with

Table 5.11: IC348 1 Properties

Property	Value
R.A. (J2000)[1]	03:44:56.15
Dec. (J2000)[1]	+32:09:15.5
Spec. Type	B5
L_* $(L_\odot)$[2]	324.8
A_J[3]	0.55
T_* (K)	15400
M_* $(M_\odot)$	4.6
Dist. (pc)	220

Reference: (1) 2MASS All-Sky Point Source Catalog, (2) Luminosity estimated following the method from Kenyon & Hartmann (1995), (3) A_J estimated as described in Section 6.4.2, (4) Spectral type and stellar temperature were adopted from Luhman et al. (2003).
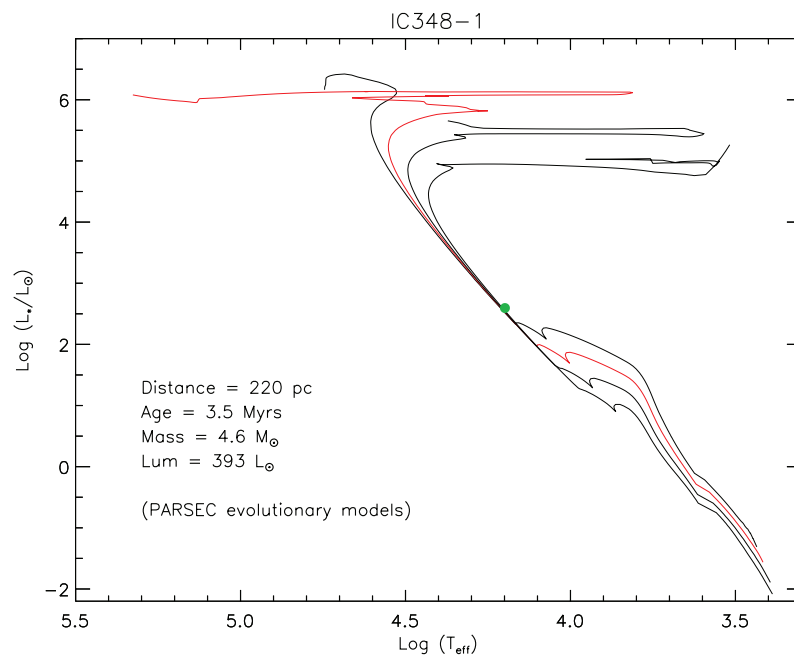
Figure 5.6: PARSEC evolutionary models for young stars (Bressan et al., 2012). Black Solid lines in descending order are 2, 3.5, 6 and 10 Myrs isochrones. Red solid line corresponds to the 3.5 Myrs isochrone used to characterised IC348−1 and then, estimate a distance to the IC348 star-forming region.

an angular separation of 0.47" and P.A. of 17.9° (Alzner, 1998) and as the only member of B spectral type in the region, it can be used to estimate a distance to it (Luhman et al., 1998). At early ages, ≤ 10 Myrs, the bolometric luminosity of these B spectral type massive stars do not vary significantly, giving an independence of the isochrone used to describe the target. This allows a spectral type conversion into effective temperature without constraints on the age of the system. Figure 5.6 presents the isochrones of 2, 3.5, 6 and 10 Myrs, as they are the most representative to describe young members of IC348. Clearly, the isochrones used to predict the stellar parameters for IC 348 LRL 1 are mostly invariant at this early stage of the stellar evolution.

We derived the stellar properties of IC 348 LRL 1 based on the spectral type and a conversion to the stellar temperature, see Table 5.11. According to the PARSEC evolutionary models (Bressan et al., 2012), a B5V object with a stellar mass of 4.2 $M_{\odot}$ should be located at a distance of 220 ± 10 pc, see Figure 5.6. Thus, a stellar luminosity of 393 $L_{\odot}$ is calculated with the dereddened J-band photometry method from Kenyon & Hartmann (1995) and A_J extinction was estimated as explained in Section 6.4.2.

Disk properties of Class II objects at the critical age of 2-3 Myr

Studying the evolution of circumstellar disks around young stellar objects is important to better comprehend how planets form. Young stellar cluster provide an opportunity to investigate disk properties of large populations that can be considered to be close to coeval (although age dispersions are not negligible). Infrared observations of young stellar clusters (Haisch Hernandez et al. 2008) show that by 2-3 Myrs, about half of the disks have already been dispersed through different processes (accretion, photoevaporation, dynamical clearing, and planet formation itself). While there is a large diversity in planetary frequencies, correlations between planets properties and the mass of the central star are emerging. In particular, giant planets are much more common around higher mass stars (1-2 $M_\odot$, Johnson et al. 2010). These correlations are likely to be the result of a correlation between disk mass and stellar mass at the epoch of giant planet formation. In the core accretion model (Pollack et al. 1996), the formation of gas giants is delayed by the formation of a massive core ($\sim 10\ M_\oplus$), which might take several Myr. As a results, the formation of giant planets might be restricted to disks that are both massive and rela-

tively long-lived. Determination of disk masses are possible through millimeter observations. Therefore, millimeter observations and the statistical analysis of young stellar clusters at an intermediate age (2-3 Myr) are a key for understanding the types of planets that might form in different types of disks, their relative number, and their dependence on stellar mass.

Statement of Contribution

This thesis is submitted as a Thesis by Compilation in accordance with
https://policies.anu.edu.au/ppl/document/ANUP_003405

I declare that the research presented in this Thesis represents original work that I carried out during my candidature at the Australian National University, except for contributions to multi-author papers incorporated in the Thesis where my contributions are specified in this Statement of Contribution.

Title and authors: ALMA SURVEY OF CLASS II DISKS IN THE IC 348 CLUSTER

Current status of paper: <u>Not Yet Submitted</u>/Submitted/Under Revision/Accepted/Published

Contribution to paper: 80, 20% advise/comments/suggestions from collaborating authors_____

Senior author or collaborating authors endorsement: _____Lucas A. Cieza_____

Dary Alexandra Ruiz-Rodriguez		10/Oct/2017
Candidate – Print Name	Signature	Date

Endorsed

David Yong		10/Oct/2017
Chair of Supervisory Panel – Print Name	Signature	Date
Gary Da Costa		10/Oct/2017
Delegated Authority – Print Name	Signature	Date
Lucas A. Cieza		10/Oct/2017
Primary Supervisor and endorsement – Print Name	Signature	Date

$\boxed{6}$

ALMA SURVEY OF CIRCUMSTELLAR DISKS IN THE YOUNG STELLAR CLUSTER IC 348

We present a 1.3 mm continuum survey of the young (2-3 Myr) stellar cluster IC 348, which lies at a distance of 270 pc, and is dominated by low-mass stars ($M_\star \sim 0.1$-0.6 $M_\odot$). We observed 136 Class II sources (disks that are optically thick in the infrared) at $0.8''$ (200 au) resolution with a 3σ sensitivity of ~ 0.45 mJy ($M_{dust} \sim 1.0$ $M_\oplus$). We detect 40 of the targets and construct a mm-continuum luminosity function. We compare the disk mass distribution in IC 348 to those of younger and older regions, taking into account the dependence on stellar mass. We find a clear evolution in disk masses from 1 to 5-10 Myr. The disk masses in IC 348 are significantly lower than those in Taurus (1-3 Myr)

and Lupus (1-3 Myr), similar to those of Chamaleon I, (2-3 Myr) and σ Ori (3-5 Myr) and significantly higher than in Upper Scorpius ($5-10$ Myr). About 20 disks in our sample ($\sim 5\%$ of the cluster members) have estimated masses (dust + gas) >1 M_{Jup} and hence might be the precursors of giant planets in the cluster. Some of the most massive disks include transition objects with inner opacity holes based on their infrared SEDs. From a stacking analysis of the 96 non-detections, we find that these disks have a typical dust mass of just $\lesssim 0.3$ $M_{\oplus}$, even though the vast majority of their infrared SEDs remain optically thick and show little signs of evolution. Such low-mass disks may be the precursors of the small rocky planets found by *Kepler* around M-type stars.

Circumstellar Disks, Dust and Gas, Interferometry.

6.1   Introduction

The evolution of protoplanetary disks has been studied for decades, and typical disk lifetimes are well established to be $\sim$2-3 Myr (Williams & Cieza, 2011). On this timescale, the dust and gas components undergo significant evolution which, together with the initial conditions, determine the outcome of the planet formation process. By an age of $\sim$5 Myr, around 90% of protoplanetary disks have already dispersed, constraining the time available for most planets to be formed (Sicilia-Aguilar et al., 2006). Determining the main process of disk dispersal is not an easy task since several physical mechanisms play a role at different time scales and radii (Alexander et al., 2014), but studying disk properties as a function of stellar mass and age can shed light on the frequency

and location of forming planets (Mordasini et al., 2012).

One important inference from exoplanet surveys is that planet occurrence generally decreases with increasing planet size: rocky planets are much more common than gas giants (Howard et al., 2012; Burke et al., 2015). Moreover, the correlation between stellar and planet properties indicates that giant planet occurrence increases with stellar mass at solar metallicity, with a percentage of 3% around M dwarfs ($\sim$0.5 $M_\odot$) increasing to 14% around A stars ($\sim$2 $M_\odot$) (Johnson et al., 2010). These exoplanet correlations are likely to be connected to disk properties as functions of stellar mass.

Dust emission of millimeter-sized grains in the disk is generally optically thin in the (sub-)millimeter regime; therefore, (sub-)millimeter continuum surveys of disks in star-forming regions with different ages ($\sim$1$-$10 Myr) can trace the distribution of disk masses as a function of age and stellar mass. This allows us to investigate how disk properties and evolution connect to the population of planets observed in the field. To exploit this observational potential, Andrews et al. (2013) performed a millimeter continuum survey with the Submillimeter Array (SMA) of the Taurus Class II members (optically thick disks) with spectral types earlier than M8.5. As a main result, they showed a correlation between the mm luminosity (L_{mm}) and the mass of the host stellar object of the form $L_{mm} \propto M_*^{1.5-2.0}$, which in turn suggests a linear relationship between the masses of the disk and that of the parent star: $M_{dust} \propto M_*$.

Various observational studies of higher sensitivity and resolution with the Atacama Large Millimeter/submillimeter Array (ALMA) add additional samples in Lupus (1 $-$ 3 Myr; Comeron, 2008; Alcalá et al., 2014; Ansdell et al., 2016),

Chamaeleon I ($2 - 3$ Myr; Luhman, 2007; Pascucci et al., 2016), σ Ori ($3 - 5$ Myr; Oliveira et al., 2002; Ansdell et al., 2016), and the Upper Scorpius OB Association ($5 - 10$ Myr; Pecaut, Mamajek & Bubar, 2012; Barenfeld et al., 2016). A Bayesian linear regression has been the standard method used to characterize the M_{dust} - M_* relations of these star-forming regions. Although, initially M_{dust} and M_* were thought to be linearly correlated in $1-3$ Myr old clusters, the main caveat of these linear relations is the simultaneous fitting of detections and upper limits, which is complicated by the fact that the latter dominate the aforementioned surveys. This adds more uncertainty to the M_{dust} - M_* relationship because the limited sensitivity implies lower detection rates for late-type stars and brown dwarfs, allowing for the possibility of a steeper relation. Indeed, Pascucci et al. (2016) reanalysed all the submillimeter fluxes and stellar properties available for Taurus, Lupus, and Upper Sco, and found steeper correlations than linear for these clusters. They also obtained a steep dust mass-stellar mass scaling relation in the ~ 2 Myr Cha I star-forming region, hence concluding that the same M_{dust} - M_* relation is shared by star-forming regions that are 1-3 Myr old (Pascucci et al., 2016). More recently, a similar steepening of the M_{dust} - M_* relation was found by Ansdell et al. (2017) for the σ Ori star-forming region. This steeper relation possibly indicates 1) undetected large pebbles or 2) an efficient inward drift in disks around the lowest-mass stars. In addition, this steepening of the M_{dust} - M_* correlation with age suggests a faster decline of circumstellar dust mass with time in late-type stars. From these relations, at an age of 10 Myrs, disks around 0.1 and 0.5 $M_\odot$ stars might have dispersed millimeter-sized grains by factors of 5 and 2.5, respectively, faster than earlier-type objects (Pascucci et al., 2016).

Following these studies, the IC 348 star-forming region, with a fraction of disks of 36% in the IR regime, is an excellent benchmark to characterize the relationship between the masses of the disk and that of the host star by comparing to other star-forming regions. In fact, the first millimeter observations of protoplanetary disks in IC348 star-forming region were made by Lee, Williams & Cieza (2011), and with a detection rate of only $\sim 12\%$, they concluded that most of the solids in the IR-detected disks have aggregated beyond millimeter sizes, resulting in low luminosities at millimeter wavelengths.

In this work, we present a 1.3 mm/230 GHz study of $\sim$136 Class II objects in the IC 348 star-forming region. This paper is organised as follows: Section 6.2 describes the target selection. Section 6.3 summarizes the ALMA observations and data reduction. In Section 6.4, we estimate the stellar properties of our sample, and present our ALMA results, which are compared to previous findings in other regions in Section 6.5. The main conclusions are discussed in Section 6.6.

6.2   TARGET SELECTION AND PROPERTIES

IC 348 is a rich and compact (2×2 pc) young stellar cluster in the Perseus molecular cloud, whose $\sim$480 members have been identified initially by Hα emission (Herbig, 1954) and subsequently by optical and IR photometry and spectroscopy (Lada & Lada, 1995; Herbig, 1998; Luhman et al., 1998; Luhman, 1999; Luhman et al., 2003; Luhman, 2003, 1999; Luhman, McLeod & Goldenson, 2005; Luhman, Esplin & Loutrel, 2016). Most of the known T Tauri stars in the IC348 star-forming region have been well studied and spectrally
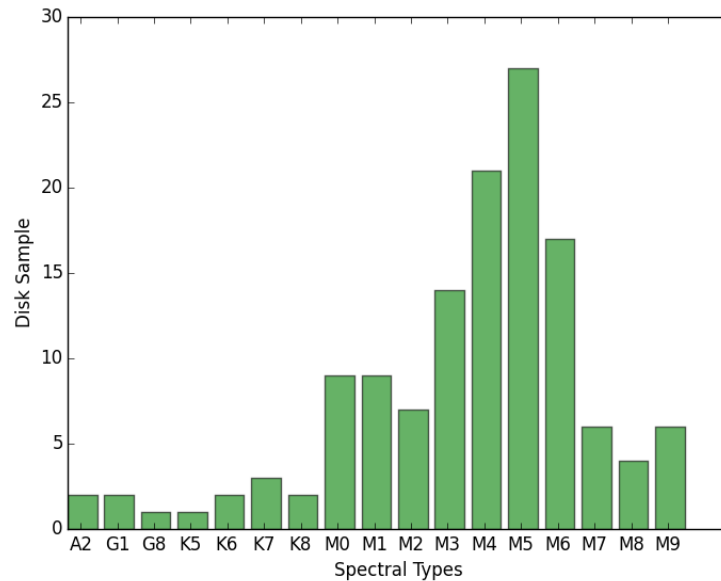
Figure 6.1: Distribution of stellar spectral types for our sample in the IC 348 star-forming region. These targets were selected from Muench et al. (2007) and Lada et al. (2006) and are listed in Table 6.1

classified (Luhman et al., 2003; Muench et al., 2007): see Figure 6.1.

Our sample was selected specifically from the work of Lada et al. (2006), whose sample was based on Luhman et al. (2003), and from Muench et al. (2007). These programs used *Spitzer*-IRAC photometry to investigate both the frequency and nature of the circumstellar disk population in the IC348 cluster on the basis of the IR SED slope between 3.6 and 8.0 μm, $\alpha_{3.6-8.0\mu m}$. In general, Lada et al. (2006) and Muench et al. (2007) used $\alpha_{3.6-8.0\mu m}$ to classify the objects as follows:

1. Class I (protostars): $\alpha_{3.6-8.0\mu m} > -0.5$;

2. Class II (thick-disks): $-0.5 > \alpha_{3.6-8.0\mu m} > -1.8$;

3. Class II/III (anemic disks): $-1.8 > \alpha_{3.6-8.0\mu m} > -2.56$;

4. Class III (disk-less stars): $\alpha_{3.6-8.0\mu m} < -2.56$.

We selected *Spitzer* sources with $\alpha_{3.6-8.0\mu m}$ values between -1.8 and -0.5, which corresponds to Class II T Tauri stars with optically thick disks. From Lada et al. (2006), we selected 91 objects classified as optically "THICK" disks (hereafter Class II sources to keep the nomenclature consistent), and from Muench et al. (2007), we selected 42 objects classified as Class II objects. We also included Cl* IC 348 LRL 31, Cl* IC 348 LRL 67 and Cl* IC 348 LRL 329, which are Class III sources based on their $\alpha_{3.6-8.0\mu m}$ values, but their 24 μm fluxes indicate that they are transitional objects with optically thick outer disks (Lada et al., 2006; Espaillat et al., 2012). We note that the standard YSO Class system (Greene et al., 1994) is based on the SED slope between $\sim$2 and $\sim$20 μm, but most IC 348 members lack *Spitzer* 24 μm detections. With these caveats, our final target list (Table 6.1) is composed of 136 Class II disk objects with stellar spectral types in the range of G1$-$M9. Figure 6.2 shows the positions of our targets. Among the objects selected, Cl* IC 348 LRL 237, V* V716 Per, Cl* IC 348 LRL 135 and Cl* IC 348 LRL 97 are classified by Espaillat et al. (2012) as transitional disks. Our sample also includes Cl* IC 348 LRL 31 and Cl* IC 348 LRL 135, which have known close stellar companions at separations of 38.1$\pm$ 5.3 mas and 82.1$\pm$ 0.3 mas, respectively (Ruíz-Rodríguez et al., 2016b).

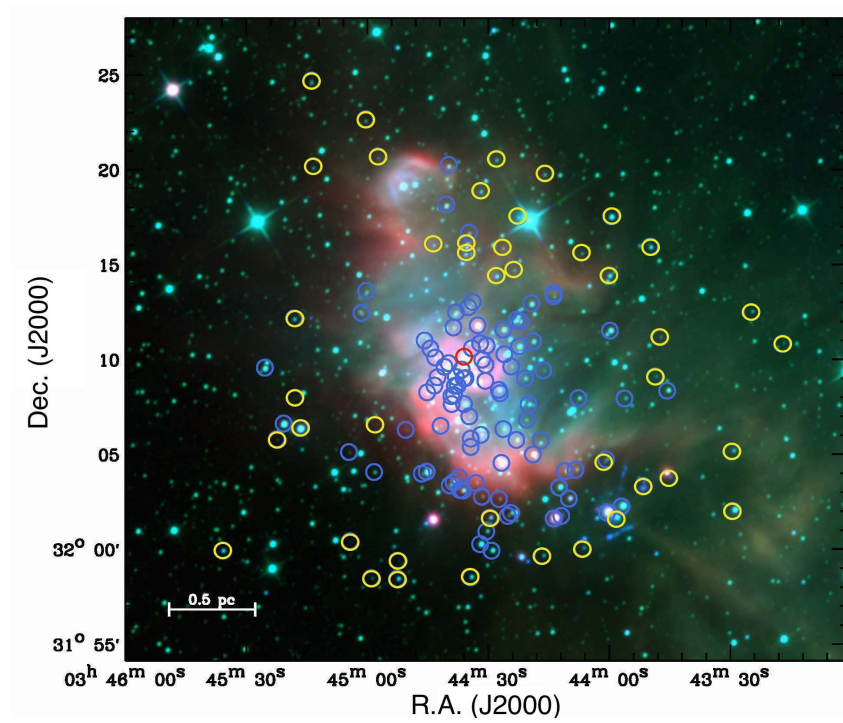Figure 6.2: IR map of IC 348 star-forming region with our ALMA targets. ALLWISE 3-color image with RGB mapped to 22 (W4), 4.6 (W2), and 3.4 (W1) μm. Yellow and blue circles correspond to the sampled selected from Muench et al. (2007) and Lada et al. (2006), respectively. At the center of the map, a red circle indicates the position of the A2 type star IC 348 12, which has been observed by Gaia.

6.3   ALMA Observations and Data Reduction

ALMA observations toward our IC 348 targets were carried out in Band 6 (211-275 GHz) under the project code: 2015.1.01037.S. Our science goal was executed in Cycle 3 with the C40-4 array configuration and was observed between the 23rd and 27th June, 2015. The Band 6 continuum observations were conducted with a total on-source integration time of $\sim$1 min per target over 3 execution blocks, each one targeting all 136 objects for 0.3 min. The adopted setup included two spectral windows for continuum observations with effective bandwidths of 1.875 GHz centered at 218.0 and 233.0 GHz, for a mean frequency of 225.676 GHz ($\sim$1.3 mm). The typical (1σ) noise level reached is $\sim$0.15 mJy/beam. We also targeted the molecular lines ^{12}CO, ^{13}CO, and C^{18}O (J = 2$-$1), centered on 230.535, 220.395, 219.557 GHz, respectively. Each line was observed with a resolution of 242 kHz (0.3 km s^{-1}) and a bandwidth of 117.2 MHz. The ALMA data were reduced using the Common Astronomy Software Application (CASA) package, version 4.5.3 (McMullin et al., 2007). Initial calibration (i.e. water vapor radiometer corrections, phase and amplitude calibrations) was performed by the ALMA science operations team during quality assurance. The flux calibrator was J0237+2848. J0238+1636 and J0336+3218 were chosen as bandpass calibrators and J0510+1800 as a phase calibrator. To reach the requested synthesized beam size of $\sim$0.8 arcsec, we applied the CLEAN algorithm to the calibrated visibilities and extract the continuum images by applying a Briggs weighting with a robust parameter of +2, which is close to a natural weighting. Using the *uvcontsub* routine, we subtracted the continuum emission from the spectral windows to extract the ^{12}CO, ^{13}CO, and C^{18}O spectral line data from the calibrated visibilities.

6.4 Results

6.4.1 Detection Criteria

We searched for 1.3 mm continuum emission centered on the 2MASS positions of the 136 targets, listed in Table 6.1. From the continuum images, we determined the peak flux and rms using the task *imstat* and thus, estimated the signal to noise (S/N, ratio between peak and rms) for each image. Peak fluxes were derived from a $4''$ radius circle, and the rms from a 4-$7''$ radius annulus centered on the expected source position. A source with S/N < 4 is considered a non-detection. For these sources, we measured the flux densities by using the *uvmodefit* routine in CASA and by fitting a point source in the *uv* plane. If the flux density is less than 4σ, the point source fit is applied to the visibilities with the pointing center as a free parameter. If the flux density is less than 3σ it is fit with a point source with the offset position fixed. Table 6.2 lists integrated flux density ($F_{1.3\,mm}$) and rms for non-detected sources.

For detections (S/N > 4), flux densities were measured by applying an elliptical Gaussian model to the visibility data using *uvmodelfit* in CASA. This model is centered at the nominal source position and provides the parameters $F_{1.3\,mm}$, the FWHM along the major axis, aspect ratio, position angle of the major axis (P.A.), and coordinate offsets ($\Delta\alpha$, and $\Delta\delta$). These parameters are listed in Table 6.3. A disadvantage of fitting the brightness profile of a source in the UV-plane directly is the possibility of including emission from a second source in the fitting process. To avoid any contamination in the measured flux of each field, we visually inspected the image plane for pixels with significant brightness

($>4\sigma$). Applying these methods, we detect 40 out of the 136 IC 348 targets at $> 4\ \sigma$ significance. Images of the 40 sources are displayed in Figure 6.3. We find that 10 of the targets are partially resolved. For these objects, the source sizes (deconvolved from the beam) are listed in Table 6.3.

Using standard approaches (e.g. Hildebrand, 1983), the millimeter flux can be translated into a disk mass according

$$M_{dust} = \frac{F_\nu d^2}{\kappa_\nu B_\nu (T_{dust})},\qquad(6.1)$$

where F_ν is the integrated flux, d is the distance to the target, $B_\nu(T_{dust})$ is the Planck function at the average disk temperature, and κ_ν is the total opacity. Thus, adopting a distance of 270 pc (Section 6.4.2) and making standard assumptions concerning the disc temperature ($T_{dust} = 20$K) and dust opacity ($\kappa_\nu = 2.3$ cm^{2}g^{-1} at 1.33 mm; Andrews & Williams (2005, and references therein)), we estimate disk masses for all detected targets and report them in Table 6.3. Similarly, the 3σ upper limits of $\sim$0.45 mJy for most of our targets correspond to a dust mass of $M_{Dust} \sim 1.0$ M$_\oplus$.

Table 6.1: Targeted Class II Objects in IC 348.

Source ID	Target	R.A.	Dec.	Spec. type	Ref.
1	IC 348 12	03 44 35.33945	+32 10 04.8843	A2	1
2	V* V909 Per	03 44 26.027	+32 04 30.41	G8	1
3	Cl* IC 348 LRL 13	03 43 59.649	+32 01 53.98	M0.5	1
4	V* V926 Per	03 44 44.721	+32 04 02.48	M0.5	1
5	Cl* IC 348 LRL 19	03 44 30.82	+32 09 55.8	A2	1
6	Cl* IC 348 LRL 26	03 43 56.028	+32 02 13.21	K7	1
7	V* V920 Per	03 44 37.881	+32 08 04.18	K7	1
8	V* V715 Per	03 44 38.457	+32 07 35.70	K6	1
9	V* V712 Per	03 44 37.980	+32 03 29.66	K6	1
10	V* V910 Per	03 44 29.726	+32 10 39.84	K8	1
11	V* V697 Per	03 44 21.614	+32 10 37.68	K7	1
12	Cl* IC 348 LRL 46	03 44 11.623	+32 03 13.18	XXX	1
13	IRAS 03410+3152	03 44 12.980	+32 01 35.50	XX	1
14	Cl* IC 348 LRL 55	03 44 31.373	+32 00 14.05	M0.5	1
15	V* V716 Per/58*	03 44 38.541	+32 08 00.65	M1.25	1, 3
16	V* V698 Per	03 44 22.288	+32 05 42.79	K8	1
17	Cl* IC 348 LRL 63	03 43 58.905	+32 11 27.07	M1.75	1
18	Cl* IC 348 LRL 68	03 44 28.513	+31 59 54.00	M3.5	1
19	V* V719 Per	03 44 43.768	+32 10 30.41	M1.25	1
20	Cl* IC 348 LRL 76	03 44 39.797	+32 18 04.19	M3.75	1
21	V* V710 Per	03 44 37.411	+32 09 00.91	M1	1
22	V* V922 Per	03 44 39.196	+32 09 44.90	M2	1
23	Cl* IC 348 LRL 97*	03 44 25.549	+32 06 17.13	M2.25	1,3
24	V* V695 Per	03 44 19.238	+32 07 34.74	M3.75	1
25	V* V905 Per	03 44 22.321	+32 12 00.70	M1	1
26	V* V925 Per	03 44 44.585	+32 08 12.54	M2	1
27	V* V919 Per	03 44 37.391	+32 12 24.20	M2	1
28	Cl* IC 348 LRL 128	03 44 20.178	+32 08 56.59	M2	1
29	Cl* IC 348 LRL 129	03 44 21.295	+32 11 56.34	M2	1
30	Cl* IC 348 LRL 135*	03 44 39.184	+32 20 08.93	M4.5	1,3
31	V* V907 Per	03 44 25.303	+32 10 12.80	M4.75	1
32	Cl* IC 348 LRL 140	03 44 35.685	+32 03 03.54	M3.25	1
33	Cl* IC 348 LRL 149	03 44 36.98	+32 08 34.2	M4.75	1
34	Cl* IC 348 LRL 153	03 44 42.761	+32 08 33.77	M4.75	1
35	Cl* IC 348 LRL 156	03 44 06.783	+32 07 54.09	M4.25	1
36	V* V902 Per	03 44 18.579	+32 12 53.08	M2.75	1
37	Cl* IC 348 LRL 165	03 44 35.457	+32 08 56.35	M5.25	1
38	Cl* IC 348 LRL 166A	03 44 42.581	+32 10 02.50	M4.25	1
39	Cl* IC 348 LRL 168	03 44 31.348	+32 10 46.98	M4.25	1
40	Cl* IC 348 LRL 173	03 44 10.126	+32 04 04.50	M5.75	1
41	Cl* IC 348 LRL 192	03 44 23.648	+32 01 52.69	M4.5	1
42	V* V713 Per	03 44 38.006	+32 11 37.03	M4	1

Table 6.1 – Continued

Source	Target	R.A.	Dec.	Spect. type	Ref.
43	Cl* IC 348 LRL 202	03 44 34.282	+32 12 40.73	M3.5	1
44	Cl* IC 348 LRL 203	03 44 18.102	+32 10 53.44	M0.75	1
45	Cl* IC 348 LRL 205	03 44 29.804	+32 00 54.58	M6	1
46	Cl* IC 348 LRL 214	03 44 07.506	+32 04 08.81	M4.75	1
47	Cl* IC 348 LRL 221	03 44 40.241	+32 09 33.13	M4.5	1
48	SSTc2d J034431.2+320559	03 44 31.19	+32 05 58.9	M0.5	1
49	Cl* IC 348 LRL 229*	03 44 57.856	+32 04 01.60	M5.25	1, 3
50	Cl* IC 348 LRL 237	03 44 23.569	+32 09 33.88	M5	1
51	Cl* IC 348 LRL 241	03 44 59.83	+32 13 31.9	M4.5	1
52	Cl* IC 348 LRL 248	03 44 35.951	+32 09 24.31	M5.25	1
53	Cl* IC 348 LRL 256	03 43 55.265	+32 07 53.31	M5.75	1
54	Cl* IC 348 LRL 272	03 44 34.129	+32 16 35.77	M4.25	1
55	Cl* IC 348 LRL 276	03 44 09.208	+32 02 37.68	M0	1
56	Cl* IC 348 H 149	03 44 34.051	+32 06 57.05	M7.25	1
57	Cl* IC 348 LRL 292	03 43 59.873	+32 04 41.44	M5.75	1
58	Cl* IC 348 LRL 297	03 44 33.210	+32 12 57.46	M4.5	1
59	Cl* IC 348 LRL 300	03 44 38.968	+32 03 19.69	M5	1
60	Cl* IC 348 LRL 319	03 45 01.001	+32 12 22.21	M5.5	1
61	Cl* IC 348 LRL 324	03 44 45.221	+32 10 55.75	M5.75	1
62	Cl* IC 348 LRL 325	03 44 30.06	+32 08 48.9	M6	1
63	Cl* IC 348 LRL 334	03 44 26.664	+32 02 36.32	M5.75	1
64	Cl* IC 348 LRL 336	03 44 32.374	+32 03 27.48	M5.5	1
65	Cl* IC 348 LRL 341	03 44 12.977	+32 13 15.61	M5.25	1
66	Cl* IC 348 LRL 366	03 44 35.017	+32 08 57.34	M4.75	1
67	Cl* IC 348 LRL 382	03 44 30.956	+32 02 44.18	M5.5	1
68	Cl* IC 348 LRL 407	03 45 04.141	+32 05 04.38	M7	1
69	Cl* IC 348 LRL 415	03 44 29.970	+32 09 39.45	M6.5	1
70	2MASS J03444593+3203567	03 44 45.935	+32 03 56.78	M5.75	1
71	Cl* IC 348 LRL 462	03 44 24.457	+32 01 43.71	M3	1
72	Cl* IC 348 LRL 468	03 44 11.070	+32 01 43.60	M8.25	1
73	Cl* IC 348 LRL 555	03 44 41.215	+32 06 27.14	M5.75	1
74	Cl* IC 348 LRL 603	03 44 33.42	+32 10 31.5	M8.5	1
75	[PSZ2003] J034437.6+320832	03 44 37.644	+32 08 32.90	M5.5	1
76	[PSZ2003] J034426.4+320809	03 44 26.367	+32 08 09.94	M9	1
77	Cl* IC 348 LRL 690	03 44 36.38	+32 03 05.4	M8.75	1
78	Cl* IC 348 LRL 703	03 44 36.62	+32 03 44.2	M8	1
79	[PSZ2003] J034433.7+320521	03 44 33.699	+32 05 20.67	M6	1
80	[PSZ2003] J034433.7+320547	03 44 33.691	+32 05 46.71	M8.75	1
81	Cl* IC 348 LRL 746	03 44 49.962	+32 06 14.61	M5	1
82	[PSZ2003] J034419.7+320645	03 44 19.666	+32 06 45.93	M7	1
83	Cl* IC 348 LRL 2096	03 44 12.937	+32 13 24.06	M6	1
84	[PSZ2003] J034416.2+320540	03 44 16.176	+32 05 40.96	M9	1
85	Cl* IC 348 TJ 72	03 44 31.982	+32 11 43.95	G0	1
86	[BNM2013] 32.03 53	03 44 42.009	+32 08 59.98	M4.25	1

Table 6.1 – Continued

Source	Target	R.A.	Dec.	Spect. type	Ref.
87	Cl* IC 348 LRL 8078	03 44 26.682	+32 08 20.35	M0.5	1
88	Cl* IC 348 LRL 9024	03 44 35.371	+32 07 36.24	M0	1
89	Cl* IC 348 H 110	03 44 25.576	+32 11 30.24	M2	1
90	2MASS J03452514+3209301	03 45 25.145	+32 09 30.18	M3.75	1
91	2MASS J03452046+3206344	03 45 20.463	+32 06 34.48	M1	1
92	Cl* IC 348 LRL 31*	03 44 18.167	+32 04 57.04	G1	1
93	Cl* IC 348 LRL 329*	03 44 15.581	+32 09 21.83	M7.5	1
94	Cl* IC 348 LRL 67*	03 43 44.614	+32 08 17.76	M0.75	1
95	2MASS J03435856+3217275	03 43 58.569	+32 17 27.53	M3.5(IR)	2
96	Cl* IC 348 LRL 117	03 43 59.080	+32 14 21.31	M3.5(IR)	2
97	2MASS J03442724+3214209	03 44 27.249	+32 14 20.98	M3.5(IR)	2
98	2MASS J03434881+3215515	03 43 48.810	+32 15 51.55	M4.5(IR)	2
99	Cl* IC 348 LRL 179	03 44 34.986	+32 15 31.15	M3.5(IR)	2
100	Cl* IC 348 LRL 199	03 43 57.22	+32 01 33.9	M6.75(IR)	2
101	Cl* IC 348 LRL 215	03 44 28.947	+32 01 37.85	M3.25(IR)	2
102	2MASS J03443112+3218484	03 44 31.126	+32 18 48.49	M3.25(IR)	2
103	2MASS J03443468+3216000*	03 44 34.687	+32 16 00.09	M3.5(IR)	2, 3
104	2MASS J03441522+3219421	03 44 15.224	+32 19 42.18	M4.75(IR)	2
105	2MASS J03442294+3214404	03 44 22.943	+32 14 40.43	M5.5(IR)	2
106	2MASS J03440599+3215321	03 44 05.993	+32 15 32.15	M6.5(IR)	2
107	Cl* IC 348 LRL 364	03 44 43.013	+32 15 59.67	M4.75(IR)	2
108	Cl* IC 348 LRL 368	03 44 25.702	+32 15 49.27	M5.5(IR)	2
109	Cl* IC 348 LRL 406	03 43 46.444	+32 11 05.94	M5.75(IR)	2
110	2MASS J03445853+3158270	03 44 58.535	+31 58 27.03	M6.5(IR)	2
111	2MASS J03432845+3205058	03 43 28.454	+32 05 05.82	M4(IR)	2
112	Cl* IC 348 LRL 753	03 44 57.617	+32 06 31.25	XXX	2
113	2MASS J03445688+3220355	03 44 56.883	+32 20 35.52	M6(IR)	2
114	Cl* IC 348 LRL 1379	03 44 52.00	+31 59 21.5	M9.75	2
115	2MASS J03445205+3158252	03 44 52.059	+31 58 25.21	M3.5(IR)	2
116	Cl* IC 348 LRL 1683	03 44 15.834	+31 59 36.77	M5.25(IR)	2
117	Cl* IC 348 LRL 1707	03 43 47.635	+32 09 02.56	M7(IR)	2
118	2MASS J03451307+3220053	03 45 13.071	+32 20 05.32	M5(IR)	2
119	2MASS J03442721+3220288	03 44 27.214	+32 20 28.82	M5(IR)	2
120	2MASS J03435056+3203180	03 43 50.565	+32 03 18.00	M8.75(IR)	2
121	Cl* IC 348 LRL 1881	03 44 33.792	+31 58 30.28	M3.75(IR)	2
122	2MASS J03432355+3212258	03 43 23.557	+32 12 25.82	M4.5(op)	2
123	V* V338 Per	03 43 28.201	+32 01 59.12	M1.75(IR)	2
124	Cl* IC 348 LRL 1923	03 44 00.471	+32 04 32.71	M5(IR)	2
125	Cl* IC 348 LRL 1925	03 44 05.766	+32 00 01.10	M5.5(IR)	2
126	EM* LkHA 99	03 45 16.349	+32 06 19.95	K5(op)	2
127	2MASS J03445997+3222328	03 44 59.979	+32 22 32.83	M5.25	2
128	2MASS J03451782+3212058	03 45 17.826	+32 12 05.85	M3.75(op)	2
129	2MASS J03431581+3210455	03 43 15.812	+32 10 45.53	M4.5(IR)	2
130	2MASS J03453563+3159544	03 45 35.637	+31 59 54.44	M4.5(IR)	2

Table 6.1 – Continued

Source	Target	R.A.	Dec.	Spect. type	Ref.
131	2MASS J03452212+3205450	03 45 22.128	+32 05 45.01	M8(IR)	2
132	2MASS J03442186+3217273	03 44 21.864	+32 17 27.31	M4.75(op)	2
133	Cl* IC 348 LRL 22865	03 45 17.647	+32 07 55.33	L0	2
134	Cl* IC 348 LRL 40182	03 45 03.83	+32 00 23.3	XXX	2
135	Cl* IC 348 LRL 54299	03 43 44.27	+32 03 42.6	XXX	2
136	2MASS J03451349+3224347	03 45 13.498	+32 24 34.71	M4.25	2

Ref.: (1) Lada et al. (2006), (2) Muench et al. (2007), (3) Espaillat et al. (2012).

∗ Transitional Disk

6.4.2   Target Properties

Most of our ALMA targets have fundamental stellar parameters such as extinction, stellar masses, luminosity, effective temperature, etc, reported in previous studies. However, not all values have been obtained in homogeneous manner, and uncertainties might be larger due to systematic differences in methodology or the adopted distance to IC 348. Considering that the first data releases of the Gaia space mission and Pan-STARRS-1 (PS1) are available, we seek for uniformity in these estimations. We adopt a distance of 270±65 pc based on the preliminary Gaia parallax measurement of 3.70 ± 0.93 mas for IC 348 12 (Michalik, Lindegren & Hobbs, 2015), the A2 type star at the center of the cluster (Figure 6.2). To estimate the visual extinction (A_v), we use the extinction relations $\frac{A_{\lambda_{eff}}}{A_v}$ listed in Table 6.4, which are calculated using the extinction law presented in Cardelli, Clayton & Mathis (1989). We use PS1 colours r−z and z−y (Magnier et al., 2013), in order of preference, and adopt the relations
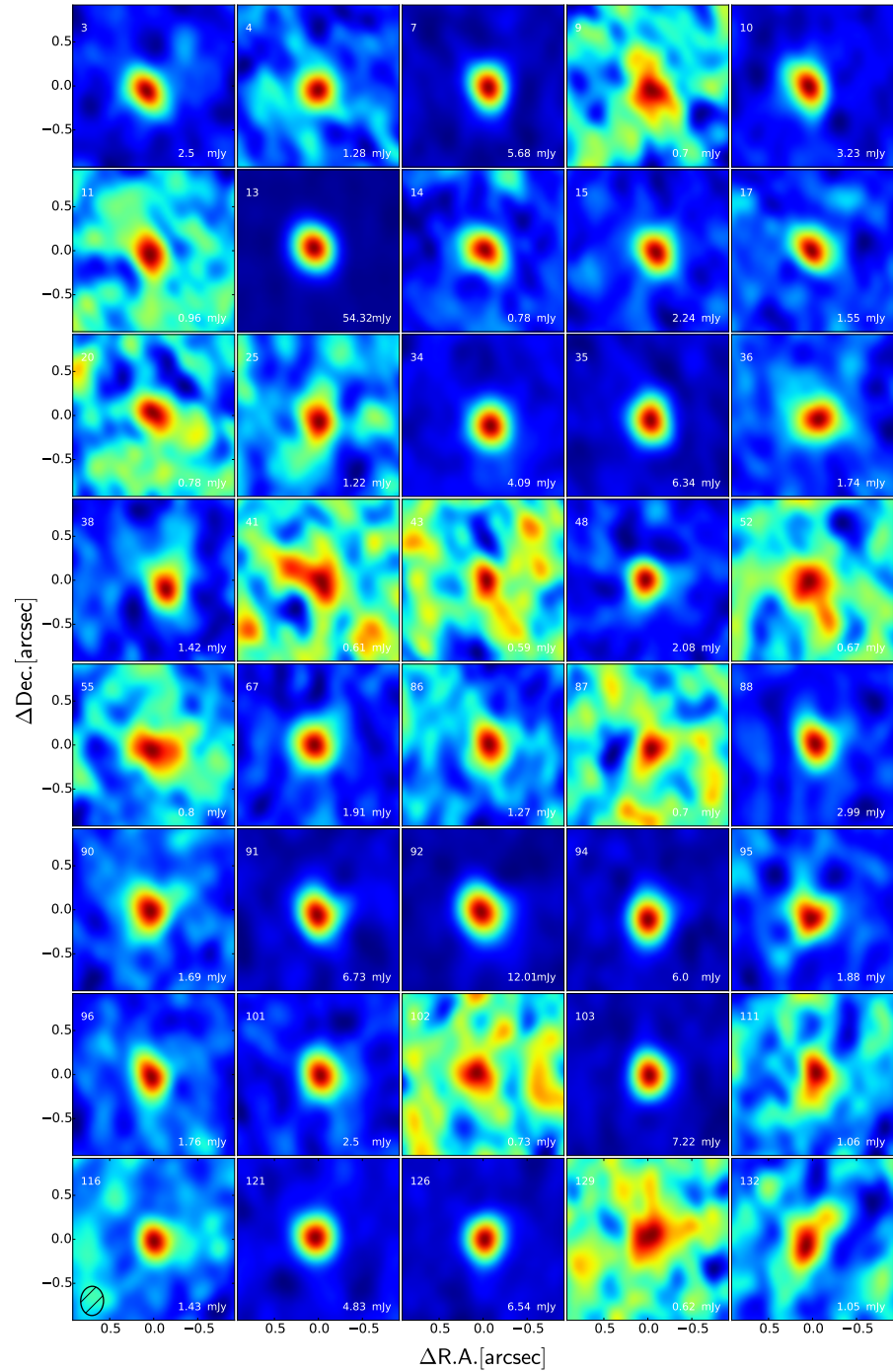
Figure 6.3: 1.3 mm continuum images meeting our detection criteria ($>4\sigma$) in the IC 348 region, see Section 6.4.1. Each image covers 1.7" X 1.7" size with an average beam size of $0.8''$ X $0.7''$. Integrated flux density values are presented at the low-right corner as reported in Table 6.3.
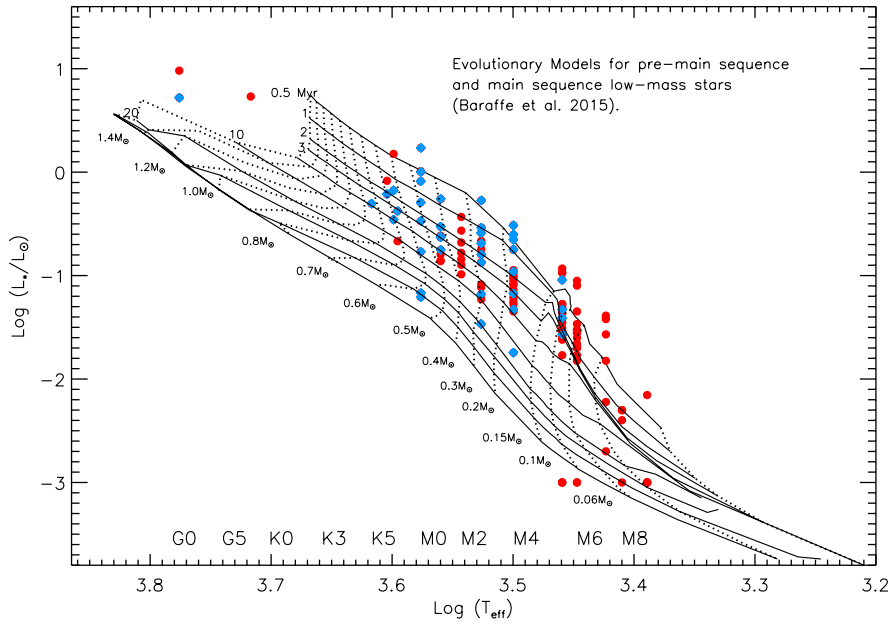
Figure 6.4: Inferred stellar parameters for IC 348 members (Table 6.5; Sec. 6.4.2) with theoretical models from Baraffe et al. (2015) for low mass young stars overlaid. Solid lines in descending order are 0.5, 1, 2, 3, 5, 10, 20, 50 and 100 Myrs isochrones and dashed lines represent the evolutionary tracks in the range of 0.06 and 1.4 $M_\odot$. Blue diamonds represent IC 348 detected members, while red circles correspond to non-detections.

$A_z = 1.4[(r - z) - (r - z)_0]$ and $A_y = 6.3[(z - y) - (z - y)_0]$, where $(r - z)_0$ and $(z - y)_0$ are the expected PS1 colours of a main-sequence star generated from MARCS synthetic fluxes (Gustafsson et al., 2008). In the special case of Class II objects lacking PS1 photometry in the necessary bands, we adopted A_v from Currie & Kenyon (2009).

The stellar luminosities ($L_\star$) of IC 348 members are calculated via the dereddened J-band photometry method of Kenyon & Hartmann (1995) and adopting the distance of 270 pc. We derived the stellar properties based on the spectral types taken from Luhman et al. (2003) and Muench et al. (2007) and a conversion from spectral type to the effective temperature (T_{eff}) taken from Pecaut & Mamajek (2013) with uncertainties of $\pm$ 1 spectral subclass (Table 6.5). Using T_{eff} and $L_\star$, and assuming all targets are single star systems, we estimated the stellar masses ($M_\star$) and ages from comparisons with theoretical pre-MS evolutionary tracks. Masses and ages of targets with stellar masses between 0.01 and 1.4 $M_\odot$ were derived from models presented in Baraffe et al. (2015) and stellar masses $>$1.4 $M_\odot$ from the PARSEC evolutionary models (Bressan et al., 2012). Age uncertainties are based mainly on the H-R diagram placement and the determination of $L_\star$, incorporating the estimated observational photometry, J-band bolometric correction and extinction uncertainties. Nevertheless, the dominant sources of error on the $L_\star$ uncertainties are the $\sim$ 20% distance and extinction uncertainties (Cieza et al., 2007). Stellar mass uncertainties are dominated by the $\pm$ 1 spectral subclass and determined by their spectral type. For these T Tauri stars, whose metallicity values are unknown, we adopted solar composition, and we held the surface gravity fixed at the value log g = 4.0, typical for PMS stars. Table 6.5 lists the resulting adopted T_{eff}, estimated

stellar age, A_v, $L_\star$ and estimated stellar mass of these objects. Figure 6.4 shows Baraffe evolutionary models with our IC 348 target selection. The stars are clustered around the 2 to 3 Myr isochrones, in agreement with previous age estimates for the region.

Table 6.2: Non-Detected Class II Sources in IC 348

Source	$F_{1.3\,mm}$ [mJy]	rms [mJy beam^{-1}]	Source	$F_{1.3\,mm}$ [mJy]	rms [mJy beam^{-1}]
1	0.19 ± 0.13	0.14	71	0.35 ± 0.13	0.13
2	0.51 ± 0.13	0.13	72	0.06 ± 0.13	0.13
5	0.31 ± 0.15	0.13	73	0.4 ± 0.14	0.13
6	0.52 ± 0.15	0.13	74	0.04 ± 0.13	0.14
8	0 ± 0.14	0.14	75	0.3 ± 0.14	0.13
12	-0.07 ± 0.14	0.14	76	-0.02 ± 0.14	0.14
16	-0.05 ± 0.14	0.14	77	-0.19 ± 0.15	0.14
18	0.17 ± 0.13	0.12	78	0.08 ± 0.14	0.13
19	0.06 ± 0.15	0.13	79	0.36 ± 0.13	0.14
21	0.04 ± 0.14	0.14	80	0.27 ± 0.13	0.14
22	0.12 ± 0.13	0.13	81	0.08 ± 0.13	0.14
23	-0.09 ± 0.14	0.14	82	-0.11 ± 0.13	0.13
24	0.13 ± 0.12	0.13	83	0.2 ± 0.14	0.13
26	0.41 ± 0.14	0.14	84	0.09 ± 0.13	0.13
27	-0.42 ± 0.13	0.14	85	0.26 ± 0.13	0.15
28	-0.15 ± 0.13	0.14	89	0.49 ± 0.14	0.14
29	0.15 ± 0.15	0.14	93	0.26 ± 0.13	0.14
30	0.26 ± 0.15	0.14	97	0.32 ± 0.14	0.12
31	0.03 ± 0.13	0.14	98	0.16 ± 0.13	0.13
32	0.36 ± 0.14	0.13	99	0.25 ± 0.14	0.14
33	0.16 ± 0.15	0.13	100	0.41 ± 0.15	0.13
37	0.02 ± 0.12	0.14	104	0.16 ± 0.13	0.13
39	0.37 ± 0.15	0.13	105	0.21 ± 0.13	0.14
40	0.31 ± 0.14	0.14	106	0.24 ± 0.12	0.13
42	0.16 ± 0.13	0.14	107	0.38 ± 0.14	0.13
44	0.19 ± 0.13	0.14	108	0.36 ± 0.14	0.13
45	0.35 ± 0.14	0.14	109	-0.31 ± 0.13	0.12
46	0.24 ± 0.13	0.14	110	0.14 ± 0.14	0.14
47	-0.13 ± 0.13	0.14	112	-0.38 ± 0.14	0.13
49	-0.13 ± 0.13	0.14	113	0.21 ± 0.14	0.13
50	0.2 ± 0.13	0.13	114	0.05 ± 0.13	0.12
51	0.05 ± 0.13	0.13	115	0.03 ± 0.13	0.13
53	0.09 ± 0.13	0.13	117	0.25 ± 0.14	0.13
54	0.5 ± 0.13	0.13	118	0.28 ± 0.14	0.15
56	0.04 ± 0.14	0.14	119	0.35 ± 0.13	0.14
57	0.33 ± 0.14	0.13	120	-0.44 ± 0.17	0.19
58	0.15 ± 0.12	0.13	122	0.02 ± 0.12	0.13
59	-0.28 ± 0.13	0.14	123	0.21 ± 0.13	0.14
60	0.2 ± 0.17	0.16	124	0.36 ± 0.13	0.14
61	-0.18 ± 0.13	0.14	125	0.15 ± 0.14	0.13
62	0.24 ± 0.12	0.13	127	-0.06 ± 0.15	0.14
63	0.17 ± 0.14	0.12	128	-0.04 ± 0.13	0.14
64	0.14 ± 0.13	0.14	130	0.32 ± 0.13	0.13
65	0.02 ± 0.14	0.14	131	-0.08 ± 0.14	0.14
66	-0.18 ± 0.13	0.14	133	0.05 ± 0.13	0.13
68	0.45 ± 0.15	0.13	134	-0.06 ± 0.12	0.15
69	0.37 ± 0.13	0.14	135	0.07 ± 0.13	0.13
70	0.15 ± 0.14	0.14	136	0.18 ± 0.14	0.14

Table 6.3: Continuum Detections of Class II Sources in IC 348

[1ex]	Source	$F_{1.3\,mm}$*	rms	$\Delta\alpha$	$\Delta\delta$	a	i	P.A.	M_{Dust}
		[mJy]	[mJy beam^{-1}]	['']	['']	['']	[deg.]	[deg.]	[$M_\oplus$]
	3	2.5 ± 0.24	0.14	0.19	-0.16	0		0	5.3 ± 0.3
	4	1.28 ± 0.15	0.13	0.06	-0.13	0		0	2.71 ± 0.28
	7	5.68 ± 0.45	0.13	-0.09	-0.08	0		0	12.05 ± 0.28
	9	0.7 ± 0.14	0.13	-0.02	-0.1	0		0	1.48 ± 0.28
	10	3.23 ± 0.29	0.14	0.12	-0.06	0		0	6.85 ± 0.3
	11	0.96 ± 0.14	0.13	0.11	-0.12	0		0	2.04 ± 0.28
	13	54.32 ± 4.41	0.27	0.14	0.03	0.19	0	0	115.2 ± 0.57
	14	0.78 ± 0.22	0.13	-0.02	-0.14	0		0	1.65 ± 0.28
	15	2.24 ± 0.22	0.14	-0.13	-0.08	0		0	4.75 ± 0.3
	17	1.55 ± 0.17	0.14	0.07	-0.04	0		0	3.29 ± 0.3
	20	0.78 ± 0.15	0.13	-0.34	-0.4	0		0	1.65 ± 0.28
	25	1.22 ± 0.17	0.13	0.01	-0.2	0		0	2.59 ± 0.28
	34	4.09 ± 0.36	0.13	-0.14	-0.28	0.157	0	0	8.67 ± 0.28
	35	6.34 ± 0.54	0.13	-0.01	-0.15	0.331	47.5 1	73.7	13.45 ± 0.28
	36	1.74 ± 0.2	0.14	-0.09	-0.08	0		0	3.69 ± 0.3
	38	1.42 ± 0.17	0.13	-0.23	-0.25	0		0	3.01 ± 0.28
	41	0.61 ± 0.13	0.13	0.17	0.18	0		0	1.29 ± 0.28
	43	0.59 ± 0.14	0.14	-0.06	-0.06	0		0	1.25 ± 0.3
	48	2.08 ± 0.2	0.13	0.1	-0.03	0		0	4.41 ± 0.28
	52	0.67 ± 0.14	0.14	0.1	-0.04	0		0	1.42 ± 0.3
	55	0.8 ± 0.15	0.14	0.1	-0.17	0		0	1.7 ± 0.3
	67	1.91 ± 0.21	0.13	0.13	-0.04	0		0	4.05 ± 0.28
	86	1.27 ± 0.17	0.13	-0.1	-0.31	0		0	2.69 ± 0.28
	87	0.7 ± 0.14	0.13	-0.02	-0.13	0		0	1.48 ± 0.28
	88	2.99 ± 0.28	0.13	-0.02	-0.03	0		0	6.34 ± 0.28
	90	1.69 ± 0.2	0.15	0.11	-0.08	0.396	24.7	43.6	3.58 ± 0.32
	91	6.73 ± 0.58	0.15	0.08	-0.17	0.422	75.3	65.4	14.27 ± 0.32
	92	12.01 ± 1.12	0.16	0.09	-0.09	0.476	0	0	25.47 ± 0.34
	94	6 ± 0.5	0.14	0.05	-0.27	0.308	51	24.5	12.72 ± 0.3
	95	1.88 ± 0.22	0.14	0.09	-0.26	0		0	3.99 ± 0.3
	96	1.76 ± 0.19	0.14	0.1	-0.1	0		0	3.73 ± 0.3
	101	2.5 ± 0.24	0.14	-0.01	-0.06	0		0	5.3 ± 0.3
	102	0.73 ± 0.14	0.14	0.2	0.01	0		0	1.55 ± 0.3
	103	7.22 ± 0.58	0.14	0.02	-0.06	0.308	64.6	28.4	15.31 ± 0.3
	111	1.06 ± 0.16	0.13	-0.02	-0.01	0		0	2.25 ± 0.28
	116	1.43 ± 0.16	0.13	0.04	-0.08	0		0	3.03 ± 0.28
	121	4.83 ± 0.41	0.14	0.11	0	0.198	0	0	10.24 ± 0.3
	126	6.54 ± 0.52	0.13	0	-0.04	0		0	13.87 ± 0.28
	129	0.62 ± 0.15	0.12	0.18	-0.29	0.523	0	0	1.31 ± 0.25
	132	1.05 ± 0.15	0.13	0.17	-0.17	0		0	2.23 ± 0.28

*The elliptical Gaussian model applied to the resolved sources generates five free parameters: integrated flux density (S_ν), FWHM along the major axis (a), position angle (P.A.), right ascension offset from the phase center ($\Delta\alpha$), and declination offset from the phase center ($\Delta\delta$).

Filter ID	$A_{\lambda_{eff}}$	$\frac{A_{\lambda_{eff}}}{A_v}$	Zero Point
	[Å]		[Jy]
g	4775.6	1.19	3631
r	6129.5	0.89	3631
i	7484.6	0.67	3631
z	8657.8	0.51	3631
y	9603.1	0.44	3631

Table 6.4: Extinction relations calculated by following the Cardelli, Clayton & Mathis (1989) extinct law with $R_v = 3.1$.

Table 6.5: Stellar Properties for Class II Sources in IC 348.

Source ID	Log T_{eff} [K]	A_v [mag]	Log $L_\star$ [$L_\odot$]	$M_\star$ [$M_\odot$]	Source ID	Log T_{eff} [K]	A_v [mag]	Log $L_\star$ [$L_\odot$]	$M_\star$ [$M_\odot$]
1	$3.95^{+0.02}_{-0.01}$	2.87 ± 0.08	$1.89^{+0.16}_{-0.19}$	$3.17^{+0.0}_{0.0}$	69	$3.45^{+0.01}_{-0.02}$	2.85 ± 0.16	$-1.82^{+0.24}_{-0.38}$	$0.04^{+0.01}_{0.01}$
2	$3.72^{+0.01}_{-0.01}$	4.6 ± 0.03	$0.73^{+0.17}_{-0.21}$	$1.8^{+0.0}_{0.0}$	70	$3.45^{+0.01}_{-0.02}$	4.18 ± 0.11	$-1.67^{+0.24}_{-0.38}$	$0.05^{+0.01}_{0.01}$
3	$3.58^{+0.01}_{-0.02}$	13.93 ± 1.89	$0.23^{+0.2}_{-0.26}$	$0.57^{+0.03}_{0.04}$	71	$3.53^{+0.02}_{-0.03}$	9.34 ± 0.24	$-1.23^{+0.24}_{-0.33}$	$0.29^{+0.05}_{0.07}$
4	$3.58^{+0.01}_{-0.02}$	2.22 ± 0.03	$-0.09^{+0.23}_{-0.3}$	$0.42^{+0.03}_{0.04}$	72	$3.41^{+0.01}_{-0.02}$	4.38 ± 0.49	$-2.32^{+0.27}_{-0.93}$	$0.02^{+0.0}_{0.0}$
5	$3.95^{+0.02}_{-0.01}$	1.3 ± 0.01	$0.96^{+0.16}_{-0.19}$	$1.89^{+0.0}_{0.0}$	73	$3.45^{+0.01}_{-0.02}$	1.7 ± 0.08	$-1.6^{+0.24}_{-0.38}$	$0.05^{+0.01}_{0.01}$
6	$3.6^{+0.01}_{-0.0}$	8.99 ± 0.36	$0.18^{+0.18}_{-0.2}$	$0.6^{+0.0}_{0.01}$	74	$3.41^{+0.01}_{-0.02}$	4.11 ± 0.89	$-2.33^{+0.27}_{-0.93}$	$0.02^{+0.0}_{0.0}$
7	$3.6^{+0.01}_{-0.0}$	3.6 ± 0.06	$-0.18^{+0.19}_{-0.21}$	$0.69^{+0.02}_{0.01}$	75	$3.46^{+0.04}_{-0.01}$	5.4 ± 0	$-3.01^{+0.2}_{-0.19}$	$0.07^{+0.04}_{0.01}$
8	$3.6^{+0.01}_{-0.01}$	2.52 ± 0.06	$-0.08^{+0.21}_{-0.22}$	$0.68^{+0.05}_{0.02}$	76	$3.39^{+0.0}_{-0.0}$	1.6 ± 0	$-3.1^{+0.16}_{-0.19}$	$0.05^{+0.0}_{0.0}$
9	$3.6^{+0.01}_{-0.01}$	2.32 ± 0.12	$-0.21^{+0.21}_{-0.22}$	$0.71^{+0.05}_{0.02}$	77	$3.39^{+0.02}_{-0.0}$	4.39 ± 0.53	$-2.18^{+0.26}_{-1.03}$	$0.01^{+0.0}_{0.0}$
10	$3.6^{+0.0}_{-0.01}$	2.67 ± 0.09	$-0.38^{+0.17}_{-0.24}$	$0.69^{+0.01}_{0.02}$	78	$3.41^{+0.01}_{-0.02}$	3.87 ± 0.34	$-2.36^{+0.27}_{-0.94}$	$0.03^{+0.0}_{0.0}$
11	$3.6^{+0.01}_{-0.0}$	3.94 ± 0.12	$-0.46^{+0.19}_{-0.21}$	$0.72^{+0.02}_{0.01}$	79	$3.45^{+0.0}_{-0.0}$	1.6 ± 0	$-3.13^{+0.16}_{-0.19}$	$0.06^{+0.0}_{0.0}$
12	$3.58^{+0.01}_{-0.02}$	9.44 ± 0.07	$0.01^{+0.2}_{-0.26}$	$0.46^{+0.03}_{0.04}$	80	$3.39^{+0.0}_{-0.0}$	1.5 ± 0	$-2.85^{+0.16}_{-0.19}$	$0.06^{+0.0}_{0.0}$
13	$3.58^{+0.01}_{-0.02}$	10.78 ± 1.03	$-0.77^{+0.25}_{-0.27}$	$0.52^{+0.03}_{0.04}$	81	$3.46^{+0.0}_{-0.0}$	1.8 ± 0	$-3.01^{+0.16}_{-0.19}$	$0.07^{+0.0}_{0.0}$
14	$3.58^{+0.01}_{-0.02}$	12.46 ± 0.23	$0.0^{+0.2}_{-0.26}$	$0.46^{+0.03}_{0.04}$	82	$3.42^{+0.0}_{-0.0}$	0 ± 0	$-2.82^{+0.16}_{-0.19}$	$0.07^{+0.0}_{0.0}$
15	$3.56^{+0.02}_{-0.02}$	1.74 ± 0.06	$-0.53^{+0.26}_{-0.31}$	$0.41^{+0.05}_{0.04}$	83	$3.45^{+0.0}_{-0.0}$	1.1 ± 0	$-3.36^{+0.16}_{-0.19}$	$0.06^{+0.0}_{0.0}$
16	$3.6^{+0.0}_{-0.01}$	2.26 ± 0.18	$-0.67^{+0.17}_{-0.24}$	$0.7^{+0.01}_{0.02}$	84	$3.39^{+0.0}_{-0.0}$	1.3 ± 0	$-3.01^{+0.16}_{-0.19}$	$0.05^{+0.0}_{0.0}$
17	$3.56^{+0.02}_{-0.02}$	1.6 ± 0.11	$-0.62^{+0.26}_{-0.31}$	$0.43^{+0.05}_{0.04}$	85	$3.78^{+0.01}_{-0.01}$	5.94 ± 0.14	$0.98^{+0.17}_{-0.21}$	$1.51^{+0.0}_{0.0}$
18	$3.53^{+0.02}_{-0.03}$	1.06 ± 0.06	$-0.67^{+0.26}_{-0.34}$	$0.27^{+0.03}_{0.04}$	86	$3.5^{+0.03}_{-0.04}$	1.93 ± 0.04	$-0.51^{+0.27}_{-0.38}$	$0.2^{+0.04}_{0.04}$
19	$3.56^{+0.02}_{-0.02}$	0 ± 0	$-0.86^{+0.18}_{-0.22}$	$0.48^{+0.05}_{0.05}$	87	$3.58^{+0.01}_{-0.02}$	7.48 ± 0.36	$-0.29^{+0.2}_{-0.26}$	$0.45^{+0.03}_{0.04}$
20	$3.53^{+0.02}_{-0.03}$	1.69 ± 0.06	$-0.69^{+0.26}_{-0.35}$	$0.27^{+0.03}_{0.05}$	88	$3.58^{+0.01}_{-0.02}$	2.55 ± 0.04	$-0.47^{+0.23}_{-0.3}$	$0.52^{+0.04}_{0.05}$
21	$3.56^{+0.02}_{-0.02}$	1.27 ± 0.2	$-0.8^{+0.26}_{-0.31}$	$0.44^{+0.05}_{0.04}$	89	$3.54^{+0.02}_{-0.02}$	2.53 ± 0.04	$-0.68^{+0.24}_{-0.27}$	$0.33^{+0.04}_{0.03}$
22	$3.54^{+0.02}_{-0.02}$	1.55 ± 0.11	$-0.78^{+0.28}_{-0.3}$	$0.35^{+0.04}_{0.03}$	90	$3.5^{+0.03}_{-0.04}$	1.61 ± 0.1	$-0.65^{+0.27}_{-0.38}$	$0.18^{+0.04}_{0.04}$
23	$3.54^{+0.02}_{-0.02}$	5.37 ± 0.6	$-0.56^{+0.24}_{-0.27}$	$0.36^{+0.04}_{0.03}$	91	$3.56^{+0.02}_{-0.02}$	1.18 ± 0.02	$-0.26^{+0.26}_{-0.31}$	$0.42^{+0.04}_{0.03}$
24	$3.5^{+0.03}_{-0.04}$	0.43 ± 0.13	$-1.08^{+0.31}_{-0.28}$	$0.17^{+0.04}_{0.06}$	92	$3.78^{+0.01}_{-0.01}$	10.9 ± 0.08	$0.72^{+0.18}_{-0.22}$	$1.56^{+0.0}_{0.0}$
25	$3.56^{+0.02}_{-0.02}$	1.93 ± 0.07	$-0.75^{+0.26}_{-0.31}$	$0.45^{+0.05}_{0.05}$	93	$3.42^{+0.02}_{-0.01}$	2.87 ± 0.14	$-1.57^{+0.34}_{-0.31}$	$0.04^{+0.01}_{0.0}$
26	$3.54^{+0.02}_{-0.02}$	1.18 ± 0.08	$-0.99^{+0.28}_{-0.3}$	$0.39^{+0.05}_{0.04}$	94	$3.56^{+0.02}_{-0.02}$	1.22 ± 0.05	$-0.63^{+0.23}_{-0.28}$	$0.43^{+0.05}_{0.04}$
27	$3.54^{+0.02}_{-0.02}$	6.9 ± 0.17	$-0.43^{+0.24}_{-0.27}$	$0.33^{+0.03}_{0.03}$	95	$3.53^{+0.02}_{-0.03}$	1.96 ± 0.07	$-0.59^{+0.23}_{-0.31}$	$0.26^{+0.03}_{0.05}$
28	$3.54^{+0.02}_{-0.02}$	1.87 ± 0.02	$-0.84^{+0.28}_{-0.3}$	$0.36^{+0.04}_{0.04}$	96	$3.53^{+0.02}_{-0.03}$	1.76 ± 0.12	$-1.18^{+0.23}_{-0.31}$	$0.26^{+0.04}_{0.06}$
29	$3.54^{+0.02}_{-0.02}$	1.24 ± 0.02	$-0.89^{+0.28}_{-0.3}$	$0.37^{+0.04}_{0.04}$	97	$3.53^{+0.02}_{-0.03}$	0.66 ± 0.32	$-1.09^{+0.26}_{-0.29}$	$0.28^{+0.04}_{0.06}$
30	$3.5^{+0.03}_{-0.04}$	1.1 ± 0.02	$-0.95^{+0.31}_{-0.36}$	$0.2^{+0.04}_{0.06}$	98	$3.5^{+0.03}_{-0.04}$	0 ± 0	$-1.21^{+0.28}_{-0.23}$	$0.17^{+0.05}_{0.06}$
31	$3.46^{+0.04}_{-0.01}$	2.42 ± 0.15	$-0.93^{+0.4}_{-0.27}$	$0.11^{+0.04}_{0.02}$	99	$3.53^{+0.02}_{-0.03}$	4.01 ± 0.1	$-0.87^{+0.24}_{-0.33}$	$0.27^{+0.03}_{0.05}$
32	$3.53^{+0.02}_{-0.03}$	4.69 ± 0.7	$-1.12^{+0.24}_{-0.33}$	$0.28^{+0.04}_{0.06}$	100	$3.42^{+0.02}_{-0.01}$	7.88 ± 0.31	$-1.42^{+0.34}_{-0.31}$	$0.05^{+0.01}_{0.0}$
33	$3.46^{+0.04}_{-0.01}$	2.73 ± 0.11	$-0.97^{+0.4}_{-0.27}$	$0.11^{+0.04}_{0.02}$	101	$3.53^{+0.02}_{-0.03}$	11.29 ± 0.74	$-0.87^{+0.24}_{-0.33}$	$0.29^{+0.04}_{0.05}$
34	$3.46^{+0.04}_{-0.01}$	2.7 ± 0.08	$-1.04^{+0.4}_{-0.27}$	$0.1^{+0.04}_{0.02}$	102	$3.53^{+0.02}_{-0.03}$	4.59 ± 0.82	$-1.46^{+0.24}_{-0.33}$	$0.28^{+0.06}_{0.06}$
35	$3.5^{+0.03}_{-0.04}$	0.41 ± 0.01	$-1.18^{+0.31}_{-0.28}$	$0.18^{+0.05}_{0.05}$	103	$3.53^{+0.02}_{-0.03}$	15.43 ± 1.27	$-0.54^{+0.23}_{-0.34}$	$0.27^{+0.03}_{0.05}$
36	$3.53^{+0.02}_{-0.03}$	11.2 ± 1.05	$-0.27^{+0.24}_{-0.33}$	$0.27^{+0.03}_{0.04}$	104	$3.46^{+0.04}_{-0.01}$	3.28 ± 0.11	$-1.35^{+0.4}_{-0.27}$	$0.07^{+0.06}_{0.01}$
37	$3.46^{+0.04}_{-0.01}$	3.43 ± 0.1	$-0.97^{+0.4}_{-0.27}$	$0.11^{+0.04}_{0.02}$	105	$3.46^{+0.04}_{-0.01}$	1.93 ± 0.07	$-1.57^{+0.4}_{-0.27}$	$0.06^{+0.06}_{0.01}$
38	$3.5^{+0.03}_{-0.04}$	7.78 ± 0.17	$-0.6^{+0.29}_{-0.44}$	$0.19^{+0.04}_{0.04}$	106	$3.45^{+0.01}_{-0.02}$	2.59 ± 0.05	$-1.52^{+0.24}_{-0.38}$	$0.05^{+0.01}_{0.01}$
39	$3.5^{+0.03}_{-0.04}$	3.47 ± 0.12	$-1.02^{+0.29}_{-0.44}$	$0.18^{+0.04}_{0.06}$	107	$3.46^{+0.04}_{-0.01}$	5.61 ± 0.2	$-1.27^{+0.4}_{-0.27}$	$0.08^{+0.05}_{0.01}$
40	$3.45^{+0.01}_{-0.02}$	2.62 ± 0.1	$-1.05^{+0.24}_{-0.38}$	$0.08^{+0.02}_{0.01}$	108	$3.46^{+0.04}_{-0.01}$	5.78 ± 0.15	$-1.42^{+0.4}_{-0.27}$	$0.07^{+0.05}_{0.01}$
41	$3.5^{+0.03}_{-0.04}$	10.26 ± 0.15	$-0.75^{+0.29}_{-0.44}$	$0.18^{+0.04}_{0.05}$	109	$3.45^{+0.01}_{-0.02}$	3.72 ± 0.15	$-1.65^{+0.24}_{-0.38}$	$0.05^{+0.01}_{0.01}$
42	$3.5^{+0.03}_{-0.04}$	2.71 ± 0.13	$-1.05^{+0.29}_{-0.44}$	$0.18^{+0.04}_{0.06}$	110	$3.45^{+0.01}_{-0.02}$	5.57 ± 0.28	$-1.7^{+0.24}_{-0.38}$	$0.05^{+0.01}_{0.01}$
43	$3.53^{+0.02}_{-0.03}$	12.2 ± 1.42	$-0.8^{+0.24}_{-0.33}$	$0.27^{+0.03}_{0.04}$	111	$3.5^{+0.03}_{-0.04}$	8.21 ± 0.5	$-1.32^{+0.24}_{-0.44}$	$0.18^{+0.06}_{0.06}$
44	$3.56^{+0.02}_{-0.02}$	12.52 ± 1.83	$-0.85^{+0.22}_{-0.26}$	$0.48^{+0.05}_{0.05}$	112	$3.45^{+0.01}_{-0.02}$	0 ± 0	$-3.3^{+0.16}_{-0.19}$	$0.06^{+0.0}_{0.01}$
45	$3.45^{+0.01}_{-0.02}$	3.79 ± 0.06	$-1.1^{+0.24}_{-0.38}$	$0.08^{+0.01}_{0.01}$	113	$3.45^{+0.01}_{-0.02}$	14.3 ± 0	$-1.76^{+0.16}_{-0.19}$	$0.05^{+0.01}_{0.01}$
46	$3.46^{+0.04}_{-0.01}$	0.79 ± 0.07	$-1.33^{+0.4}_{-0.27}$	$0.08^{+0.05}_{0.01}$	114	$3.39^{+0.0}_{-0.0}$	0 ± 0	$-3.11^{+0.16}_{-0.19}$	$0.05^{+0.0}_{0.0}$
47	$3.5^{+0.03}_{-0.04}$	4.19 ± 0.25	$-1.13^{+0.29}_{-0.44}$	$0.18^{+0.05}_{0.06}$	115	$3.53^{+0.02}_{-0.03}$	6.86 ± 0.21	$-0.74^{+0.24}_{-0.33}$	$0.28^{+0.03}_{0.04}$
48	$3.58^{+0.01}_{-0.02}$	6.89 ± 0.75	$-1.21^{+0.2}_{-0.26}$	$0.57^{+0.02}_{0.03}$	116	$3.46^{+0.04}_{-0.01}$	2.43 ± 0.12	$-1.41^{+0.4}_{-0.27}$	$0.07^{+0.06}_{0.01}$
49	$3.46^{+0.04}_{-0.01}$	1.2 ± 0.1	$-1.32^{+0.4}_{-0.27}$	$0.08^{+0.05}_{0.01}$	117	$3.42^{+0.02}_{-0.01}$	1.42 ± 0.09	$-1.82^{+0.34}_{-0.31}$	$0.03^{+0.02}_{0.0}$
50	$3.46^{+0.04}_{-0.01}$	1.36 ± 0.11	$-1.3^{+0.4}_{-0.27}$	$0.08^{+0.05}_{0.01}$	118	$3.46^{+0.04}_{-0.01}$	4.48 ± 0.15	$-1.54^{+0.4}_{-0.27}$	$0.07^{+0.06}_{0.01}$
51	$3.5^{+0.03}_{-0.04}$	4.5 ± 0.11	$-1.02^{+0.29}_{-0.44}$	$0.18^{+0.04}_{0.06}$	119	$3.46^{+0.04}_{-0.01}$	2.45 ± 0.13	$-1.28^{+0.4}_{-0.27}$	$0.08^{+0.06}_{0.01}$
52	$3.46^{+0.04}_{-0.01}$	2.69 ± 0.13	$-1.33^{+0.4}_{-0.27}$	$0.08^{+0.05}_{0.01}$	120	$3.39^{+0.02}_{-0.0}$	0 ± 0	$-2.87^{+0.16}_{-0.19}$	$0.02^{+0.0}_{0.0}$
53	$3.45^{+0.01}_{-0.02}$	1.57 ± 0.09	$-1.35^{+0.24}_{-0.37}$	$0.06^{+0.02}_{0.02}$	121	$3.5^{+0.03}_{-0.04}$	4.03 ± 0.27	$-0.96^{+0.29}_{-0.44}$	$0.2^{+0.04}_{0.06}$
54	$3.5^{+0.03}_{-0.04}$	5.52 ± 0.1	$-1.09^{+0.29}_{-0.44}$	$0.17^{+0.04}_{0.06}$	122	$3.5^{+0.03}_{-0.04}$	3.54 ± 0.05	$-1.25^{+0.29}_{-0.44}$	$0.16^{+0.05}_{0.06}$

Table 6.5 – Continued

Source ID	Log T_{eff} [K]	A_v [mag]	Log $L_\star$ [$L_\odot$]	$M_\star$ [$M_\odot$]	Source ID	Log T_{eff} [K]	A_v [mag]	Log $L_\star$ [$L_\odot$]	$M_\star$ [$M_\odot$]
55	$3.58^{+0.01}_{-0.02}$	9.65 ± 0.4	$-1.17^{+0.2}_{-0.26}$	$0.58^{+0.02}_{0.03}$	123	$3.56^{+0.02}_{-0.02}$	0.28 ± 0.14	$-0.61^{+0.26}_{-0.25}$	$0.43^{+0.05}_{0.04}$
56	$3.42^{+0.02}_{-0.01}$	2.45 ± 0.12	$-1.39^{+0.34}_{-0.3}$	$0.05^{+0.01}_{0.01}$	124	$3.46^{+0.04}_{-0.01}$	0 ± 0	$-3.88^{+0.2}_{-0.19}$	$0.04^{+0.04}_{0.0}$
57	$3.45^{+0.01}_{-0.02}$	2.26 ± 0.08	$-1.47^{+0.24}_{-0.38}$	$0.06^{+0.02}_{0.02}$	125	$3.46^{+0.04}_{-0.01}$	0 ± 0	$-2.92^{+0.2}_{-0.19}$	$0.06^{+0.05}_{0.01}$
58	$3.5^{+0.03}_{-0.04}$	10.56 ± 0.36	$-0.98^{+0.29}_{-0.44}$	$0.19^{+0.04}_{0.06}$	126	$3.62^{+0.02}_{-0.01}$	3.42 ± 0.25	$-0.31^{+0.18}_{-0.2}$	$0.86^{+0.08}_{0.05}$
59	$3.46^{+0.04}_{-0.01}$	1.26 ± 0.15	$-1.56^{+0.4}_{-0.27}$	$0.07^{+0.06}_{0.01}$	127	$3.46^{+0.04}_{-0.01}$	2.7 ± 0.08	$-1.51^{+0.4}_{-0.27}$	$0.07^{+0.06}_{0.01}$
60	$3.46^{+0.04}_{-0.01}$	2.4 ± 0.09	$-1.46^{+0.4}_{-0.27}$	$0.07^{+0.06}_{0.01}$	128	$3.5^{+0.03}_{-0.04}$	2.1 ± 0.09	$-1.28^{+0.29}_{-0.44}$	$0.18^{+0.05}_{0.06}$
61	$3.45^{+0.01}_{-0.02}$	2.9 ± 0.13	$-1.55^{+0.24}_{-0.38}$	$0.05^{+0.01}_{0.01}$	129	$3.5^{+0.03}_{-0.04}$	6.45 ± 0.54	$-1.75^{+0.29}_{-0.44}$	$0.15^{+0.07}_{0.05}$
62	$3.45^{+0.01}_{-0.02}$	3.17 ± 0.19	$-1.56^{+0.24}_{-0.38}$	$0.05^{+0.01}_{0.01}$	130	$3.5^{+0.03}_{-0.04}$	6.72 ± 0.12	$-0.75^{+0.29}_{-0.44}$	$0.18^{+0.05}_{0.06}$
63	$3.45^{+0.01}_{-0.02}$	1.21 ± 0.1	$-1.69^{+0.24}_{-0.33}$	$0.05^{+0.01}_{0.01}$	131	$3.41^{+0.01}_{-0.02}$	0 ± 0	$-3.0^{+0.16}_{-0.19}$	$0.06^{+0.0}_{0.0}$
64	$3.46^{+0.04}_{-0.01}$	3.46 ± 0.16	$-1.62^{+0.4}_{-0.27}$	$0.06^{+0.06}_{0.01}$	132	$3.46^{+0.04}_{-0.01}$	0 ± 0	$-1.57^{+0.2}_{-0.19}$	$0.06^{+0.06}_{0.01}$
65	$3.46^{+0.04}_{-0.01}$	2.39 ± 0.14	$-1.6^{+0.4}_{-0.27}$	$0.06^{+0.06}_{0.01}$	133	$...^{+...}_{-...}$	0 ± 0	$-2.55^{+0.16}_{-0.19}$	$0.0^{+0.0}_{0.0}$
66	$3.46^{+0.04}_{-0.01}$	1.99 ± 0.14	$-1.78^{+0.4}_{-0.27}$	$0.07^{+0.05}_{0.01}$	134	$3.58^{+0.0}_{-0.0}$	0 ± 0	$...^{+...}_{-...}$	$0.0^{+0.0}_{0.0}$
67	$3.46^{+0.04}_{-0.01}$	6.26 ± 0.22	$-1.57^{+0.4}_{-0.27}$	$0.06^{+0.06}_{0.01}$	135	$3.58^{+0.0}_{-0.0}$	0 ± 0	$...^{+...}_{-...}$	$0.0^{+0.0}_{0.0}$
68	$3.42^{+0.02}_{-0.01}$	4.27 ± 0.35	$-2.21^{+0.34}_{-0.31}$	$0.02^{+0.01}_{0.0}$	136	$3.5^{+0.03}_{-0.04}$	4.4 ± 0	$-1.34^{+0.29}_{-0.44}$	$0.18^{+0.06}_{0.05}$

In Figure 5, we plot the SEDs of all targets detected at 1.3 mm, including photometry from PS1 (0.48, 0.62, 0.75, 0.87, 0.96 μm), 2MASS (1.25, 1.65, 2.22 μm) and Spitzer/IRAC (3.6, 4.5, 5.8, 8 and 24 μm) (Skrutskie et al., 2006; Evans et al., 2003; Currie & Kenyon, 2009). The photometric data were dereddened using the Mathis (1990) approach. To calculate the stellar synthetic photometry with a fixed temperature $T_\star$, which is approximated by T_{eff}, we interpolated the response curves for the set of filters used in the fitting, and used the BT-Settl spectral models for the corresponding $T_\star$ (Allard, 2014). Then, we convolved the filter response curves with the synthetic spectra, to match the spectral resolution. Because the PS1, 2MASS, IRAC, and 24 μm data have photometric uncertainties between a few percent and 0.1 mag for the objects investigated here, systematic effects can contribute up to 0.1 mag. To account for flux variability of the objects, we added an observational error of 15%. A multiplicative dilution factor, $\left(\frac{R_\star}{d}\right)^2$, relating the central star radius ($R_\star$) and the distance to the object (d) is used to normalize the optical bands.

In Figure 6.6, we plot millimeter flux as a function of stellar mass. The 8 transition disks in our sample are indicated as red symbols. Some of these objects are among the most massive disks in the cluster, with disk masses of several M_{Jup}, assuming a standard gas to dust mass ratio of 100. In particular, 3 of the 6 brightest disks in the entire sample are transition objects based on their SEDs (Cl* IC 348 LRL 31, Cl* IC 348 LRL 67, and 2MASS J03443468+3216000), a trend that was already reported by Cieza et al. (2015) based on shallower SCUBA-2 observations of the cluster at 850 μm.

Three transition disks (Cl* IC 348 LRL 97*, Cl* IC 348 LRL 229*, Cl* IC 348 LRL 329) remained undetected. These results fit well in the scenario proposed
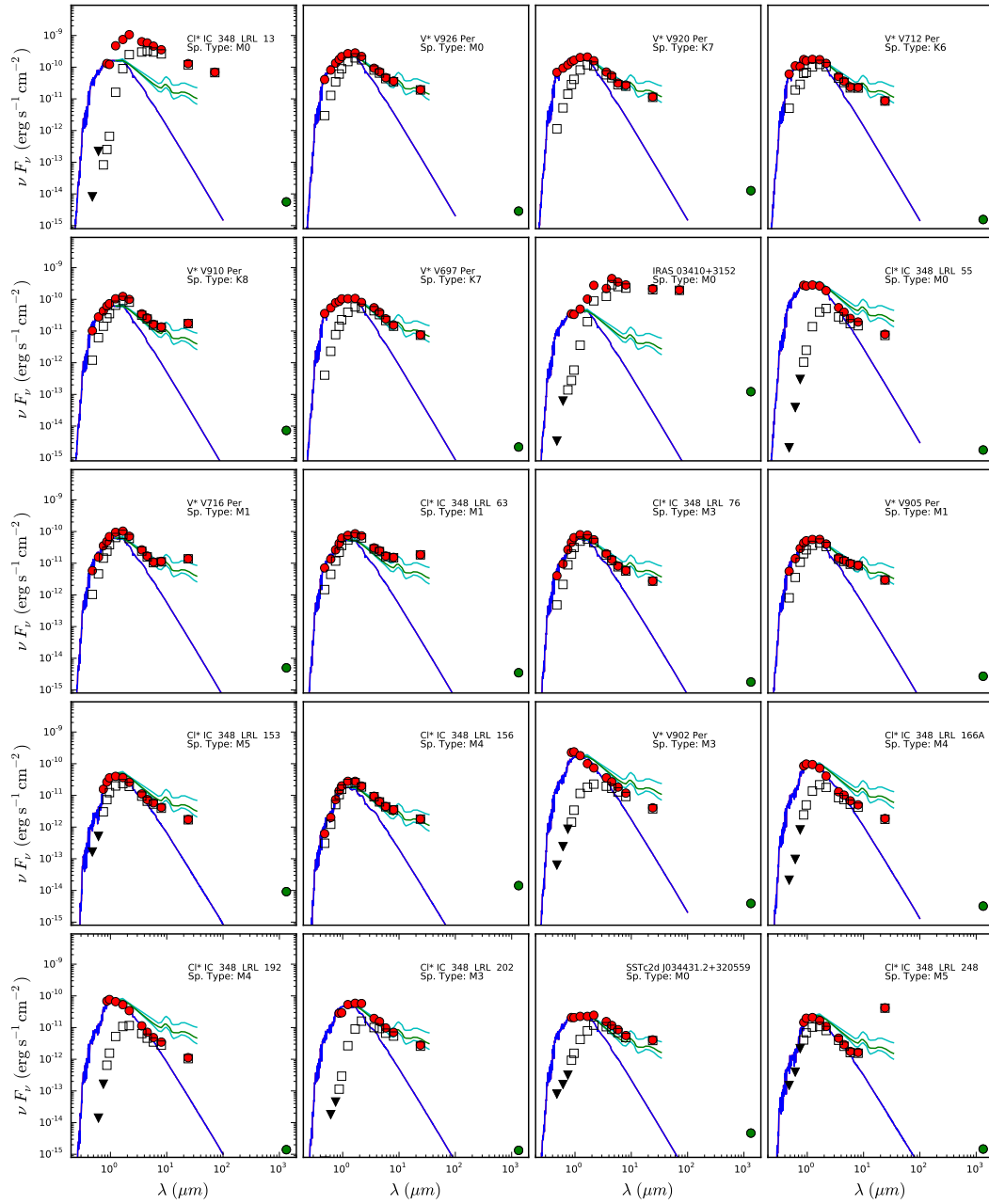
Figure 6.5: Spectral energy distributions of the sources detected at 1.3 mm in the IC 348 sample. Red dots show photometric data acquired from the literature; blue lines are the BT-settl spectra model according to the spectral type. A_v values used are in Table 6.5. The green lines correspond to the median SEDs of K5−M2 CTTSs calculated by Furlan et al. (2006).
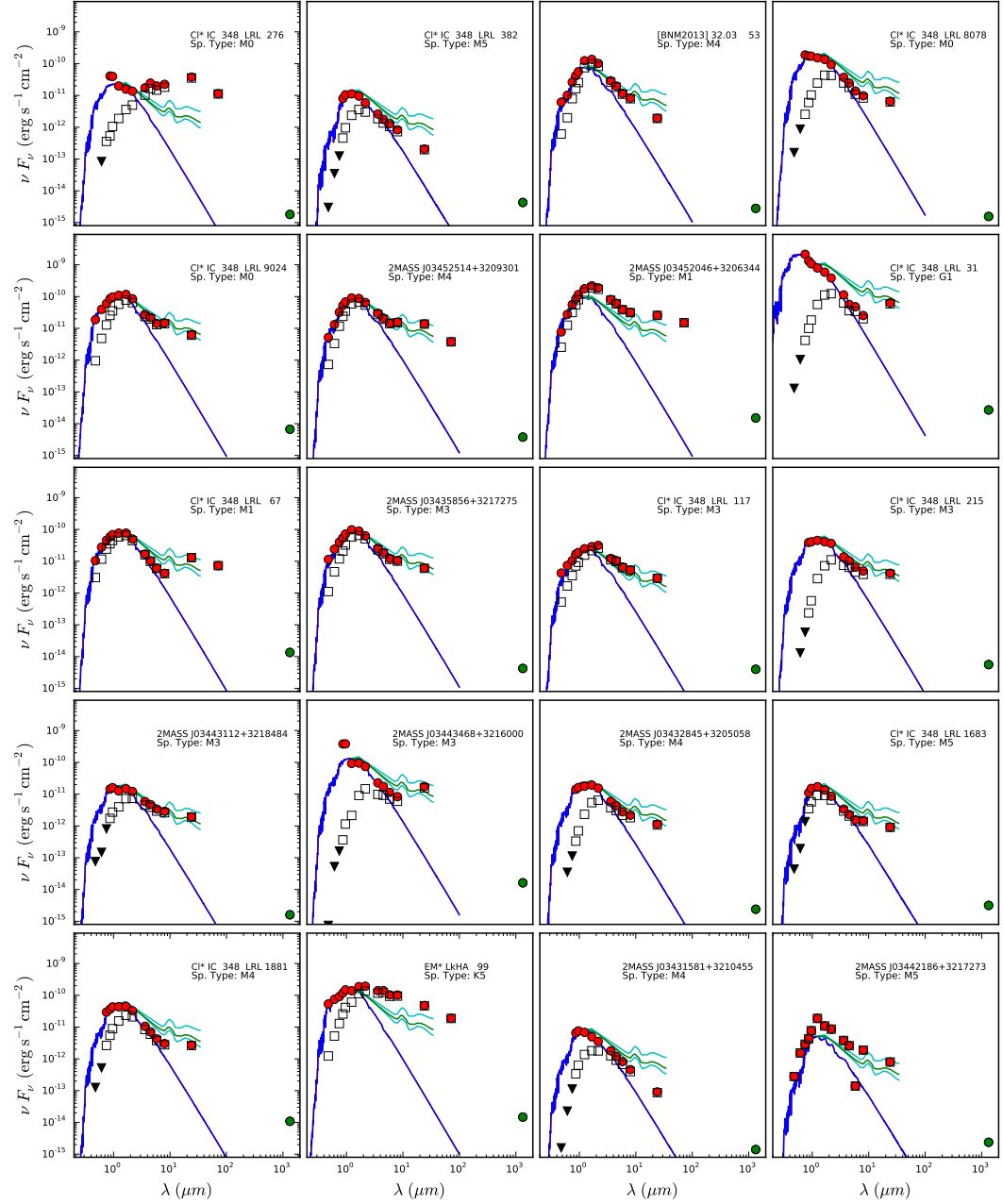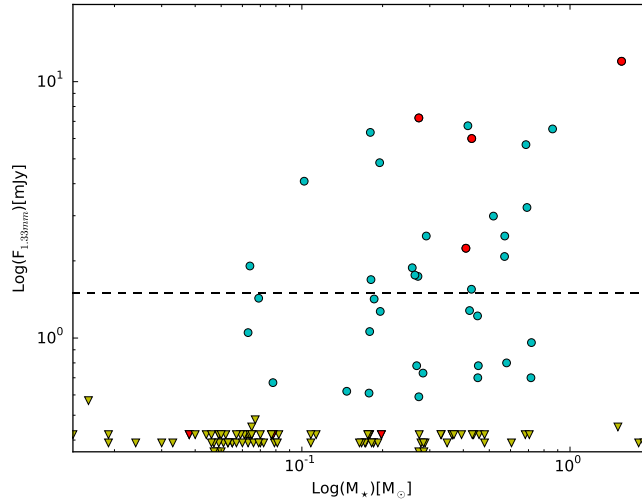
Figure 6.5: Continued.

Figure 6.6: 1.3 mm continuum flux as a function of stellar mass for IC 348 Class II sources. The horizontal dashed-line indicates the flux level corresponding to a disk mass of ~1 M_{Jup} assuming a gas to dust mass ratio of 100. Four transition objects (red symbols) are among the most massive disks in the sample.

by Owen & Clarke (2012b) and Cieza et al. (2012b), in which there are at least two types of transition disks with inner opacity cavities that are the result of distinct processes: 1) gas-accreting transition disks that are massive and have large inner holes caused by the formation of giant planets, (multiple) lower mass planets or subsequent migration (van der Marel et al., 2018), and 2) non-accreting transition objects with low disk masses that have inner holes carved by photoevaporation during the final stages of disk dissipation.

6.5   Discussion

6.5.1   Non-Detections

The ensemble of undetected sources can be used to estimate the typical disk mass of the faint sources in IC 348. Initially, for the stacking analysis, we produced average images of two subsamples (SpT: A2-M4 and M5-L0), and we did not find a significant emission in those images. Then, we stack the 96 non-detections, after centering each field on the expected stellar position, to create an average image that has noise which is a factor of $\sim$7 lower than in the individual fields. After doing so, we find a clear signal 0.14 ± 0.02 mJy (Figure 6.7), indicating that there are many targets in IC 348 with fluxes very close to the 1σ noise of our observations. The 0.14 mJy flux measurement resulting from the stacking exercise suggests that the average dust mass of the disks that were not individually detected is only $\sim$0.30 $M_\oplus$. This implies that, for most disks in the IC 348 cluster, the amount of millimeter-sized dust that is still available for planet formation is of the order of the mass of the planet Mars. *Kepler* has recently found that M-type stars host an average of 2.2 $\pm$0.3 planets with radii of $\sim$1 $R_\oplus$ and orbital periods of 1.5 to 180 days (Gaidos et al., 2016); therefore, it is expected that most stars in IC 348 should form multiple rocky planets even though most of the cluster members have already lost their disks (within the stringent limits imposed by the infrared observations) or have very little dust left. Thus, we conclude that most disks around IC 348 members contain several Earth masses worth of solids in bodies that are large enough to become undetectable by ALMA observations (at least several cm

in size). More significantly, this suggests that these protoplanetary disks are likely sites of already formed planetary systems like our own. In addition, IR emission from disks not detected at mm wavelengths connotes the existence of small optically thick disks with extensions of < 1 au. Our observations also constrain the amount of second-generation dust produced in the systems not detected by ALMA to be < 0.3 M$_\oplus$, which still leaves significant room to explain the observed IR excesses. In fact, a small amount of warm grains of micron sizes (¡1 lunar mass) is sufficient to produce the observed excesses at 10 μm (e.g. Nagel et al., 2010).

In addition, our survey with an RMS of $\sim$0.15 mJy results in a large number of non-detections, with respect to other surveys, mainly because of a lower sensitivity at late spectral types (M4-M9) at a distance of 270 pc. Detecting such late M stars individually (with S/N of >4) at 1.3 mm would require 10$\times$ our exposure time. However, we note that objects with a disk mass of $\sim$1 M$_\oplus$ are individually detected with a S/N of $\sim$10 in the Lupus survey thanks to the much smaller (150 pc) distance of some of the Lupus PMS stars and, to a lesser extent, the use of a shorter observing wavelength (Ansdell et al., 2016).

6.5.2   Disk Evolution

Disk properties determine possible planet formation scenarios. Investigating basic disk parameters such as mass and size at different evolutionary stages is thus vital for planet-formation theory. Nearby star-forming regions like Taurus (1-3 Myr), Lupus (1-3 Myr), Cha I (2-3 Myr), σ Ori (3-5 Myr), and Upper Sco (5-10 Myr) are ideal targets to track evolutionary patterns because the
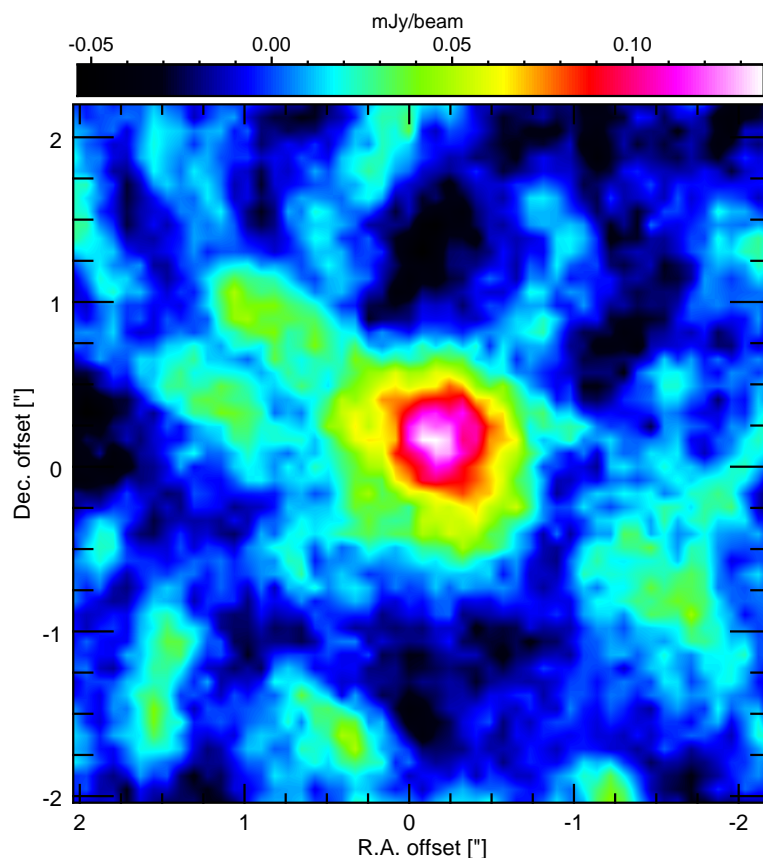
Figure 6.7: Stacked image for the 96 non-detections, which clearly shows a detection at the 6σ level.
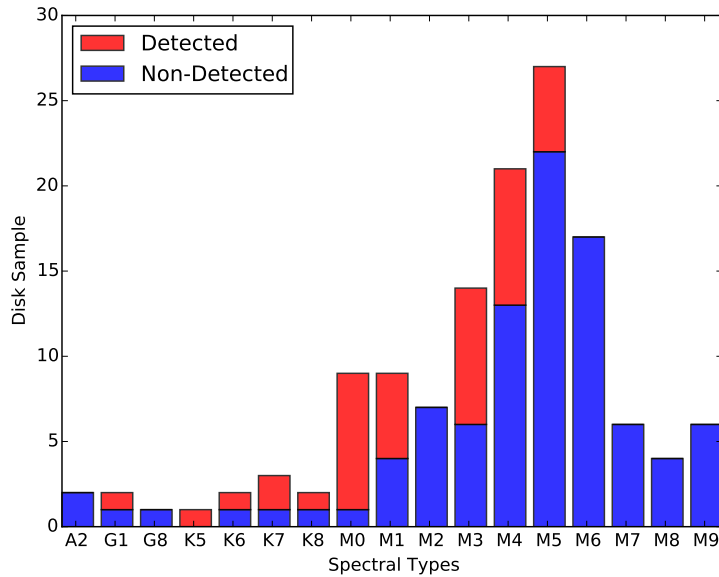
Figure 6.8: Distribution of stellar spectral types for the detected and non-detected sources in IC 348 targeted by our ALMA survey (Tables 6.2 and 6.3).

ages of these populations cover the disk dispersal timescale. Recently, (sub-)mm continuum flux surveys of these star-forming regions have shown that disk masses decline with age and that there is a strong dependence of mm-wavelength luminosity on stellar mass (Andrews et al., 2013; Ansdell et al., 2016, 2017; Barenfeld et al., 2016; Pascucci et al., 2016). Therefore, in order to compare IC 348 to other regions and investigate the evolution of disk masses as a function of stellar age, we need to take into account that disk masses and millimeter detection rates depend on spectral types and stellar mass. Figure 6.8 displays the distribution of stellar spectral types for the detected and non-detected sources, showing the low detection rate at later spectral types (Tables 6.2 and 6.3).

Because estimates of stellar masses depend sensitively on inputs such as dis-

tances and theoretical models, here we used the statistical methodology presented in Andrews et al. (2013) based on spectral types. While solar-mass stars evolve in spectral types during pre-main-sequence stages, lower-mass stars (0.1-0.7 $M_\odot$ evolve at almost constant temperature for the first ~10 Myr (see evolutionary models in Figure 6.4). This supports the use of spectral types as a proxy for stellar mass in the mass range of the stars in our IC 348 sample. Hence, to statistically compare samples from different regions, we perform Monte Carlo simulations, whose "reference" sample is IC 348, while a "comparison" sample can be Taurus, Chamaeleon I, Lupus, Upper Sco, or σ Ori. The "comparison" sample is appropriately scaled to the IC 348 distance (270 pc) and modified for the respective observing wavelengths using the mean (sub-)millimeter flux ratios observed in Taurus ($F_\lambda = F_{1.3mm} \times (1.3mm/\lambda)^{2.5}$). Upper limit inputs for the "comparison" samples are as reported in the literature: three times the rms noise of the observations for Taurus, Lupus, Cha I, and Orionis, while the upper limits in Upper Sco are given by three times the rms noise plus any positive measured flux density. To construct our simulations, we first define a set of spectral type bins ranging from A2 to M6, corresponding to the distribution of the IC 348 sample, and place the comparison objects in those bins. Then, disk mm-wave luminosities are randomly drawn from the reference region (IC 348) in each of these spectral type bins, such that the reference and comparison samples have the same spectral type distributions. In this manner, we simulate 10^6 synthetic "reference" disk ensembles that are used to construct Cumulative Distribution Functions (CDF); see Figure 6.9. Each of these CDFs is compared to the comparison sample to estimate the probability that the two distributions are drawn from the same parent population using a censored statistical test (i.e the Gehan test: Feigelson & Nelson, 1985). The result is a list
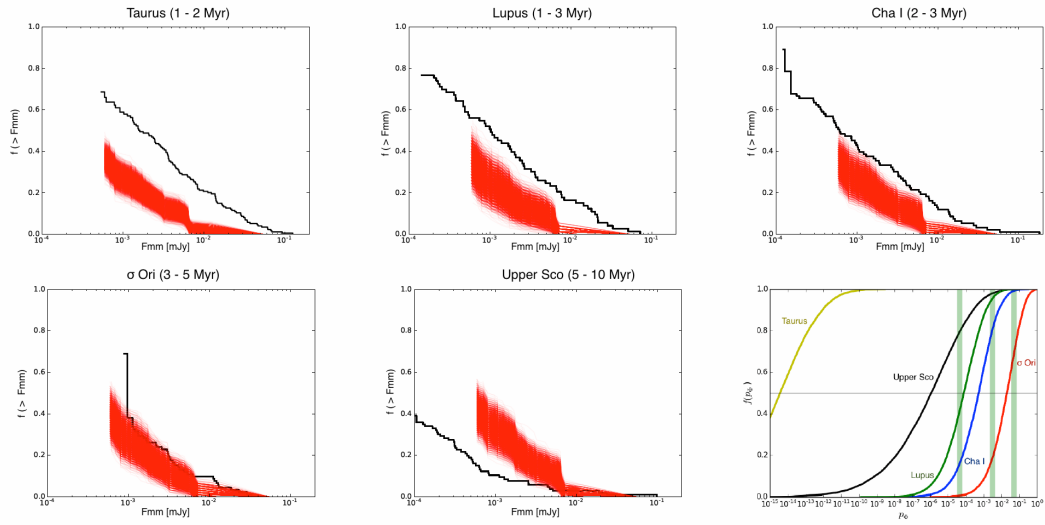
Figure 6.9: Cumulative Distribution Functions of the disk luminosities in IC 348 (red) and the 10^6 synthetic "reference" disk draws, Taurus (1-2 Myr), Lupus (1-3 Myr), Cha I (2-3 Myr), σ Ori (3-5 Myr), and Upper Sco (5-10 Myr), in black colour. At the right bottom, the comparison between the disk luminosity distribution of IC 348 and the "reference" sample shows the probability that IC 348 and the "reference" sample belong to the same population. The vertical green bars indicate the nominal 2, 3, and 4σ probabilities.

of 10^6 such probabilities for each comparison region. The cumulative distributions for these probabilities, $f(p_\phi)$, are also shown in Figure 6.9 (bottom-right panel).

Relative Flux Densities

The CDFs for the scaled flux densities show that the disks orbiting IC 348 stars are fainter on average than disks in Taurus, Lupus, Cham I and σ Ori. Cieza et al. (2015) presented a similar statistical analysis based on shallower SCUBA-2 observations of IC 348 and found that the fluxes in this cluster were slightly lower than in Taurus. Here, we confirm that the fluxes in IC 348 are $\sim$

$5\times$ fainter than in Taurus with a very high level of significance: virtually all 10^6 tests indicate that the probability that disk luminosities in Taurus and IC 348 are drawn from the same parent population is $< 10^{-9}$. Similarly, we find that the younger Lupus and Cha I regions have substantially brighter distributions compared to the older IC 348 region, at the $\gtrsim 3\sigma$ level. The difference between the luminosity distributions of IC 348 and σ Ori are marginal, with IC 348 being slightly fainter than σ Ori. This might suggest that IC 348 is actually more evolved than σ Ori, despite the fact that it is usually assigned a younger age in the literature. Indeed, we note that adopting a distance of 250 pc, Bell et al. (2013) derived an age of 6 Myr for IC 348 (e.g. Ripepi et al., 2014). In addition, Upper Sco is also very different from IC 348 (all tests indicate differences $>$ 3σ), but in the opposite sense: the Upper Sco disks are fainter than disks in IC 348, which reflects the fact that the mean mass dust is lower at the 5-10 Myr age of Upper Sco. In summary, these millimeter observations trace the population of millimeter/centimeter-sized grains at radial distances >10 au, confirming a significant dispersal process in the outer disk over a timescale of $\sim 1-10$ Myr.

Previously, infrared surveys with the *Spitzer Space Telescope*, at IRAC wavelengths ($3.6-4.5$ μm), already established that the fraction of optically thick dust disk decreases, yielding disk fractions (%) of 63 ± 4 in Taurus, 52 ± 5 in Lupus, 52 ± 6 in Cha I, 39 ± 6 in σ Ori, 36 ± 3 in IC 348, and only 16 ± 6 in Upper Sco (Ribas et al., 2014). These IR observations probe the dispersion of micron-sized grains within a few au (< 10 au) from the central star. While IR disks observations are very sensitive and typically less biased with respect to spectral type, (sub-)millimetre detection rates are much lower and usually very

biased against the lower end of the stellar mass function (M4-M9), making the interpretation of the results difficult.

Continuum Luminosity Distributions

Figure 6.9 (bottom-right panel) compares the disc luminosity distributions of the "comparison" and "reference" samples. Where p_ϕ is the probability that the two distributions are drawn from the same parent population and the vertical green bars indicate the nominal 2σ, 3σ and 4σ probabilities. The cumulative distributions derived from the the Peto-Prentice test indicate medians of $p_\phi = 3.8$ x 10^{-15} and 1.3 x 10^{-6} for Taurus and Upper Sco, respectively, implying a $>4\sigma$ difference. The Lupus and Cha I samples appear to have a difference of $>3\sigma$ in their luminosity distributions, as indicated by medians of $p_\phi = 7.7$ x 10^{-5} and $p_\phi = 5.4$ x 10^{-4}, respectively. Meanwhile, the σ Ori has a luminosity distribution that is only marginally ($\gtrsim 2\sigma$) different from the IC 348 sample, with $p_\phi = 2.0$ x 10^{-2}.

It is noteworthy that the disc luminosity distribution of our IC 348 sample is significantly different from those of the Taurus and Upper Sco samples. As mentioned above, IC 348 is fainter than Taurus and Upper Sco is fainter than IC 348, which is not surprising, considering their relative ages and their IR disc fractions (Taurus: 63 per cent, Upper Sco: 16 per cent, IC 348: 36 per cent (Ribas et al., 2014)). Also, σ Ori, with an IR disc fraction of 39 per cent and slightly brighter than IC 348, seems to undergo a similar evolutionary stage in terms of dispersal timescales.

Distance Uncertainty: Recent results for a similar analysis applied to the millimeter surveys of discs towards other star-forming regions (Taurus, Lupus, Cha I, Ori, Upper ScoI), also reveal a significant decrease of disk masses with "age", which has been interpreted as a signature of evolution. However, ages are difficult to determine at early times (<10 Myr) and are highly dependent on the adopted distances and theoretical models (Hillenbrand, Bauermeister & White, 2008). In the literature, the distance to the IC 348 region has been estimated in a wide range between 220 - 380 pc (Harris, Morgan & Roman, 1954; Cernis, 1993; Herbig, 1998; Scholz et al., 1999; de Zeeuw et al., 1999; Luhman et al., 2003; Luhman, Esplin & Loutrel, 2016). Here, we have adopted a distance value based on the Gaia DR1 despite its large error bar ($\sim$270 $\pm$65 pc). However, if the distance is closer than the adopted value of 270 pc, IC 348 is expected to be even older than 5 Myr. Similarly, a larger distance would imply a younger age. For a distance of $\sim$320 pc, the luminosities would increase by approximately 30% and the inferred age would be around 1-3 Myr (Herbig, 1998; Luhman et al., 2003). Adopting a distance of 320 pc, the IC 348 mm emission distribution becomes similar similar to the Lupus and Cha I distributions, while the σ Ori distribution would be slightly less luminous than IC 348, and Upper Sco considerably lower than IC 348. On the other hand, if the distance is actually $\sim$380 pc, the luminosities would increase by approximately 50% and the mean age would be $\sim$1 Myr, which is not consistent with the IR disk fraction of the cluster ($\sim$36%). Unfortunately, we do not have a more accurate distance measurement to date and given the sensitivity of the available data, it is plausible that IC 348 Class II members are in an earlier evolutionary stage. Here, our Montecarlo simulations are scaled to a distance of 270 pc and emphasize that the comparisons of the disc luminosities are highly

dependent on the adopted distance and spectral types.

In addition, adopting spectral types as a proxy for mass also introduces uncertainties as pre-main-sequence stars, specially higher mass objects, can significantly evolve in spectral type over time. Given that the mm-emission from disks depends on the host stellar mass, the results of our statistical analysis can be influenced by the difference in stellar masses at different evolutionary stages and spectral types.

6.5.3   Disk mass vs. Stellar mass

A commonly used approximation to estimate disk masses is the use of flux densities in the millimeter wavelength regime, where the disk luminosity is proportional to the dust mass (Beckwith et al., 1990). In recent years, a Bayesian linear regression approach analysis of ALMA surveys of star-forming regions at different ages have revealed a positive relationship between dust mass and stellar mass but with a steepening of the M_{dust} - M_* relation. (e.g. Andrews et al., 2013; Ansdell et al., 2016; Pascucci et al., 2016). This method accounts for measurement errors in linear regression for detected and undetected sources, allowing one to correlate measurement errors, and to account for intrinsic scatter in the regression relationship (Kelly, 2007). Indeed, studies of Taurus, Lupus, and Chamaeleon I show that the dependence of disk mass on stellar mass is similar at an age of $\sim$ 1-3 Myr, while older regions such as σ Ori and Upper Sco present a steeper disk mass vs. stellar mass relation (Pascucci et al., 2016; Ansdell et al., 2017). The steepening of this relation with age has been interpreted in terms of an efficient inward drift of mm-sized grains (Pascucci
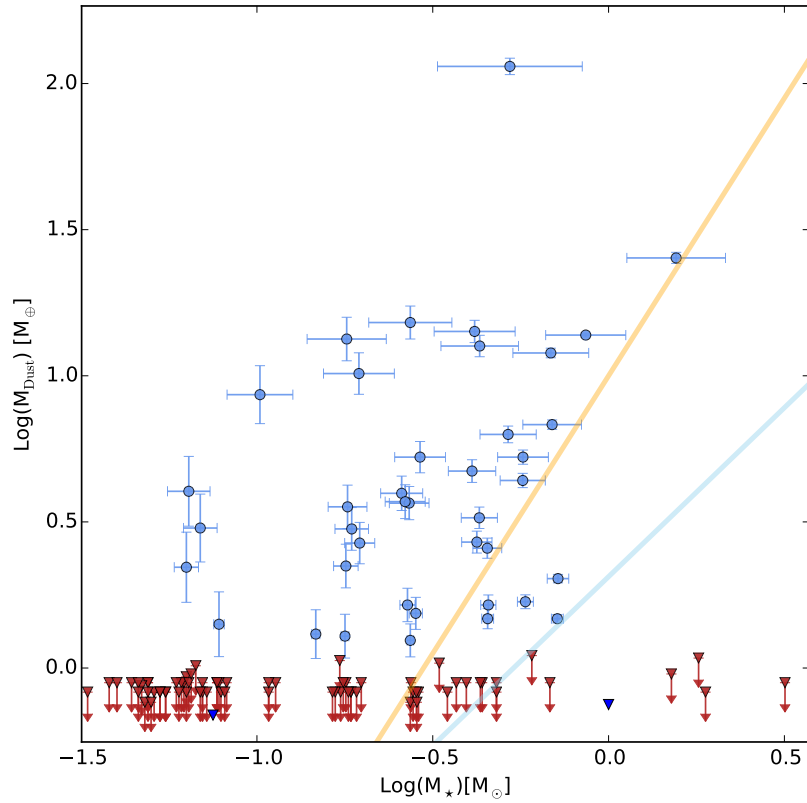
Figure 6.10: Disk dust mass as a function of stellar mass for IC 348 region. Blue circles represent the detected sources, while red triangles are 4σ upper limits for non-detections. The blue and orange solid lines represent the Bayesian linear regression obtained for IC 348 and σ Ori, respectively; see Section 6.5.3.

et al., 2016). However, the parameters describing the dependence of disk mass on stellar mass are very sensitive to the mm detection fraction and the treatment of the upper limits. In the case of IC 348, the detection fraction is low ($\sim$30 %) and is a strong function of stellar mass. As a result, most of the detections are restricted to a narrow range of stellar masses. Given these issues, a linear regression fit is not accurate enough to allow a meaningful comparison to other star-forming regions. Nevertheless, we report the resulting parameters from the "standard" methodology used in the previous studies mentioned above.

Considering all IC 348 sources in our ALMA sample, we derive slope and intercept values of $\beta = 1.13 \pm 0.25$ and $\alpha = 0.30 \pm 0.20$, where β and α are the slope and intercept, respectively. Figure 6.10 shows the linear fit obtained from the Bayesian method. Because of the difficulty in obtaining a reliable fit, we only use σ Ori as a comparison to illustrate differences between our fitting and other investigations with a wider mass range. The linear regression for σ Ori data generated values of 1.95 ± 0.37, 1.00 ± 0.20, and 0.65 ± 0.15 for β, α and δ, respectively, consistent with the values estimated by Ansdell et al. (2017). Moreover, such measurements are subject to systematic uncertainties in the assumed parameters, such as the adopted disk temperature and distances to the star-forming regions. The fitted linear regression for IC 348 provides a large intrinsic scatter of $\delta = 1.01 \pm 0.18$. Similar large intrinsic dispersions were estimated for Taurus, Lupus, Cha I, σ Ori, and Upper Sco (Pascucci et al., 2016; Ansdell et al., 2017). As previously suggested by Pascucci et al. (2016), the dispersion can be an intrinsic property of the disk population (i.e. disk masses, dust temperatures, and grain sizes) reflected in the diversity of

planetary systems.

6.5.4   CO Emission From IRAS 03410+3152

The brightest millimeter source in our sample, IRAS 03410+3152, which has a bolometric temperature of 463 K and luminosity of 1.6 $L_\odot$ (Hatchell et al., 2007), was observed previously with the Submillimeter Array by Lee, Williams & Cieza (2011). They detected a bipolar shape in the ^{12}CO emission, with prominent emission outflow lobes and a moderate opening angle. From our observations at a resolution of $0.3''$, we are able to estimate position angle (P.A.), mass and kinematics of the of the outflow following the process presented in Ruíz-Rodríguez et al. (2017c). Here, we used the ^{13}CO emission to correct for the CO optical depth and estimated the mass, momentum and kinetic energy of the outflow, see Figure 6.12. Using the C^{18}O line, we estimated a systemic velocity of ~ 8.0 km s^{-1}. Because ^{12}CO traces the bipolar and extension cavities of the outflow, we drew a line along the rotation axis to estimate a P.A. of $\sim$ -155° north through east. Additionally, taking the extent of ~ 3800 au ($14''$) and maximum speed of the ^{12}CO emission, we estimated a kinematic age of 1800 yr.

To compute the ^{12}CO mass, we apply the correction factor to all the channels with ^{13}CO detection above 4σ. In order to ensure emission only from the outflow, we built a mask around IRAS 03410+3152 of radius $3.0''$, where emission inside this area was removed from the integration. Thus, separating the red- and blue-shifted components, the blue-shifted outflow kinematics were estimated by integrating channels in the range between 5.0 and 8.0 km s^{-1} for
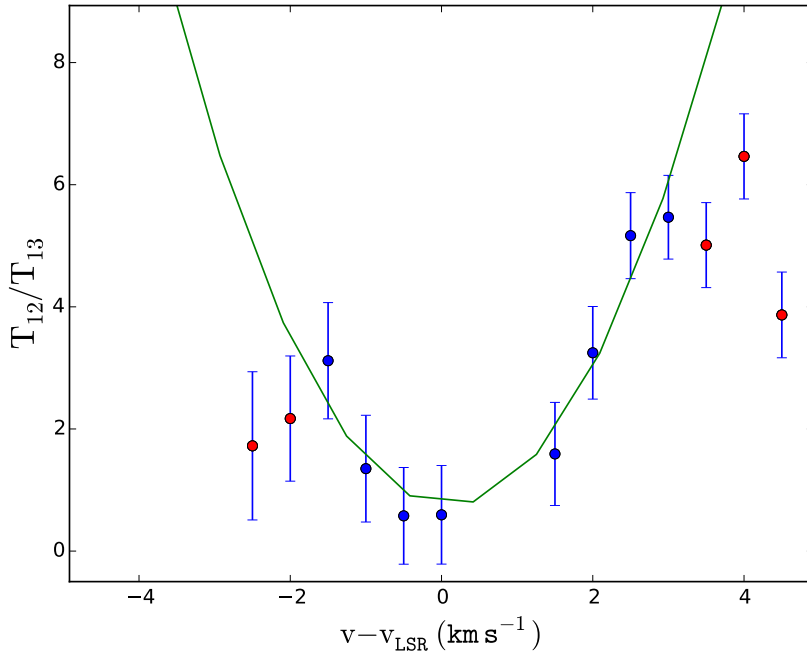
Figure 6.11: Intensity ratio between ^{12}CO and ^{13}CO function of velocity. The green solid curve is the best-fit second-order polynomial using the blue data points, more details in Ruíz-Rodríguez et al. (2017c)

^{12}CO and, 5.0 and 8.0 km s^{-1} for ^{13}CO. The range of channels in the redshifted emission is between 9.5 and 17.5 km s^{-1} for ^{12}CO and, 9.5 and 11.5 km s^{-1} for ^{13}CO. To apply the correction factor to all the channels with ^{12}CO detection, we extrapolate values from a parabola fitted to the weighted mean values, where the minimum ratio value was fixed at zero velocity. In the fitting process, we did not include those data points presented as red dots in Figure 6.11, because at these velocities ^{12}CO starts becoming optically thin. The fitted parabola has the form:

$$\frac{T_{12}}{T_{13}} = 0.11 + 0.40(\text{v-v}_{\text{LSR}})^2. \tag{6.2}$$

Table 6.6 shows the estimates at temperatures of 20 and 50 K and without correcting for inclination effects. Correcting for the ^{12}CO optical depth increases the estimated mass of the outflow, the momentum and the kinetic energy by factors of 7.5-43, 5-27, and 4-23, respectively, at a temperature of 20 K.

IRAS 03410+3152 has been identified as an optically thick Class II protostar with a slope of $\alpha_{3.6-8.0\mu m} \sim$ -0.006 (Lada et al., 2006). While the highly dereddened SED peaking in the mid-infrared clearly shows that IRAS 03410+3152 is still embedded, the presence of energetic outflows suggests that this object could be a Class I. Furthermore, the estimated outflow mass on the order of 10^{-2} M$_\odot$ is consistent with the highest mass estimates of previously reported Class 0 and I outflows, after correcting for optical depth effects (Dunham et al., 2014). The differences between these estimates can be attributed to the higher ALMA sensitivities, which facilitate the detection of weak and high-velocity emission from the outflows, thus integrating over high-resolution spectra. In table 6.6, note that the measured mass of the blue-shifted outflow is a factor of $\sim$2 lower than that of the red-shifted outflow, indicating possible differences in the environment between the cavities.
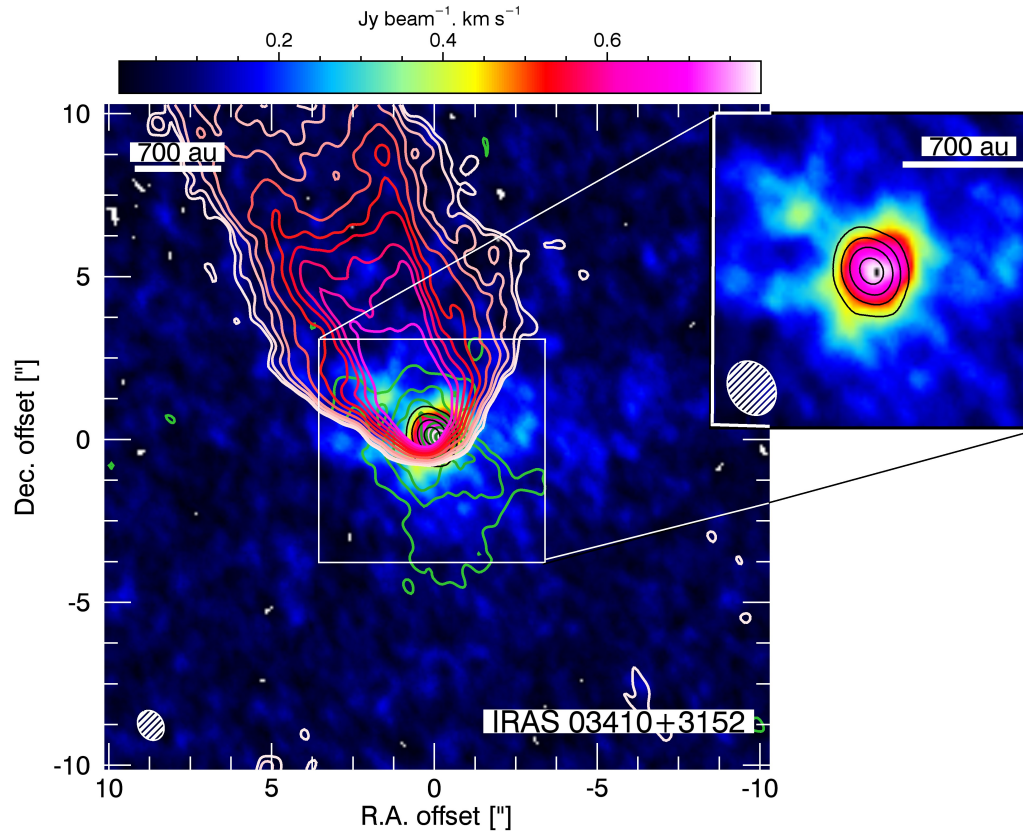
Figure 6.12: ^{13}CO intensity map (moment-0) of IRAS 03410+3152 integrated over the velocity range of 5.0 to 11.5 km s^{-1}. Black contours show the 1.3 mm continuum emission around IRAS 03410+3152 at 10, 40, 60, and 80 × rms (0.15 mJy beam^{-1}). Green and Red contours show the blue- and red- shifted moment-0 of the ^{12}CO line, respectively, at 20, 40, 80, 160 x 3σ levels. These blue- and red- shifted intensity maps are integrated over the velocity range of 5.0 to 8 km s^{-1} and 9.5 to 17.5 km s^{-1}, respectively. The synthesized beam of 0.77 arcsec × 0.63 arcsec with PA = 20.33 deg. is shown in the lower left corner. The upper right inset is a closeup ($\pm 2.5''$) of the central object.

Table 6.6: Mass, Momentum, Luminosity and Kinetic Energy of the Outflow and Envelope

Isotope	Property	Red shifted*		Blue shifted[†]	
		50 (K)	20 (K)	50 (K)	20 (K)
^{12}CO	Mass (10^{-2} M$_\odot$)	23.50 (163.40)	15.89 (110.40)	1.68 (77.73)	1.13 (52.53)
	Mass loss (10^{-6} M$_\odot$ yr^{-1})	131.18 (911.69)	88.60 (616.14)	9.36 (433.80)	6.33 (293.00)
	Momentum (10^{-2} M$_\odot$ km s^{-1})	106.00 (556.6)	72.09 (376.21)	1.53 (40.95)	1.04 (27.67)
	Energy (10^{42} ergs.)	55.38 (220.39)	37.43 (149.00)	0.25 (5.50)	0.16 (3.69)
	Luminosity (10^{-2}L$_\odot$)	25.46 (101.33)	17.21 (68.48)	0.11 (2.52)	0.08 (1.70)
^{13}CO	Mass (10^{-2} M$_\odot$)	0.16	0.11	0.08	0.55
	Mass loss (10^{-6} M$_\odot$ yr^{-1})	0.90	0.60	4.63	3.10
	Momentum (10^{-2} M$_\odot$ km s^{-1})	0.27	0.18	0.17	0.11
	Energy (10^{41} ergs.)	0.49	0.33	0.24	0.16
	Luminosity (10^{-2} L$_\odot$)	0.02	0.02	0.01	0.01

[1] Blue shifted outflow kinematics were estimated after a cut above 4σ and integration of channels between 5.0 and 8.0 km s^{-1} for ^{12}CO and 5.0 and 8.0 km s^{-1} for ^{13}CO.

[2] Red shifted outflow kinematics were estimated with a threshold value above 4σ and integration of channels between 9.5 and 17.5 km s^{-1} for ^{12}CO, and 9.5 and 11.5 km s^{-1} for ^{13}CO.

[3] Parameters inside the parentheses correspond to the computed values after applying the correction factors for optical depth effects to all the channels with ^{13}CO detection above 4σ.

6.6   Summary

We have observed 136 Class II members of the young stellar cluster IC 348 with ALMA at 1.3 mm. We reach a dust mass sensitivity of 1.0 $M_\oplus$ (3σ) and detect a total of 40 disks. The detection rate is a strong function of spectral type, as expected from the known dependence of disk mass on stellar mass. A stacking analysis of the 96 objects that were not individually detected yielded a clear 6σ detection of 0.14 mJy, indicating that these disks have a typical dust mass of just $\lesssim 0.3\ M_\oplus$, even though their infrared SEDs remain optically thick and show little signs of evolution. We compare the disk luminosity function in IC 348 to those in younger and older regions and see a clear evolution in the dust masses between 1 and 5-10 Myr. Based on the statistics of extrasolar planets (Gaidos et al., 2016; Howard et al., 2012; Burke et al., 2015), a stellar cluster like IC 348 with $\sim$400 members dominated by low-mass stars should form a very small fraction of systems ($\lesssim$5%) with giant planets, which is consistent with the number of disks with masses $> 1\ M_{\mathrm{Jup}}$ in the cluster and the presence of transition disks among this small population. The rest of the members should mostly form small rocky planets, consuming most of the primordial dust by the age of the cluster.

7

Conclusions

The main goal of this thesis is to investigate the physical components that play an important role dispersing the disk and circumstellar envelope at very early stages and thus, contribute to constrain the time availability and initial conditions for planet formation. Disk lifetimes from star-forming region observations have shown a considerable dispersion of the disk at an age of ~ 10 Myrs. While, statistical properties of circumstellar disks around young stars have shown that the fraction of young stars with optically thick primordial disks follow an exponential decay (Mamajek, 2009). Observations of these star-forming regions, especially those with a large disk frequency at early formation stages, are necessary to solve the enigma that involves the initial steps of the formation of planets.

7.0.1   Outflows in FUors

As discussed in Chapters 3 and 4, FUors are promising laboratories to investigate the core-to-star formation efficiency, early stages of disk evolution, and the dissipation of the envelope. This thesis investigates two FUor objects in particular: HBC 494 (Chapter 3) and V883 Ori (Chapter 4), using ALMA Cycle-2 observations of their molecular outflows and envelopes. HBC 494 is an FUor object embedded in the Orion A cloud and is associated with the reflection nebulae Re50 and Re50N. V883 Ori is associated with the reflection nebulosity IC 340. In both objects, we identified individual outflow and envelope structures by using ^{12}CO, ^{13}CO and C^{18}O spectral line data. The moment-1 maps of the ^{12}CO emission show the *wide* outflow cavities with opening angles of $\sim$ 150° for each object. The morphology of the wide outflow is likely to be due to the interaction between winds originating in the inner disc and the surrounding envelope.

Using these molecular line data and adopting standard methods for correcting optical depth effects, we estimate its kinematic properties, including an outflow mass. In this thesis, we note that it is important to consider the velocity range where outflows emit. For instance, a slow outflow impacts the estimates of the mass and kinematic parameters. However, it is not easy to directly compare these parameters because 1) uncertainties in the method used and 2) the few estimates in the literature differ by observing method (single dish vs. interferometer observations) and sensitivity. Nevertheless, the kinematic properties and outflow mass are of the same order as those derived in the few other FU Ori objects already published such as V2775 Ori and L1165

(Zurlo et al., 2016; Dunham et al., 2014). Future ALMA observations will provide outflow parameters the can be calculated in a systematic fashion for larger samples of FUor sources and young stellar objects in general. This will allow us to construct a more complete picture of outflows properties and the evolution of size, morphology, mass-loss rate, and angular moment dissipation across different stages (Class 0, I, and II).

ALMA long-baseline (>10 km) observations can also zoom in onto the disk of FUor sources. Recently, we observed V883 Ori at 30 mas (12 au) resolution and detect the water snow-line in a circumstellar disk for the first time (Cieza et al., 2016). The water snow-line is the region where a disk reaches the water sublimation temperature and is typically located at 3-5 au from solar-type stars. This boundary is crucial for planet formation as water ice plays a critical role in the growth of solid particles by promotion dust agglomeration and preventing fragmentation. In the case of V883 Ori, a 1.3 $M_\odot$ star, the snow-line has been moved to $\sim$40 au due to the FUor outburst, implying dramatic effects on the thermal structure of the disk. If most young stars experience a few outbursts, these sporadically events might affect the first steps of planet formation. FUOri disks are also strong candidates for gravitational instability (GI) and disk fragmentation (Zhu et al, 2012). While V883 Ori does not show evidence for GI (e.g. clumps or spiral arms) at high spatial resolution, the HBC 494 disk seems asymmetric even at low resolution hinting to structure in the disk (see Figure 3.1). To investigate the GI possibility, we have also observed HBC 494 at 30 mas (12 au) resolution in ALMA Cycle-4. The results will be presented in a future paper.

7.0.2   (Sub-)stellar Companions Dispersing Circumstellar Disks

In recent years, transition disks have atracted significant attention from the community due to their connection with different disk evolution processes. In this thesis (Chapter 5), we investigate the fraction of objects that been classified as TDs based on their SEDs that are actually circumbinary disks. Using Non-Redundant Mask interferometry, we searched for binary companions in TDs and investigated the presence of a stellar companion as a possible mechanism of material depletion in the inner region of these disks, which would prevent planet formation at distances comparable to the binary separation. The selected sample of 24 TDs belong to the nearby and young star forming regions: Ophiuchus, Taurus-Auriga and IC348. With a total of 31 objects, including 11 known TDs and circumbinary disks from the literature we find that 0.38 ± 0.09 of the SEDs of these objects are likely due to the tidal interaction between a close binary and its disk, while the remaining SEDs are likely the result of other internal processes such as photoevaporation, grain growth, planet disk interactions.

Previous observations with *Spitzer* have shown that mid-separation binaries (a $\sim$ 20-50 au) tend to destroy disks completely, removing any detectable IR excesses (Kraus & Ireland, 2012). Our close (sub-)stellar companions are detected at projected separations of only $\sim 2-10$ au, and thus are likely to inhibit planet formation at distances of up to $\sim$5-20 au from the binary systems. Since the SEDs of our targets indicate the presence of outer disks, circumbinary planets might still form at larger distances from the central stars. With future ALMA

observations of these circumbinary disk systems, we will be able to measure their basic properties (masses, sizes, and surface density profiles) and establish their planet-formation potential. Meanwhile, transition disks around single stars continue to be a focus of detail observations to investigate their origins and their connection with planet formation. Transition disks, and later pre-transition disks were originally defined as objects showing evidence for inner cavities and gaps as opposed to "continuous disks" lacking such structures. Since then, high-resolution images from ALMA (ALMA Partnership et al., 2015; Andrews, 2015) have shown that "continuous disks" might actually be the exception rather than the rule. In this context, objects previously identified as transition and pre-transition disks based on there SEDs might be a part of a continuum of objects showing structures of different scales.

7.0.3 Disk Evolution

Young stellar clusters provide an opportunity to investigate the distribution of disk properties at a given (characteristic) age. In Chapter 6, we used ALMA to study Class II objects that belong to IC 348, a benchmark 2-3 Myr stellar cluster dominates by M-type stars, and construct its disk luminosity function at 1.3 mm. By now, many other nearby clusters have been observed with ALMA at similar wavelengths allowing us to compare the results in IC 348 to those from younger and older regions. We find a clear evolution in disk masses from 1 to 5-10 Myr. The disk masses in IC 348 are significantly lower than those in Taurus (1-2 Myr) and Lupus (1-3 Myr), similar to those of Chamaleon I, (2-3 Myr) and σ-Ori (3-5 Myr) and significantly higher than in Upper Scorpius (5-10 Myr).

Statistics of extrasolar planets imply that a stellar cluster like IC 348 with $\sim$400 members dominated by low-mass stars should form a handful of systems ($\sim$5%) with giant planets (Gaidos et al., 2016; Howard et al., 2012; Burke et al., 2015). This is consistent with the number of disks with masses > 1 M_{JUP} in the IC 348 star-forming region and the presence of massive transition disks among this small population. The rest of the cluster members should mostly form small rocky planets, consuming most of the primordial dust by the age of the cluster. These basic connections between disk evolution and planet demographics are promising. However, disk mass is not only a function of stellar age, as it also depends on stellar mass, multiplicity, and even environment. Similarly, there are parameters other than disk mass than are important for planet formation, including sizes, surface density profiles, and metallicities. Investigating all relevant disk properties as a function of age, stellar mass, multiplicity, and environment will require larger samples and deeper (sub-)millimeter observations at higher resolution. Meanwhile, our knowledge of planet demographics is continuously expanding, and we can expect to see the fields of disk evolution and extrasolar planets to get closer together with time.

Bibliography

Ahn C. P. et al., 2012, ApJS, 203, 21

Alcalá J. M. et al., 2014, A&A, 561, A2

Alexander R., Pascucci I., Andrews S., Armitage P., Cieza L., 2014, Protostars
and Planets VI, 475

Alexander R. D., Armitage P. J., 2007, MNRAS, 375, 500

Alexander R. D., Clarke C. J., Pringle J. E., 2006a, MNRAS, 369, 216

Alexander R. D., Clarke C. J., Pringle J. E., 2006b, MNRAS, 369, 229

Allard F., 2014, in IAU Symposium, Vol. 299, IAU Symposium, Booth M.,
Matthews B. C., Graham J. R., eds., pp. 271–272

Allen D. A., Strom K. M., Grasdalen G. L., Strom S. E., Merrill K. M., 1975,
MNRAS, 173, 47P

ALMA Partnership et al., 2015, ApJL, 808, L3

Alves F. O., Girart J. M., Caselli P., Franco G. A. P., Zhao B., Vlemmings
W. H. T., Evans M. G., Ricci L., 2017, A&A, 603, L3

Alzner A., 1998, A&AS, 132, 237

Ambartsumian V. A., 1937, Astron. Zh., 14, 207

André P., 2002, in EAS Publications Series, Vol. 3, EAS Publications Series, Bouvier J., Zahn J.-P., eds., pp. 1–38

Andrews S. M., 2015, PASP, 127, 961

Andrews S. M., Rosenfeld K. A., Kraus A. L., Wilner D. J., 2013, ApJ, 771, 129

Andrews S. M., Williams J. P., 2005, ApJ, 631, 1134

Andrews S. M., Williams J. P., 2007, ApJ, 671, 1800

Andrews S. M., Wilner D. J., Espaillat C., Hughes A. M., Dullemond C. P., McClure M. K., Qi C., Brown J. M., 2011, ApJ, 732, 42

Ansdell M., Williams J. P., Manara C. F., Miotello A., Facchini S., van der Marel N., Testi L., van Dishoeck E. F., 2017, AJ, 153, 240

Ansdell M. et al., 2016, ArXiv e-prints

Arce H. G., Goodman A. A., 2001, ApJ, 554, 132

Arce H. G., Sargent A. I., 2004, ApJ, 612, 342

Arce H. G., Sargent A. I., 2006, ApJ, 646, 1070

Armitage P. J., Livio M., Pringle J. E., 2001, MNRAS, 324, 705

Artymowicz P., Lubow S. H., 1994, ApJ, 421, 651

Aso Y. et al., 2015, ApJ, 812, 27

Aspin C., 2011, AJ, 142, 135

Audard M. et al., 2014, Protostars and Planets VI, 387

Bai X.-N., 2016, ApJ, 821, 80

Bai X.-N., Stone J. M., 2013, ApJ, 769, 76

Bai X.-N., Ye J., Goodman J., Yuan F., 2016, ApJ, 818, 152

Baraffe I., Homeier D., Allard F., Chabrier G., 2015, A&A, 577, A42

Barenfeld S. A., Carpenter J. M., Ricci L., Isella A., 2016, ApJ, 827, 142

Bastian U., Mundt R., 1985, A&A, 144, 57

Basu S., 1998, ApJ, 509, 229

Batalha N. M., 2014, Proceedings of the National Academy of Science, 111, 12647

Bayo A., Rodrigo C., Barrado Y Navascués D., Solano E., Gutiérrez R., Morales-Calderón M., Allard F., 2008, A&A, 492, 277

Beckwith S. V. W., Sargent A. I., Chini R. S., Guesten R., 1990, AJ, 99, 924

Bell C. P. M., Naylor T., Mayne N. J., Jeffries R. D., Littlefair S. P., 2013, MNRAS, 434, 806

Bernstein R., Shectman S. A., Gunnels S. M., Mochnacki S., Athey A. E., 2003, in , Vol. 4841, Instrument Design and Performance for Optical/Infrared Ground-based Telescopes, Iye M., Moorwood A. F. M., eds., pp. 1694–1704

Beuermann K. et al., 2011, A&A, 526, A53

Bjerkeli P., van der Wiel M. H. D., Harsono D., Ramsey J. P., Jørgensen J. K., 2016, Nature, 540, 406

Blandford R. D., Payne D. G., 1982, MNRAS, 199, 883

Bonnell I., Bastien P., 1992, ApJ, 401, L31

Boss A. P., 2001, ApJ, 563, 367

Bouvier J., Appenzeller I., 1992, A&AS, 92, 481

Bradshaw C., Offner S. S. R., Arce H. G., 2015, ApJ, 802, 86

Bressan A., Marigo P., Girardi L., Salasnich B., Dal Cero C., Rubele S., Nanni A., 2012, MNRAS, 427, 127

Burke C. J. et al., 2015, ApJ, 809, 8

Cabrit S., Bertout C., 1990, ApJ, 348, 530

Calvet N., D'Alessio P., Hartmann L., Wilner D., Walsh A., Sitko M., 2002, ApJ, 568, 1008

Calvet N., Hartmann L., Kenyon S. J., 1993, ApJ, 402, 623

Canovas H., Caceres C., Schreiber M. R., Hardy A., Cieza L., Ménard F., Hales A., 2016, ArXiv e-prints

Caratti o Garatti A. et al., 2012, A&A, 538, A64

Cardelli J. A., Clayton G. C., Mathis J. S., 1989, ApJ, 345, 245

Carilli C. L., Walter F., 2013, ARA&A, 51, 105

Cernis K., 1993, Baltic Astronomy, 2, 214

Chambers J., 2011, Terrestrial Planet Formation, Seager S., ed., pp. 297–317

Cheetham A. C., Kraus A. L., Ireland M. J., Cieza L., Rizzuto A. C., Tuthill P. G., 2015, ApJ, 813, 83

Chen H., Myers P. C., Ladd E. F., Wood D. O. S., 1995, ApJ, 445, 377

Chiang E., Murray-Clay R., 2007, Nature Physics, 3, 604

Chiang E. I., Goldreich P., 1997, ApJ, 490, 368

Chiang E. I., Joung M. K., Creech-Eakman M. J., Qi C., Kessler J. E., Blake G. A., van Dishoeck E. F., 2001, ApJ, 547, 1077

Chiang H.-F., Reipurth B., Walawender J., Connelley M. S., Pessev P., Geballe T. R., Best W. M. J., Paegert M., 2015, ApJ, 805, 54

Cieza L. et al., 2007, ApJ, 667, 308

Cieza L., Williams J., Kourkchi E., Andrews S., Casassus S., Graves S., Schreiber M. R., 2015, MNRAS, 454, 1909

Cieza L. A. et al., 2016, Nature, 535, 258

Cieza L. A. et al., In Prep., ApJ

Cieza L. A. et al., 2013, ApJL, 762, L12

Cieza L. A. et al., 2012a, ApJ, 752, 75

Cieza L. A. et al., 2010, ApJ, 712, 925

Cieza L. A., Schreiber M. R., Romero G. A., Williams J. P., Rebassa-Mansergas A., Merín B., 2012b, ApJ, 750, 157

Clarke C. J., Gendrin A., Sotomayor M., 2001, MNRAS, 328, 485

Cohen M., Kuhi L. V., 1979, ApJS, 41, 743

Comeron F., 2008, The Lupus Clouds, Reipurth B., ed., p. 295

Currie T., Kenyon S. J., 2009, AJ, 138, 703

Curtis E. I., Richer J. S., Swift J. J., Williams J. P., 2010, MNRAS, 408, 1516

Cutri R. M. et al., 2003, VizieR Online Data Catalog, 2246

D'Alessio P. et al., 2005, ApJ, 621, 461

Davies R., Kasper M., 2012, ARA&A, 50, 305

de Zeeuw P. T., Hoogerwerf R., de Bruijne J. H. J., Brown A. G. A., Blaauw
    A., 1999, AJ, 117, 354

Dodson-Robinson S. E., Salyk C., 2011, ApJ, 738, 131

Donati J.-F., Paletou F., Bouvier J., Ferreira J., 2005, Nature, 438, 466

Duchêne G., Ghez A. M., McCabe C., Weinberger A. J., 2003, ApJ, 592, 288

Dullemond C. P., Dominik C., Natta A., 2001, ApJ, 560, 957

Dullemond C. P., Hollenbach D., Kamp I., D'Alessio P., 2007, Protostars and
    Planets V, 555

Dullemond C. P., Monnier J. D., 2010, ARA&A, 48, 205

Dunham M. M., Arce H. G., Mardones D., Lee J.-E., Matthews B. C., Stutz
    A. M., Williams J. P., 2014, ApJ, 783, 29

Dunham M. M., Chen X., Arce H. G., Bourke T. L., Schnee S., Enoch M. L., 2011, ApJ, 742, 1

Dunham M. M., Evans N. J., Bourke T. L., Myers P. C., Huard T. L., Stutz A. M., 2010, ApJ, 721, 995

Duquennoy A., Mayor M., 1991, A&A, 248, 485

Dvorak R., Froeschle C., Froeschle C., 1986, in , Vol. 18, Bulletin of the American Astronomical Society, p. 842

Eisner J. A., Hillenbrand L. A., 2011, ApJ, 738, 9

Ercolano B., Glassgold A. E., 2013, MNRAS, 436, 3446

Espaillat C., Andrews S., Powell D., Feldman D., Qi C., Wilner D., DAlessio P., 2015, ApJ, 807, 156

Espaillat C., Calvet N., D'Alessio P., Hernández J., Qi C., Hartmann L., Furlan E., Watson D. M., 2007, ApJL, 670, L135

Espaillat C. et al., 2010, ApJ, 717, 441

Espaillat C., Furlan E., D'Alessio P., Sargent B., Nagel E., Calvet N., Watson D. M., Muzerolle J., 2011, ApJ, 728, 49

Espaillat C. et al., 2012, ApJ, 747, 103

Espaillat C. et al., 2014, Protostars and Planets VI, 497

Evans N. et al., 2009a, ArXiv e-prints

Evans, II N. J. et al., 2003, PASP, 115, 965

Evans, II N. J., Balkum S., Levreault R. M., Hartmann L., Kenyon S., 1994, ApJ, 424, 793

Evans, II N. J. et al., 2009b, ApJS, 181, 321

Federrath C., Schrön M., Banerjee R., Klessen R. S., 2014, ApJ, 790, 128

Feigelson E. D., Nelson P. I., 1985, ApJ, 293, 192

Flaherty K. M., Muzerolle J., Rieke G., Gutermuth R., Balog Z., Herbst W., Megeath S. T., Kun M., 2011, ApJ, 732, 83

Forrest W. J. et al., 2004, ApJS, 154, 443

Frank A. et al., 2014, Protostars and Planets VI, 451

Frank J., King A., Raine D. J., 2002, Accretion Power in Astrophysics: Third Edition

Frerking M. A., Langer W. D., Wilson R. W., 1982, ApJ, 262, 590

Furlan E. et al., 2016, ApJS, 224, 5

Furlan E. et al., 2006, ApJS, 165, 568

Furlan E. et al., 2011, ApJS, 195, 3

Furuya I., Nakagawa Y., 2001, in Bulletin of the American Astronomical Society, Vol. 33, AAS/Division for Planetary Sciences Meeting Abstracts #33, p. 1059

Gaidos E., Mann A. W., Kraus A. L., Ireland M., 2016, MNRAS, 457, 2877

Gardiner T. A., Frank A., Hartmann L., 2003, ApJ, 582, 269

Garufi A. et al., 2013, A&A, 560, A105

Glickman M., van D. D., 2007, Methods Mol Biol, 404, 319

Goldsmith P. F., Snell R. L., Hemeon-Heyer M., Langer W. D., 1984, ApJ, 286, 599

Green J. D. et al., 2013, ApJ, 770, 123

Green J. D., Hartmann L., Calvet N., Watson D. M., Ibrahimov M., Furlan E., Sargent B., Forrest W. J., 2006, ApJ, 648, 1099

Greene T. P., Wilking B. A., Andre P., Young E. T., Lada C. J., 1994, ApJ, 434, 614

Gressel O., Turner N. J., Nelson R. P., McNally C. P., 2015, ApJ, 801, 84

Guenther E. W., Esposito M., Mundt R., Covino E., Alcalá J. M., Cusano F., Stecklum B., 2007, A&A, 467, 1147

Gustafsson B., Edvardsson B., Eriksson K., Jørgensen U. G., Nordlund Å., Plez B., 2008, A&A, 486, 951

Hales A. S., Corder S. A., Dent W. R. D., Andrews S. M., Eisner J. A., Cieza L. A., 2015, ApJ, 812, 134

Haro G., 1953, ApJ, 117, 73

Harris D. L., Morgan W. W., Roman N. G., 1954, ApJ, 119, 622

Harris R. J., Andrews S. M., Wilner D. J., Kraus A. L., 2012, ApJ, 751, 115

Hartmann L., 2001, AJ, 121, 1030

Hartmann L., 2008, Accretion Processes in Star Formation

Hartmann L., Calvet N., 1995, AJ, 109, 1846

Hartmann L., Calvet N., Gullbring E., D'Alessio P., 1998, ApJ, 495, 385

Hartmann L., Herczeg G., Calvet N., 2016, ARA&A, 54, 135

Hartmann L., Kenyon S. J., 1985, ApJ, 299, 462

Hartmann L., Kenyon S. J., 1996, ARA&A, 34, 207

Hatchell J., Fuller G. A., Richer J. S., Harries T. J., Ladd E. F., 2007, A&A, 468, 1009

Herbig G. H., 1954, PASP, 66, 19

Herbig G. H., 1966, Vistas in Astronomy, 8, 109

Herbig G. H., 1977, ApJ, 217, 693

Herbig G. H., 1998, ApJ, 497, 736

Herbig G. H., Jones B. F., 1983, AJ, 88, 1040

Herbig G. H., Petrov P. P., Duemmler R., 2003, ApJ, 595, 384

Herczeg G. J., Hillenbrand L. A., 2008, ApJ, 681, 594

Hildebrand R. H., 1983, , 24, 267

Hillenbrand L. A., Bauermeister A., White R. J., 2008, in Astronomical Society of the Pacific Conference Series, Vol. 384, 14th Cambridge Workshop on Cool Stars, Stellar Systems, and the Sun, van Belle G., ed., p. 200

Hirota T., 2010, in 10th European VLBI Network Symposium and EVN Users Meeting: VLBI and the New Generation of Radio Arrays, p. 63

Hirota T. et al., 2008, PASJ, 60, 37

Howard A. W. et al., 2012, ApJS, 201, 15

Huélamo N., de Gregorio-Monsalvo I., Macias E., Pinte C., Ireland M., Tuthill P., Lacour S., 2015, A&A, 575, L5

Huélamo N., Lacour S., Tuthill P., Ireland M., Kraus A., Chauvin G., 2011, A&A, 528, L7

Ireland M. J., Kraus A., Martinache F., Lloyd J. P., Tuthill P. G., 2008, ApJ, 678, 463

Ireland M. J., Kraus A. L., 2008, ApJL, 678, L59

Isella A., Natta A., 2005, A&A, 438, 899

Janson M. et al., 2012, ApJ, 754, 44

Jeffreys H., 1998, Theory of probability, Oxford Classic Texts in the Physical Sciences. The Clarendon Press, Oxford University Press, New York, pp. xii+459, reprint of the 1983 edition

Johnson J. A., Aller K. M., Howard A. W., Crepp J. R., 2010, PASP, 122, 905

Jørgensen J. K., Schöier F. L., van Dishoeck E. F., 2002, A&A, 389, 908

Joy A. H., 1945, ApJ, 102, 168

Kelly B. C., 2007, ApJ, 665, 1489

Kelson D. D., 2003, PASP, 115, 688

Kenyon S. J., Hartmann L., 1995, ApJS, 101, 117

Klaassen P. D. et al., 2013, A&A, 555, A73

Klaassen P. D., Mottram J. C., Maud L. T., Juhasz A., 2016, MNRAS, 460, 627

Kley W., 2000, in IAU Symposium, Vol. 200, IAU Symposium, p. 211

Kley W., Nelson R., 2007, ArXiv e-prints

Koepferl C. M., Ercolano B., Dale J., Teixeira P. S., Ratzka T., Spezzi L., 2013, MNRAS, 428, 3327

Kohn S. A., Shkolnik E. L., Weinberger A. J., Carlberg J. K., Llama J., 2016, ApJ, 820, 2

Konigl A., Pudritz R. E., 2000, Protostars and Planets IV, 759

Königl A., Romanova M. M., Lovelace R. V. E., 2011, MNRAS, 416, 757

Kraus A. L., Andrews S. M., Bowler B. P., Herczeg G., Ireland M. J., Liu M. C., Metchev S., Cruz K. L., 2015, ApJL, 798, L23

Kraus A. L., Ireland M. J., 2012, ApJ, 745, 5

Kraus A. L., Ireland M. J., Huber D., Mann A. W., Dupuy T. J., 2016, ArXiv e-prints

Kristensen L. E. et al., 2012, A&A, 542, A8

Krumholz M. R., Klein R. I., McKee C. F., 2012, ApJ, 754, 71

Kuzuhara M. et al., 2013, ApJ, 774, 11

Kwan J., Scoville N., 1976, ApJL, 210, L39

Laakkonen T., 2000, in ESA Special Publication, Vol. 445, Star Formation from the Small to the Large Scale, Favata F., Kaas A., Wilson A., eds., p. 445

Lada C., Dickinson D. F., Penfield H., 1974, ApJL, 189, L35

Lada C. J., Lombardi M., Alves J. F., 2009, ApJ, 703, 52

Lada C. J. et al., 2006, AJ, 131, 1574

Lada E. A., Lada C. J., 1995, AJ, 109, 1682

Lafrenière D., Jayawardhana R., van Kerkwijk M. H., 2008, ApJL, 689, L153

Langer W. D., Penzias A. A., 1993, ApJ, 408, 539

Le Blanc T. S., Covey K. R., Stassun K. G., 2011, AJ, 142, 55

Lee C.-F., Ho P. T. P., 2005, ApJ, 624, 841

Lee C.-F., Mundy L. G., Reipurth B., Ostriker E. C., Stone J. M., 2000, ApJ, 542, 925

Lee J.-E., Park S., Green J. D., Cochran W. D., Kang W., Lee S.-G., Sung H.-I., 2015, ApJ, 807, 84

Lee N., Williams J. P., Cieza L. A., 2011, ApJ, 736, 135

Léna P., Rouan D., Lebrun F., Mignard F., Pelat D., 2012, Observational Astrophysics

Liu Y., Joergens V., Bayo A., Nielbock M., Wang H., 2015, A&A, 582, A22

Lodato G., Clarke C. J., 2004, MNRAS, 353, 841

Loinard L., Torres R. M., Mioduszewski A. J., Rodríguez L. F., 2008, in IAU Symposium, Vol. 248, IAU Symposium, Jin W. J., Platais I., Perryman M. A. C., eds., pp. 186–189

Lubow S. H., Artymowicz P., 2000, Protostars and Planets IV, 731

Lubow S. H., Seibert M., Artymowicz P., 1999, ApJ, 526, 1001

Luhman K. L., 1999, ApJ, 525, 466

Luhman K. L., 2003, in IAU Symposium, Vol. 211, Brown Dwarfs, Martín E., ed., p. 103

Luhman K. L., 2007, ApJS, 173, 104

Luhman K. L., Esplin T. L., Loutrel N. P., 2016, ApJ, 827, 52

Luhman K. L., Mamajek E. E., Allen P. R., Cruz K. L., 2009, ApJ, 703, 399

Luhman K. L., McLeod K. K., Goldenson N., 2005, ApJ, 623, 1141

Luhman K. L., Rieke G. H., Lada C. J., Lada E. A., 1998, ApJ, 508, 347

Luhman K. L., Stauffer J. R., Muench A. A., Rieke G. H., Lada E. A., Bouvier J., Lada C. J., 2003, ApJ, 593, 1093

Magnier E. A. et al., 2013, ApJS, 205, 20

Mamajek E. E., 2008, Astronomische Nachrichten, 329, 10

Mamajek E. E., 2009, in American Institute of Physics Conference Series, Vol. 1158, American Institute of Physics Conference Series, Usuda T., Tamura M., Ishii M., eds., pp. 3–10

Marois C., Macintosh B., Barman T., Zuckerman B., Song I., Patience J., Lafrenière D., Doyon R., 2008, Science, 322, 1348

Martin R. G., Lubow S. H., 2011, ApJL, 740, L6

Martinache F., 2011, in Society of Photo-Optical Instrumentation Engineers (SPIE) Conference Series, Vol. 8151, Society of Photo-Optical Instrumentation Engineers (SPIE) Conference Series

Mathis J. S., 1990, in Astronomical Society of the Pacific Conference Series, Vol. 12, The Evolution of the Interstellar Medium, Blitz L., ed., pp. 63–77

McMullin J. P., Waters B., Schiebel D., Young W., Golap K., 2007, in Astronomical Society of the Pacific Conference Series, Vol. 376, Astronomical Data Analysis Software and Systems XVI, Shaw R. A., Hill F., Bell D. J., eds., p. 127

Meeus J., 1992, Journal of the British Astronomical Association, 102, 109

Menten K. M., Reid M. J., Forbrich J., Brunthaler A., 2007, A&A, 474, 515

Merín B. et al., 2010, ApJ, 718, 1200

Metchev S. A., Hillenbrand L. A., 2009, ApJS, 181, 62

Michalik D., Lindegren L., Hobbs D., 2015, A&A, 574, A115

Miller A. A. et al., 2011, ApJ, 730, 80

Mordasini C., Alibert Y., Benz W., Klahr H., Henning T., 2012, A&A, 541, A97

Mottram J. C., van Dishoeck E. F., Schmalzl M., Kristensen L. E., Visser R., Hogerheijde M. R., Bruderer S., 2013, A&A, 558, A126

Mould J. R., Hall D. N. B., Ridgway S. T., Hintzen P., Aaronson M., 1978, ApJL, 222, L123

Muench A. A., Lada C. J., Luhman K. L., Muzerolle J., Young E., 2007, AJ, 134, 411

Muzerolle J., Allen L. E., Megeath S. T., Hernández J., Gutermuth R. A., 2010, ApJ, 708, 1107

Nagel E., D'Alessio P., Calvet N., Espaillat C., Sargent B., Hernández J., Forrest W. J., 2010, ApJ, 708, 38

Najita J. R., Andrews S. M., Muzerolle J., 2015, MNRAS, 450, 3559

Najita J. R., Carr J. S., Glassgold A. E., Valenti J. A., 2007, Protostars and Planets V, 507

Nakajima T., Nagata T., Nishida M., Sato S., Kawara K., 1986, MNRAS, 221, 483

Nelson R. P., Papaloizou J. C. B., Masset F., Kley W., 2000, MNRAS, 318, 18

Nomura H. et al., 2016, ApJL, 819, L7

Offner S. S. R., Clark P. C., Hennebelle P., Bastian N., Bate M. R., Hopkins P. F., Moraux E., Whitworth A. P., 2014, Protostars and Planets VI, 53

Oliveira J. M., Jeffries R. D., Kenyon M. J., Thompson S. A., Naylor T., 2002, A&A, 382, L22

Olofsson J., Szűcs L., Henning T., Linz H., Pascucci I., Joergens V., 2013, A&A, 560, A100

Orellana M., Cieza L. A., Schreiber M. R., Merín B., Brown J. M., Pellizza L. J., Romero G. A., 2012, A&A, 539, A41

Ostriker E. C., Lee C.-F., Stone J. M., Mundy L. G., 2001, ApJ, 557, 443

Owen J. E., Clarke C. J., 2012a, MNRAS, 426, L96

Owen J. E., Clarke C. J., 2012b, MNRAS, 426, L96

Pascucci I., Apai D., Hardegree-Ullman E. E., Kim J. S., Meyer M. R., Bouwman J., 2008, ApJ, 673, 477

Pascucci I. et al., 2016, ApJ, 831, 125

Pecaut M. J., Mamajek E. E., 2013, ApJS, 208, 9

Pecaut M. J., Mamajek E. E., Bubar E. J., 2012, ApJ, 746, 154

Pelletier G., Pudritz R. E., 1992, ApJ, 394, 117

Pérez L. M., Isella A., Carpenter J. M., Chandler C. J., 2014, ApJL, 783, L13

Petrov P. P., Herbig G. H., 1992, ApJ, 392, 209

Pinilla P., Benisty M., Birnstiel T., 2012, A&A, 545, A81

Pollack J. B., Hubickyj O., Bodenheimer P., Lissauer J. J., Podolak M., Greenzweig Y., 1996, Icarus, 124, 62

Pott J.-U., Perrin M. D., Furlan E., Ghez A. M., Herbst T. M., Metchev S., 2010, ApJ, 710, 265

Powell S. L., Irwin M., Bouvier J., Clarke C. J., 2012, MNRAS, 426, 3315

Pravdo S. H., Shaklan S. B., Wiktorowicz S. J., Kulkarni S., Lloyd J. P., Martinache F., Tuthill P. G., Ireland M. J., 2006, ApJ, 649, 389

Principe D. A. et al., In Prep., MNRAS

Pudritz R. E., Norman C. A., 1986, ApJ, 301, 571

Pudritz R. E., Ouyed R., Fendt C., Brandenburg A., 2007, Protostars and Planets V, 277

Quanz S. P., Henning T., Bouwman J., van Boekel R., Juhász A., Linz H., Pontoppidan K. M., Lahuis F., 2007, ApJ, 668, 359

Raga A., Cabrit S., 1993, A&A, 278, 267

Raghavan D. et al., 2010, ApJS, 190, 1

Rameau J. et al., 2013, ApJL, 779, L26

Ramsey L. W. et al., 1998, in SPIE, Vol. 3352, Advanced Technology Optical/IR Telescopes VI, Stepp L. M., ed., pp. 34–42

Rapson V. A., Kastner J. H., Millar-Blanchaer M. A., Dong R., 2015, ArXiv e-prints

Rebollido I. et al., 2015, ArXiv e-prints

Rebull L. M. et al., 2010, ApJS, 186, 259

Reipurth B., 1985, A&AS, 61, 319

Reipurth B., Bally J., 1986, Nature, 320, 336

Reipurth B., Hartmann L., Kenyon S. J., Smette A., Bouchet P., 2002, AJ, 124, 2194

Ribas Á., Merín B., Bouy H., Maud L. T., 2014, A&A, 561, A54

Rice W. K. M., Armitage P. J., Wood K., Lodato G., 2006a, MNRAS, 373, 1619

Rice W. K. M., Lodato G., Pringle J. E., Armitage P. J., Bonnell I. A., 2006b, MNRAS, 372, L9

Ripepi V. et al., 2014, MNRAS, 437, 906

Roell T., Neuhäuser R., Seifahrt A., Mugrauer M., 2012, A&A, 542, A92

Romanova M. M., Ustyugova G. V., Koldoba A. V., Lovelace R. V. E., 2005, ApJL, 635, L165

Rosotti G. P., Ercolano B., Owen J. E., 2015, ArXiv e-prints

Ruíz-Rodríguez D., Cieza L. A., Williams J. P., Principe D., Tobin J. J., Zhu Z., Zurlo A., 2017a, MNRAS, 468, 3266

Ruíz-Rodríguez D. et al., 2017b, MNRAS, 466, 3519

Ruíz-Rodríguez D. et al., 2017c, MNRAS, 466, 3519

Ruíz-Rodríguez D., Ireland M., Cieza L., Kraus A., 2016a, MNRAS, 463, 3829

Ruíz-Rodríguez D., Ireland M., Cieza L., Kraus A., 2016b, MNRAS, 463, 3829

Saha S. K., 2007, Diffraction-Limited Imaging with Large and Moderate Telescopes

Sandell G., Weintraub D. A., 2001, ApJS, 134, 115

Scholz A., Froebrich D., Wood K., 2013, MNRAS, 430, 2910

Scholz R.-D. et al., 1999, A&AS, 137, 305

Seale J. P., Looney L. W., 2008, ApJ, 675, 427

Semkov E. H., Peneva S. P., Munari U., Milani A., Valisa P., 2010, A&A, 523, L3

Semkov E. H. et al., 2012, A&A, 542, A43

Shakura N. I., Sunyaev R. A., 1973, in IAU Symposium, Vol. 55, X- and Gamma-Ray Astronomy, Bradt H., Giacconi R., eds., p. 155

Shang H., Shu F. H., Glassgold A. E., 1998, ApJ, 493, L91

Shu F. H., Najita J. R., Shang H., Li Z.-Y., 2000, Protostars and Planets IV, 789

Sicilia-Aguilar A. et al., 2006, ApJ, 638, 897

Siess L., 2001, in Astronomical Society of the Pacific Conference Series, Vol. 243, From Darkness to Light: Origin and Evolution of Young Stellar Clusters, Montmerle T., André P., eds., p. 581

Siess L., Dufour E., Forestini M., 2000, An internet server for pre-main sequence tracks of low- and intermediate-mass stars

Simon M. et al., 1995, ApJ, 443, 625

Skrutskie M. F. et al., 2006, AJ, 131, 1163

Snell R. L., Loren R. B., Plambeck R. L., 1980, ApJ, 239, L17

Strom K. M., Strom S. E., 1993, ApJL, 412, L63

Strom K. M., Strom S. E., Edwards S., Cabrit S., Skrutskie M. F., 1989, AJ, 97, 1451

Sun K., Kramer C., Ossenkopf V., Bensch F., Stutzki J., Miller M., 2006, A&A, 451, 539

Terebey S., Shu F. H., Cassen P., 1984, ApJ, 286, 529

Terquem C., Eislöffel J., Papaloizou J. C. B., Nelson R. P., 1999, ApJ, 512, L131

Tull R. G., 1998, in SPIE, Vol. 3355, Optical Astronomical Instrumentation, D'Odorico S., ed., pp. 387–398

Vacca W. D., Sheehy C. D., Graham J. R., 2007, ApJ, 662, 272

van der Marel N., van Dishoeck E. F., Bruderer S., Andrews S. M., Pontoppidan K. M., Herczeg G. J., van Kempen T., Miotello A., 2016, A&A, 585, A58

van der Marel N., van Dishoeck E. F., Bruderer S., Pérez L., Isella A., 2015, A&A, 579, A106

van der Marel N. et al., 2018, ArXiv e-prints

Velusamy T., Langer W. D., 1998, Nature, 392, 685

Vorobyov E. I., Basu S., 2005, ApJ, 633, L137

Watson D. M. et al., 2015, ArXiv e-prints

Welty A. D., Strom S. E., Edwards S., Kenyon S. J., Hartmann L. W., 1992, ApJ, 397, 260

Wilking B. A., Gagné M., Allen L. E., 2008, Star Formation in the ρ Ophiuchi Molecular Cloud, Reipurth B., ed., p. 351

Williams J. P., Best W. M. J., 2014, ApJ, 788, 59

Williams J. P., Cieza L. A., 2011, ARA&A, 49, 67

Wu Y., Wei Y., Zhao M., Shi Y., Yu W., Qin S., Huang M., 2004, A&A, 426, 503

Yelda S., Lu J. R., Ghez A. M., Clarkson W., Anderson J., Do T., Matthews K., 2010, ApJ, 725, 331

Zhu Z., Hartmann L., Gammie C., McKinney J. C., 2009, ApJ, 701, 620

Zurlo A. et al., 2016, MNRAS